GRANT / LEWIS

2187

OSU

The Ohio State University

IN-29074

A HIGH FREQUENCY ANALYSIS OF ELECTROMAGNETIC PLANE WAVE SCATTERING BY PERFECTLY-CONDUCTING SEMI-INFINITE PARALLEL PLATE AND RECTANGULAR WAVEGUIDES WITH ABSORBER COATED INNER WALLS

Noh Hoon Myung
Prabhakar H. Pathak

The Ohio State University
ElectroScience Laboratory
Department of Electrical Engineering
Columbus, Ohio 43212

Technical Report 715723-1
Grant NAG 3-476
September 1986

National Aeronautics and Space Administration
Lewis Research Center
21000 Brookpark Road
Cleveland, Ohio 44135

NOTICES

When Government drawings, specifications, or other data are used for any purpose other than in connection with a definitely related Government procurement operation, the United States Government thereby incurs no responsibility nor any obligation whatsoever, and the fact that the Government may have formulated, furnished, or in any way supplied the said drawings, specifications, or other data, is not to be regarded by implication or otherwise as in any manner licensing the holder or any other person or corporation, or conveying any rights or permission to manufacture, use, or sell any patented invention that may in any way be related thereto.

TABLE OF CONTENTS

LIST OF FIGURES vi

LIST OF TABLES xx

I. INTRODUCTION 1

II. ANALYSIS OF EXACT MODAL AND APPROXIMATE RAY SOLUTIONS FOR AN INFINITELY LONG PARALLEL PLATE WAVEGUIDE WITH AN IMPEDANCE BOUNDARY CONDITION ON ITS INNER WALLS 9

2.1 Formulation of the problem 9

2.2 Surface waves in the modal and ray solutions 33

2.3 Convergence test of the modal and ray solutions 43

III. ANALYSIS OF ELECTROMAGNETIC SCATTERING FROM AN OPEN-ENDED PARALLEL PLATE WAVEGUIDE WITH LOSSY INNER WALLS 56

3.1 Ray solution for the interior fields of an open-ended parallel plate waveguide with an impedance boundary condition on its inner walls 56
3.1.1 Geometrical optics (GO) field 57
3.1.2 Edge diffracted rays 61
3.1.3 Total UTD ray field 66
3.2 Ray solution for the interior fields of an open-ended parallel plate waveguide coated with an absorbing material on its inner walls . 85
3.3 Ray solution for the interior fields of an open-ended parallel plate waveguide coated with an absorbing material on its inner walls and with a planar termination inside 86
3.4 Field backscattered from a semi-infinite parallel plate waveguide with an impedance boundary condition on its inner walls 98
3.5 Field radiated from the interior cavity region formed by the semi-infinite waveguide and its interior planar termination 101

IV. ANALYSIS OF ELECTROMAGNETIC SCATTERING FROM A RECTANGULAR WAVEGUIDE WITH LOSSY INNER WALLS 131
4.1 Ray solution for the interior fields of a semi-infinite rectangular waveguide with lossy interior walls 131
4.1.1 Geometrical Optics (GO) fields 133
4.1.2 Edge diffracted fields 140
4.2 Ray solution for the interior field of a semi-infinite rectangular waveguide with an absorber coating on its inner walls and with a planar termination inside 148

4.3 Field scattered into the exterior region by a semi-infinite rectangular waveguide with an absorber coating on its inner walls and with a planar termination inside 157

V. SUMMARY AND CONCLUSION 173

A. BOUNDARY CONDITIONS AT AN IMPEDANCE WALL 176

B. CONSTRUCTION OF ONE DIMENSIONAL GREEN'S FUNCTIONS 179

C. A METHOD FOR THE NUMERICAL SOLUTION OF MODAL EIGENVALUES 183

D. REFLECTION COEFFICIENTS FOR AN IMPEDANCE BOUNDARY 185

E. TRANSITION FUNCTION 188

F. REFLECTION COEFFICIENTS FOR A DIELECTRIC/FERRITE SLAB ON A PERFECTLY CONDUCTING GROUND PLANE 189

REFERENCES 193

LIST OF FIGURES

1 Coupling and scattering of electromagnetic plane wave by an open-ended semi-infinite parallel plate waveguide with inner impedance walls and perfectly-conducting outer walls. 4

2 Infinitely long (in $\pm\hat{z}$) parallel plate waveguide excited by an interior line source. 5

3 Dominant ray paths for the problem in Figure 2. 6

4 Poles in the complex k_x and k_z planes with an integration path in the k_z plane. 14

5 Ray trajectories for $m = 1,2,3,4$ and $n = 0$ case. P' and P are source and observation points, respectively. 17

6 Integration path in complex α plane. 19

7 Magnitude of G for an infinitely-long parallel plate waveguide excited by an electric line source as a function of the normalized distance kz. 24

8 Magnitude of G for an infinitely-long parallel plate waveguide excited by an electric line source as a function of the normalized distance kz. 25

9 Magnitude of G for an infinitely-long parallel plate waveguide excited by an electric line source as a function of the normalized distance kz. 26

10 Magnitude of G for an infinitely-long parallel plate waveguide excited by an electric line source as a function of the normalized distance kz. 27

11 Magnitude of G for an infinitely-long parallel plate waveguide excited by an electric line source as a function of the normalized distance kz. 28

12 Magnitude of G for an infinitely-long parallel plate waveguide excited by a magnetic line source as a function of the normalized distance kz. 29

13 Magnitude of G for an infinitely-long parallel plate waveguide excited by a magnetic line source as a function of the normalized distance kz. 30

14 Magnitude of G for an infinitely-long parallel plate waveguide excited by a magnetic line source as a function of the normalized distance kz. 31

15 Magnitude of G for an infinitely-long parallel plate waveguide excited by a magnetic line source as a function of the normalized distance kz. 32

16 Magnitude of G for an infinitely-long parallel plate waveguide excited by a magnetic line source as a function of normalized distance kx for fixed kz. 34

17 Magnitude of G for a magnetic line source without surface wave contributions to both modal and ray solutions when both source and field points are near the lower wall. 36

18 Magnitude of G for the case in Figure 17 except that the surface waves are included in both solutions but the surface transition function is not included in the ray solution. 40

19 Integration path and a surface wave pole α_p which is near the saddle point α_s. 41

20 Magnitude of G in the case of Figure 18 except that the *uniform* transition function is included in the ray solution. 44

21 Magnitude of G for a magnetic line source when a source point is near the lower wall and a field point is near the upper wall. . . . 45

22 Magnitude of G for a magnetic line source when both source and field points are on the lower wall. 46

23 Convergence of the modal and ray solutions for an electric line source and for a fixed kz. 48

24 Convergence of the modal and ray solutions for an electric line source and for a fixed kz. 49

25 Convergence of the modal and ray solutions for an electric line source and for a fixed kz. 50

26 Convergence of the modal and ray solutions for an electric line source and for a fixed kz. 51

27 Convergence of the modal and ray solutions for a magnetic line source and for a fixed kz. 52

28 Convergence of the modal and ray solutions for a magnetic line source and for a fixed kz. 53

29 Convergence of the modal and ray solutions for a magnetic line source and for a fixed kz. 54

30 Convergence of the modal and ray solutions for a magnetic line source and for a fixed kz. 55

31 Dominant ray paths for the problem in Figure 1. 57

32 Semi-infinite parallel plate waveguide showing different combinations of geometric optical direct, singly and multiply reflected rays in each region of the waveguide. 58

33 Semi-infinite parallel plate waveguide showing direct, singly reflected, doubly reflected, direct diffracted and multiply diffracted–reflected rays. 60

34 Rays associated with the problem of line source excitation of an impenetrable half plane with two face impedances. 63

35 A plane wave incident on a half plane geometry with perfectly-conducting on one side and impedance surface on the other side. . 66

36 Each ray field for an incident plane wave of unit strength which is polarized such that $\mathbf{E}^i = \hat{\mathbf{y}}\, E^i_y$. 68

37 Each ray field for an incident plane wave of unit strength which is polarized such that $\mathbf{E}^i = \hat{\mathbf{y}}\, E^i_y$. 69

38 Each ray field for an incident plane wave of unit strength which is polarized such that $\mathbf{E}^i = \hat{\mathbf{y}}\, E^i_y$. 70

39 Each ray field for an incident plane wave of unit strength which is polarized such that $\mathbf{E}^i = \hat{\mathbf{y}}\, E^i_y$. 71

40 Each ray field for an incident plane wave of unit strength which is polarized such that $\mathbf{E}^i = \hat{\mathbf{y}}\, E^i_y$. 72

41 Each ray field for an incident plane wave of unit strength which is polarized such that $\mathbf{H}^i = \hat{\mathbf{y}}\, H^i_y$. 73

42 Each ray field for an incident plane wave of unit strength which is polarized such that $\mathbf{H}^i = \hat{\mathbf{y}}\, H_y^i$. 74
43 Each ray field for an incident plane wave of unit strength which is polarized such that $\mathbf{H}^i = \hat{\mathbf{y}}\, H_y^i$. 75
44 Each ray field for an incident plane wave of unit strength which is polarized such that $\mathbf{H}^i = \hat{\mathbf{y}}\, H_y^i$. 76
45 Each ray field for an incident plane wave of unit strength which is polarized such that $\mathbf{H}^i = \hat{\mathbf{y}}\, H_y^i$. 77
46 Semi-infinite parallel plate waveguide geometry showing the incident plane wave and the angle of incidence. 78
47 Each ray field within a semi-infinite parallel plate waveguide with impedance walls plotted as a function of the axial distance from the open end to the field point for an incident plane wave with a parallel polarization (TM_y). 79
48 Each ray field within a semi-infinite parallel plate waveguide with impedance walls plotted as a function of the axial distance from the open end to the field point for an incident plane wave with a parallel polarization (TM_y). 80
49 Each ray field within a semi-infinite parallel plate waveguide with impedance walls plotted as a function of the axial distance from the open end to the field point for an incident plane wave with a parallel polarization (TM_y). 81
50 Each ray field within a semi-infinite parallel plate waveguide with impedance walls plotted as a function of the axial distance from the open end to the field point for an incident plane wave with a perpendicular polarization (TE_y). 82

51 Each ray field within a semi-infinite parallel plate waveguide with impedance walls plotted as a function of the axial distance from the open end to the field point for an incident plane wave with a perpendicular polarization (TE_y). 83

52 Each ray field within a semi-infinite parallel plate waveguide with impedance walls plotted as a function of the axial distance from the open end to the field point for an incident plane wave with a perpendicular polarization (TE_y). 84

53 Each ray field within a semi-infinite parallel plate waveguide coated with a dielectric/ferrite material plotted as a function of the axial distance from the open end to the field point for an incident plane wave with a parallel polarization (TM_y) case. 87

54 Each ray field within a semi-infinite parallel plate waveguide coated with a dielectric/ferrite material plotted as a function of the axial distance from the open end to the field point for an incident plane wave with a parallel polarization (TM_y) case. 88

55 Each ray field within a semi-infinite parallel plate waveguide coated with a dielectric/ferrite material plotted as a function of the axial distance from the open end to the field point for an incident plane wave with a parallel polarization (TM_y) case. 89

56 Each ray field within a semi-infinite parallel plate waveguide coated with a dielectric/ferrite material plotted as a function of the axial distance from the open end to the field point for an incident plane wave with a parallel polarization (TM_y) case. 90

57 Each ray field within a semi-infinite parallel plate waveguide coated with a dielectric/ferrite material plotted as a function of the axial distance from the open end to the field point for an incident plane wave with a parallel polarization (TM_y) case. 91
58 Each ray field within a semi-infinite parallel plate waveguide coated with a dielectric/ferrite material plotted as a function of the axial distance from the open end to the field point for an incident plane wave with a parallel polarization (TM_y) case. 92
59 Each ray field within a semi-infinite parallel plate waveguide coated with a dielectric/ferrite material plotted as a function of the axial distance from the open end to the field point for an incident plane wave with a parallel polarization (TM_y) case. 93
60 Each ray field within a semi-infinite parallel plate waveguide coated with a dielectric/ferrite material plotted as a function of the axial distance from the open end to the field point for an incident plane wave with a parallel polarization (TM_y) case. 94
61 Each ray field within a semi-infinite parallel plate waveguide coated with a dielectric/ferrite material plotted as a function of the axial distance from the open end to the field point for an incident plane wave with a parallel polarization (TM_y) case. 95
62 Each ray field within a semi-infinite parallel plate waveguide coated with a dielectric/ferrite material plotted as a function of the axial distance from the open end to the field point for an incident plane wave with a parallel polarization (TM_y) case. 96

63 Each ray field within a semi-infinite parallel plate waveguide coated with a dielectric/ferrite material plotted as a function of the axial distance from the open end to the field point for an incident plane wave with a parallel polarization (TM_y) case. 97

64 A semi-infinite parallel plate waveguide with a planar termination showing singly reflected ray by the upper wall and doubly reflected ray by the upper and the termination. 98

65 Each ray field within a semi-infinite parallel plate waveguide coated with a dielectric/ferrite material and with a planar termination inside when a plane wave with parallel polarization is incident. . . . 99

66 Each ray field within a semi-infinite parallel plate waveguide coated with a dielectric/ferrite material and with a planar termination inside when a plane wave with perpendicular polarization is incident. 100

67 Plane wave backscattering by a semi-infinite parallel plate waveguide with an impedance boundary condition on its inner walls as a function of incident angle for the parallel polarization case. 102

68 Plane wave backscattering by a semi-infinite parallel plate waveguide with an impedance boundary condition on its inner walls as a function of incident angle for the perpendicular polarization case. . 103

69 Plane wave backscattering by a semi-infinite parallel plate waveguide with an impedance boundary condition on its inner walls as a function of the waveguide width for the parallel polarization case. 104

70 Plane wave backscattering by a semi-infinite parallel plate waveguide with an impedance boundary condition on its inner walls as a function of the waveguide width for the perpendicular polarization case. 105

71 Backscattered field as a function of waveguide width for a perpendicular polarization case. 106
72 Radiation of the field reflected from the interior termination. . . . 108
73 Equivalent configurations for calculating the cavity radiation field. 109
74 Kirchhoff or physical optics approximated versions of the equivalent problem in Figure 73(b). 110
75 A ray tube reflected back from the termination. 111
76 Rays incident on the open end of the semi-infinite parallel plate waveguide with an incident angle ϕ' and a simple planar termination at $z = L$. 114
77 EM plane wave scattering by a semi-infinite parallel plate waveguide with inner impedance walls and with an interior termination as a function of aspect angle ϕ for the parallel polarization case. 116
78 EM plane wave scattering by a semi-infinite parallel plate waveguide with inner impedance walls and with an interior termination as a function of aspect angle ϕ for the perpendicular polarization case. 117
79 EM plane wave scattering by a semi-infinite parallel plate waveguide with inner impedance walls and with an interior termination as a function of aspect angle ϕ for the parallel polarization case. 118
80 EM plane wave scattering by a semi-infinite parallel plate waveguide with inner impedance walls and with an interior termination as a function of aspect angle ϕ for the perpendicular polarization case. 119
81 EM plane wave scattering by a semi-infinite parallel plate waveguide with inner impedance walls and with an interior termination as a function of aspect angle ϕ for the parallel polarization case. 120

82 EM plane wave scattering by a semi-infinite parallel plate waveguide with inner impedance walls and with an interior termination as a function of aspect angle ϕ for the perpendicular polarization case. 121

83 EM plane wave scattering by a semi-infinite parallel plate waveguide coated with a dielectric/ferrite material and with an interior termination as a function of aspect angle ϕ for the parallel polarization case. 122

84 EM plane wave scattering by a semi-infinite parallel plate waveguide coated with a dielectric/ferrite material and with an interior termination as a function of aspect angle ϕ for the perpendicular polarization case. 123

85 EM plane wave scattering by a semi-infinite parallel plate waveguide coated with a dielectric/ferrite material and with an interior termination as a function of aspect angle ϕ for the parallel polarization case. 124

86 EM plane wave scattering by a semi-infinite parallel plate waveguide coated with a dielectric/ferrite material and with an interior termination as a function of aspect angle ϕ for the perpendicular polarization case. 125

87 EM plane wave scattering by a semi-infinite parallel plate waveguide coated with a dielectric/ferrite material and with an interior termination as a function of aspect angle ϕ for the parallel polarization case. 126

88 EM plane wave scattering by a semi-infinite parallel plate waveguide coated with a dielectric/ferrite material and with an interior termination as a function of aspect angle ϕ for the perpendicular polarization case. 127

89 Comparison of the plane wave scattering patterns obtained by the present method and by the MSM for the parallel polarization case. 129

90 Comparison of the plane wave scattering patterns obtained by the present method and by the MSM for the parallel polarization case. 130

91 Geometry of an open-ended semi-infinite rectangular waveguide coated with a thin, uniform layer of lossy or absorbing material on its inner wall. 132

92 Top and unfolded side views of the ray path in Figure 91. 134

93 Rectangular waveguide showing the assignment of the wall numbers to the waveguide. 136

94 An electric field $\mathbf{E}^i$ incident on $x-y$ plane with incident angles θ' and ϕ'. 138

95 The incident field $\mathbf{E}_o^i$ in Figure 94 in the plane of incidence. 140

96 Ray fixed coordinate system used for 3–D diffraction. 142

97 Comparison of the *ray fixed coordinate system* and the *edge fixed coordinate system*. The incident and reflected rays are perpendicular to the page and directed outward. 143

98 Geometry for finding the diffraction point along the rim edge at the open end of a waveguide. 146

99 Each ray field coupled into a semi-infinite rectangular waveguide with an impedance boundary condition on its inner walls for the perpendicularly polarized plane wave incidence. 149
100 Each ray field coupled into a semi-infinite rectangular waveguide with an impedance boundary condition on its inner walls for the parallel polarized plane wave incidence. 150
101 Each ray field coupled into a semi-infinite rectangular waveguide with an impedance boundary condition on its inner walls for the parallel polarized plane wave incidence. 151
102 Each ray field coupled into a semi-infinite rectangular waveguide with an impedance boundary condition on its inner walls for the perpendicularly polarized plane wave incidence. 152
103 Each ray field coupled into a semi-infinite waveguide coated with a dielectric/ferrite material on its inner walls and parallel polarized plane wave incidence. 153
104 Each ray field coupled into a semi-infinite waveguide coated with a dielectric/ferrite material on its inner walls and perpendicularly polarized plane wave incidence. 154
105 Each ray field coupled into a semi-infinite waveguide coated with a dielectric/ferrite material on its inner walls and parallel polarized plane wave incidence. 155
106 Each ray field coupled into a semi-infinite waveguide coated with a dielectric/ferrite material on its inner walls and parallel polarized plane wave incidence. 156
107 Each ray field for a rectangular waveguide with impedance inner walls and a planar termination inside for a parallel polarization. . 158

108 Each ray field for a rectangular waveguide with impedance inner walls and a planar termination inside for a perpendicular polarization. 159

109 Each ray field for a rectangular waveguide coated with a dielectric/ferrite material with a planar termination inside for a parallel polarization. 160

110 Each ray field for a rectangular waveguide coated with a dielectric/ferrite material with a planar termination inside for a perpendicular polarization. 161

111 Equivalent currents $\mathbf{I}_{eq}$ and $\mathbf{M}_{eq}$ on the rim at the open end of the waveguide. 164

112 Angles β_o, β, ψ' and ψ which occur in the wedge diffraction coefficients D_M and D_E. 165

113 Far zone pattern in the $x-z$ plane of the field scattered by a semi-infinite rectangular waveguide with an interior termination illuminated by an external plane wave whose electric field is polarized parallel to the plane of incidence. 166

114 Far zone pattern in the $x-z$ plane of the field scattered by a semi-infinite rectangular waveguide with an interior termination illuminated by an external plane wave whose electric field is polarized parallel to the plane of incidence. 167

115 Far zone pattern in the $x-z$ plane of the field scattered by a semi-infinite rectangular waveguide with an interior termination illuminated by an external plane wave whose electric field is polarized parallel to the plane of incidence. 168

116 Far zone pattern in the $x-z$ plane of the field scattered by a semi-infinite rectangular waveguide with an interior termination illuminated by an external plane wave whose electric field is polarized parallel to the plane of incidence. 170

117 Far zone pattern in the $x-z$ plane of the field scattered by a semi-infinite rectangular waveguide with an interior termination illuminated by an external plane wave whose electric field is polarized parallel to the plane of incidence. 171

118 Far zone pattern in the $x-z$ plane of the field scattered by a semi-infinite rectangular waveguide with an interior termination illuminated by an external plane wave whose electric field is polarized parallel to the plane of incidence. 172

119 An infinitely long parallel plate waveguide excited by a $\hat{y}$ directed magnetic line source (TE_y). 177

120 A plane wave obliquely incident on a surface impedance boundary. 186

121 The magnitude and phase of the transition function. 188

122 A Dielectric/ferrite slab grounded by a perfectly conductor of electricity. 190

123 Equivalent transmission-line circuit for Figure 122. 190

LIST OF TABLES

2.1 Poles on k_x and k_z planes for an electric line source for $ka = 50.0$ and $Z_l = Z_u = 0.1 + j0.3$ 22

2.2 Ordinary and surface wave poles on k_x and k_z planes for a magnetic line source for $ka = 50.0$ and $Z_l = Z_u = 0.1 + j0.3$ 37

CHAPTER I

INTRODUCTION

An approximate but sufficiently accurate high frequency solution is developed in this study for the problem of electromagnetic (EM) plane wave scattering by an open-ended, perfectly-conducting, semi-infinite hollow rectangular waveguide (or duct) with a thin, uniform layer of lossy or absorbing material on its inner wall, and with a planar termination inside. This high frequency solution is based on a combination of the uniform geometrical theory of diffraction (UTD) [1] ray technique with the aperture integration (AI) method. The UTD is a modification of Keller's geometrical theory of diffraction (GTD) [2] such that it remains valid even within the transition regions adjacent to the shadow boundaries associated with the discontinuities of the geometrical optics incident and reflected rays. Basically, the reflected fields in the present UTD analysis are characterized by a Fresnel reflection coefficient that is associated with the problem of plane wave reflection from a uniform layer of dielectric/ferrite coated perfectly-conducting surface of infinite extent. Likewise, the diffracted fields here are characterized by a uniform diffraction coefficient that is associated with the problem of plane wave diffraction by the edge of a perfectly-conducting half-plane which is coated on one side by a uniform layer of dielectric/ferrite material. The total field scattered by the semi-infinite waveguide consists firstly of the fields scattered from the edges of the aperture at the open end, and secondly of the fields which are coupled into

the waveguide from the exterior and then reflected from the interior termination to radiate out of the open end. The first contribution to the scattered field can be found directly via the UTD ray method; whereas, the second contribution is found via the AI method which employs rays to describe the fields in the aperture that arrive there after reflecting from the interior termination. The approximate ray method of analysis in combination with AI is selected here because of its conceptual simplicity and efficiency. It is assumed in the present study that the direction of the incident plane wave and the direction of observation lie well inside the forward half space that exists on the other side of the half space which contains the semi-infinite waveguide geometry. Also, the medium exterior to the waveguide is assumed to be free space.

While the problems of EM scattering and radiation by perfectly-conducting semi-infinite, open-ended parallel plate, rectangular and circular waveguides have been analyzed in the past using a variety of techniques, e.g. the Wiener–Hopf method (for the semi-infinite parallel plate and circular waveguides) [3], the mode matching precedure [4,5,6], a hybrid combination of ray and modal techniques [7], etc., there does not appear to be much work done on the EM scattering and radiation by semi-infinite perfectly-conducting waveguides with an absorber (dielectric/ferrite material) coating on its inner walls. Besides the present work, the only other related study which is available in the open literature (or as a report) appears to be that conducted by Lee et al. [8]; the latter deals with the plane wave scattering by a perfectly-conducting semi-infinite circular waveguide with an absorber coating on its inner wall. A purely modal description is used for the fields inside the waveguide in [8]; this is in contrast to the present work which employs rays to do the same. As in the present approach, the one in [8] also employs the AI method to find the fields radiated from the interior of the waveguide; however,

the field in the aperture, which is required in the AI calculation, is expressed in terms of modes in [8] rather than in terms of rays as done here, obviously because the work in [8] employs a modal description for the interior fields.

In addition to developing a high frequency solution for the three dimensional (3–D) problem of the scattering by a semi-infinite rectangular waveguide, a high frequency solution for the less difficult but useful problem of the EM scattering by a two dimensional (2–D), semi-infinite parallel plate waveguide with an absorber coating on the inner walls is also developed as a first step. In the case of the simpler semi-infinite 2–D parallel plate geometry excited by an EM plane wave as shown in Figure 1, it is initially assumed that a uniform surface impedance boundary condition exists on the inner walls. The impedance boundary condition in this problem serves to model a thin layer of lossy dielectric/ferrite coating on the otherwise perfectly-conducting interior waveguide walls. The reason for initially choosing this simpler parallel plate problem with an impedance boundary condition on the interior walls was to examine the accuracy and efficiency of an approximate ray method of analysis while retaining the essential features of the absorber coated rectangular duct geometry but without the added complexity of the latter.

A rigorous representation for the fields inside the waveguide region is usually given in terms of a modal expansion. It is noted, of course, that at high frequencies where the width of the parallel plate waveguide becomes large in terms of the wavelength, one "generally" requires many modes to represent the fields within the waveguide. In addition, for waveguides with lossy walls, the determination of eigenvalues which characterize the modal sets becomes difficult and inefficient. On the other hand, one may anticipate that the ray procedure can become more efficient if the impedance surface is lossy as is true for inlets with absorber coating on the inner walls. In order to study the utility and relative efficiencies of the ray and

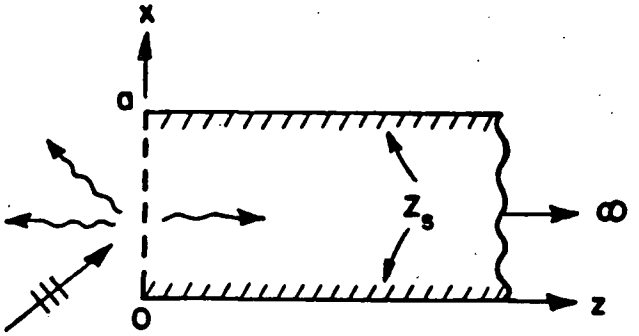

Figure 1: Coupling and scattering of electromagnetic plane wave by an open-ended semi-infinite parallel plate waveguide with inner impedance walls and perfectly-conducting outer walls.

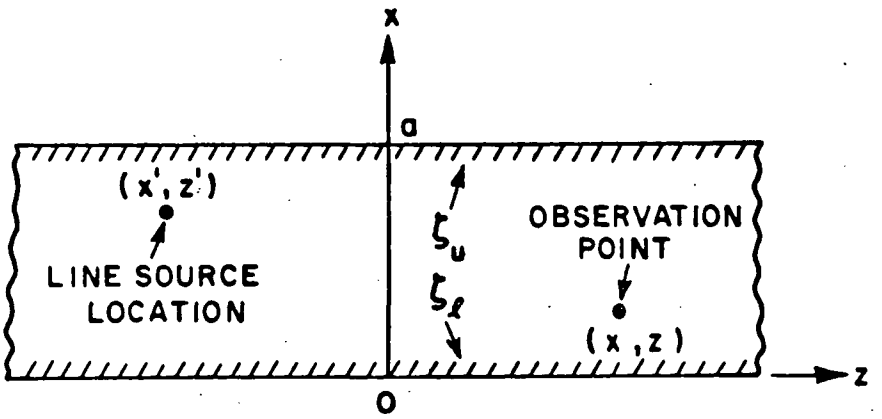

Figure 2: Infinitely long (in $\pm\hat{z}$) parallel plate waveguide excited by an interior line source.

modal approaches for describing the fields within the lossy walled parallel plate waveguide region, it became necessary to study a second problem directly related to the first one in Figure 1. The configuration of the second problem consists of an interior line source exciting a parallel plate waveguide with an impedance boundary condition on its inner walls as shown in Figure 2. It is important to note that the geometry in Figure 2 is infinitely long; whereas, that in Figure 1 is semi-infinite. An exact modal solution can be obtained for this source-excited infinite waveguide problem in Figure 2 in terms of a waveguide Green's function [7,9]. Basically, an integral representation for the waveguide Green's function is developed in which the fields interior to the waveguide are proportional to the Green's function. A formal modal expansion for the waveguide fields is readily obtained via an application of the *Cauchy residue theorem* to the above mentioned integral representation. Due to the surface impedance boundary condition, the modal eigenvalues cannot be determined *analytically* and must therefore have to be determined *numerically* in this problem from the resonant denominator of the integrand (pertaining to the integral representation of the waveguide Green's function). Once the roots of the resonant denominator are found numerically, the modal (eigenfunction) expansion for the interior impedance walled parallel plate waveguide Green's function can also be computed numerically. Furthermore, an asymptotic approximation of the integral representation for the waveguide Green's function (after the resonant denominator is expressed as a geometric series) yields the approximate ray solution for the fields inside the waveguide. The latter ray solution is the one which is of major interest in this study. Some of the dominant ray paths in the ray solution for this problem in Figure 2 are shown in Figure 3. In the ray method, the field from a source point to an observation point propagates along ray paths that obey the rules of geometrical optics. Some of the advantages of the purely ray

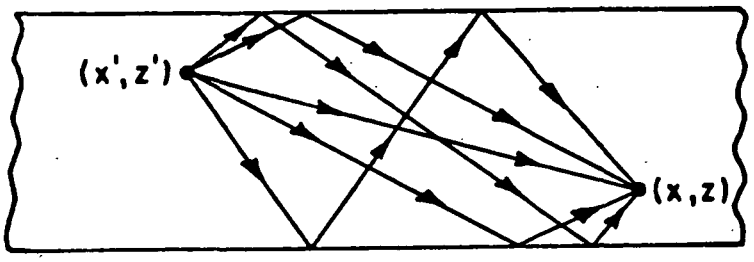

Figure 3: Dominant ray paths for the problem in Figure 2.

approach are as follows. The ray solution provides some physical insight into the scattering mechanisms particularly in connection with the coupling of the fields from the exterior to the interior regions in the case of the semi-infinite waveguide configuration, as well as into the effect of the wall impedance on the fields in the interior waveguide region. Also, the ray solution does not require one to evaluate the eigenvalues which are essential for the construction of the modal solution. This eigenvalue equation must be solved numerically for different impedance values and for each mode, thereby making the modal approach far more cumbersome as compared to the ray approach. Furthermore, it has been found from a numerical study of the modal and ray solutions that, in general, the ray solution converges much faster than the modal solution for the case of interest, namely, when the wall surface impedance is lossy; furthermore, it has also been found in this work that, in general, the rate of convergence of the modal solution does not improve significantly even with the presence of loss in the wall surface impedance.

After establishing the usefulness of the ray representation inside the line source excited, impedance walled infinitely long parallel plate waveguide (see Figure 2) in Chapter II, the EM plane scattering by the semi-infinite parallel plate waveguide

geometry of Figure 1, with perfectly-conducting outer walls and with an impedance boundary condition on its inner walls, is then analyzed in Chapter III. In Chapter III, the UTD is employed to calculate the contribution to the field scattered by the edges of the aperture at the open end, and it is also used to provide a description for the field coupled into the waveguide region. The latter ray field propagates within the waveguide and undergoes reflection at the interior termination to arrive back at the aperture and radiate into the exterior region. The radiation is found by integrating that reflected ray field over the aperture using a physical optics (PO) type approximation in the AI method. Next, the impedance boundary condition on interior walls is relaxed, and the above solution is extended to provide a more accurate analysis, also in Chapter III, which accounts for the presence of an absorber coating with finite thickness. The latter analysis sets the stage for the analysis of the main problem of interest in this work, namely that of the EM scattering by a 3–D perfectly-conducting, open-ended semi-infinite rectangular waveguide with an absorber coating on its inner walls as discussed in Chapter IV. Numerical results are presented and discussed in each chapter. Finally, a summary and some conclusions are presented in Chapter V.

It is found that, in general, the ray solution converges faster than the modal solution for the case of interest, namely, when the interior wall coating is lossy. Furthermore, it is also found in this work that, in general, the rate of convergence of the modal solution does not improve significantly even with the presence of loss in the wall coating. In addition, the level of the fields which are coupled into the interior of the semi-infinite waveguide and then radiate from the open end, after undergoing reflection at the interior termination, can be controlled by changing the value of the absorber lining on the interior of the waveguide walls as might be expected. If these fields radiated from the open end are made sufficiently small,

the only other contribution to the total exterior scattered field, which comes from the diffraction by the edges of the aperture at the open end, will then be dominant. Various analytical details are given in Appendices A through F.

An $e^{+j\omega t}$ time dependence is assumed and suppressed in this analytical development. In addition, a character with a bar ($\overline{E}$), with a cap ($\hat{\mathbf{E}}$) or with bold type style ($\mathbf{E}$) represents a vector quantity; also several abbreviations used in this study are listed below.

EM	:	Electromagnetic
GTD	:	Geometrical Theory of Diffraction
UTD	:	Uniform Geometrical Theory of Diffraction
PTD	:	Physical Theory of Diffraction
GO	:	Geometrical Optics
PO	:	Physical Optics
2-D	:	Two Dimensional
3-D	:	Three Dimensional
G	:	Green's function
SDP	:	Steepest Descent Path
ISB	:	Incident Shadow Boundary
RSB	:	Reflection Shadow Boundary
AI	:	Aperture Integration
ECM	:	Equivalent Current Method
MSM	:	Multiple Scattering Method

CHAPTER II

ANALYSIS OF EXACT MODAL AND APPROXIMATE RAY SOLUTIONS FOR AN INFINITELY LONG PARALLEL PLATE WAVEGUIDE WITH AN IMPEDANCE BOUNDARY CONDITION ON ITS INNER WALLS

2.1 Formulation of the problem

The problem of a line source excited two dimensional (2-D) parallel plate waveguide of infinite extent with impedance walls is analyzed in this chapter. The 2-D time harmonic wave equation for the parallel plate Green's function G due to a line source at $x = x'$ and $z = z'$ in the waveguide geometry of Figure 2 is given by

$$\left[\frac{\partial^2}{\partial x^2} + \frac{\partial^2}{\partial z^2} + k^2 \right] G = -\delta(x - x')\,\delta(z - z') \tag{2.1}$$

where k is the free-space wavenumber and $\delta(x)$ is the Dirac delta function. In this 2-D problem, the EM fields can be simply related to the Green's function G because one can scalarize the problem separating it into the TE_y and TM_y cases. One notes that the magnetic field has only a $\hat{\mathbf{y}}$ component for the TE_y case and likewise, the electric field has only a $\hat{\mathbf{y}}$ component for the TM_y case. Thus, let $\mathbf{H} = \hat{\mathbf{y}} H_y$ represent the magnetic field in the TE_y case; likewise let $\mathbf{E} = \hat{\mathbf{y}} E_y$ represent the electric field in the TM_y case. The excitation in the TE_y case can be a magnetic line source of strength M at (x', z'); likewise, an electric line source

of strength I at (x', z') generates the TM_y fields. These line sources are of infinite extent in the $\hat{\mathbf{y}}$ direction. It can be shown that $H_y = -jkYMG$ and $E_y = -jkZIG$ where Z (or Y) is the free-space impedance (or admittance), provided G satisfies the following boundary conditions:

$$\frac{\partial G}{\partial z} \pm jk\, G = 0 \qquad as\ |z| \to \infty \tag{2.2}$$

$$\frac{\partial G}{\partial x} - jk\, \varsigma_l\, G = 0 \qquad at\ x = 0 \tag{2.3}$$

$$\frac{\partial G}{\partial x} + jk\, \varsigma_u\, G = 0 \qquad at\ x = a \tag{2.4}$$

where

$$\varsigma_{l,u} = \begin{cases} Z_{l,u} & for\ TE_y\ case \\ Y_{l,u} & for\ TM_y\ case \end{cases} \tag{2.5}$$

and $Z_{l,u}$ (or $Y_{l,u}$) is the surface impedance (or admittance) at $x = 0$ and $x = a$ which is normalized to the free-space wave impedance (or admittance). The boundary condition in Equation (2.2) is also known as the radiation condition and the impedance boundary conditions for G given by Equation (2.3) and (2.4) are derived in Appendix A in detail. Using separation of variables, the Green's function $G(x, x'; z, z')$ is represented in terms of the one dimensional Green's functions $G_x(x, x')$ and $G_z(z, z')$ as [7,9,10,11]

$$G(x, x'; z, z') = -\frac{1}{2\pi j} \int_{C_{z_0}} G_x(x, x') \cdot G_z(z, z')\, d\lambda_z \tag{2.6}$$

where the integration contour C_{z_0} in the above equation encloses only the singularities of G_z. Solving Equation (2.1) for G_x subject to the boundary conditions

in Equations (2.3) and (2.4), $G_x(x,x')$ is found to be:

$$G_x(x,x') = \frac{(e^{j\sqrt{\lambda_x}\,x_<} + R_l e^{-j\sqrt{\lambda_x}\,x_<})\,(e^{-j\sqrt{\lambda_x}\,x_>} + R_u e^{j\sqrt{\lambda_x}\,x_>})}{2j\sqrt{\lambda_x}\,(1 - R_l R u)} \tag{2.7}$$

where $x_<$ and $x_>$ denote the values of x which satisfy $x < x'$ and $x > x'$, respectively and

$$R_l = \frac{\sqrt{\lambda_x} - k\varsigma_l}{\sqrt{\lambda_x} + k\varsigma_l} \tag{2.8}$$

$$R_u = \frac{\sqrt{\lambda_x} - k\varsigma_u}{\sqrt{\lambda_x} + k\varsigma_u}\, e^{-j2\sqrt{\lambda_x}\,a} \tag{2.9}$$

In addition

$$\lambda_x + \lambda_z = k^2 \tag{2.10}$$

Now $G_z(z,z')$ which satisfies the radiation condition given in Equation (2.2) for $|z| \to \infty$ is likewise given by:

$$G_z(z,z') = \frac{e^{-j\sqrt{\lambda_z}\,|z-z'|}}{2j\sqrt{\lambda_z}} \tag{2.11}$$

The one dimensional Green's functions $G_x(x,x')$ and $G_z(z,z')$ given in Equations in (2.7) and (2.11), respectively, are derived in detail in Appendix B.

Therefore, $G(x,x';z,z')$ becomes via Equations (2.6), (2.7) and (2.11), the following:

$$G = -\frac{1}{2\pi j}\int_{C_{z_0}} \frac{(e^{j\sqrt{\lambda_x}\,x_<} + R_l e^{-j\sqrt{\lambda_x}\,x_<})\,(e^{-j\sqrt{\lambda_x}\,x_>} + R_u e^{j\sqrt{\lambda_x}\,x_>})}{2j\sqrt{\lambda_x}\,(1 - R_l R u)}$$

$$\cdot \frac{e^{-j\sqrt{\lambda_z}\,|z-z'|}}{2j\sqrt{\lambda_z}}\, d\lambda_z$$

$$= \frac{1}{2\pi j} \int_{C_z} \frac{(e^{jk_x\,x<} + R_l e^{-jk_x\,x<})\,(e^{-jk_x\,x>} + R_u e^{jk_x\,x>})}{2k_x\,(1 - R_l Ru)} \cdot e^{-jk_z\,|z-z'|}\, dk_z \tag{2.12}$$

where $\sqrt{\lambda_x} = k_x$ and $\sqrt{\lambda_z} = k_z$ transformations are used and the integration path is also changed from C_{z_o} to C_z accordingly. An evaluation of the above integral in Equation (2.12) via the residue theorem yields a representation for G in terms of a summation of the conventional guided modes propagating along the z direction; namely:

$$G = \sum_{n=0}^{\infty} \frac{1}{2k_x} \frac{(e^{jk_{xn}\,x<} + R_l e^{-jk_{xn}\,x<})\,(e^{-jk_{xn}\,x>} + R_u e^{jk_{xn}\,x>})}{\frac{\partial(R_l R_u)}{\partial k_z}} \cdot e^{-jk_{zn}\,|z-z'|} \tag{2.13}$$

where

$$R_l = \frac{k_x - k\varsigma_l}{k_x + k\varsigma_l} \tag{2.14}$$

$$R_u = \frac{k_x - k\varsigma_u}{k_x + k\varsigma_u}\, e^{-j2k_x\,a} \tag{2.15}$$

It is noted that the modes arise from the residues of the poles in the integrand of Equation (2.12). The zeros of the denominator of the integrand in Equation (2.12) yields the required poles. Also these zeros yield the eigenvalues of the modes. Specifically, these eigenvalues are obtained by solving the transcendental equation $1 - R_l R_u = 0$ in the integrand of Equation (2.12) via a numerical '*Newton-Raphson*' iteration method which is described in Appendix C. One typical figure showing a

set of singularities in k_x and k_z plane is shown in Figure 4 for $Z_u = 0.1 + j0.3$ and $Z_l = 0.0 + j0.0$ with a waveguide electrical height ka being 50. Note that the singularity marked with a small dot in the complex k_x plane corresponds to the same one in the complex k_z plane. For an e^{+jwt} time convention, the closed integration path (C_z) encloses all the singularities in the lower half plane as shown in the figure ($C_z = C_z^r + C_z^i$). Also, note that all the singularities on the k_x and k_z planes would lie on the real or imaginary axis for lossless case. When the surface is lossy, the poles are displaced away from the real and imaginary axes as shown in Figure 4.

An alternative ray expansion representation for G is obtained by expanding the resonant denominator of the integral in Equation (2.12) into a geometric series,

$$\frac{1}{1 - R_l R_u} = \sum_{n=0}^{\infty} (R_l R_u)^n \tag{2.16}$$

Then, noting that for the employed time convention the contribution from C_z^i is zero, one obtains

$$\begin{aligned} G &= -\frac{j}{4\pi} \int_{C_z^r} \sum_{n=0}^{\infty} \frac{(e^{jk_x x<} + R_l e^{-jk_x x<})\,(e^{-jk_x x>} + R_u e^{jk_x x>})}{k_x} \\ &\quad \cdot e^{-jk_z|z-z'|}\,(R_l R_u)^n\, dk_x \end{aligned} \tag{2.17}$$

It is convenient for subsequent evaluation of Equation (2.17) to introduce further transformations

$$k_x = k\cos\alpha \tag{2.18}$$

$$k_z = k\sin\alpha \tag{2.19}$$

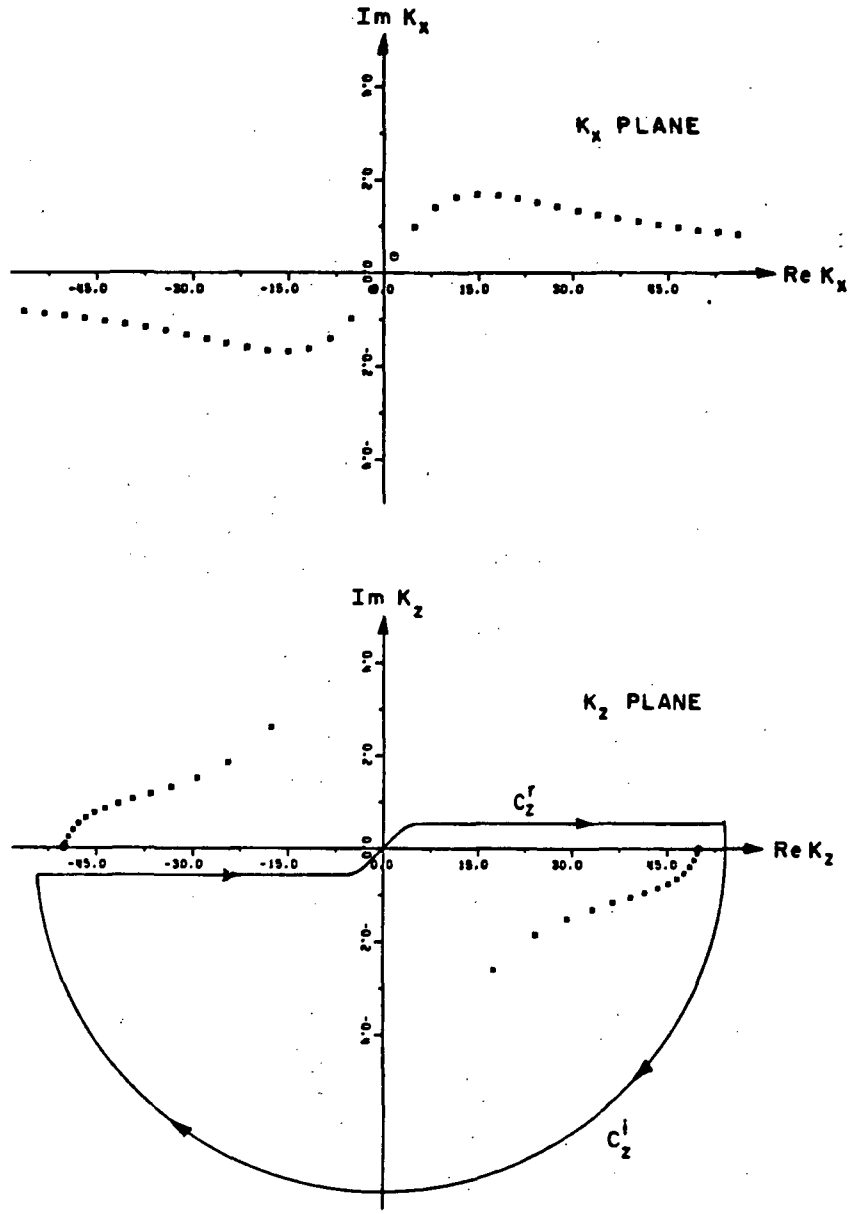

Figure 4: Poles in the complex k_x and k_z planes with an integration path in the k_z plane.

The Green's function $G(x,x';z,z')$ of Equation (2.17) is now expressed in the complex α plane as

$$G = -\frac{j}{4\pi}\int_C \sum_{n=0}^{\infty} \left(e^{jk\cos\alpha\, x<} + R_l e^{-jk\cos\alpha\, x<}\right)\left(e^{-jk\cos\alpha\, x>} + R_u e^{jk\cos\alpha\, x>}\right) \cdot e^{-jk\sin\alpha\,|z-z'|}\,(R_l R_u)^n\, d\alpha \tag{2.20}$$

where

$$R_l = \frac{\cos\alpha - \zeta_l}{\cos\alpha + \zeta_l} \tag{2.21}$$

$$R_u = \frac{\cos\alpha - \zeta_u}{\cos\alpha + \zeta_u}\, e^{-j2ka\cos\alpha} \tag{2.22}$$

and C is the contour obtained by transforming C_z^r using Equations (2.18) and (2.19).

After interchanging the orders of summation and integration, each of the integrals in the sum is evaluated asymptotically for large $k\sqrt{(x-x')^2+(z-z')^2}$ term by term via the method of steepest descent to arrive at the ray expansion. For convenience, let G be expressed as

$$G = \sum_{n=0}^{\infty}\sum_{m=1}^{4} G_{mn} \tag{2.23}$$

where

$$G_{1n} = -\frac{j}{4\pi}\int_C e^{+jk\left[\cos\alpha(x_<-x_>)-\sin\alpha|z-z'|\right]} \cdot (R_l R_u)^n\, d\alpha \tag{2.24}$$

$$G_{2n} = -\frac{j}{4\pi}\int_C e^{+jk\left[\cos\alpha(x_<+x_>)-\sin\alpha|z-z'|\right]} \cdot R_l^n R_u^{n+1}\, d\alpha \tag{2.25}$$

$$G_{3n} = -\frac{j}{4\pi}\int_C e^{-jk\left[\cos\alpha(x_<+x_>)+\sin\alpha|z-z'|\right]} \cdot R_l^{n+1}R_u^n \, d\alpha \qquad (2.26)$$

$$G_{4n} = -\frac{j}{4\pi}\int_C e^{-jk\left[\cos\alpha(x_<-x_>)+\sin\alpha|z-z'|\right]} \cdot (R_lR_u)^{n+1} \, d\alpha \qquad (2.27)$$

Note that each G_{mn} corresponds to each term of the integrand of Equation (2.20) and the relation between the index m and the number of reflections at upper or lower boundaries is as follows:

$m = 1$: n reflections at both boundaries.

$m = 2$: n reflections at lower boundary and
$n + 1$ reflections at upper boundary.

$m = 3$: $n + 1$ reflections at lower boundary and
n reflections at upper boundary.

$m = 4$: $n + 1$ reflections at both boundaries.

The ray trajectories for each m are shown in Figure 5 for $n = 0$ case.

For analytical details, an asymptotic evaluation of G_{mn} is considered here for $m = 1$ case. From Equation (2.24), G_{mn} for $m = 1$ may be represented by

$$G_{1n} = -\frac{j}{4\pi}\int_C F(\alpha)\, e^{kf(\alpha)} \, d\alpha \qquad (2.28)$$

where

$$F(\alpha) = \left(R_lR_u^{'}\right)^n \qquad (2.29)$$

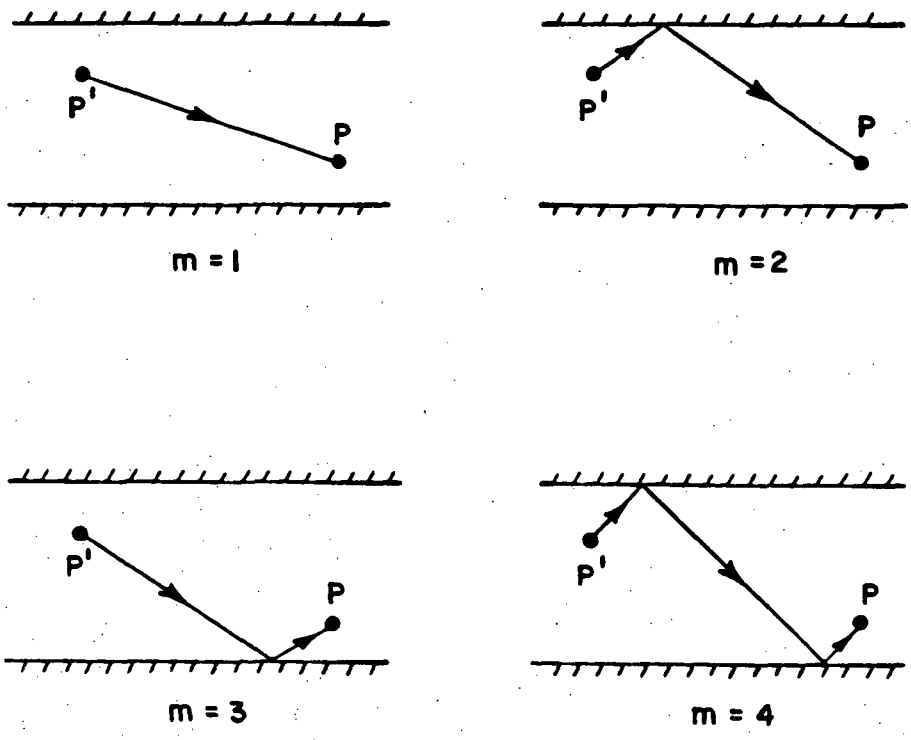

Figure 5: Ray trajectories for $m = 1, 2, 3, 4$ and $n = 0$ case. P' and P are source and observation points, respectively.

$$f(\alpha) = j\left[\cos\alpha\,(x_< - x_> - 2na) - \sin\alpha\,|z-z'|\right]$$
$$\equiv jr\,\cos(\alpha+\beta) \tag{2.30}$$

$$R_u' = \frac{\cos\alpha - \varsigma_u}{\cos\alpha + \varsigma_u} \tag{2.31}$$

$$r = \sqrt{(x_< - x_> - 2na)^2 + (z-z')^2} \tag{2.32}$$

$$\beta = \tan^{-1}\left(\frac{|z-z'|}{x_< - x_> - 2na}\right) \tag{2.33}$$

Note that the exponential term in R_u is involved in the phase term $f(\alpha)$ in the integrand of Equation (2.28). Then, employing the method of steepest descent [9,11] to Equation (2.28) gives

$$G_{1n} = -\frac{j}{4\pi}\left[\,R_l(\alpha_s)R_u'(\alpha_s)\,\right]^n \cdot \left|\sqrt{\frac{-2\pi}{jkr}}\,\right| \cdot e^{-j(kr-\pi/4)} \tag{2.34}$$

where the saddle point α_s is given by

$$\alpha_s = \beta = \tan^{-1}\left(\frac{|z-z'|}{x_< - x_> - 2na}\right) \tag{2.35}$$

The steepest descent integration path (C_{SDP}) and the saddle point (α_s) in the above equation are shown in Figure 6. Then, the ray field can be obtained using Equation (2.34). Since the ray decays considerably as it travels bouncing back and forth inside the waveguide, only a few terms (upto $n = 2$ or 3) are summed up in the first summation in Equation (2.23) depending on the impedance values of the

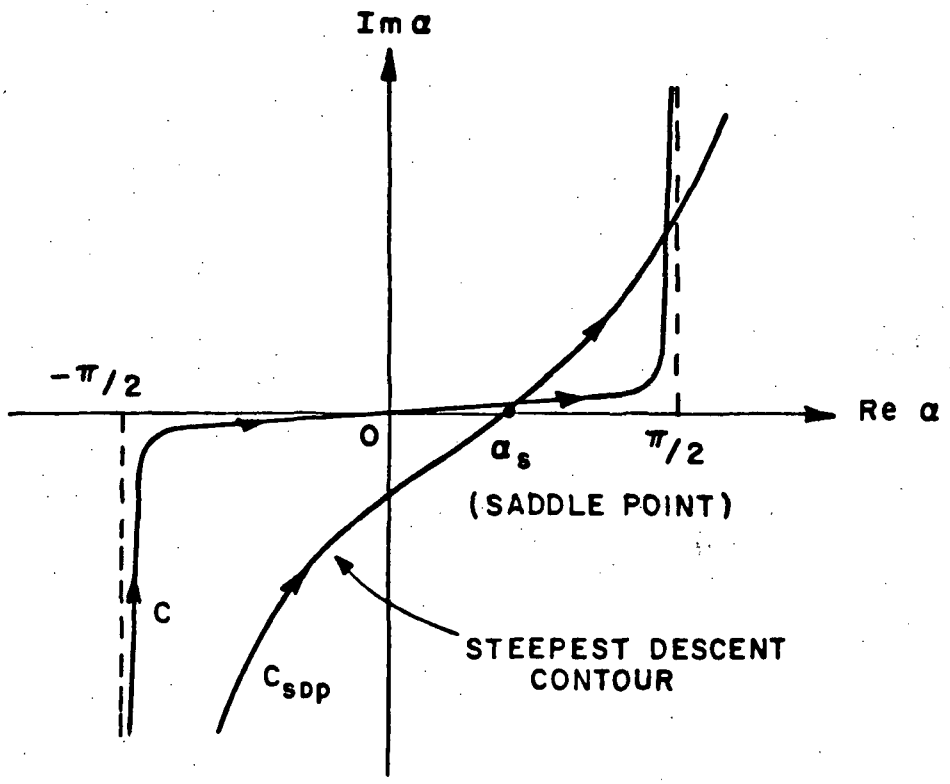

Figure 6: Integration path in complex α plane.

inner walls. The analysis for $m = 2, 3$ and 4 cases are very similar and therefore ommitted here.

It is noted that the ray solution in Equation (2.23) could also be constructed directly from the geometrical optics considerations. In order to assess the accuracy of the ray field representation which is mentioned above, the magnitude of the ray asymptotic approximation to the Green's function in Equation (2.23) is examined by comparing this with the magnitude of the exact guided mode series in Equation (2.13) which is used as a reference solution in this study. The magnitude of the Green's function in terms of the *exact modal solution* is plotted against the normalized distance kz as a *solid line* in each of the figures, while that of the *ray solution* is plotted as a *dashed line*. For the sake of convenience, the various parameters which appear in these figures are defined below.

ka : normalized waveguide height

kx' : normalized x-coordinate of the source point

kx : normalized x-coordinate of the observation point

kz : normalized z-coordinate of the observation point

pm : number of propagating modes inside the waveguide

em : number of evanescent modes included in the calculation

n : number of terms which have been included in the summation of the ray expansion of Equation (2.23)

R_l : resistance of the lower waveguide wall ($x = 0$)

X_l : reactance of the lower waveguide wall ($x = 0$)

R_u : resistance of the upper waveguide wall ($x = a$)

X_u : reactance of the upper waveguide wall ($x = a$)

k : wave number in the medium given by $k = 2\pi/\lambda$

λ : wavelength in free-space

It is noted that the term *propagating mode* (pm) cannot be defined for the lossy case because all poles corresponding to each mode are complex valued and each imaginary part of the complex eigenvalues causes attenuation with propagation of the modal field. In this study, however, each mode is defined as *propagating* (or *evanescent* (em)) mode for convenience if the real part of k_x of the corresponding pole is less (or greater) than ka. As shown in Table (2.1), if the real part of k_x is greater than ka ($i \geq 17$ cases in Table (2.1)), the imaginary part of the corresponding k_z becomes very big and it results in a very rapid attenuation for the field as it propagates. For $ka = 50.0$, there are 16 propagating modes for an electric line source and the modal solution is plotted as a *solid line* in Figure 7 for the range $1.0 < kz < 41.0$ which is examined here. The source and observation points are

Table 2.1: Poles on k_x and k_z planes for an electric line source for $ka = 50.0$ and $Z_l = Z_u = 0.1 + j0.3$

i	k_{x_i}	k_{z_i}
1	$3.104+j\ 0.012$	$49.904-j\ 0.001$
2	$6.209+j\ 0.025$	$49.613-j\ 0.003$
3	$9.313+j\ 0.037$	$49.125-j\ 0.007$
4	$12.417+j\ 0.049$	$48.434-j\ 0.013$
5	$15.522+j\ 0.061$	$47.530-j\ 0.020$
6	$18.626+j\ 0.073$	$46.401-j\ 0.029$
7	$21.731+j\ 0.085$	$45.031-j\ 0.041$
8	$24.836+j\ 0.096$	$43.396-j\ 0.055$
9	$27.940+j\ 0.108$	$41.465-j\ 0.073$
10	$31.045+j\ 0.119$	$39.194-j\ 0.094$
11	$34.151+j\ 0.130$	$36.521-j\ 0.122$
12	$37.256+j\ 0.141$	$33.347-j\ 0.158$
13	$40.362+j\ 0.152$	$29.513-j\ 0.207$
14	$43.468+j\ 0.162$	$24.712-j\ 0.285$
15	$46.574+j\ 0.172$	$18.197-j\ 0.440$
16	$49.680+j\ 0.181$	$5.857-j\ 1.539$
17	$52.787+j\ 0.191$	$0.595-j16.934$
18	$55.894+j\ 0.200$	$0.447-j24.985$
19	$59.001+j\ 0.209$	$0.393-j31.324$
20	$62.108+j\ 0.217$	$0.366-j36.845$
⋮	⋮	⋮
⋮	⋮	⋮

both equi-distant from the waveguide walls in this case. The corresponding ray field is shown as a *dashed line* for the same range. Only $n = 3$ is used in the ray solution in contrast with 16 modes in the modal summation. As seen from the figure, there is a good agreement between the modal and ray solutions for the range $kz > 15.0$. The discrepancy for $kz < 15.0$ is due to the fact that the contribution of the evanescent modes is strong when the observation point is near the source point. When this evanescent field contribution is included in the modal solution, it is then found to agree with the ray solution very well except in the region where the observation point is very near the source point ($kz < 3.0$) as shown in Figure 8 where the ray solution looses accuracy. It is anticipated that the modal and ray solutions will show excellent agreement even in this region ($kz < 3.0$) if the cylindrical wave (line source excitation) type behaviour in the asymptotic ray solution of Equation (2.23) is replaced by the more exact representation in terms of a Hankel function of the second kind. Hence, the first three evanescent modes are included in the modal solution shown in all the other figures. In Figures 9–11, the ray solution is compared again with the modal solution for different impedance values of the waveguide wall. As shown in the figures, the ray solution shows very good agreement with the corresponding modal solution. The magnitude of G is again plotted for a magnetic line source in Figures 12–15. From Figures 8–15, it may be concluded that the ray solution converges faster than the modal solution. This convergence of the two solutions is examined in detail later in this chapter.

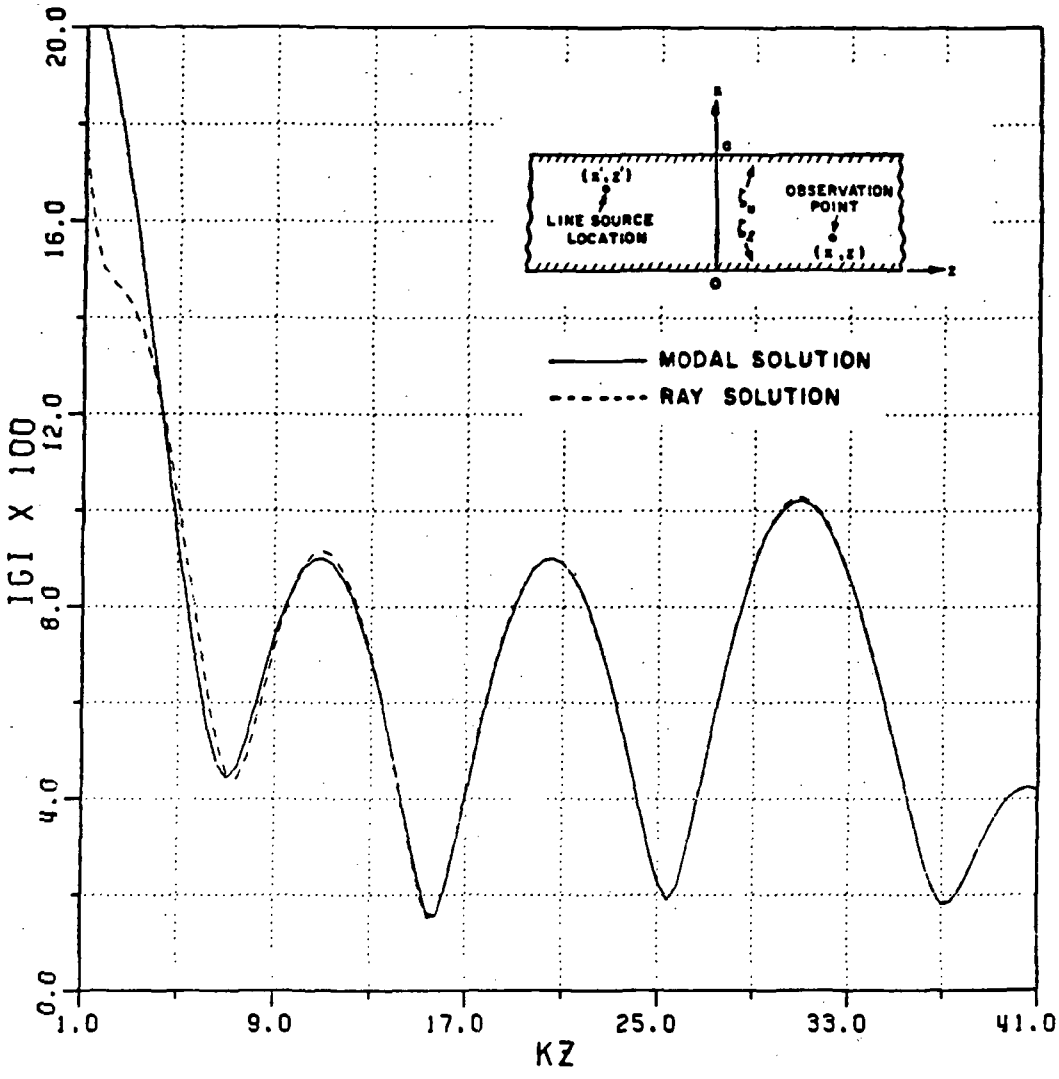

KA = 50.0	N= 3.0	RL= 0.1
KX'= 25.0	PM= 16.0	XL= 0.3
KX = 25.0	EM= 0.0	RU= 0.1
		XU= 0.3

Figure 7: Magnitude of G for an infinitely-long parallel plate waveguide excited by an electric line source as a function of the normalized distance kz.

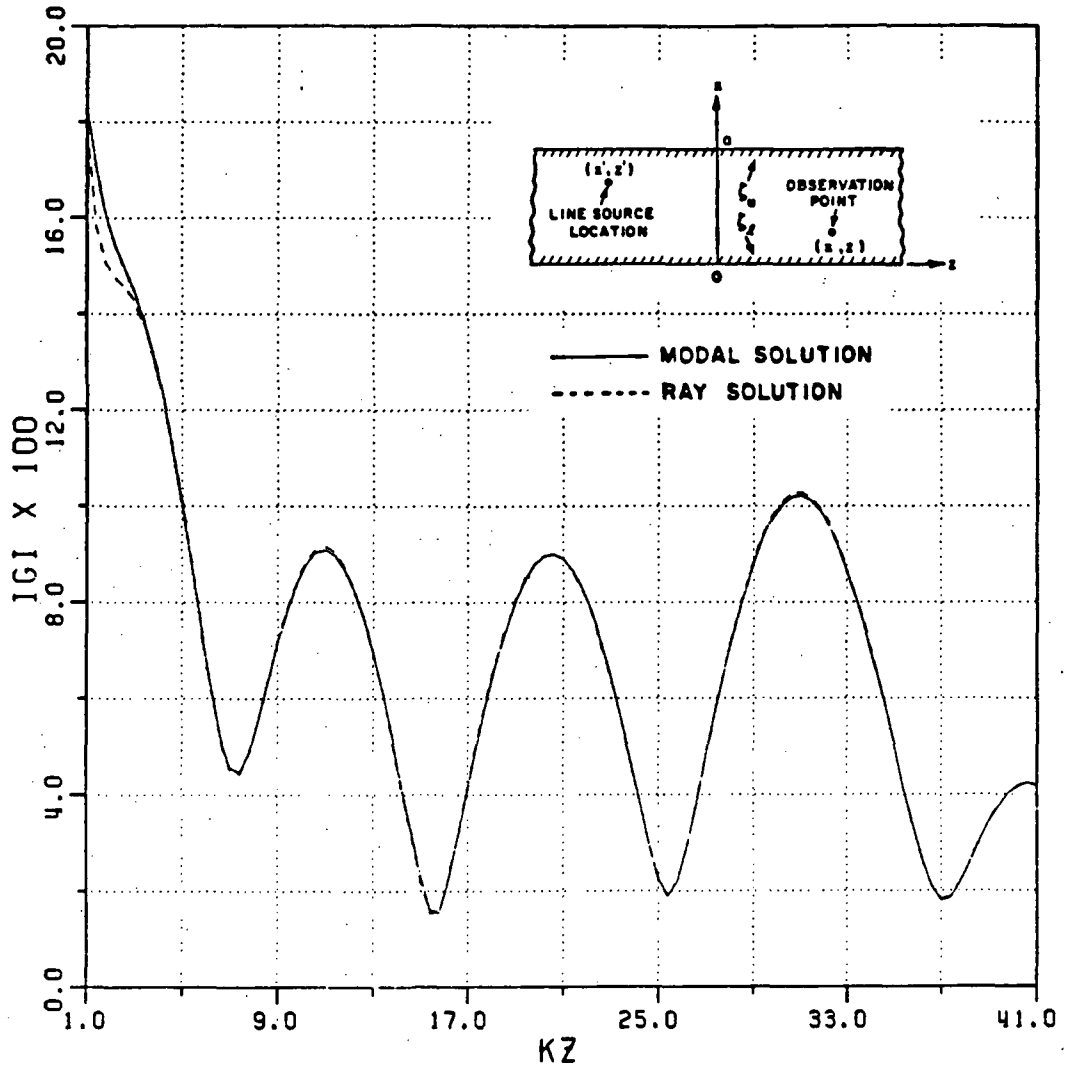

Figure 8: Magnitude of G for an infinitely-long parallel plate waveguide excited by an electric line source as a function of the normalized distance kz.

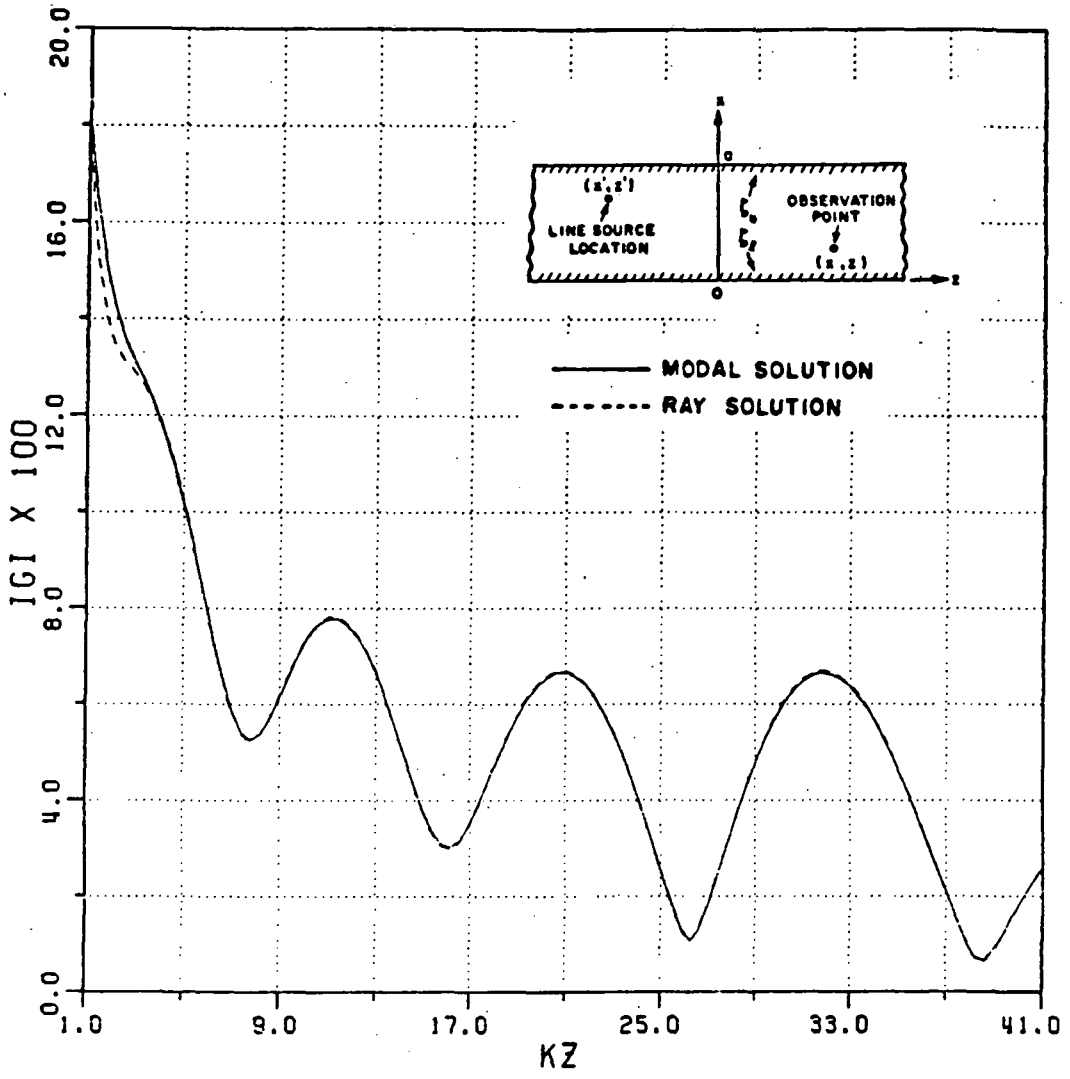

KA = 50.0	N= 3.0	RL= 0.5
KX'= 25.0	PM= 16.0	XL= 0.5
KX = 25.0	EM= 3.0	RU= 0.5
		XU= 0.5

Figure 9: Magnitude of G for an infinitely-long parallel plate waveguide excited by an electric line source as a function of the normalized distance kz.

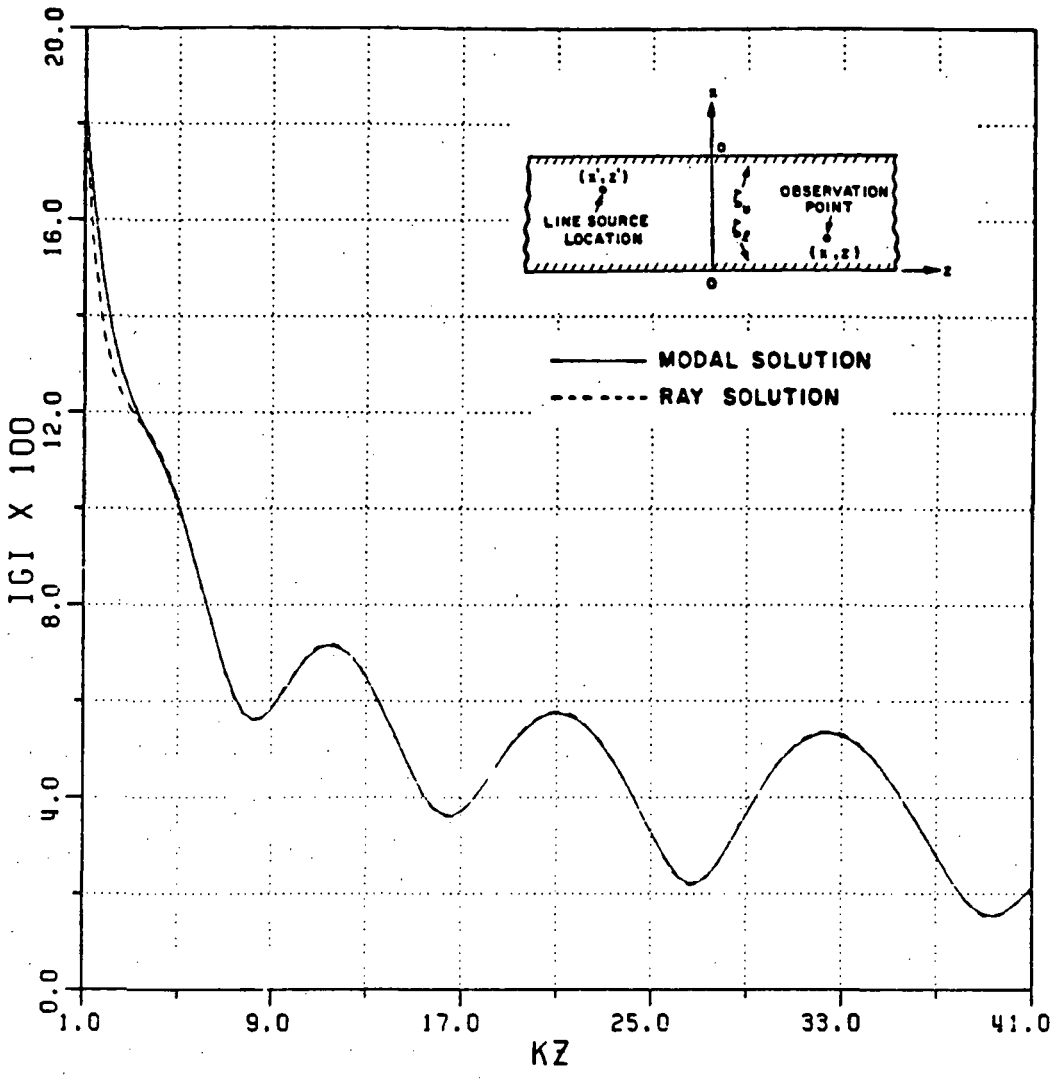

KA = 50.0	N= 3.0	RL= 0.8
KX'= 25.0	PM= 16.0	XL= 0.5
KX = 25.0	EM= 3.0	RU= 0.8
		XU= 0.5

Figure 10: Magnitude of G for an infinitely-long parallel plate waveguide excited by an electric line source as a function of the normalized distance kz.

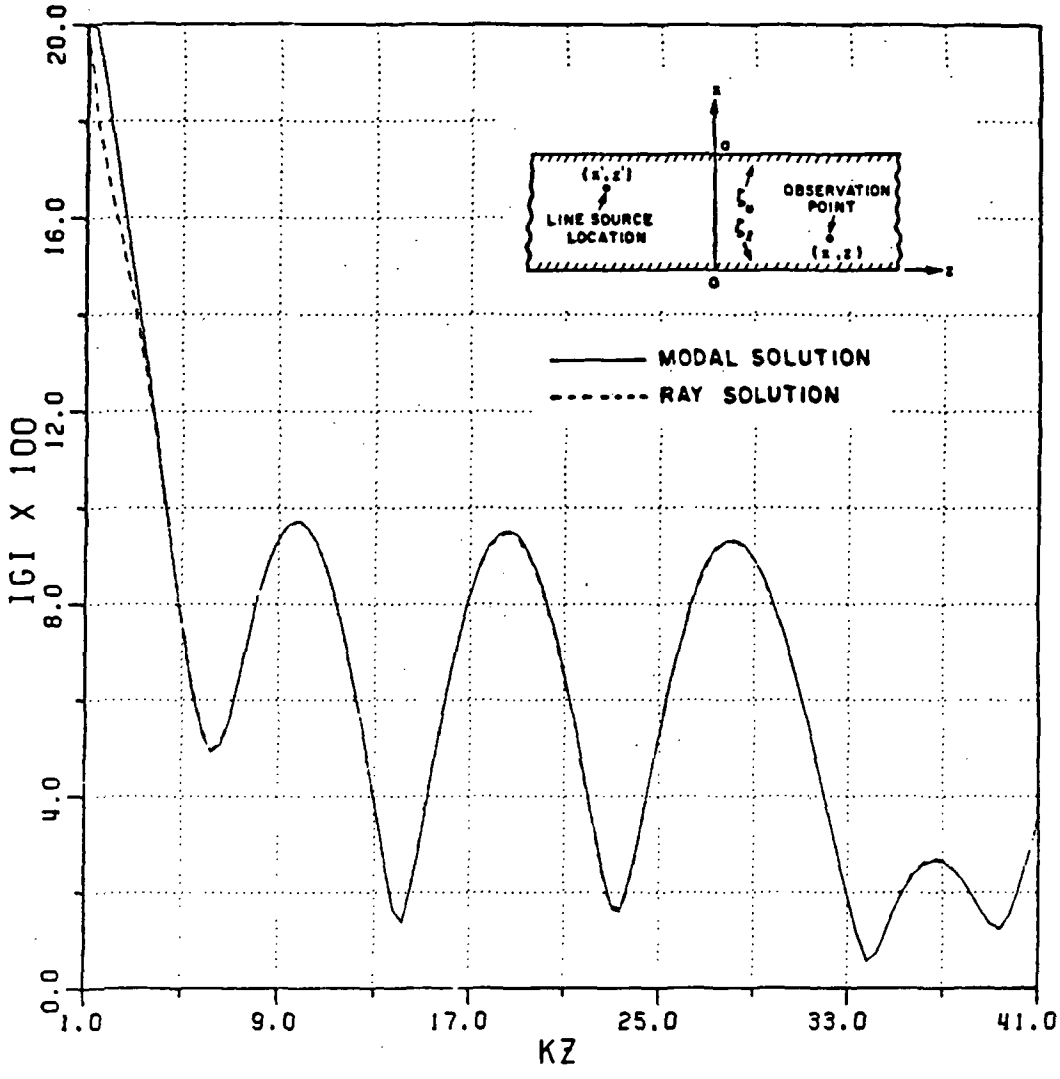

KA = 50.0	N= 3.0	RL= 0.2
KX'= 25.0	PM= 15.0	XL= -0.3
KX = 25.0	EM= 3.0	RU= 0.2
		XU= -0.3

Figure 11: Magnitude of G for an infinitely-long parallel plate waveguide excited by an electric line source as a function of the normalized distance kz.

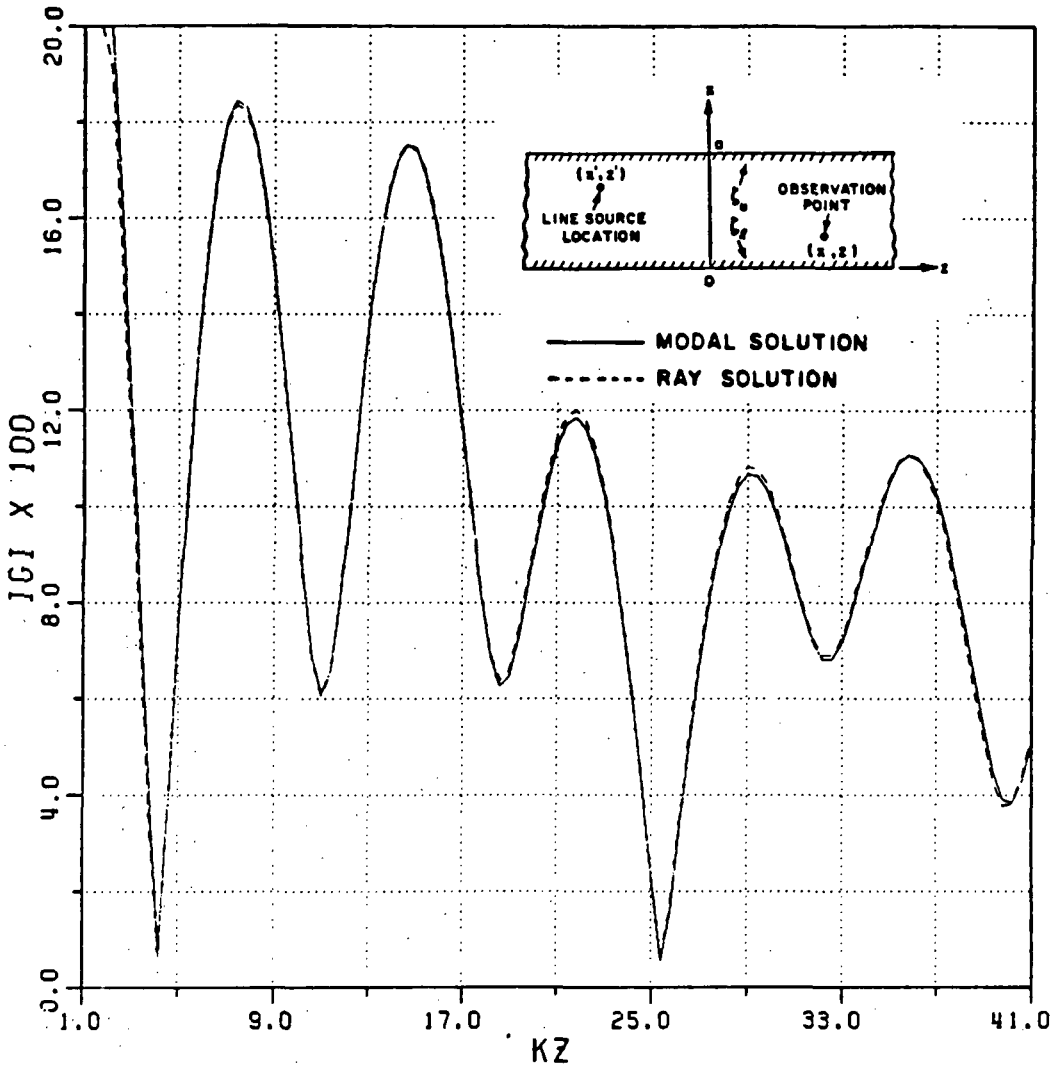

KA = 50.0 N= 7.0 RL = 0.1
KX'= 25.0 PM= 15.0 XL = 0.3
KX = 25.0 EM= 3.0 RU= 0.1
XU= 0.3

Figure 12: Magnitude of G for an infinitely-long parallel plate waveguide excited by a magnetic line source as a function of the normalized distance kz.

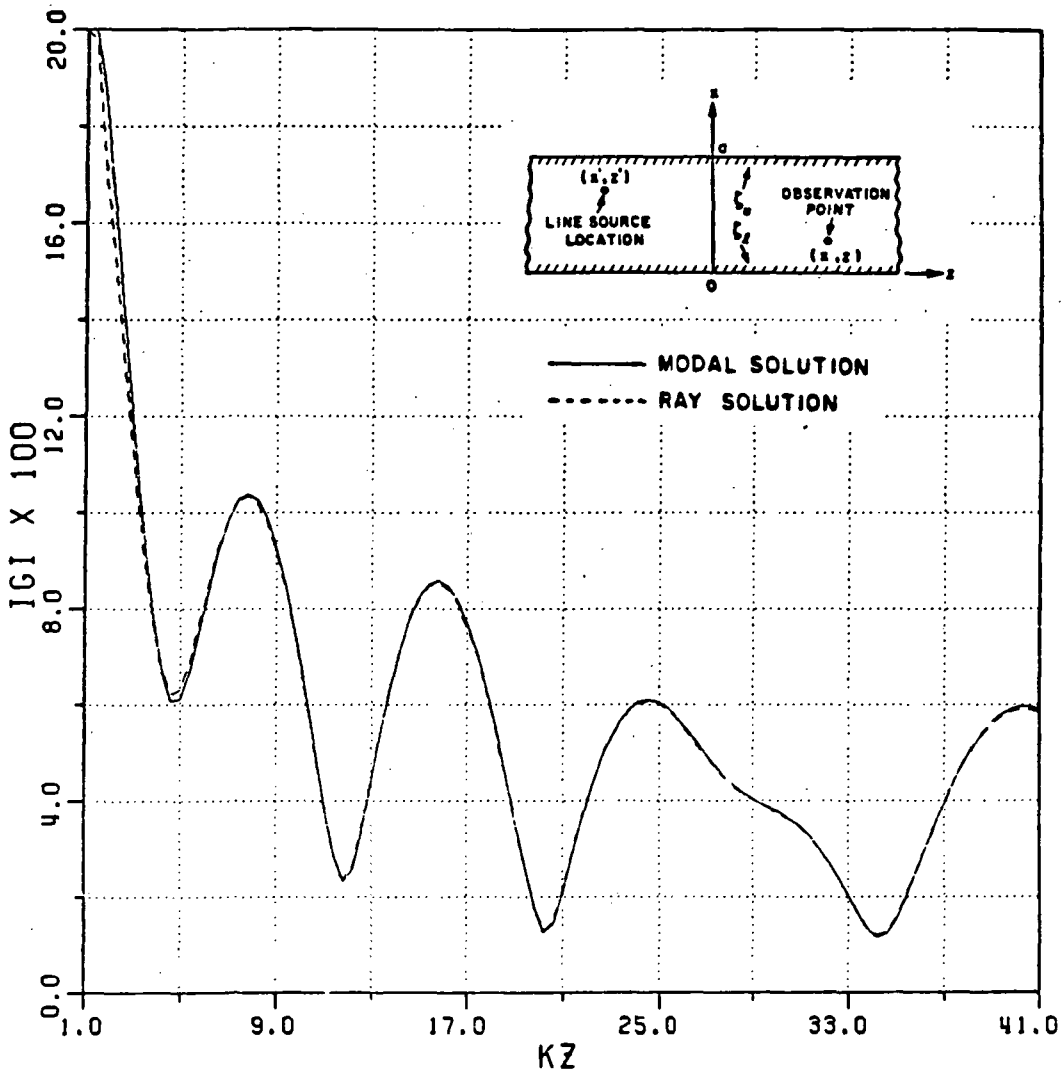

Figure 13: Magnitude of G for an infinitely-long parallel plate waveguide excited by a magnetic line source as a function of the normalized distance kz.

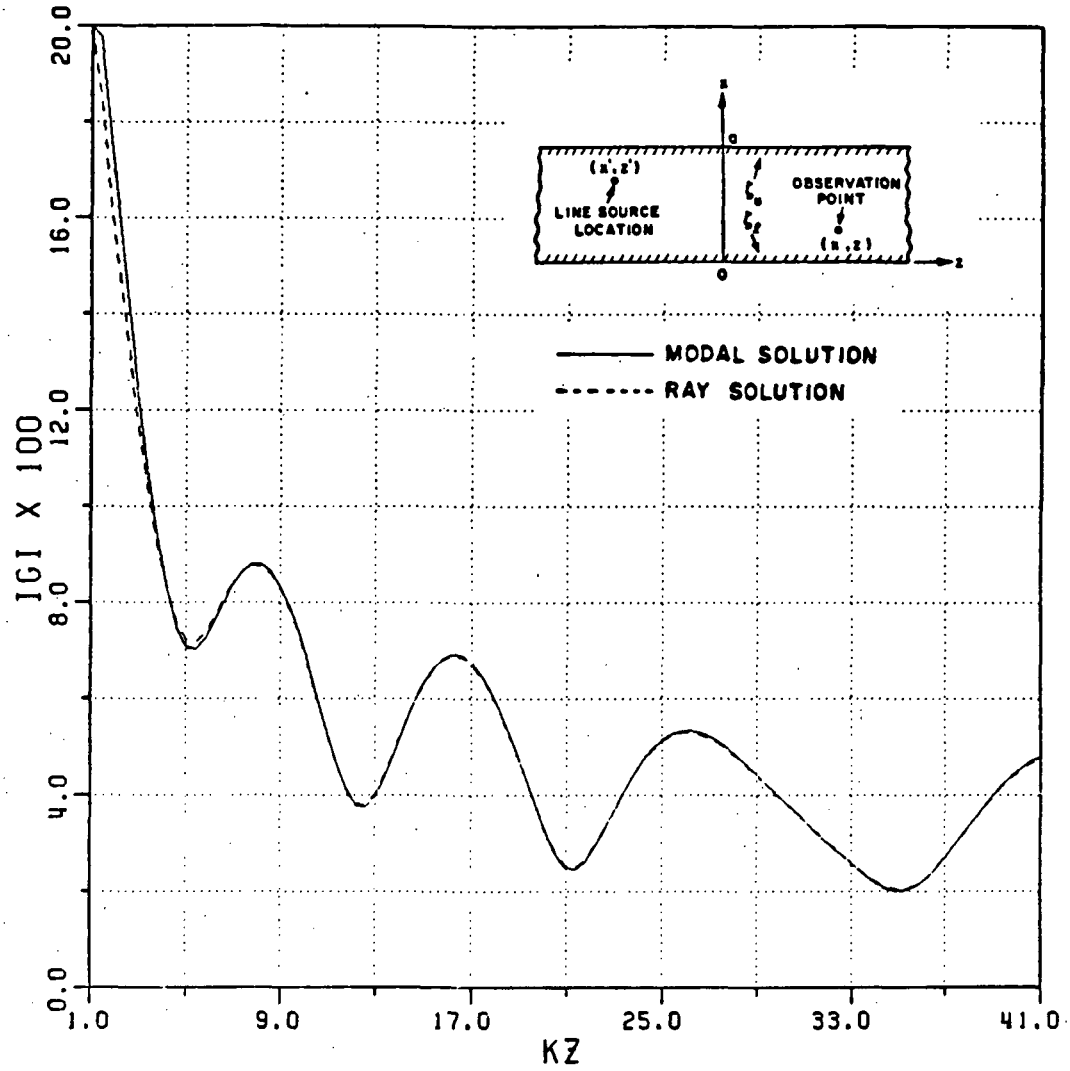

KA = 50.0	N= 7.0	RL= 0.8
KX'= 25.0	PM= 15.0	XL= 0.5
KX = 25.0	EM= 3.0	RU= 0.8
		XU= 0.5

Figure 14: Magnitude of G for an infinitely-long parallel plate waveguide excited by a magnetic line source as a function of the normalized distance kz.

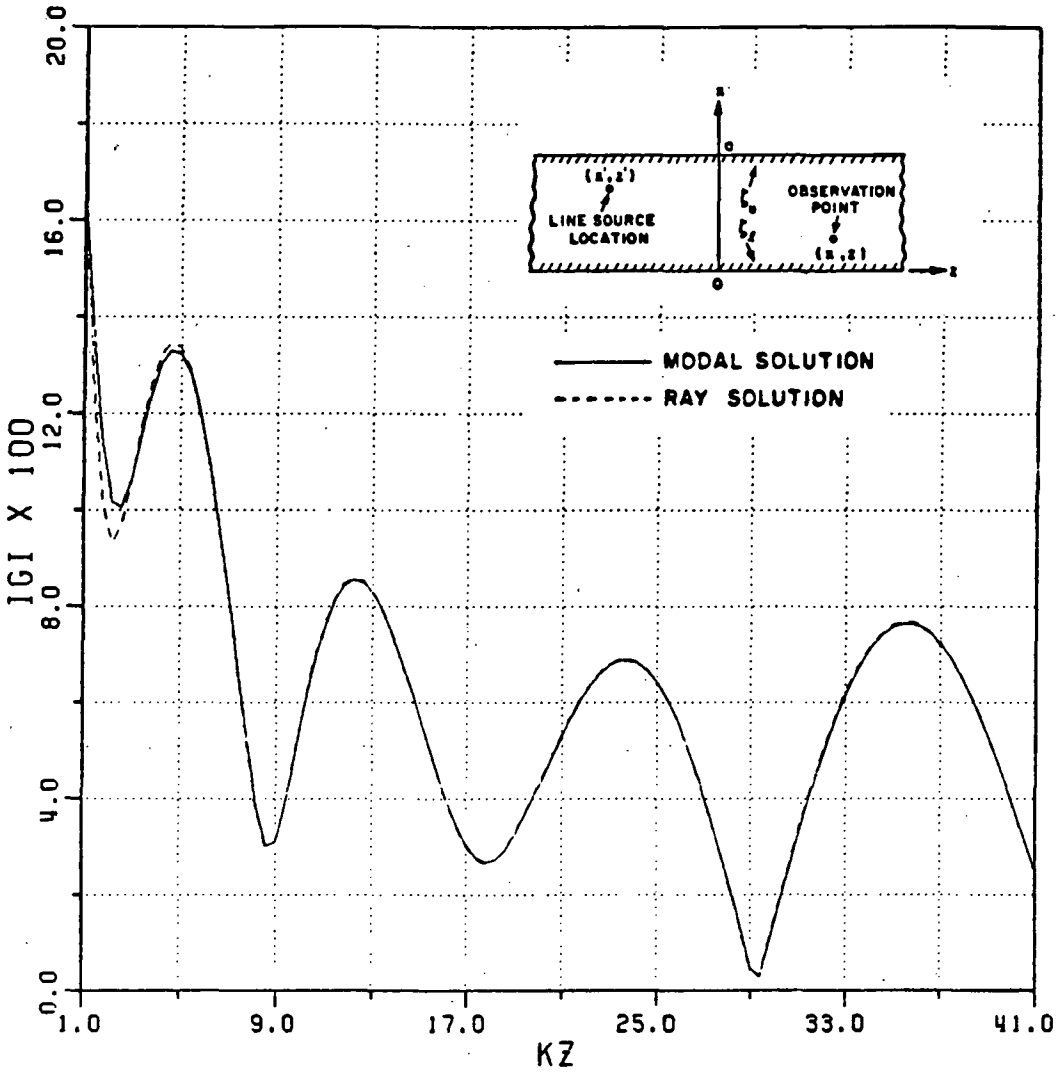

KA = 50.0	N= 7.0	RL= 0.2
KX'= 25.0	PM= 16.0	XL= -0.3
KX = 25.0	EM= 3.0	RU= 0.2
		XU= -0.3

Figure 15: Magnitude of G for an infinitely-long parallel plate waveguide excited by a magnetic line source as a function of the normalized distance kz.

2.2 Surface waves in the modal and ray solutions

Another interesting phenomenon which can take place in the case of a waveguide with impedance walls is that pertaining to the excitation of *surface wave* type fields. In the modal expression for the configuration in Figure 2, there are two surface wave type modes in addition to the usual waveguide type modes which are excited if the impedance is *inductively* (or *capacitively*) reactive when the excitation is due to a *magnetic* (or an *electric*) line source within the waveguide. These surface wave modes are distinct from the other waveguide modes; in particular, these modes exhibit the behaviour of the usual bound surface wave fields that can exist on a single impedance surface excited by a line source if the wall spacing is made sufficiently large.

An important characteristic of these surface wave type fields is that the energy associated with these fields is guided very close to the impedance surface. To check this characteristic, the magnitude of G for a magnetic line source is plotted in Figure 16 as a function of normalized *transverse* distance kx for fixed kz when the source is very near the lower wall. As shown in the figure, the two solutions show discrepancy when both the source and the field points are near the same impedance wall. This is because the surface wave contribution to the ray solution is anticipated to be very strong in that case and this surface wave contribution is *not* included in the ray solution in that figure. Note that the surface wave is included in the modal solution in the Figure 16. The details of the analysis which include the surface wave for both solutions are presented later in this section. However, as the field point moves to the upper wall for a given source point which is close to the lower wall, the two solutions agree well again. This good agreement is to be expected because the surface wave in the ray solution becomes weak and

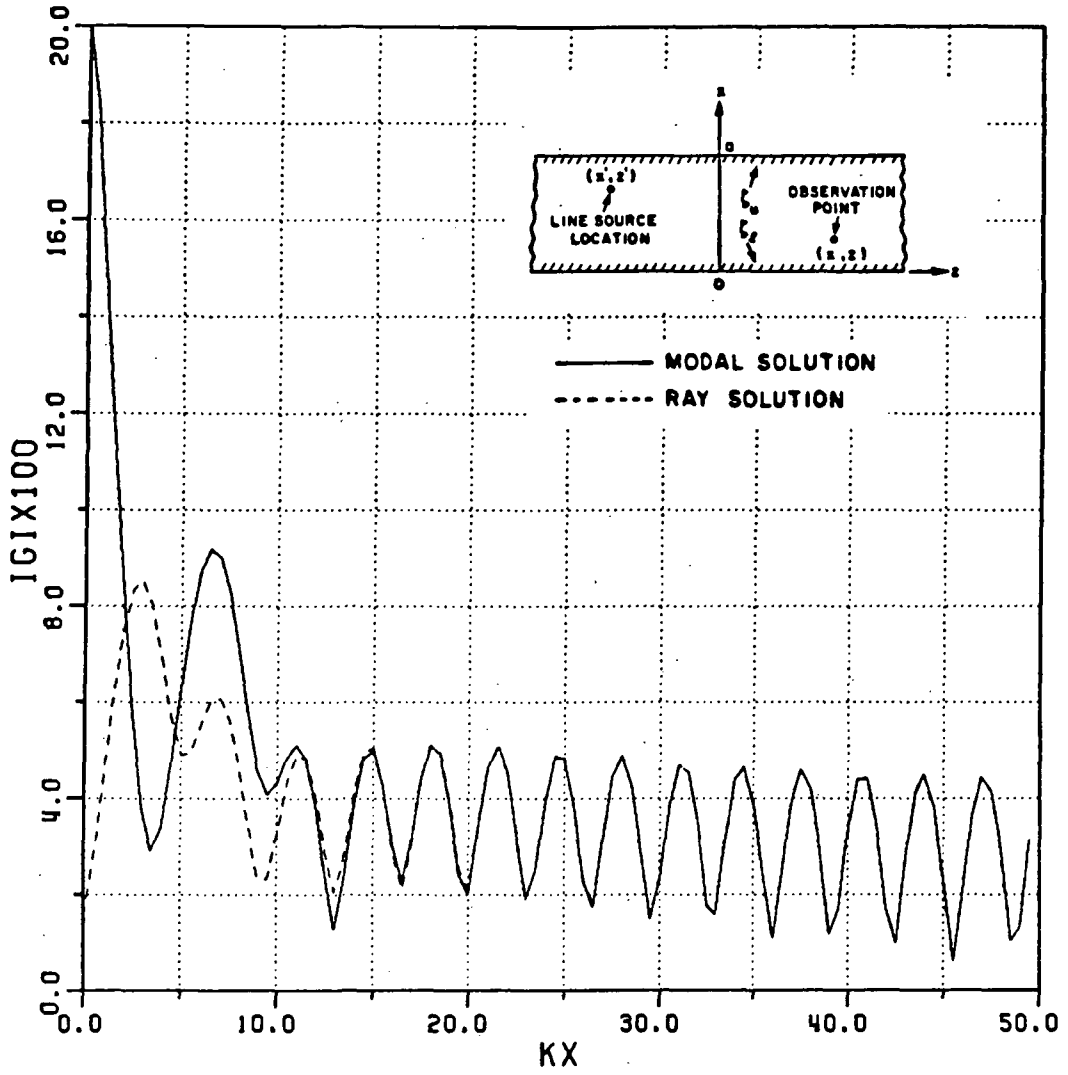

KA = 50.0 N= 7.0 R_L = 0.1
KX = 1.0 PM= 15.0 X_L = 0.3
KZ = 10.0 EM= 3.0 R_U = 0.1
X_U = 0.3

Figure 16: Magnitude of G for an infinitely-long parallel plate waveguide excited by a magnetic line source as a function of normalized distance kx for fixed kz.

contributes negligibly due to the exponential decay of the surface wave field as the field point is moved away from the impedance surface in whose vicinity the source is located. Figure 17 shows the fields inside the waveguide of Figure 2 when the source and observation points are both located close to one of the impedance walls of the waveguide, and the impedance is chosen to be inductively reactive for a magnetic line source excitation so that surface wave modes can exist. Note that the surface wave type fields are *not* included in either the modal or the ray solutions in the figure.

The surface wave modes can be included in the modal solution by simply evaluating the integral in Equation (2.12) via the residue theorem for the surface wave poles as done for the other ordinary modes. The distinction between the surface wave poles from the other ordinary poles is that the real part of k_z of the surface wave pole is greater than ka as shown in Table (2.2). It is clear that the surface wave pole at $\alpha = \alpha_p$ in the complex angular spectrum or α plane of Figure 19 is complex valued. Therefore, this complex valued surface wave pole (at $\alpha = \alpha_p$) cannot be excited by a plane wave which has a real valued angle of incidence. When the plane wave is incident on the edges at the open end of the semi-infinite waveguide with a non-zero surface impedance (or absorber coating) on its inner walls, it scatters to produce the reflected and edge diffracted fields. The scattered fields can be expressed as an integral (over a contour C of Figure 19) in the angular spectral (α) domain; an asymptotic (saddle point) approximation to this angular spectrum integral furnishes the so called "*diffracted rays*" which propagate from the edges to an observation point along localized paths or rays. A pole exists in the integrand at a real value of α; it can be captured for a certain range of observation angles to furnish the reflected field which propagates along the reflected ray. The exact integral representation in the angular spectral domain,

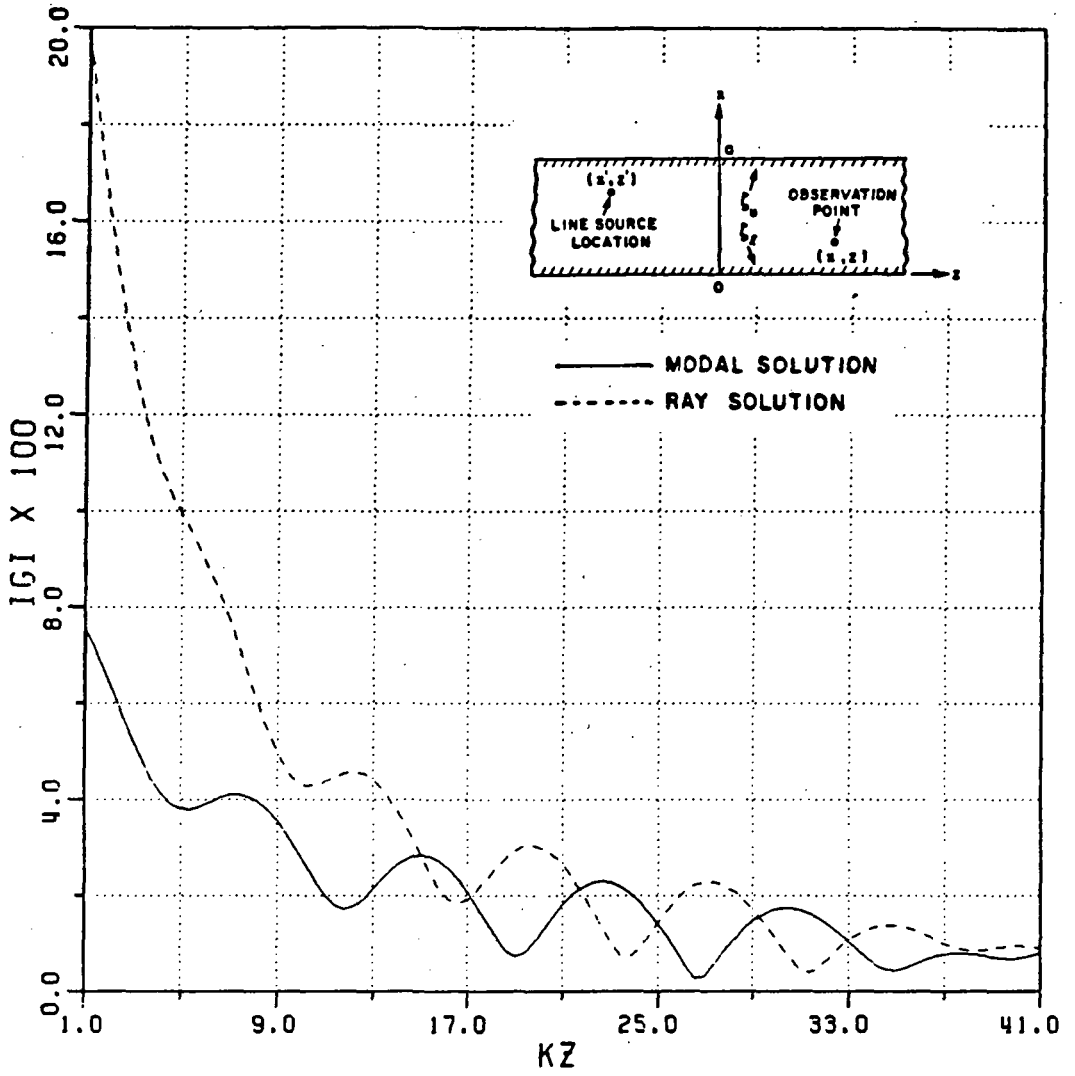

KA = 50.0	N= 7.0	R_L = 0.1
KX'= 1.0	PM= 15.0	X_L = 0.3
KX = 1.0	EM= 3.0	R_U = 0.1
		X_U = 0.3

Figure 17: Magnitude of G for a magnetic line source without surface wave contributions to both modal and ray solutions when both source and field points are near the lower wall.

Table 2.2: Ordinary and surface wave poles on k_x and k_z planes for a magnetic line source for $ka = 50.0$ and $Z_l = Z_u = 0.1 + j0.3$

i	k_{x_i}	k_{z_i}	
1	$3.559+j\ 0.154$	$49.873-j\ 0.011$	
2	$7.094+j\ 0.269$	$49.495-j\ 0.039$	
3	$10.582+j\ 0.331$	$48.869-j\ 0.072$	
4	$14.009+j\ 0.351$	$47.999-j\ 0.103$	
5	$17.379+j\ 0.347$	$46.884-j\ 0.129$	
6	$20.702+j\ 0.331$	$45.514-j\ 0.151$	
7	$23.998+j\ 0.312$	$43.871-j\ 0.170$	
8	$27.247+j\ 0.291$	$41.925-j\ 0.189$	
9	$30.486+j\ 0.272$	$39.633-j\ 0.209$	ordinary
10	$33.708+j\ 0.254$	$36.931-j\ 0.232$	poles
11	$36.917+j\ 0.238$	$33.723-j\ 0.260$	
12	$40.117+j\ 0.223$	$29.846-j\ 0.300$	
13	$43.309+j\ 0.210$	$24.990-j\ 0.363$	
14	$46.494+j\ 0.198$	$18.400-j\ 0.500$	
15	$49.674+j\ 0.187$	$5.913-j\ 1.571$	
16	$52.850+j\ 0.177$	$0.547-j17.129$	
17	$56.022+j\ 0.168$	$0.373-j25.270$	
18	$59.191+j\ 0.160$	$0.300-j31.680$	
⋮	⋮	⋮	
	$4.999+j15.000$	$51.983-j\ 1.442$	surface wave
	$5.001+j15.000$	$51.982-j\ 1.442$	poles

however, also contains a complex valued angle $\alpha = \alpha_p$ at which the integrand exhibits another pole singularity; this pole can also be captured for a certain range of angles to furnish the surface wave; i.e. the phenomenon of scattering (or diffraction) by an edge in an impedance surface can indeed excite a surface wave. Thus, the edges of the semi-infinite waveguide with an impedance boundary condition on its inner walls will excite a surface wave when they are illuminated by a plane wave. This surface wave will then propagate inside the waveguide. It is convenient to think of "*equivalent*" line currents located at the edges, which can be deduced from the expression for the edge diffracted fields, as the sources which produce the surface wave. It is therefore of interest to find the surface wave which is excited by a line source on one of the waveguide boundaries as in Figure 2 to simulate the effect of a surface wave excited by the diffraction of a plane wave which is incident on one of the edges of the semi-infinite waveguide walls. In this instance where the line source is located at (or near) one of the waveguide walls, only the $n = 0$ case in Equations (2.24)-(2.27) is important, and even for this $n = 0$ case only the corresponding $m = 2$ and $m = 3$ terms are dominant, as the remaining terms emphasize repeated interactions of the surface wave field with the opposite wall; the latter interaction is assumed to be small because the surface wave decays exponentially on the boundary on which the source is located and its field is therefore weak at the opposite wall if the wall spacing is sufficiently large.

Despite the inclusion of the surface wave effects, the agreement between the exact modal and the approximate ray solution is not so good in Figure 18, unless the distance from the source to the observer is sufficiently large. It was found that the reason for this discrepancy between the two solutions could be traced to the need for an increased accuracy in the asymptotic approximation of the ray solution near the surface when the observation point lies within the surface wave

"*transition region*" where the surface wave is not fully established. This "*transition region*" extends over a certain distance from the source depending on the value of the impedance; e.g., it becomes larger for the magnetic line source excitation of an inductively reactive impedance boundary as the inductive reactance becomes smaller. This transition region may be viewed as a "*launching*" or "*peel out*" distance required to establish the surface wave. A *uniform* asymptotic treatment of the integral representation of the waveguide Green's function which yields the ray expansion provides a simple *transition function* correction to the surface ray solution in terms of a *Fresnel integral.* The *ordinary* ray series solution including the surface wave (or ray) contribution results from a *non-uniform* asymptotic treatment of the integral for the waveguide Green's function; this ordinary ray solution is accurate only outside the *surface wave transition region.* Mathematically speaking, the observation point lies within the surface wave transition region when the surface wave pole α_p is close to the saddle point α_s as shown in Figure 19. Consider the integral given by

$$I(kr) = \int_{C_{SDP}} \frac{F(\alpha)}{\alpha - \alpha_p} e^{krf(\alpha)} \, d\alpha \tag{2.36}$$

where α_p and α_s are a surface wave pole and saddle point, respectively and the surface wave pole is near the saddle point as shown in the above figure. Then, the integral is evaluated asymptotically using the uniform saddle point approximation as in Felsen and Marcuvitz [9], and is given by

$$I(kr) = e^{-jkr} \left[\sqrt{\frac{\pi}{kr}} \, T(0) \pm j2\sqrt{\pi} F(\alpha_p) \; e^{-krb^2} \, Q(\mp jb\sqrt{kr}\,) \right] \tag{2.37}$$
$$; \; Im(b) \gtrless 0$$

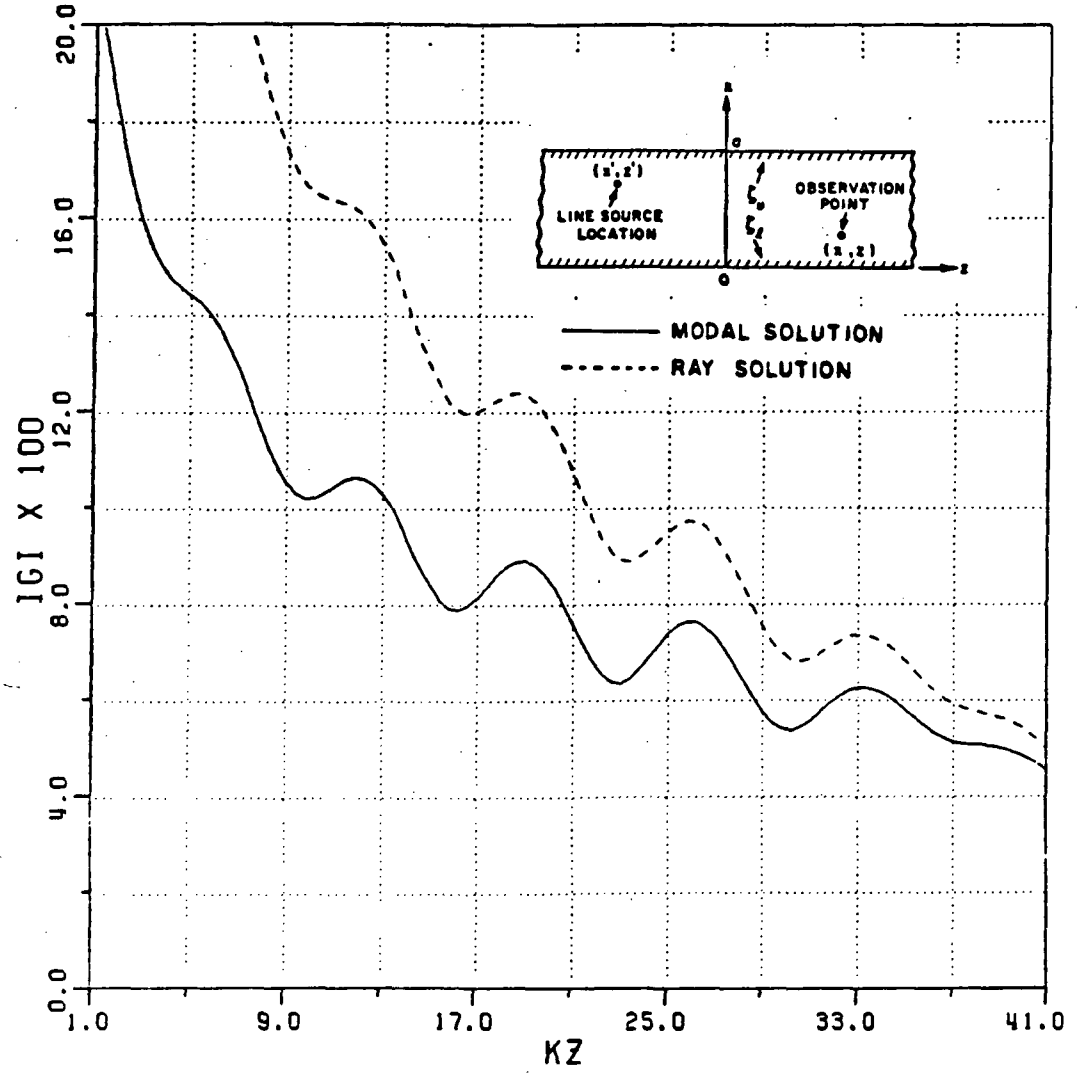

KA = 50.0	N= 7.0	R_L = 0.1
KX'= 1.0	PM= 15.0	X_L = 0.3
KX = 1.0	EM= 3.0	R_U = 0.1
		X_U = 0.3

Figure 18: Magnitude of G for the case in Figure 17 except that the surface waves are included in both solutions but the surface transition function is not included in the ray solution.

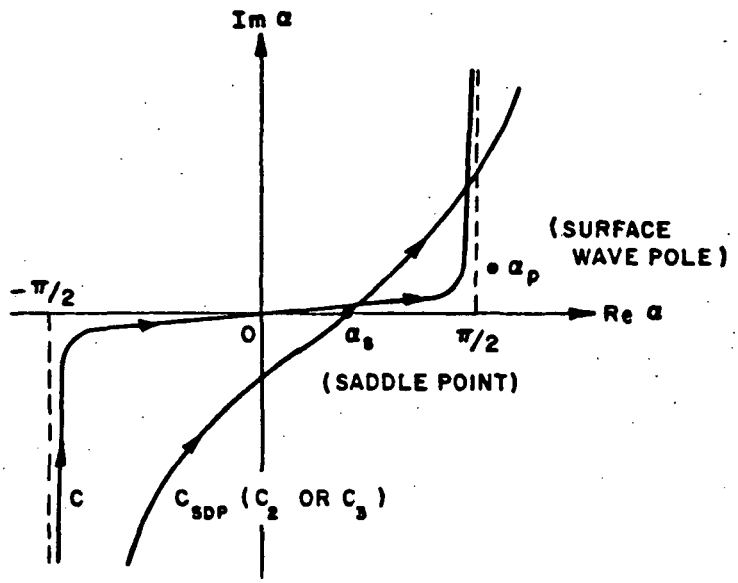

Figure 19: Integration path and a surface wave pole α_p which is near the saddle point α_s.

where

$$b = \sqrt{f(\alpha_s) - f(\alpha_p)} \tag{2.38}$$

$$T(0) = \frac{hf(\alpha_s)}{\alpha - \alpha_p} + \frac{f(\alpha_p)}{b} \tag{2.39}$$

$$h = \sqrt{\frac{-2}{f''(\alpha_s)}} \tag{2.40}$$

$$Q(y) = \int_y^\infty e^{-x^2}\, dx \tag{2.41}$$

Using the above formula, the integral in Equation (2.36) can be evaluated to obtain the surface ray field.

For analytical details, consider G_{2n} in Equation (2.25). For $n = 0$, G_{2n}

reduces to

$$G_{20} = -\frac{j}{4\pi}\int_{C_2}\frac{\cos\alpha - Z_u}{\cos\alpha + Z_u}\, e^{+jk[\cos\alpha(x_<+x_>)-\sin\alpha|z-z'|]}\, d\alpha$$

$$= -\frac{j}{4\pi}\int_{C_2}\frac{\cos\alpha - Z_u}{\cos\alpha + Z_u}\, e^{+jkr\cos(\alpha-\theta)} \tag{2.42}$$

where

$$r = \left[(x_< + x_>)^2 + (z-z')^2\right]^{1/2} \tag{2.43}$$

$$\theta = \tan^{-1}\left(\frac{|z-z'|}{x_< - x_>}\right) = \alpha_s \tag{2.44}$$

Then, the parameters in Equations (2.38)–(2.40) are expressed as

$$f(\alpha) = j\cos(\alpha - \alpha_s) \tag{2.45}$$

$$f''(\alpha) = -j\cos(\alpha - \alpha_s) \tag{2.46}$$

$$b = \sqrt{j\,(1-\cos(\alpha-\alpha_s))} \tag{2.47}$$

$$T(0) = \frac{\sqrt{2}\, e^{+j\pi/4}\, f(\alpha_s)}{\alpha_s - \alpha} + \frac{f(\alpha)}{\sqrt{2}\, e^{-j\pi/4}\sin(\frac{\alpha-\alpha_s}{2})} \tag{2.48}$$

$$h = \sqrt{2}\, e^{-j\pi/4} \tag{2.49}$$

The analysis for G_{30} is very similar and is thus ommitted here.

A comparison of the improved or *uniform* ray solution with the exact modal solution shown in Figure 20 now indicates that they are in excellent agreement.

Note that the modal solution in Figure 20 is unchanged as compared to that in Figure 18; only the ray solution has been improved in Figure 20 by including the *uniform surface wave transition function.* Since surface wave effects are dominant only in the vicinity of the boundary on which the source is located, these surface wave effects may be neglected whenever the observation point is located far from the surface near which the source is placed as shown in Figure 21. A particulary interesting result is observed when the source and observation points lie on the same impedance wall of the parallel plate waveguide as in Figure 22. In Figure 22, the ray solution which is composed of the direct ray contribution from the source together with the contribution from rays singly and multiply reflected from the walls interferes strongly with the surface wave field plus the term containing the surface wave transition effects since all of the latter surface wave effects are particulary significant at and near the surface containing the source.

The result in Figure 22 indicates that the surface wave launched by the incident wave at the edges in Figure 1 could reflect strongly from any discontinuity placed close to the walls of an absorber lined duct; the reflected surface wave could then radiate outside the semi-infinite waveguide geometry in Figure 1 again via diffraction from the edges at the waveguide opening. On the other hand, the effect of the surface wave field could be controlled to exhibit a greater attenuation along the direction of propagation with the inclusion of greater loss in the impedance surface characterizing the thin absorber lined waveguide walls.

2.3 Convergence test of the modal and ray solutions

To check the nature of the convergence of the modal and ray solutions, the magnitude of G is plotted against the number of modes and rays involved in the

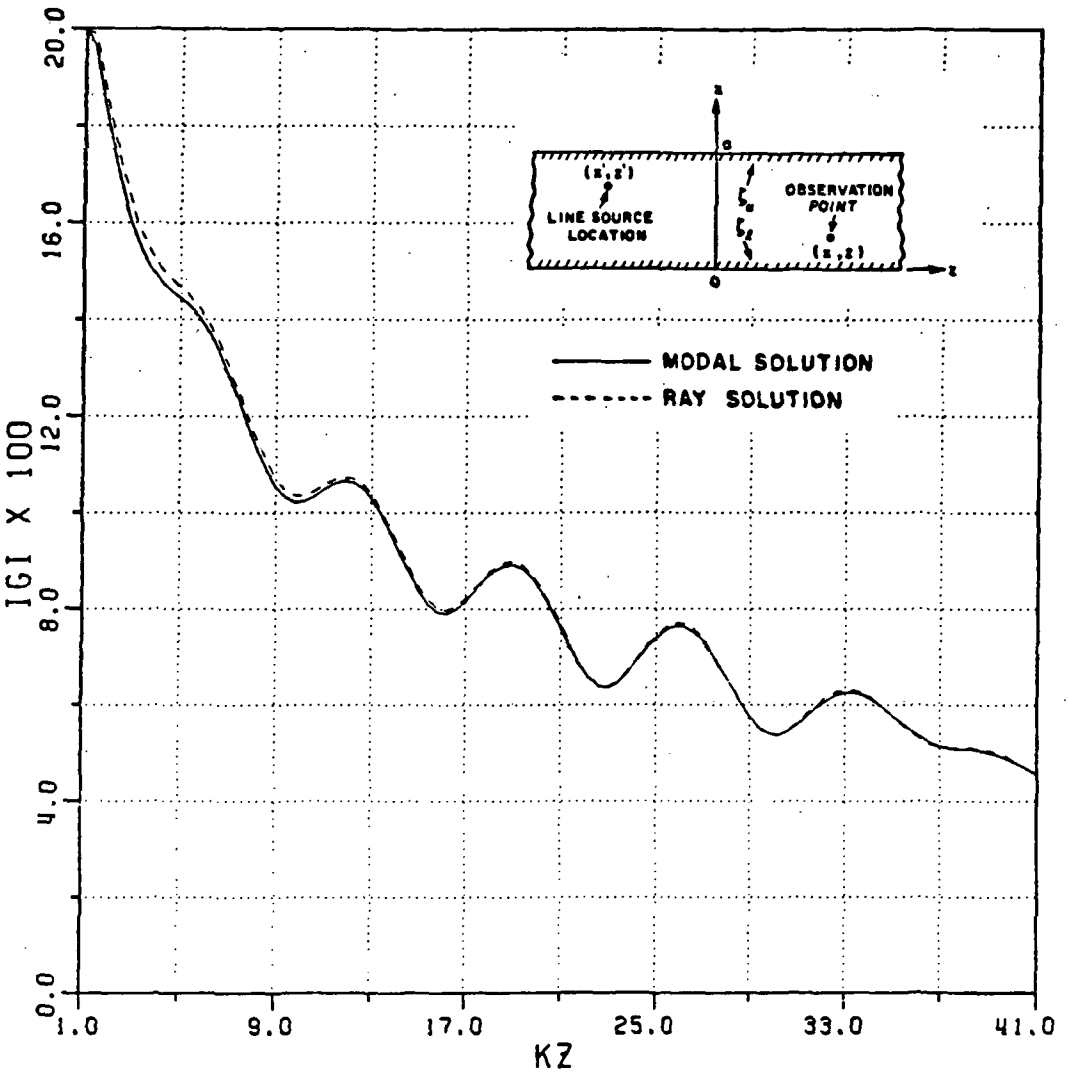

Figure 20: Magnitude of G in the case of Figure 18 except that the *uniform* transition function is included in the ray solution.

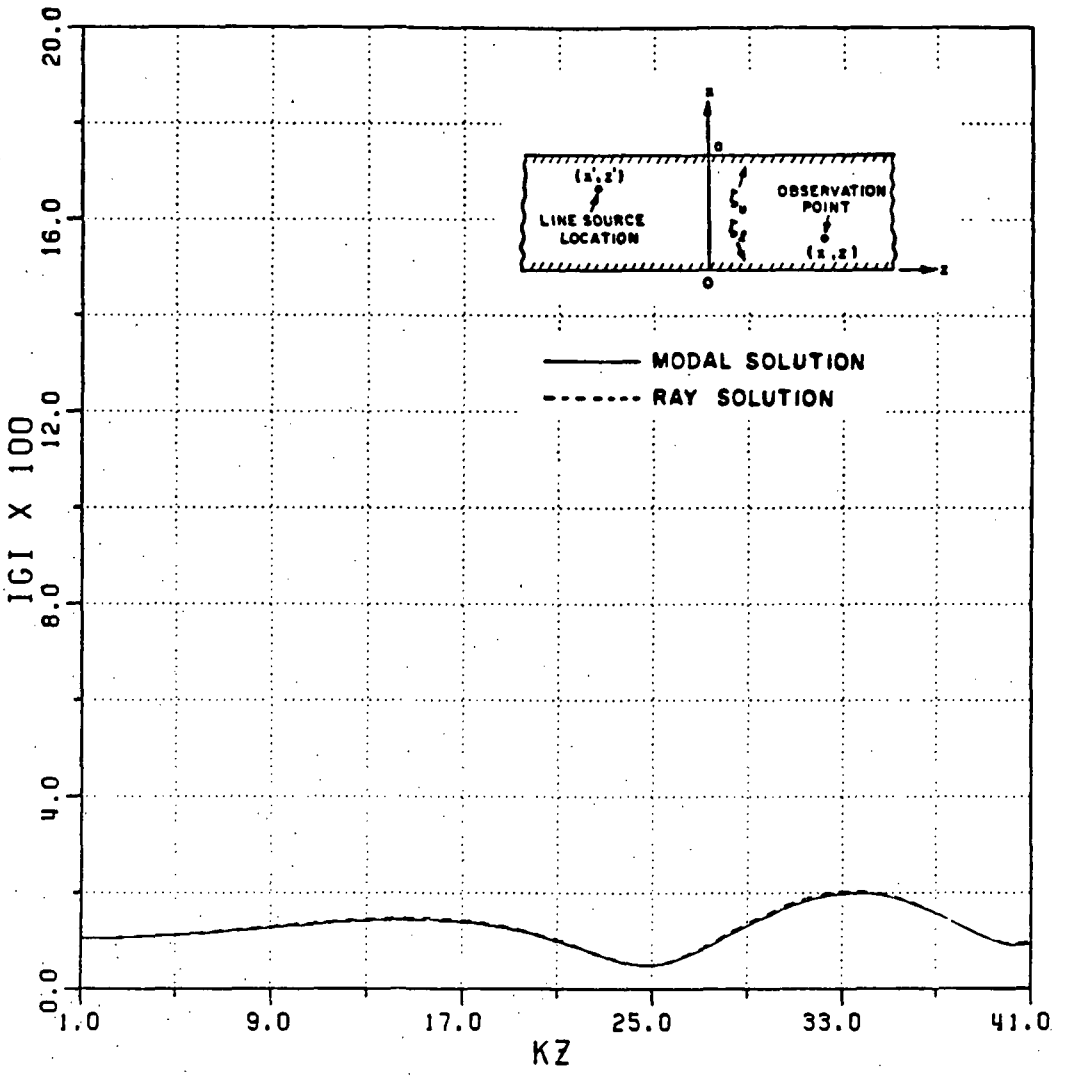

KA = 50.0	N= 7.0	RL = 0.1
KX'= 1.0	PM= 15.0	XL = 0.3
KX = 49.0	EM= 3.0	RU = 0.1
		XU = 0.3

Figure 21: Magnitude of G for a magnetic line source when a source point is near the lower wall and a field point is near the upper wall.

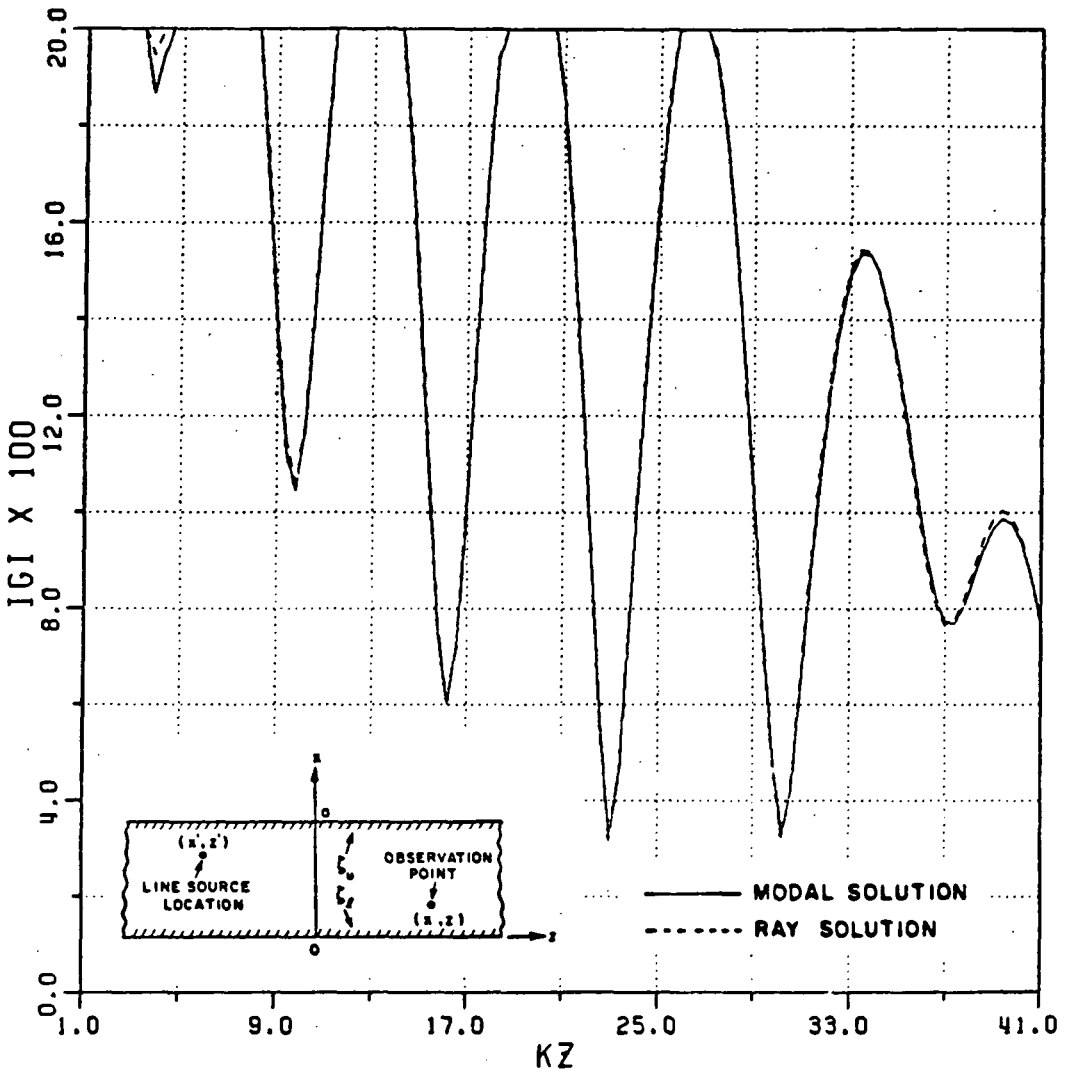

KA = 50.0 N= 7.0 RL= 0.1
KX'= 0.0 PM= 15.0 XL= 0.3
KX = 0.0 EM= 3.0 RU= 0.1
XU= 0.3

Figure 22: Magnitude of G for a magnetic line source when both source and field points are on the lower wall.

calculations for a fixed kz in Figures 23–26 which pertain to an electric line source, and in Figures 27–30 for a magnetic line source. Different impedance values are employed in each of these figures. It is observed from the figures that the modal solution reaches a stable field value after summing all the propagating modes for $kz = 20.0$. On the other hand, at most $n = 3$ terms are needed in the ray solution to arrive at the same result.

As pointed out above, it is observed from Figures 23–30 that the convergence of the ray solution is faster than the modal solution, and secondly, the convergence of the modal solution is not significantly improved by the presence of loss in the walls since all the propagating modes in this case (plus one evanescent mode near the source region) are required for convergence. On the other hand, the convergence of the ray solution is improved much as the impedance value becomes bigger (for the TE_y case) as shown in the figures. It is conceivable that a special selection of modes which contribute significantly for a given kz and kx will converge faster; however, a different selection would be required for each different kz. It is not clear at this time how such a special selection of the modes can be made.

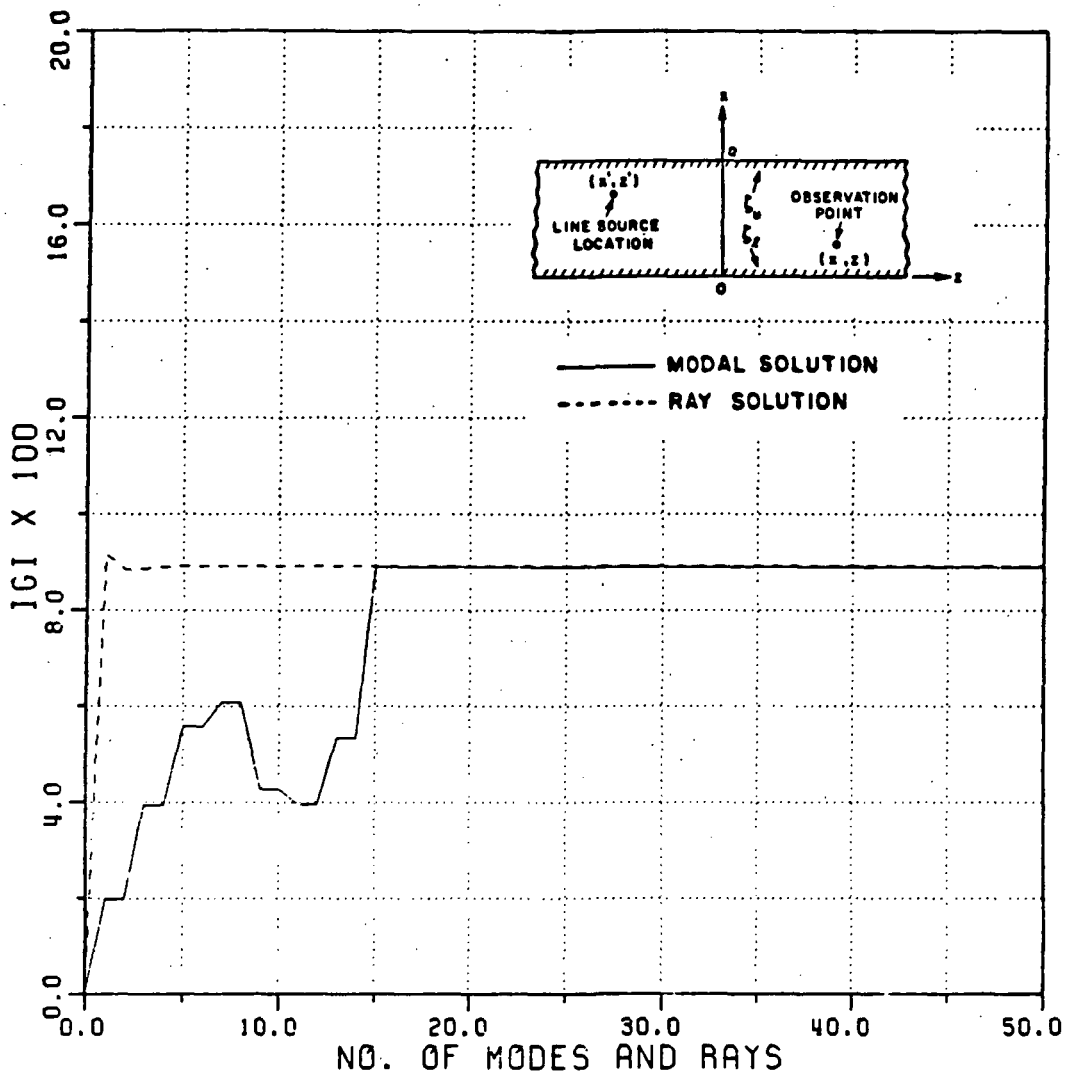

KA = 50.0 KZ= 20.0 RL = 0.1
KX'= 25.0 XL = 0.3
KX = 25.0 RU = 0.1
PM = 16.0 XU = 0.3

Figure 23: Convergence of the modal and ray solutions for an electric line source and for a fixed kz.

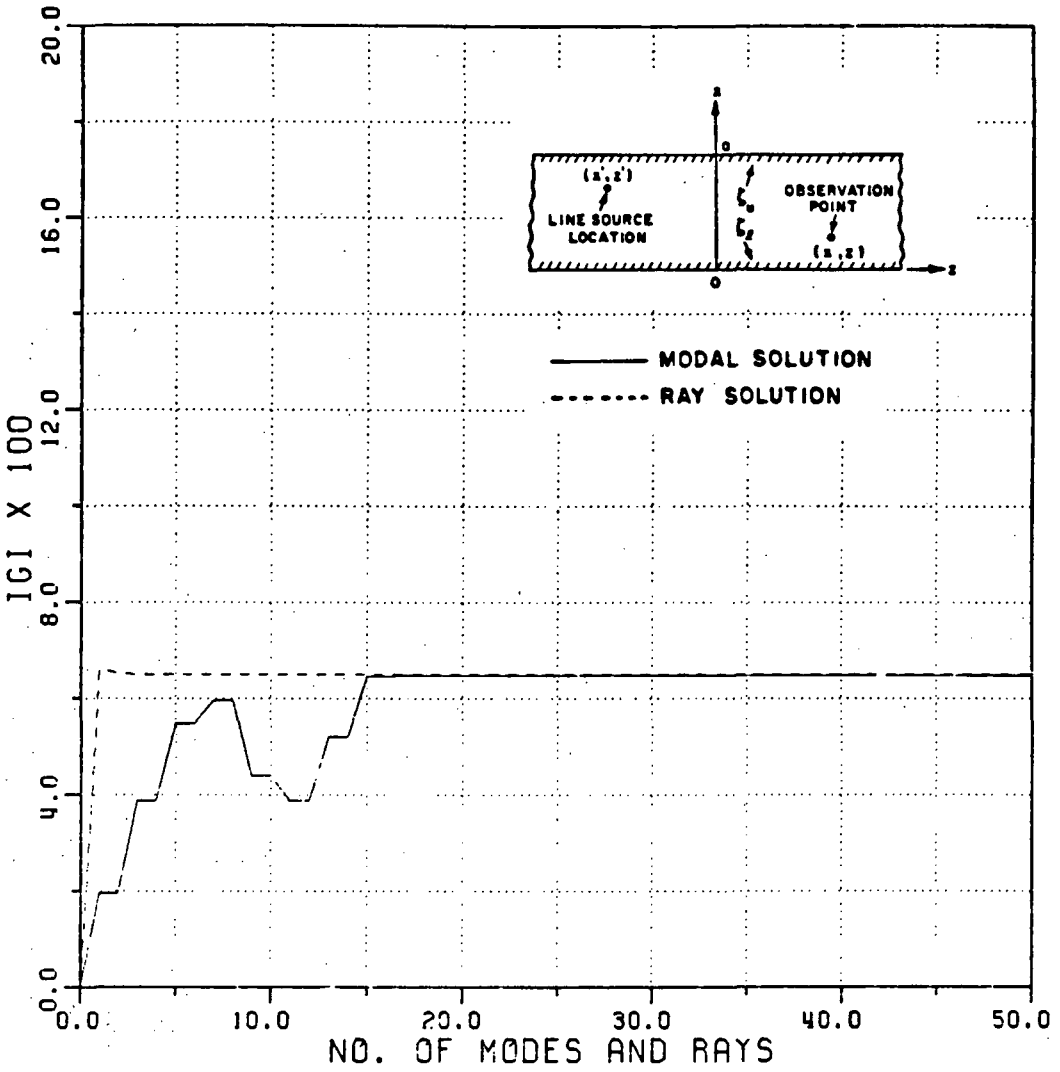

KA = 50.0 KZ= 20.0 RL = 0.5
KX'= 25.0 XL = 0.5
KX = 25.0 RU = 0.5
PM = 16.0 XU = 0.5

Figure 24: Convergence of the modal and ray solutions for an electric line source and for a fixed kz.

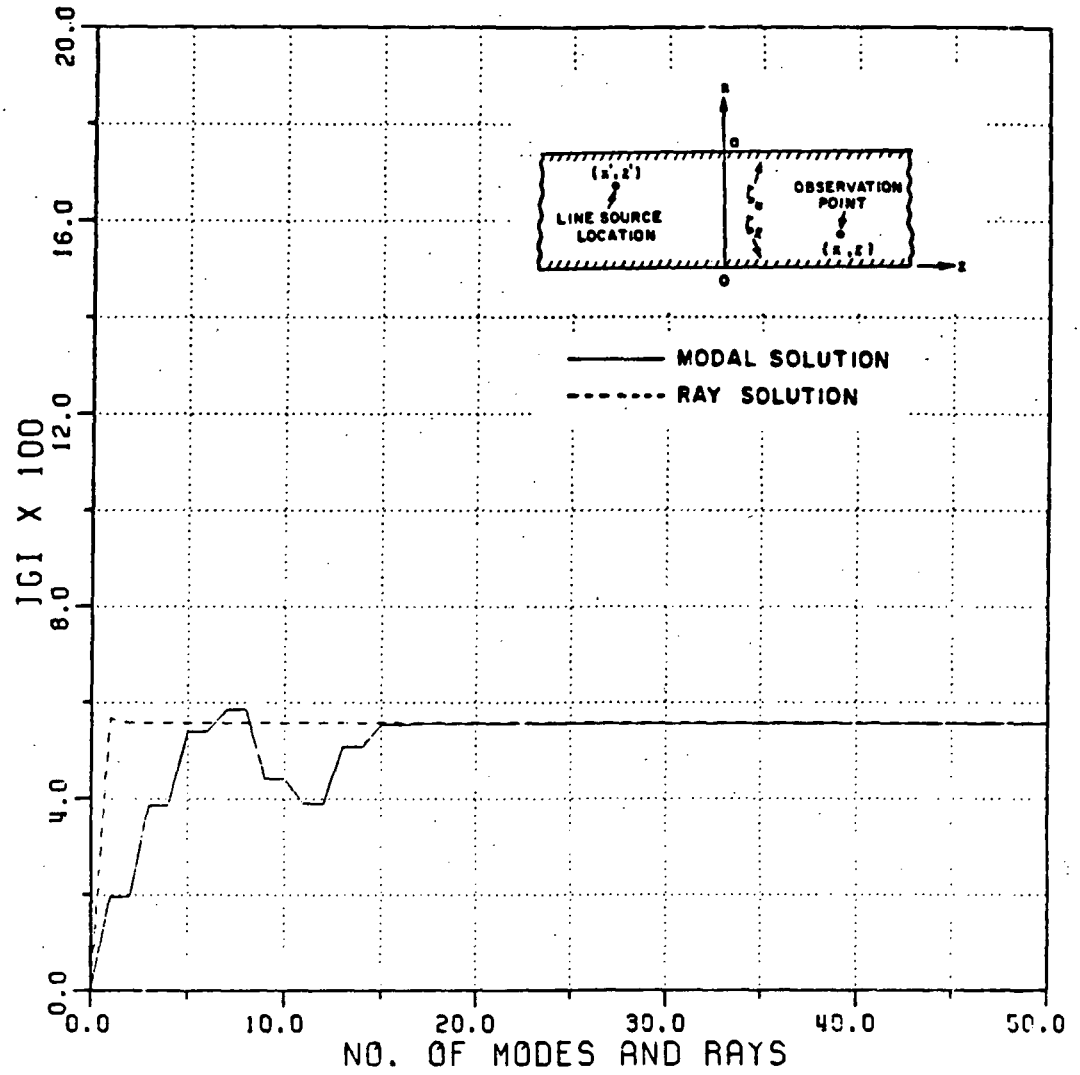

Figure 25: Convergence of the modal and ray solutions for an electric line source and for a fixed kz.

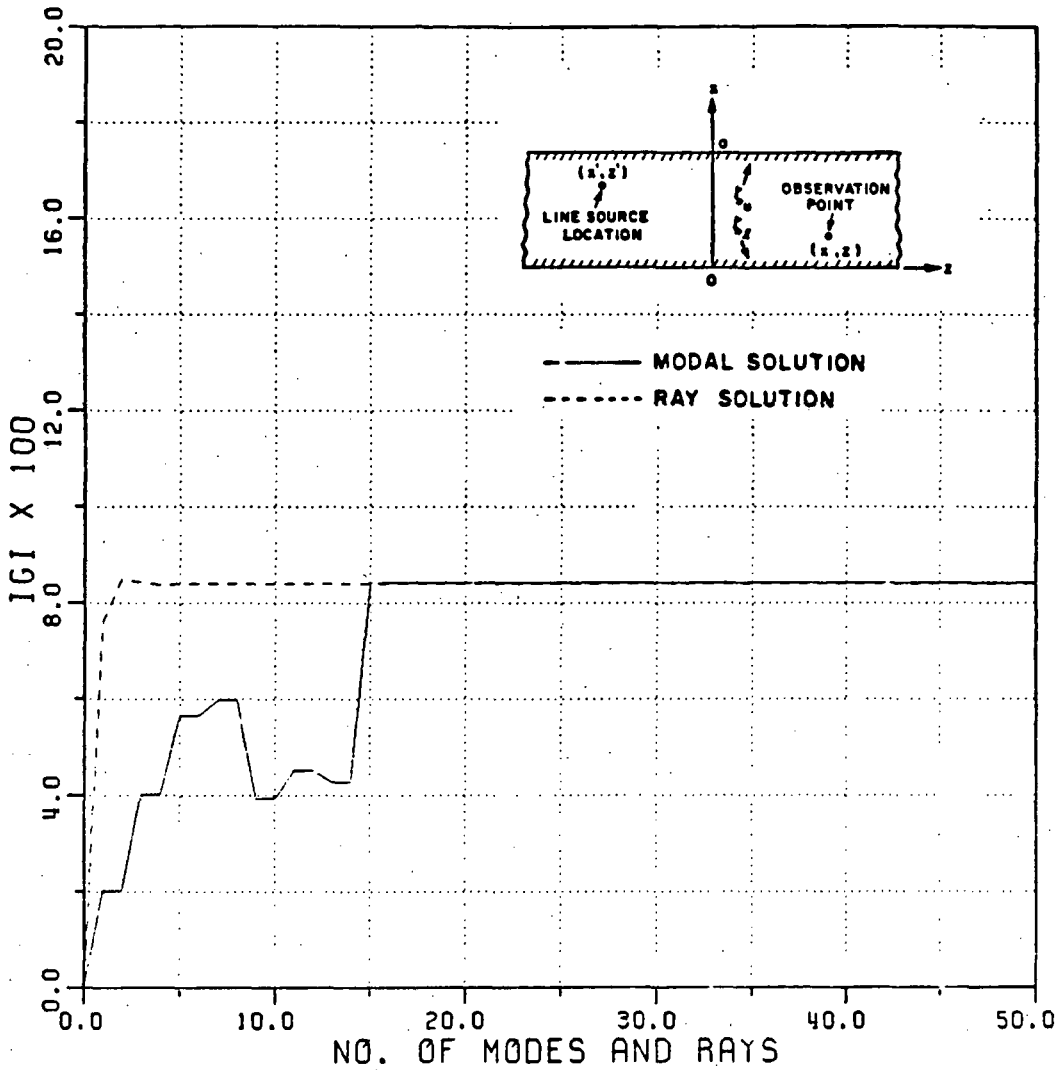

KA = 50.0 KZ = 20.0 R_L = 0.2
KX' = 25.0 X_L = -0.3
KX = 25.0 R_U = 0.2
PM = 15.0 X_U = -0.3

Figure 26: Convergence of the modal and ray solutions for an electric line source and for a fixed kz.

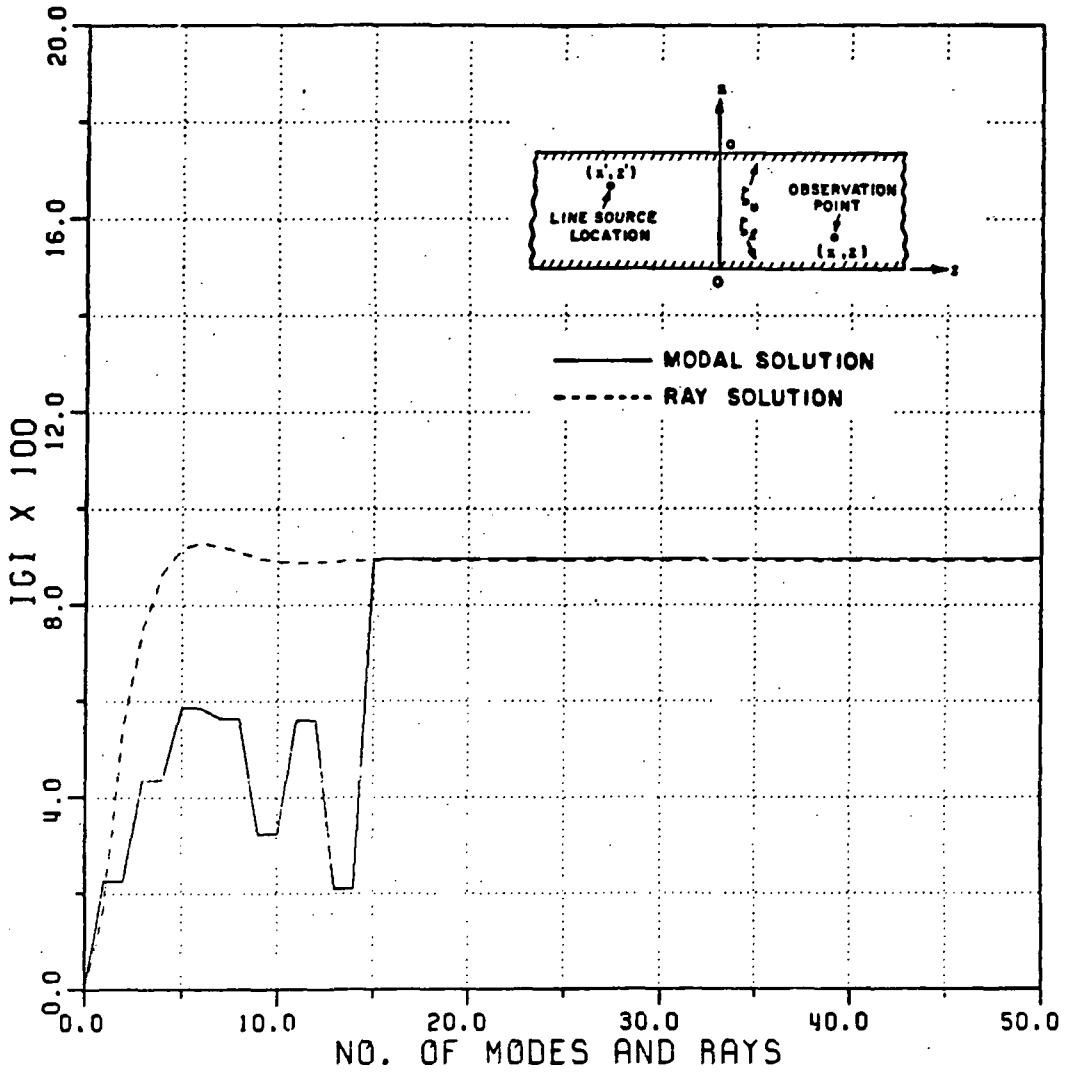

KA = 50.0 KZ = 20.0 RL = 0.1
KX' = 25.0 XL = 0.3
KX = 25.0 RU = 0.1
PM = 15.0 XU = 0.3

Figure 27: Convergence of the modal and ray solutions for a magnetic line source and for a fixed kz.

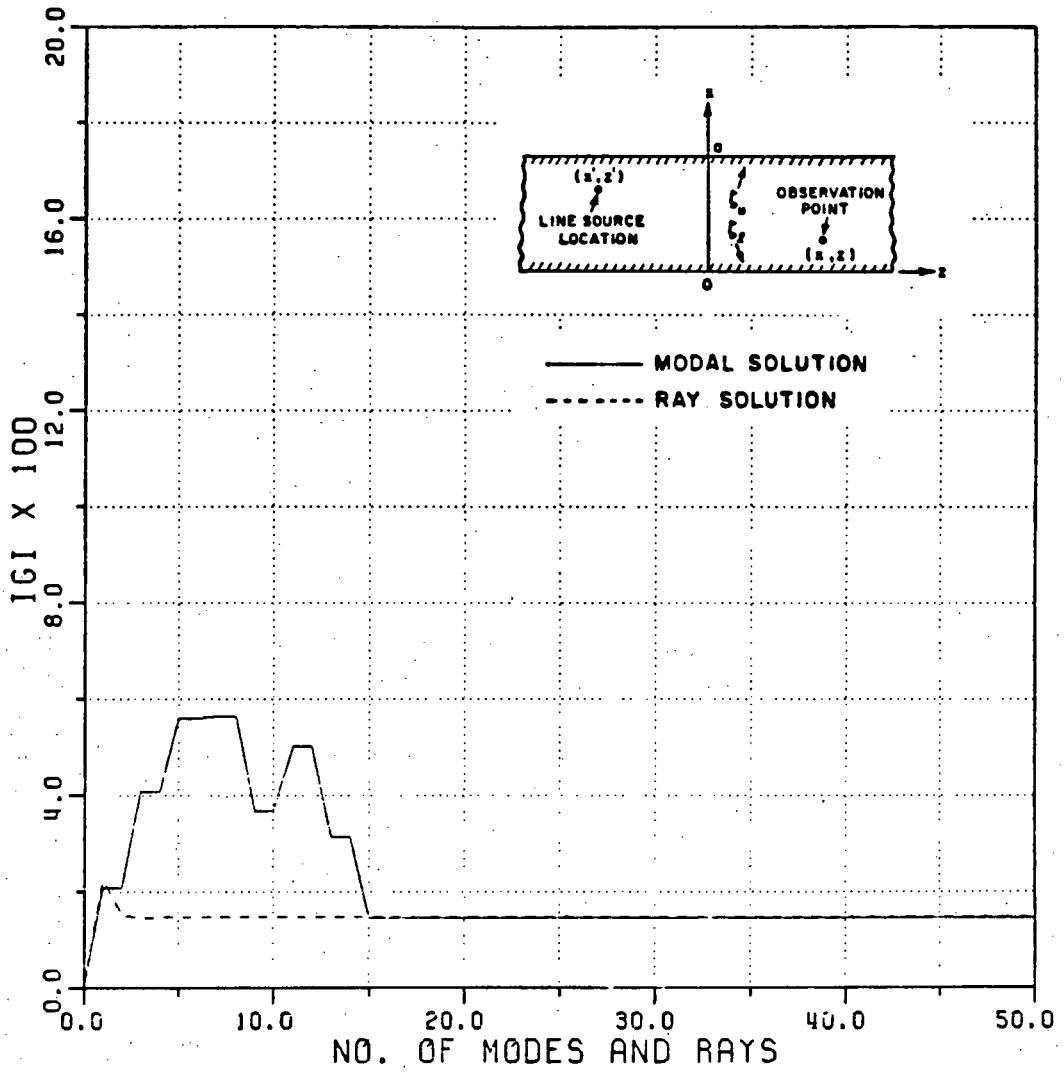

Figure 28: Convergence of the modal and ray solutions for a magnetic line source and for a fixed kz.

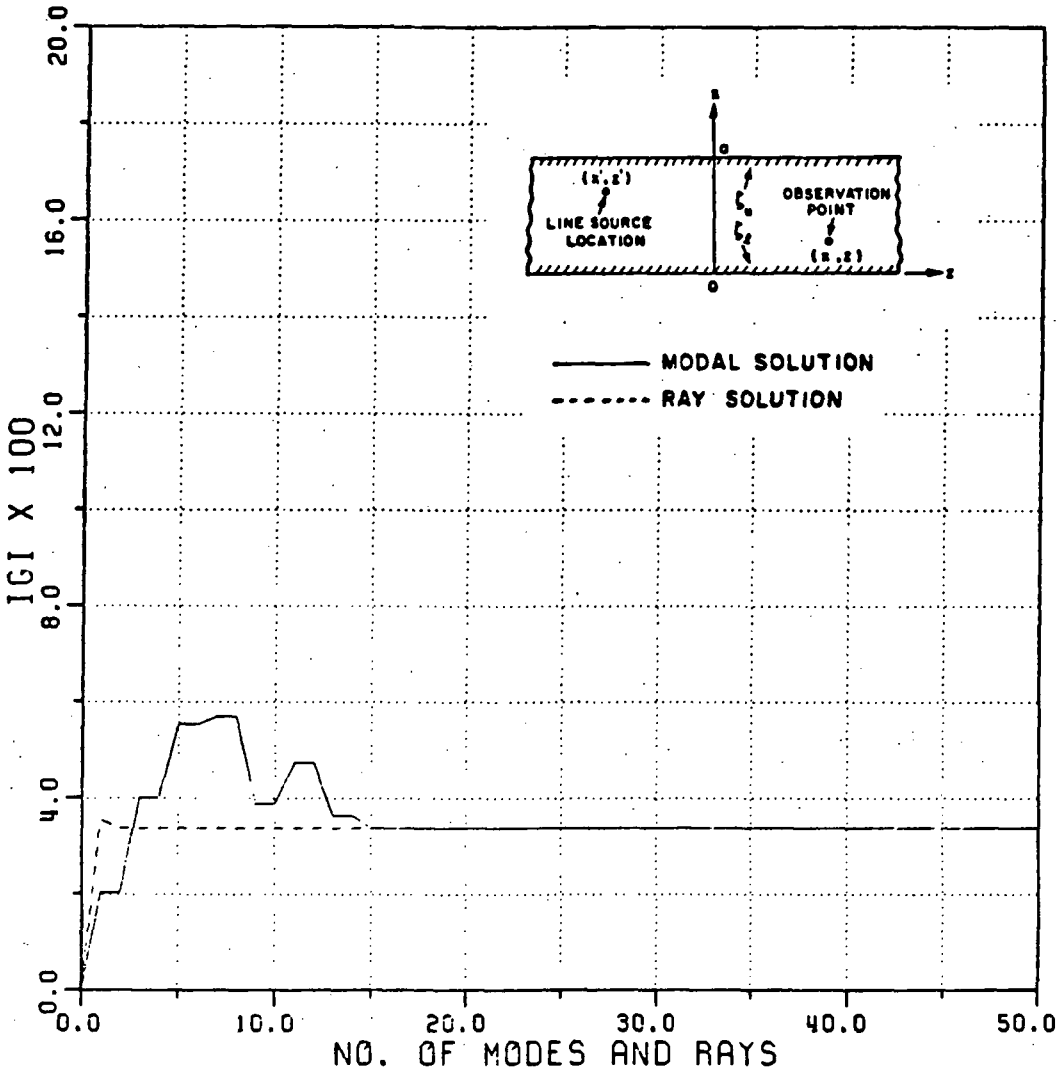

KA = 50.0 KZ= 20.0 RL= 0.8
KX'= 25.0 XL= 0.5
KX = 25.0 RU= 0.8
PM = 15.0 XU= 0.5

Figure 29: Convergence of the modal and ray solutions for a magnetic line source and for a fixed kz.

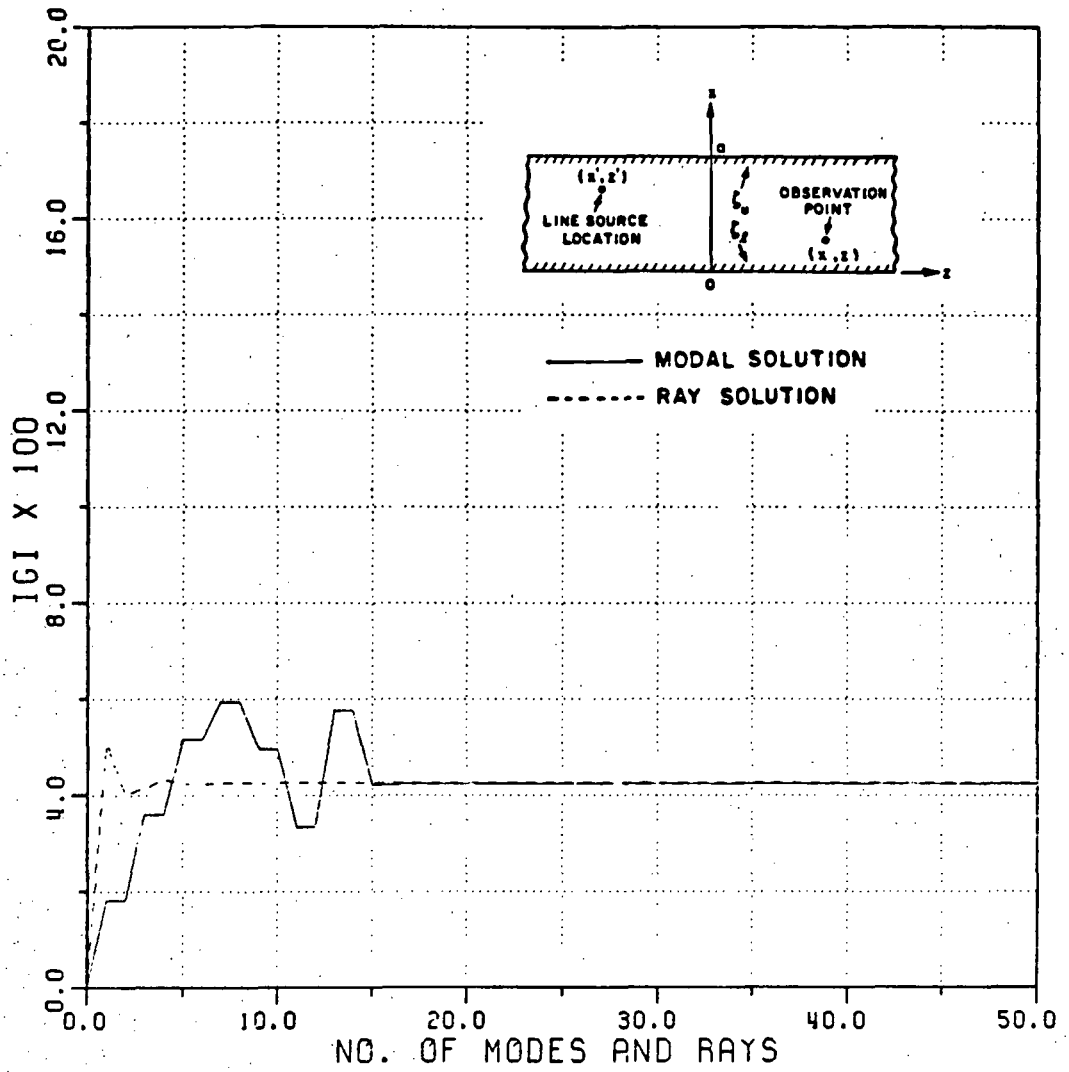

KA = 50.0 KZ= 20.0 RL= 0.2
KX'= 25.0 XL= -0.3
KX = 25.0 RU= 0.2
PM = 16.0 XU= -0.3

Figure 30: Convergence of the modal and ray solutions for a magnetic line source and for a fixed kz.

CHAPTER III

ANALYSIS OF ELECTROMAGNETIC SCATTERING FROM AN OPEN-ENDED PARALLEL PLATE WAVEGUIDE WITH LOSSY INNER WALLS

3.1 Ray solution for the interior fields of an open-ended parallel plate waveguide with an impedance boundary condition on its inner walls

The ray field inside an open-ended semi-infinite parallel plate waveguide with an impedance boundary condition on its inner walls is found via the uniform geometrical theory of diffraction (UTD) in the present section of this chapter. The analysis is later extended to include an absorber coating of finite thickness on the inner waveguide walls in the next section. According to the UTD [1,12], the total ray field U^{tot} at an observation point consists of the usual geometrical optics (GO) incident and reflected fields together with the fields diffracted by the edges such that

$$U^{tot} = U^{i} + U^{r} + U^{d} \tag{3.1}$$

Note that in the present 2-D case, U^{tot} represents the total electric field which is $\hat{y}$-directed if an electric line source is used, whereas, it represents the total magnetic field which is $\hat{y}$-directed if a magnetic line source is present (see Figure 34). The fields U^{i} and U^{r} are associated with the usual GO incident and reflected rays; whereas, the field U^{d} is associated with the edge diffracted rays. The contribution

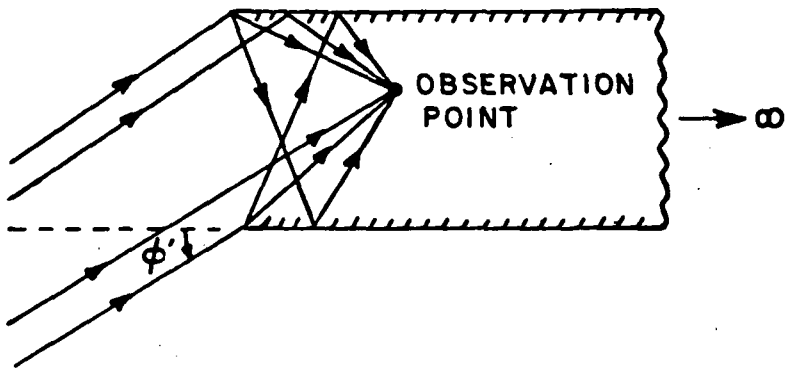

Figure 31: Dominant ray paths for the problem in Figure 1.

of the GO field is given in the first part of this section and the contribution of the edge diffracted field is described in the second part of this section. In the later sections, the effect of an interior planar termination is also included, and the total scattered field is then taken be a superposition of the field scattered by the edges at the open end, and the field which is coupled into the waveguide and then reflected back from the termination to radiate out into the exterior region from the open end of the waveguide.

3.1.1 Geometrical optics (GO) field

Returning to the problem in Figure 1, the GO field at some observation point inside the semi-infinite parallel plate waveguide is due to the incident and reflected rays which would result when an external plane wave illuminates the semi-infinite waveguide as shown in Figure 31. The GO rays inside the waveguide undergo multiple reflections which result in the separate regions (1), (2), (3) $\cdots$ etc., with boundaries as shown in Figure 32. Each region corresponds to a certain number of reflections from the top and/or bottom wall. Then according to the location of the field point inside the waveguide, different combinations of rays such as direct (or

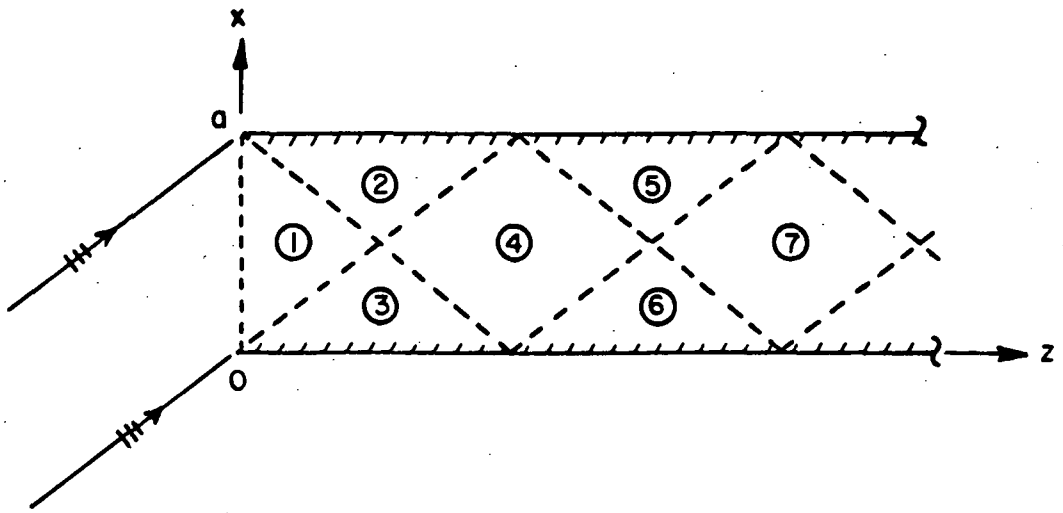

Region (1) Direct ray

(2) Direct and singly reflected rays

(3) None

(4) Singly reflected ray

(5) None

(6) Singly and doubly reflected rays

(7) Doubly reflected ray

Figure 32: Semi-infinite parallel plate waveguide showing different combinations of geometric optical direct, singly and multiply reflected rays in each region of the waveguide.

incident), reflected, and also multiply reflected rays reach the observation point. However, the GO field inside the waveguide has discontinuities when one crosses the boundaries between different regions as shown in Figure 32. These non-physical discontinuities are compensated in the UTD by the diffracted rays which originate from the edges as shown in Figure 31. The edge diffracted rays and some numerical examples are presented following this discussion of the GO field.

In this analysis, each type of rays is considered as shown in Figure 33. The direct ray field can be obtained by simply including the phase term $e^{-jk\overline{O'P}}$ for a plane wave if the phase reference is at the lower edge O such that

$$\begin{bmatrix} U_{\parallel}^{i}(P) \\ U_{\perp}^{i}(P) \end{bmatrix} = \begin{bmatrix} U_{\parallel}^{i}(O) \\ U_{\perp}^{i}(O) \end{bmatrix} \cdot e^{-jk\overline{O'P}} \tag{3.2}$$

where $U_{\parallel(\perp)}^{i}(P)$ and $U_{\parallel(\perp)}^{i}(O)$ represent the components of the incident electric or magnetic field which are polarized parallel (perpendicular) to the edge (or $\hat{y}$-direction). Note that O' is the projection of O onto the ray path. The singly reflected ray is calculated by including the phase term given by $e^{-jk\overline{O'P'}}$, where the extension of the incident ray to P' is the unfolded path of the singly reflected ray to P, and by taking into account the reflection coefficient of the walls; i.e.,

$$\begin{bmatrix} U_{\parallel}^{r}(P) \\ U_{\perp}^{r}(P) \end{bmatrix} = R_{E(M)} \begin{bmatrix} U_{\parallel}^{i}(O) \\ U_{\perp}^{i}(O) \end{bmatrix} \cdot e^{-jk\overline{O'P'}} \tag{3.3}$$

where $R_{E(M)}$ is the reflection coefficient matrix when U refers to the electric (magnetic) field. The entries of the reflection coefficient matrix are given as

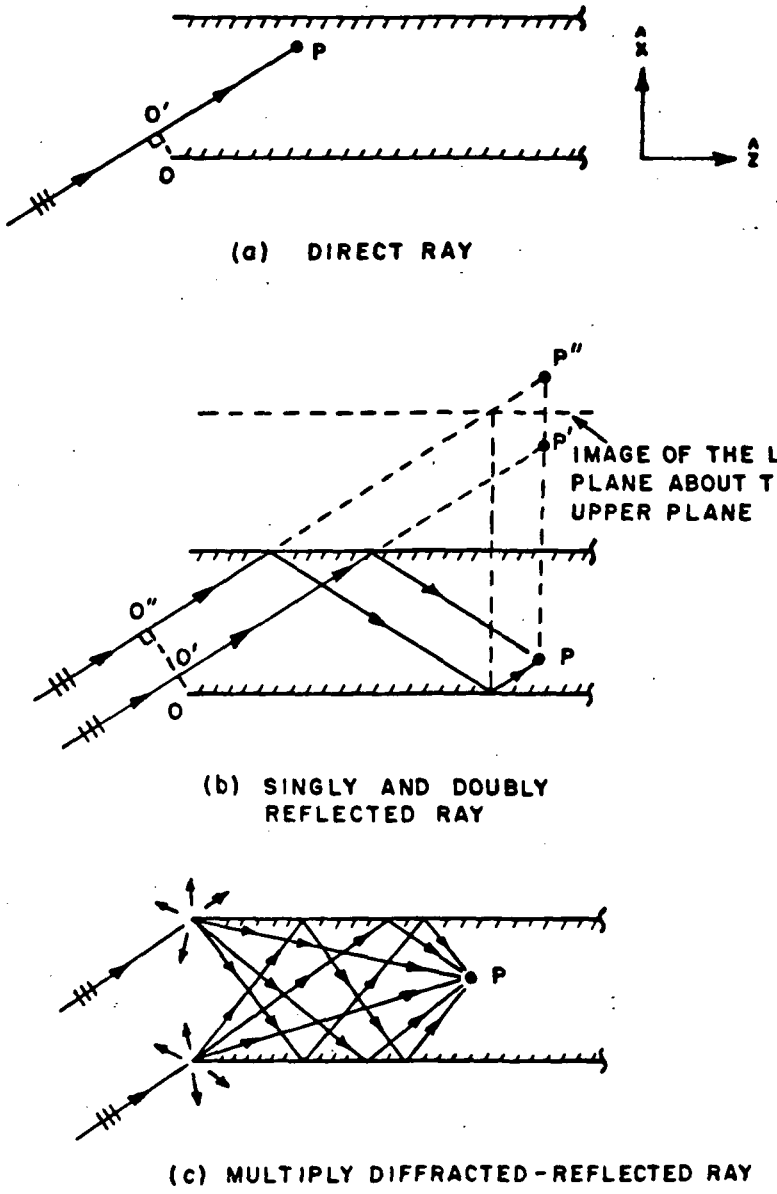

Figure 33: Semi-infinite parallel plate waveguide showing direct, singly reflected, doubly reflected, direct diffracted and multiply diffracted–reflected rays.

$$R_{E(M)} = \begin{bmatrix} \tilde{R}_{\parallel(\perp)} & 0 \\ 0 & \tilde{R}_{\perp(\parallel)} \end{bmatrix} \tag{3.4}$$

where $\tilde{R}_{\parallel(\perp)}$ is the reflection coefficient for the electric field which is polarized parallel (perpendicular) to the plane of incidence and it is derived in Appendices D and F for the impedance boundary condition and the absorber coated perfectly-conducting surfaces, respectively. Similarly, the doubly reflected ray field is calculated by including the phase term given by $e^{-jk\overline{O''P''}}$, where the extension of the incident ray to P'' is the unfolded path of the doubly reflected ray to P, and by taking into account the reflection coefficient of the walls two times in this case; i.e.,

$$\begin{bmatrix} U^r_{\parallel}(P) \\ U^r_{\perp}(P) \end{bmatrix} = R^2_{E(M)} \begin{bmatrix} U^i_{\parallel}(O) \\ U^i_{\perp}(O) \end{bmatrix} \cdot e^{-jk\overline{O''P''}} \tag{3.5}$$

It is noted that the number of reflections which the ray experiences as it propagates inside the waveguide is determined analytically by ascertaining the region in which the field point is located as shown in Figure 32. The multiply reflected rays which are diffracted by edges in Figure 33(c) follow the same analysis as the reflected GO rays as discussed above.

3.1.2 Edge diffracted rays

The incident field impinging on the edges at the open end produces diffracted rays which can be calculated via Maliuzhinets' edge diffraction coefficient [13] that is valid for the problem of plane wave diffraction by a wedge with two face impedances. Here the Maliuzhinets' result [13] can be specialized to the configuration in Figure 1 corresponding to the case of a half plane pertaining to each of

the semi-infinite waveguide walls. In particular, the half plane here is a special case of a wedge with a zero internal angle and with a non-zero impedance on one face (corresponding to the inner waveguide wall) and with a zero impedance on the other face (corresponding to the outer perfectly-conducting waveguide wall) of the half plane. An alternative, more approximate but simpler method [12] for computing the diffracted rays by the edges at open end is to modify the diffraction coefficient which is based on the UTD solution for a perfectly-conducting half plane [1,2] to make it valid for a half plane with two face impedances. In this study, the modified diffraction coefficent [12] is used for its simplicity. The simpler solution in [12] is discussed below for completeness.

Consider a line source which illuminates a half plane whose one side is perfectly-conducting and the other side is characterized by a non-zero surface impedance as shown in Figure 34. According to the regions where the observation point P is located (see Figure 34), the individual terms may be expressed in the following forms,

$$U^i(P) = \begin{cases} A_0 \frac{e^{-jks_i}}{\sqrt{s_i}} & \text{; in Regions I and II, and } A_0 \text{ is some} \\ & \text{known complex constant related to} \\ & \text{the strength of the line source.} \\ 0 & \text{; in Region III.} \end{cases} \tag{3.6}$$

$$U^r(P) = \begin{cases} U^i(Q_R)\, R_{M(E)} \frac{e^{-jks_r}}{\sqrt{s_r}} & \text{; in Region I with} \\ & U^i(Q_R) = A_0 \frac{e^{-jks''}}{\sqrt{s''}} \\ 0 & \text{; in Regions II and III.} \end{cases} \tag{3.7}$$

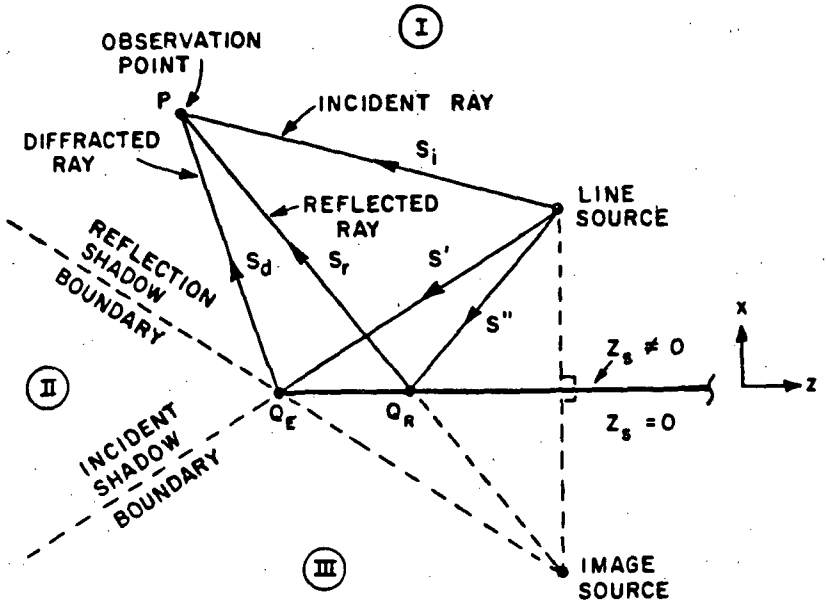

Figure 34: Rays associated with the problem of line source excitation of an impenetrable half plane with two face impedances.

$$U^d(P) = \begin{cases} U^i(Q_E)\, D_{M(E)}\, \frac{e^{-jks_d}}{\sqrt{s_d}} & ; \text{where } U^i(Q_E) = A_0\, \frac{e^{-jks'}}{\sqrt{s'}} \\ & \text{in Regions I, II and III.} \end{cases} \tag{3.8}$$

In the above, s_i (or s_r) is the distance from the source (or point of reflection Q_R) to the observation point P and s_d is the distance from the point of diffraction on the edge (Q_E) to the observation point P.

For the half plane considered here (see Figure 34), the diffraction coefficient $D_{M(E)}$ for the TE_y (TM_y) case is given by [1,12]

$$D_{M(E)} = D(1) + D(2) + \tilde{R}_{\parallel(\perp)}\, D(3) + D(4) \tag{3.9}$$

where

$$D(1) = -\frac{e^{-j\pi/4}}{2n\sqrt{2\pi k}} \cot\Big(\frac{\pi + (\phi - \phi')}{2n}\Big)\, F\Big[kLa(\phi - \phi')\Big] \tag{3.10}$$

$$D(2) = -\frac{e^{-j\pi/4}}{2n\sqrt{2\pi k}} \cot\Big(\frac{\pi - (\phi - \phi')}{2n}\Big)\, F\Big[kLa(\phi - \phi')\Big] \tag{3.11}$$

$$D(3) = -\frac{e^{-j\pi/4}}{2n\sqrt{2\pi k}} \cot\Big(\frac{\pi + (\phi + \phi')}{2n}\Big)\, F\Big[kLa(\phi + \phi')\Big] \tag{3.12}$$

$$D(4) = -\frac{e^{-j\pi/4}}{2n\sqrt{2\pi k}} \cot\Big(\frac{\pi - (\phi + \phi')}{2n}\Big)\, F\Big[kLa(\phi + \phi')\Big] \tag{3.13}$$

and

$$n = 2 \text{ for a half-plane} \tag{3.14}$$

$$L = \frac{s's_d}{s' + s_d} \tag{3.15}$$

$$a(\beta) = 2\cos^2(\beta/2)\ ;\ \beta = \phi \mp \phi' \tag{3.16}$$

$$F(x) = 2j\sqrt{x}\,e^{jx}\int_{\sqrt{x}}^{\infty} e^{-jt^2}\,dt \tag{3.17}$$

The $F(x)$ of Equation (3.17) which appears in Equations (3.10) through (3.13) is called a *transition function* and it involves a *Fresnel integral.* The magnitude and phase of the transition function is shown in Appendix E. Note that both angles ϕ' and ϕ are measured from the perfectly-conducting side of the half plane as shown in Figure 35.

The approximate UTD edge diffraction coefficient in Equation (3.9) provides continuity in the total high frequency ray field across the incident and reflection shadow boundary transition regions. It is noted from Equations (3.6) and (3.7) that the GO field is discontinuous at these shadow boundaries; thus the diffracted field must properly compensate the discontinuities in the incident and reflected fields there. In particular, the $D(\phi - \phi')$ type terms ($D(1)$ and $D(2)$) in the $D_{M,E}$ keep the total field bounded at the incident shadow boundary (ISB); likewise, the $D(\phi + \phi')$ terms ($D(3)$ and $D(4)$) do the same thing at the reflection shadow boundary (RSB).

If the line source receeds to infinity, then the field incident on the half plane is a plane wave. Normalizing the strength of the plane wave to be of unit amplitude at Q_E in Figure 34, one may write

$$U^i(Q_E) = 1 \tag{3.18}$$

$$U^i(P) = e^{jkR\cos(\phi-\phi')} \tag{3.19}$$

$$U^r(P) = R_{M(E)}\,e^{jkR\cos(\phi+\phi')} \tag{3.20}$$

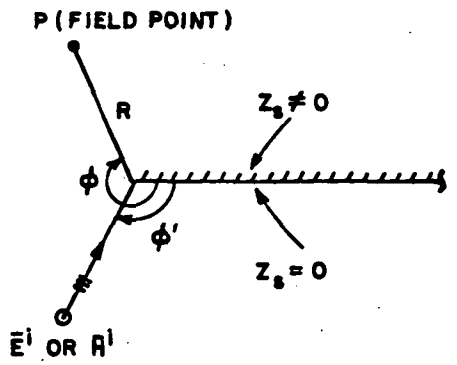

Figure 35: A plane wave incident on a half plane geometry with perfectly-conducting on one side and impedance surface on the other side.

where R, ϕ and ϕ' are defined in Figure 35. The only change in the solution for U^d in Equation (3.8) is that L in Equation (3.15) is replaced by s_d as $s' \rightarrow \infty$ for the case of plane wave incidence.

3.1.3 Total UTD ray field

Using the diffraction coefficient developed in the previous section, the incident, reflected, diffracted and total fields are examined for the half plane geometry as shown in Figure 35. The only difference between Figures 34 and 35 is that the line source is allowed to receed to infinity in Figure 35 giving rise to a plane wave illumination. In the above figure, R is the distance from the edge of the half plane to the field point, and ϕ' and ϕ are incident and observation angles, respectively as indicated earlier. In addition, one recalls that R_s and X_s correspond to the surface resistance and reactance of the impedance wall, respectively as defined in the previous chapter. For an incident TM_y plane wave of unit strength (and zero

phase at Q_E) which is polarized such that $\mathbf{E}^i = \hat{\mathbf{y}}\, E_y^i$, the corresponding GO (incident and reflected) and diffracted fields are plotted against the observation angle in Figure 36. The incident and observation angles are measured from the perfectly-conducting face in this case. The reflected field is plotted as a *dashed* line; whereas the incident field is shown as a *solid* line in the figure with vertical axis marked INCIDENT. The ripples in the magnitude of the GO field result from an interference between the incident and reflected fields. Note also that the discontinuities in the GO field are compensated by the corresponding discontinuities in the diffracted field as shown in the figures with vertical axis marked DIFFRACTED and TOTAL fields, respectively. The total ray field is thus continuous for all observation angles including the ISB ($\phi = 210°$) and RSB ($\phi = 150°$) directions. Similar plots are shown in Figures 37–40 for different incident angles. In all the figures (Figures 36–40), the total fields are continuous for all observation angles. Additional calculations are also shown in Figures 41–45 for TE_y case for the various impedance values on the same half plane. The incident and observation angles are measured from the impedance wall side in Figures 41–45. One notes that the ripples in the total fields becomes smaller as the loss or the resistive part of the wall surface impedance becomes larger, because the magnitude of reflected field decreases with higher loss.

The analysis developed above can be employed to treat the scattering and coupling problems associated with the semi-infinite parallel plate waveguide illuminated by a plane wave as shown in Figure 46 because the waveguide can be formed by two parallel half planes; one half plane corresponds to the lower wall, and the other one corresponds to the upper wall as shown in this figure. As an illustration, each type of ray field is plotted inside the waveguide configuration of Figure 46 as a function of the axial distance in Figures 47–49 for a plane wave

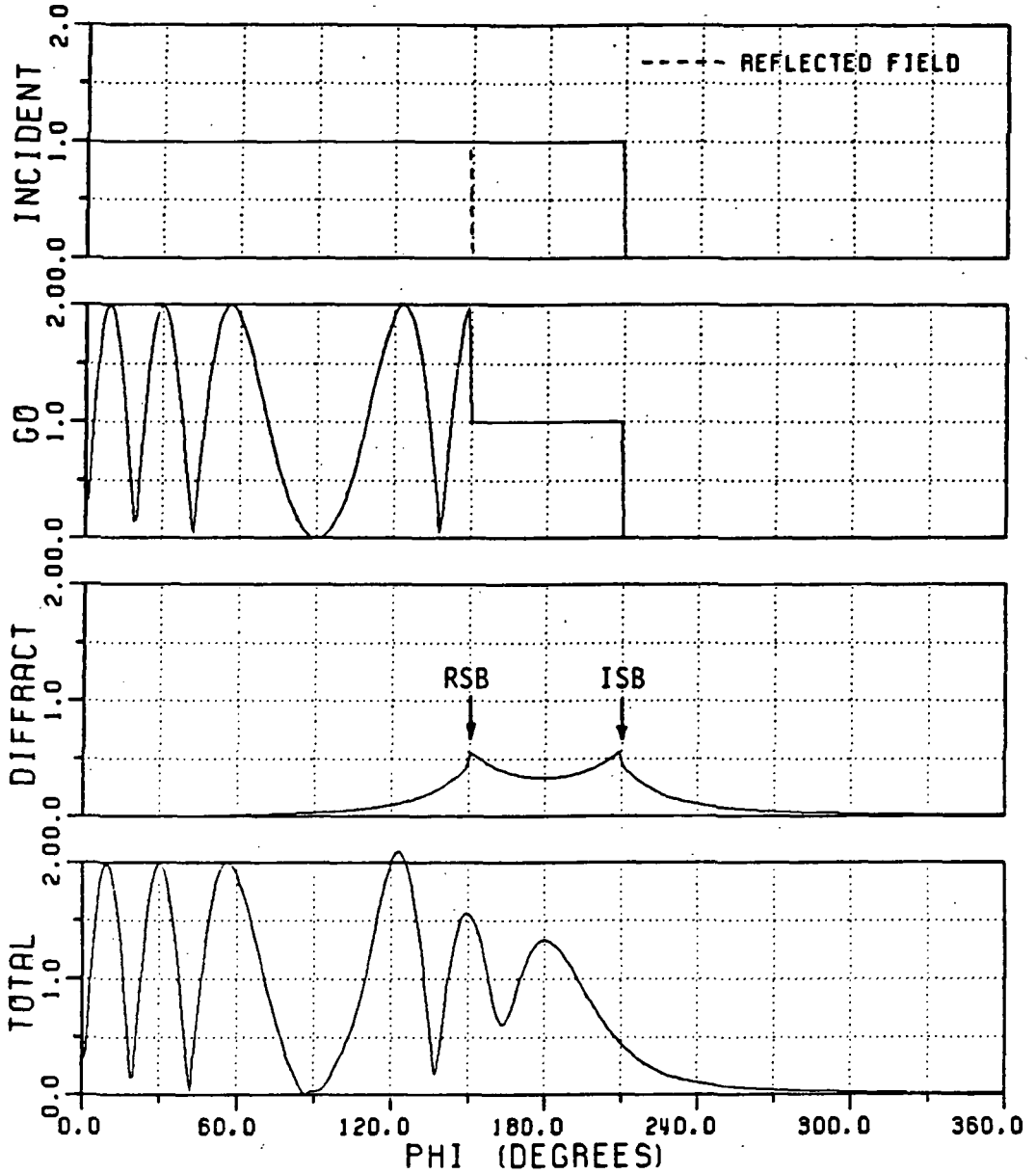

Figure 36: Each ray field for an incident plane wave of unit strength which is polarized such that $\mathbf{E}^i = \hat{\mathbf{y}}\, E^i_y$.

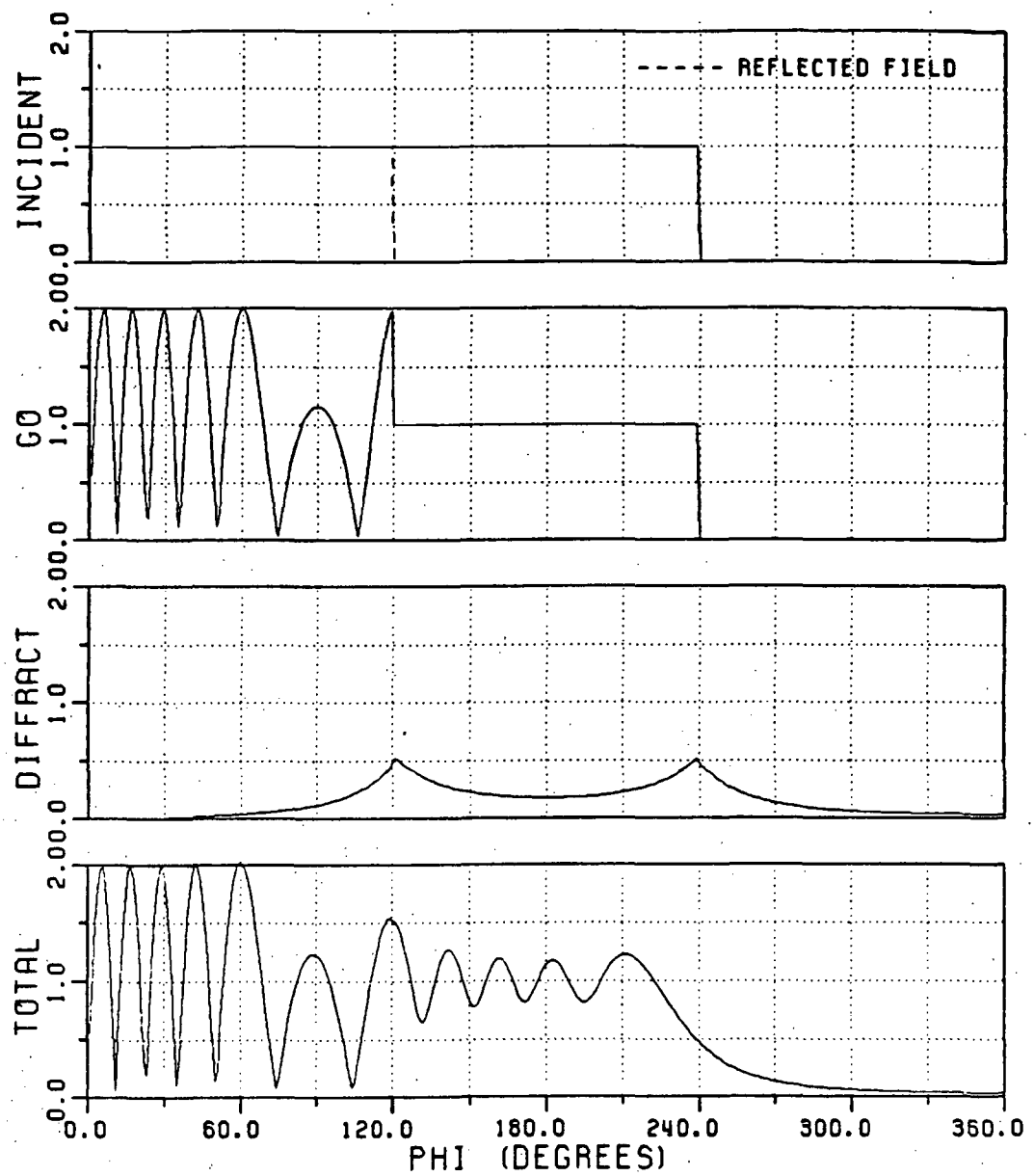

Figure 37: Each ray field for an incident plane wave of unit strength which is polarized such that $\mathbf{E}^i = \hat{\mathbf{y}}\, E^i_y$.

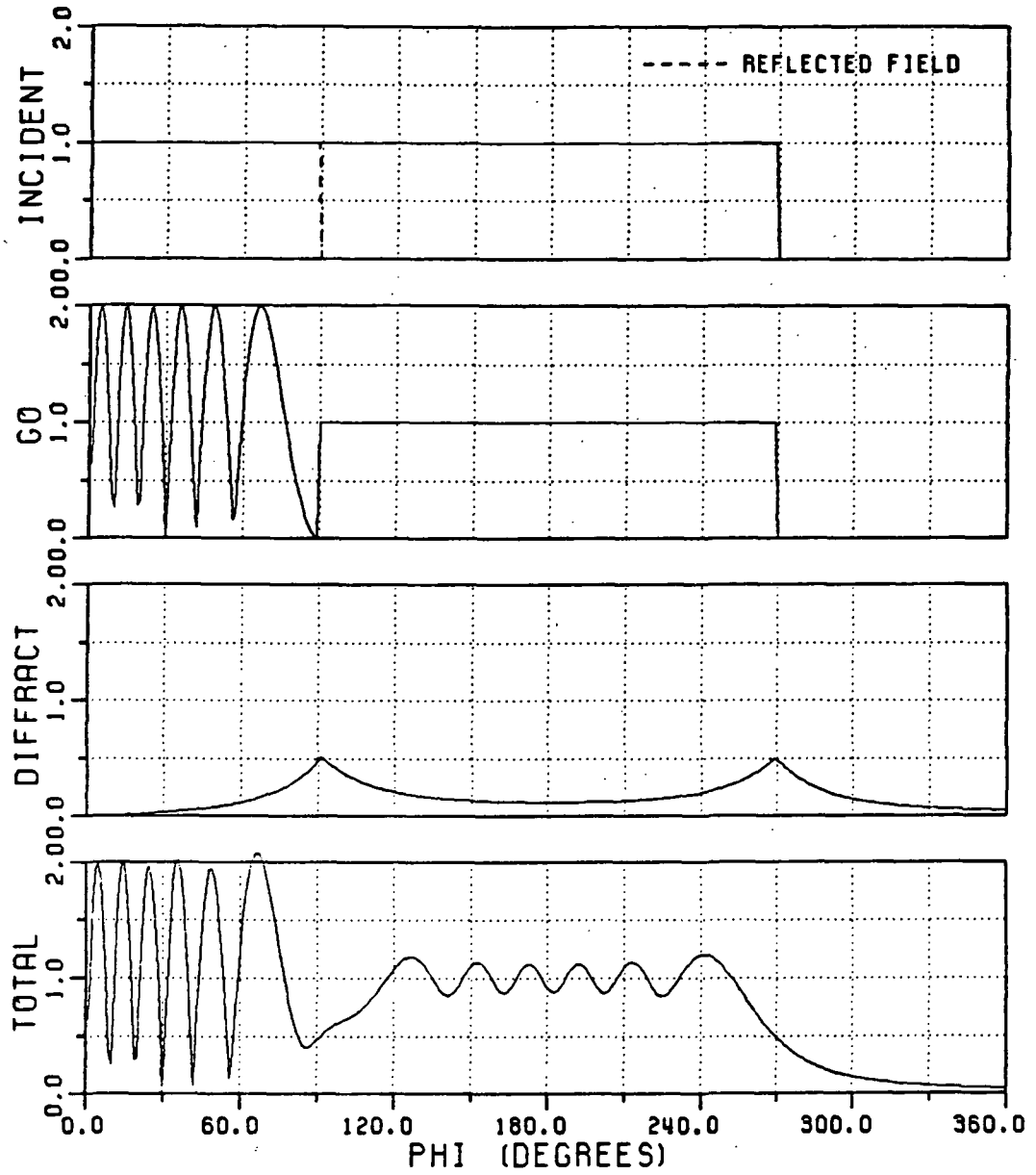

Figure 38: Each ray field for an incident plane wave of unit strength which is polarized such that $\mathbf{E}^i = \hat{\mathbf{y}}\, E_y^i$.

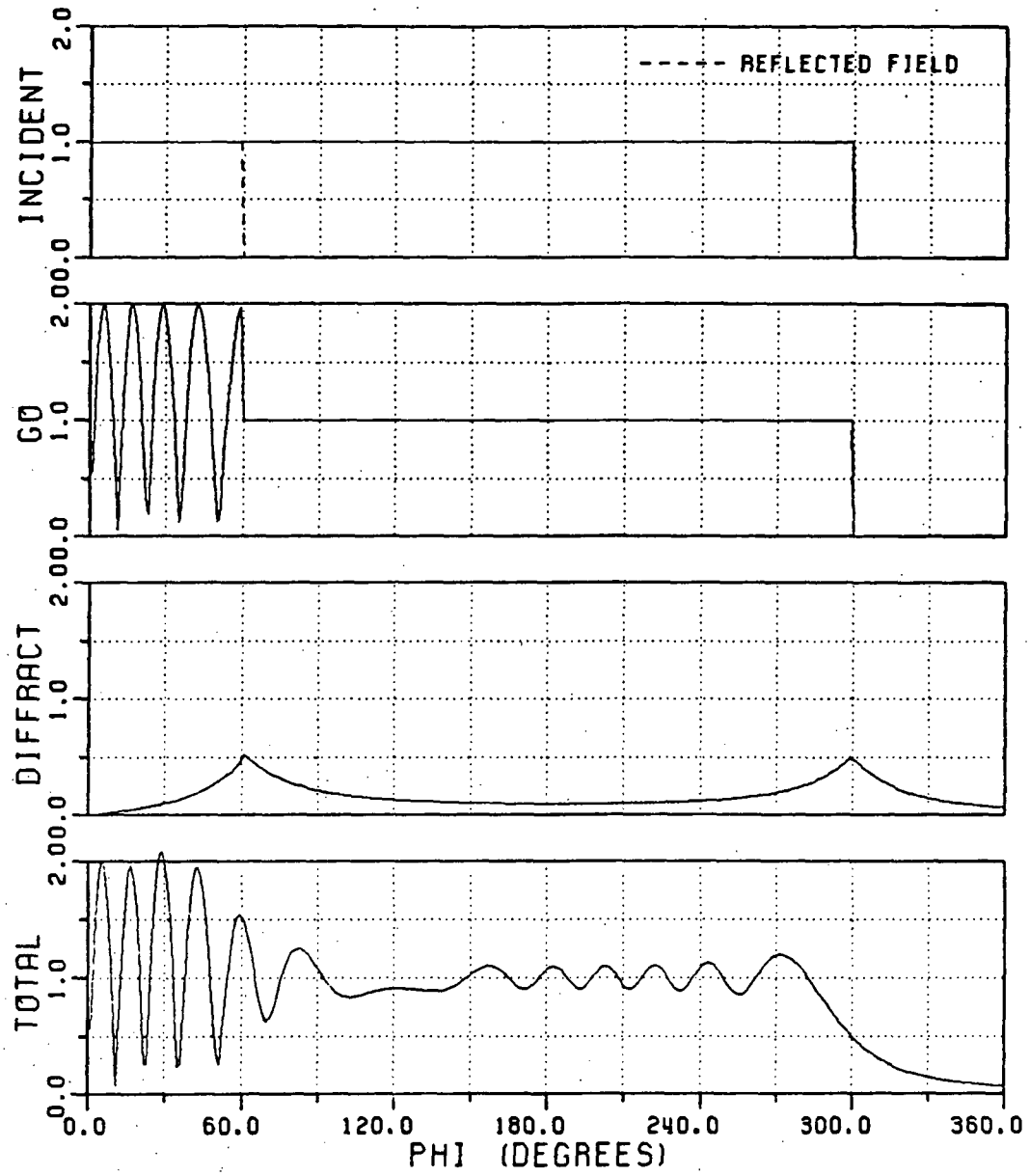

Figure 39: Each ray field for an incident plane wave of unit strength which is polarized such that $\mathbf{E}^i = \hat{\mathbf{y}}\, E_y^i$.

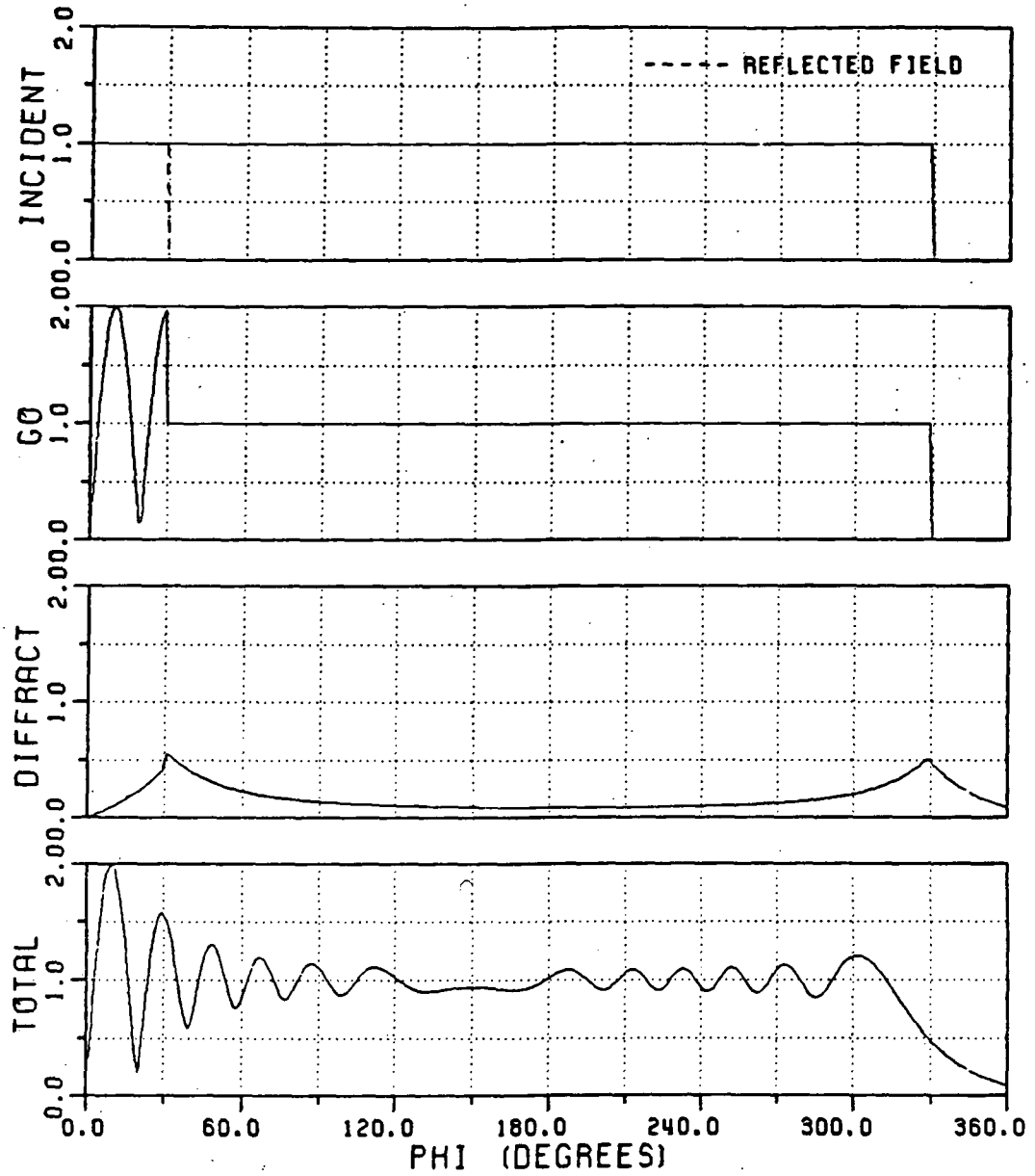

Figure 40: Each ray field for an incident plane wave of unit strength which is polarized such that $\mathbf{E}^i = \hat{\mathbf{y}}\, E^i_y$.

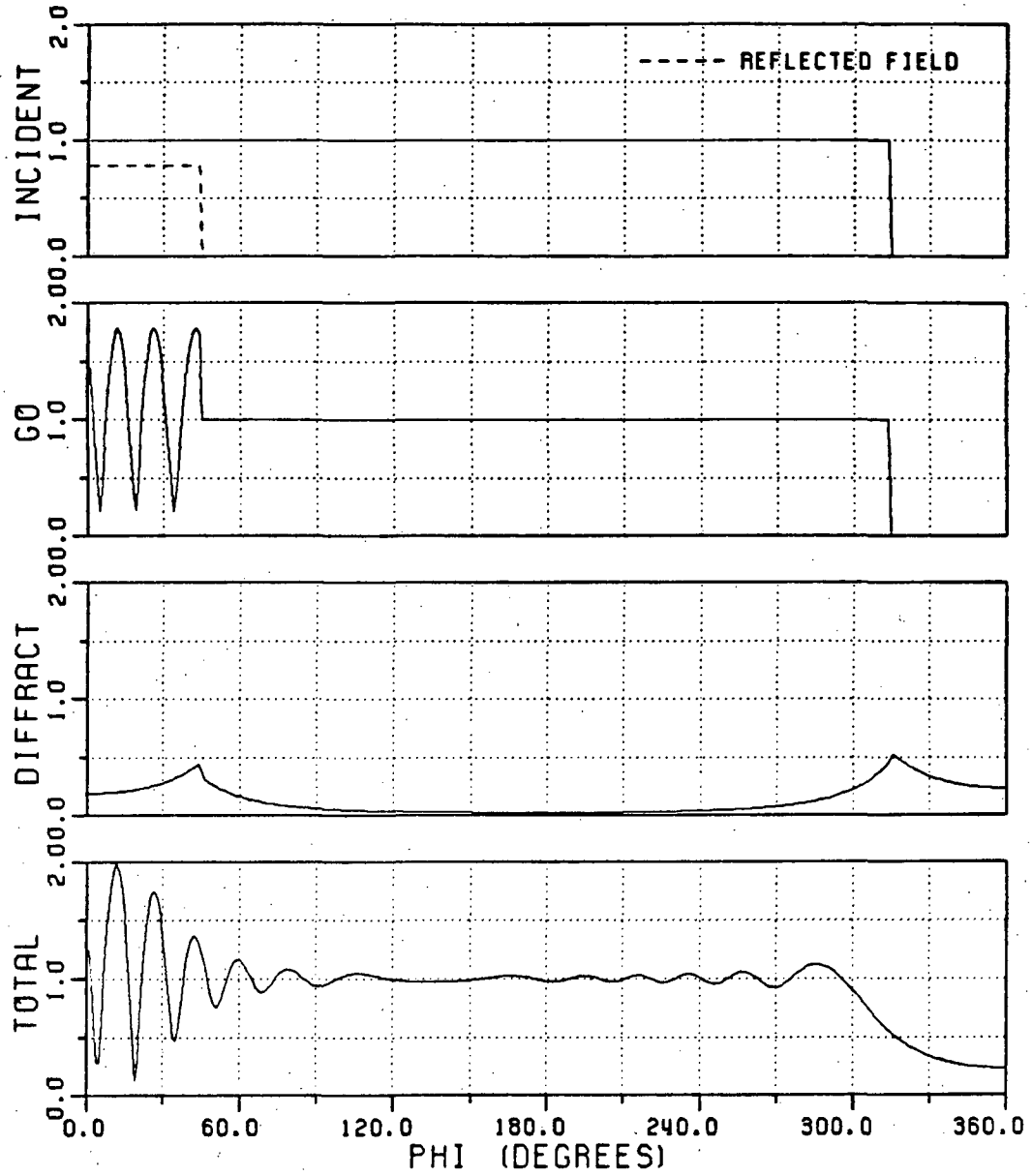

Figure 41: Each ray field for an incident plane wave of unit strength which is polarized such that $\mathbf{H}^i = \hat{\mathbf{y}}\, H_y^i$.

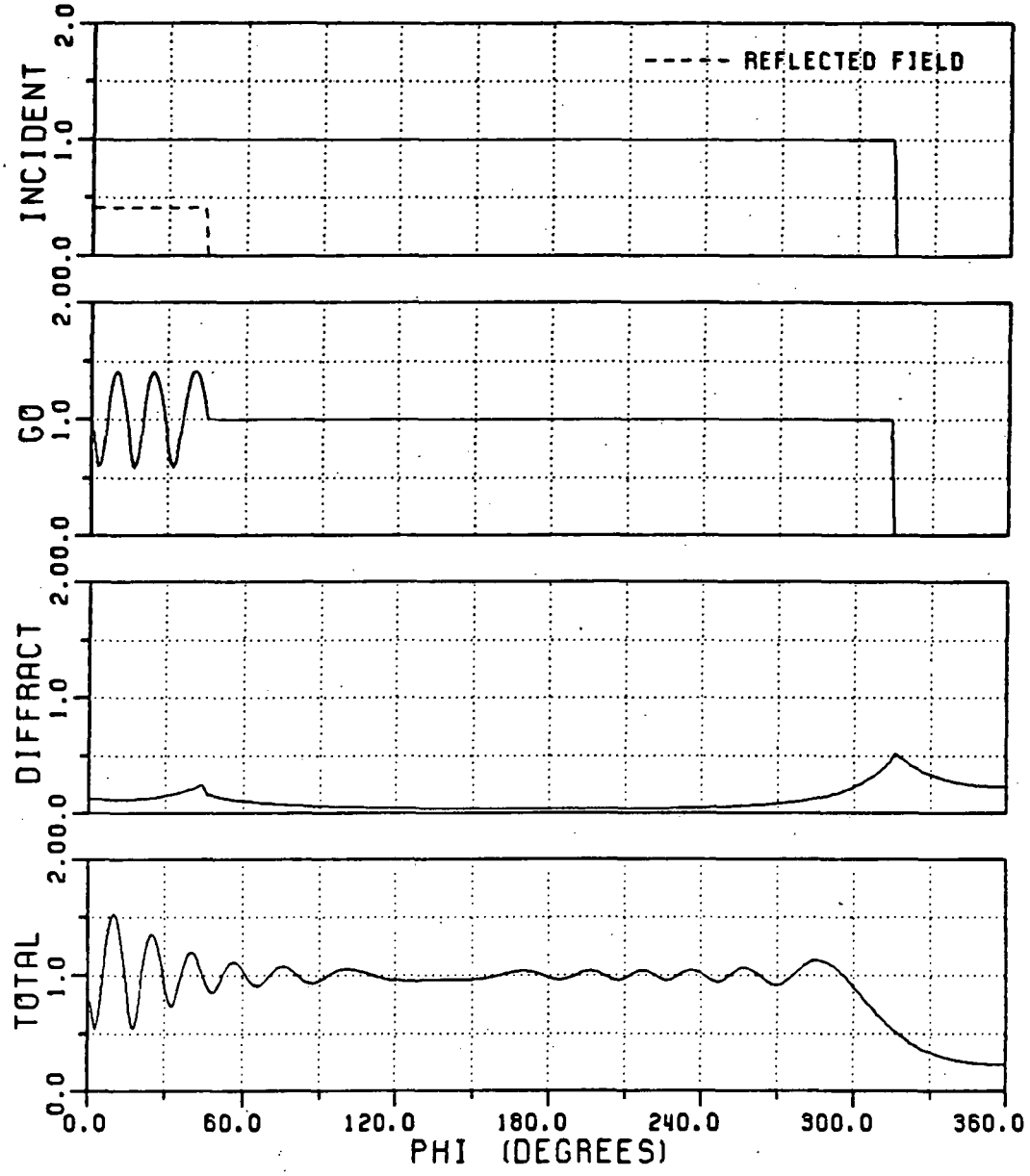

Figure 42: Each ray field for an incident plane wave of unit strength which is polarized such that $\mathbf{H}^i = \hat{\mathbf{y}}\, H_y^i$.

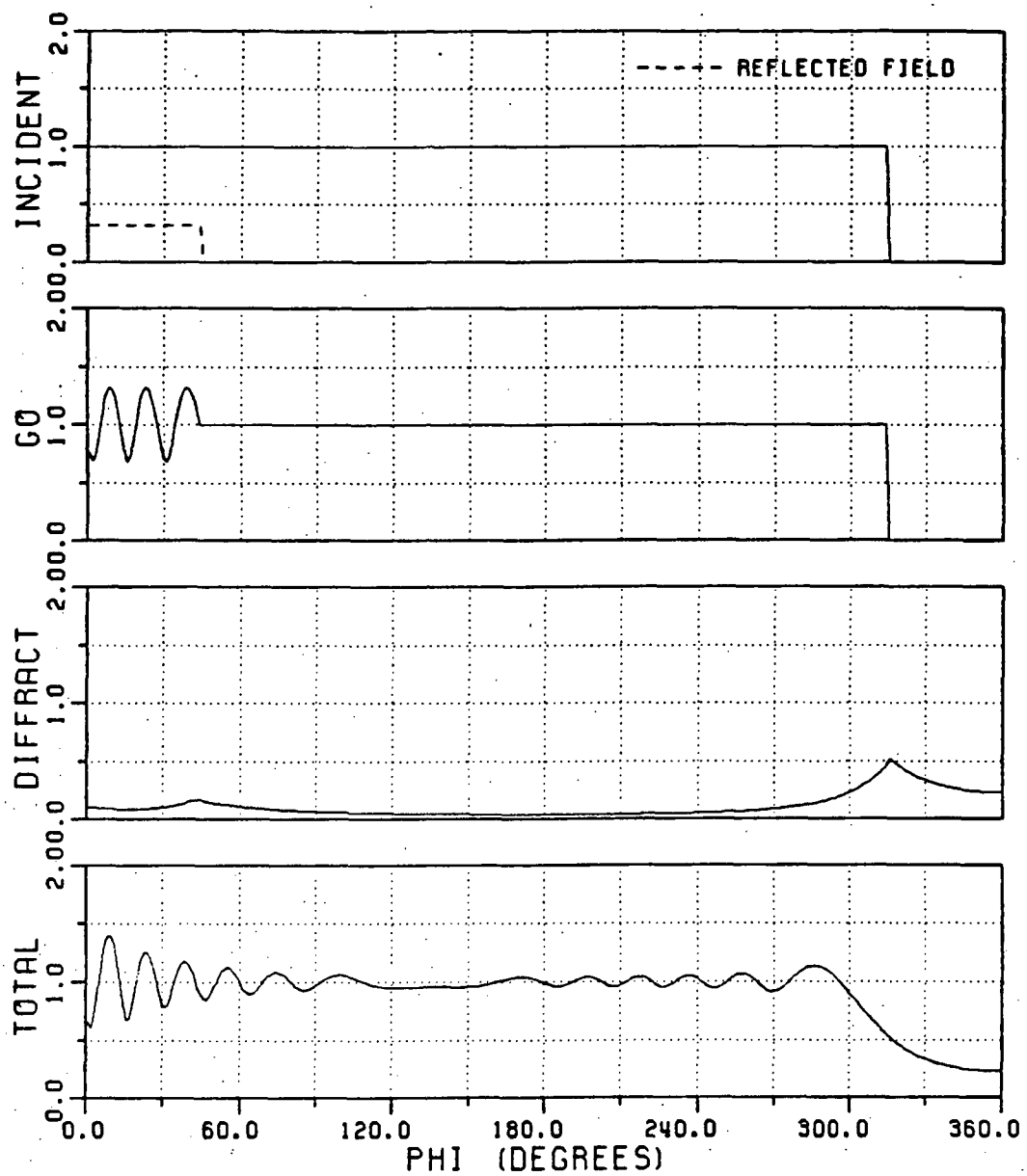

Figure 43: Each ray field for an incident plane wave of unit strength which is polarized such that $\mathbf{H}^i = \hat{\mathbf{y}}\, H_y^i$.

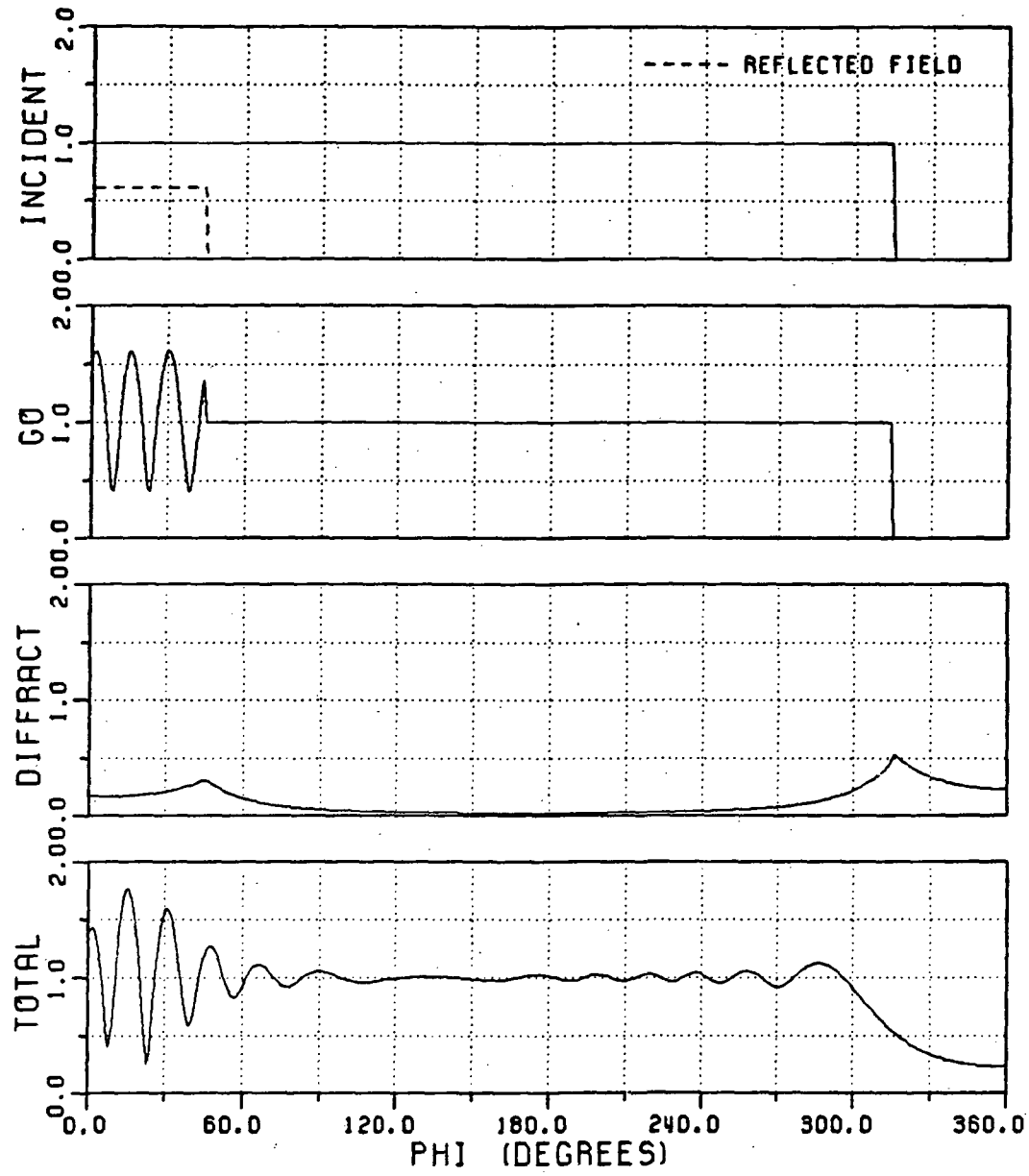

Figure 44: Each ray field for an incident plane wave of unit strength which is polarized such that $\mathbf{H}^i = \hat{\mathbf{y}}\, H_y^i$.

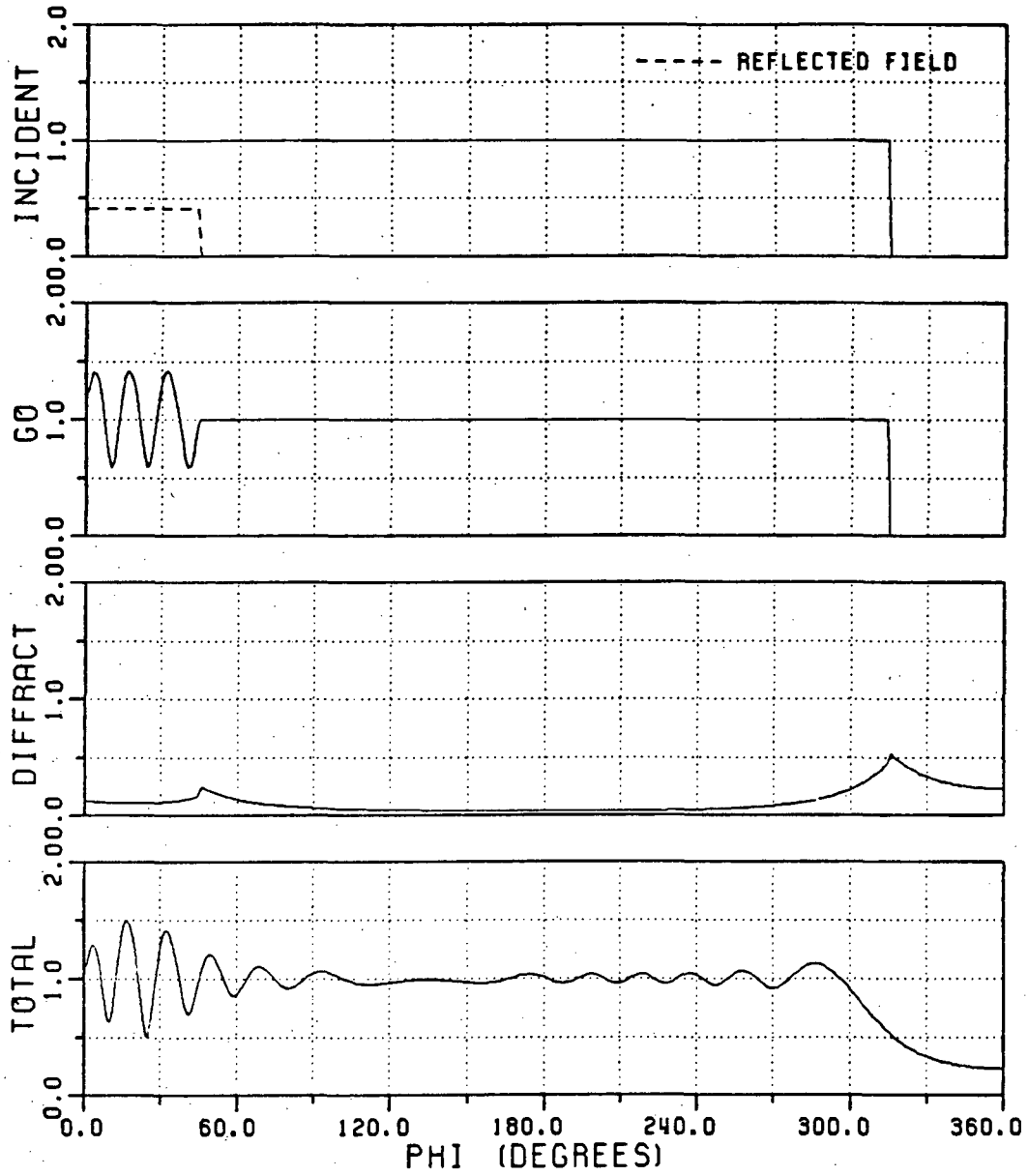

Figure 45: Each ray field for an incident plane wave of unit strength which is polarized such that $\mathbf{H}^i = \hat{\mathbf{y}}\, H_y^i$.

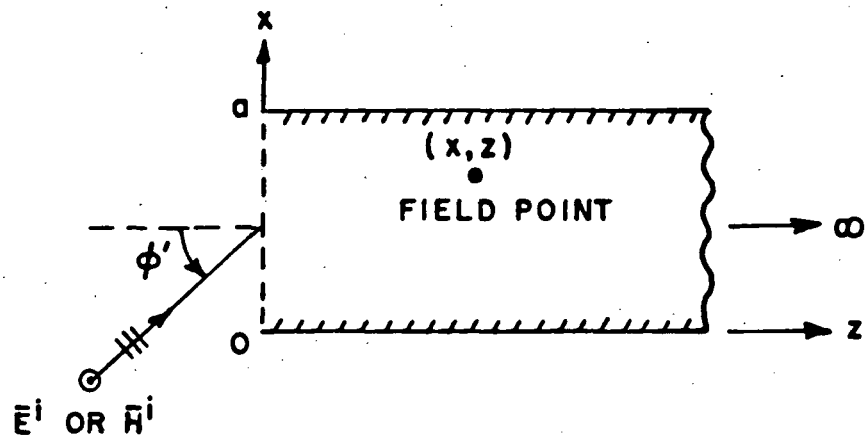

Figure 46: Semi-infinite parallel plate waveguide geometry showing the incident plane wave and the angle of incidence.

with TM_y or parallel polarization for various incidence angles. Note that the observation point in all these plots is located off the walls; hence, *the surface wave effects are not expected to be strong in this case and thus the surface wave contribution is not considered.* As shown in these plots, the total fields are continuous for all the boundaries designated in Figure 32. Similar plots are shown for different impedance values in Figures 50–52 for a TE_y incident plane wave. Note that the general shape of the total field is determined roughly by the GO (incident and reflected) fields and the total field coupled into the waveguide region can be reduced by properly choosing the value of the wall impedance. Also, the surface wave attenuates sufficiently rapidly as it propagates if the wall loss (real part of the impedance) is made even moderately large; in such a case, the surface wave effects become negligible at a sufficient distance from the open end of the waveguide.

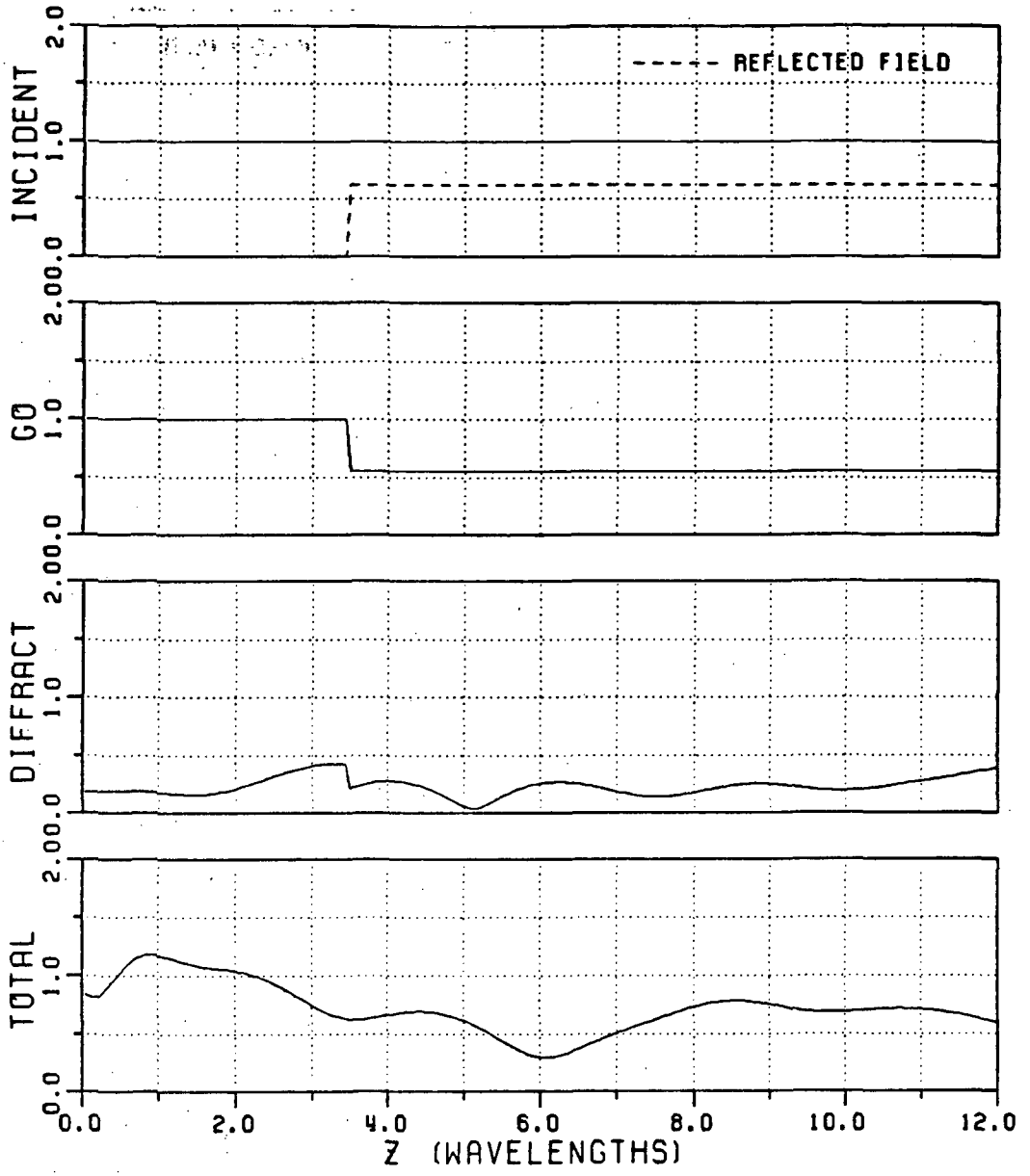

A = 10.0 (WAVELENGTHS) $\Phi^{\prime}$ = 30.0 (DEGREES)
X = 8.0 (WAVELENGTHS) Z_S = (0.5, 0.5)

Figure 47: Each ray field within a semi-infinite parallel plate waveguide with impedance walls plotted as a function of the axial distance from the open end to the field point for an incident plane wave with a parallel polarization (TM_y).

C-2

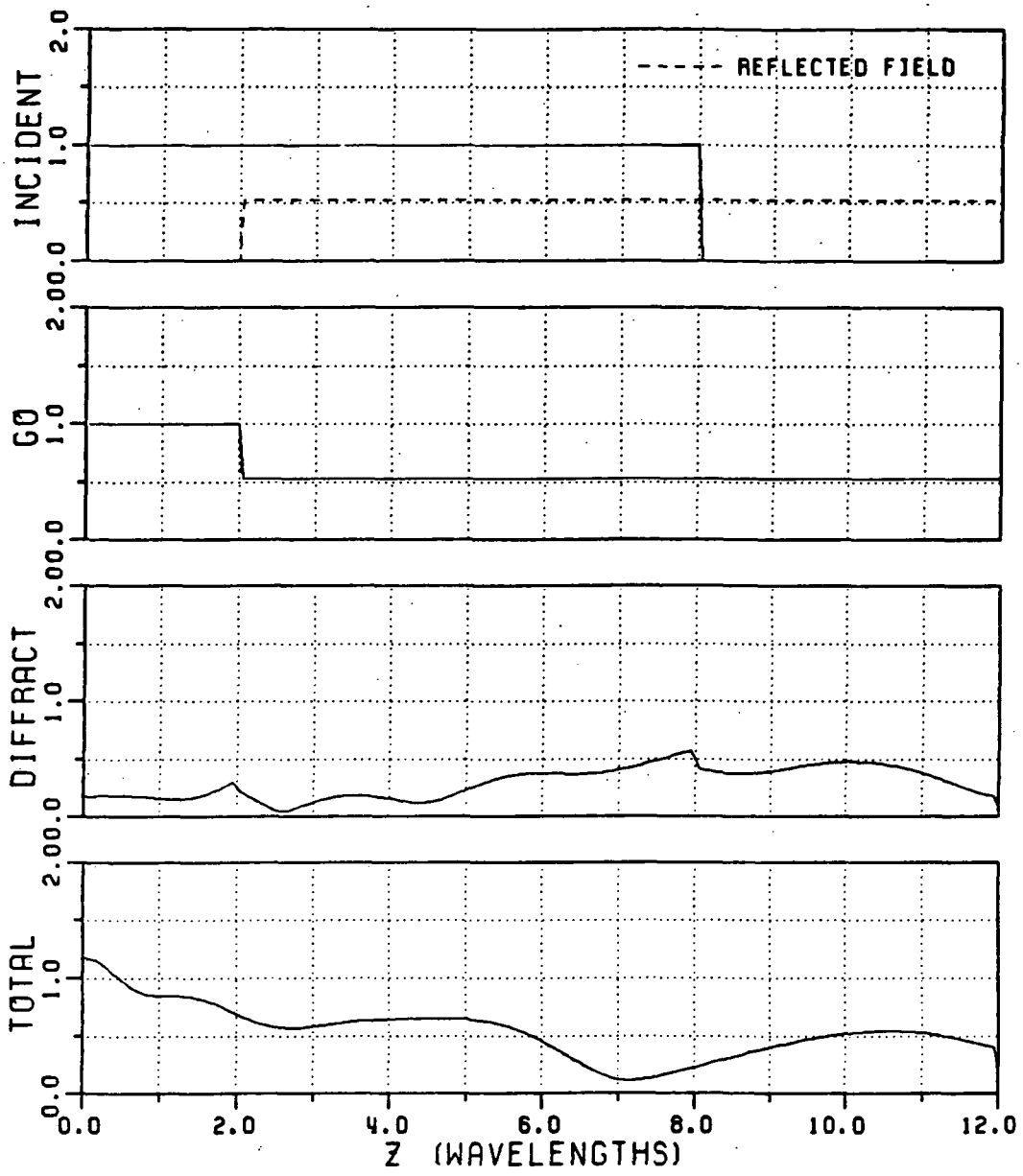

Figure 48: Each ray field within a semi-infinite parallel plate waveguide with impedance walls plotted as a function of the axial distance from the open end to the field point for an incident plane wave with a parallel polarization (TM_y).

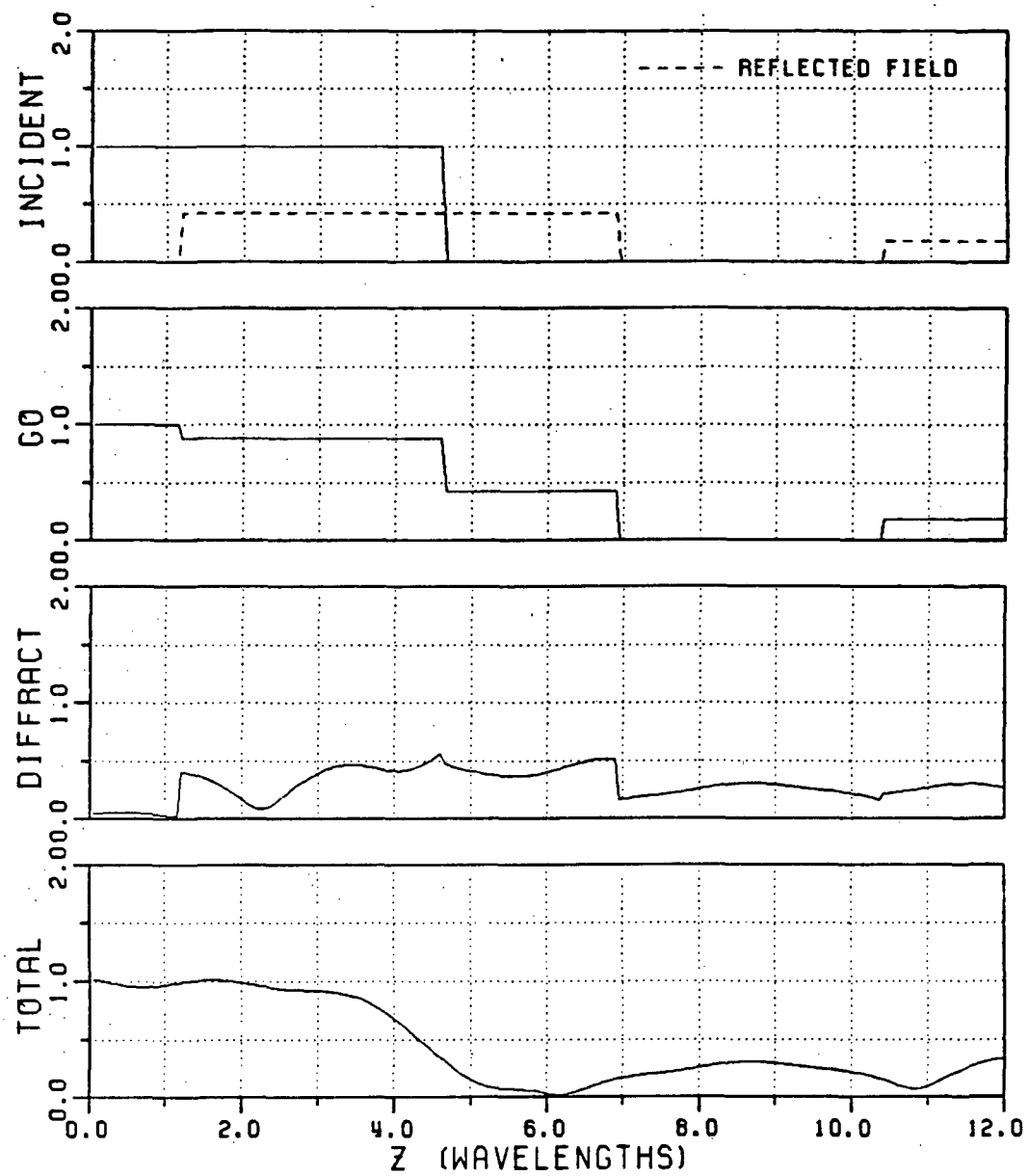

Figure 49: Each ray field within a semi-infinite parallel plate waveguide with impedance walls plotted as a function of the axial distance from the open end to the field point for an incident plane wave with a parallel polarization (TM_y).

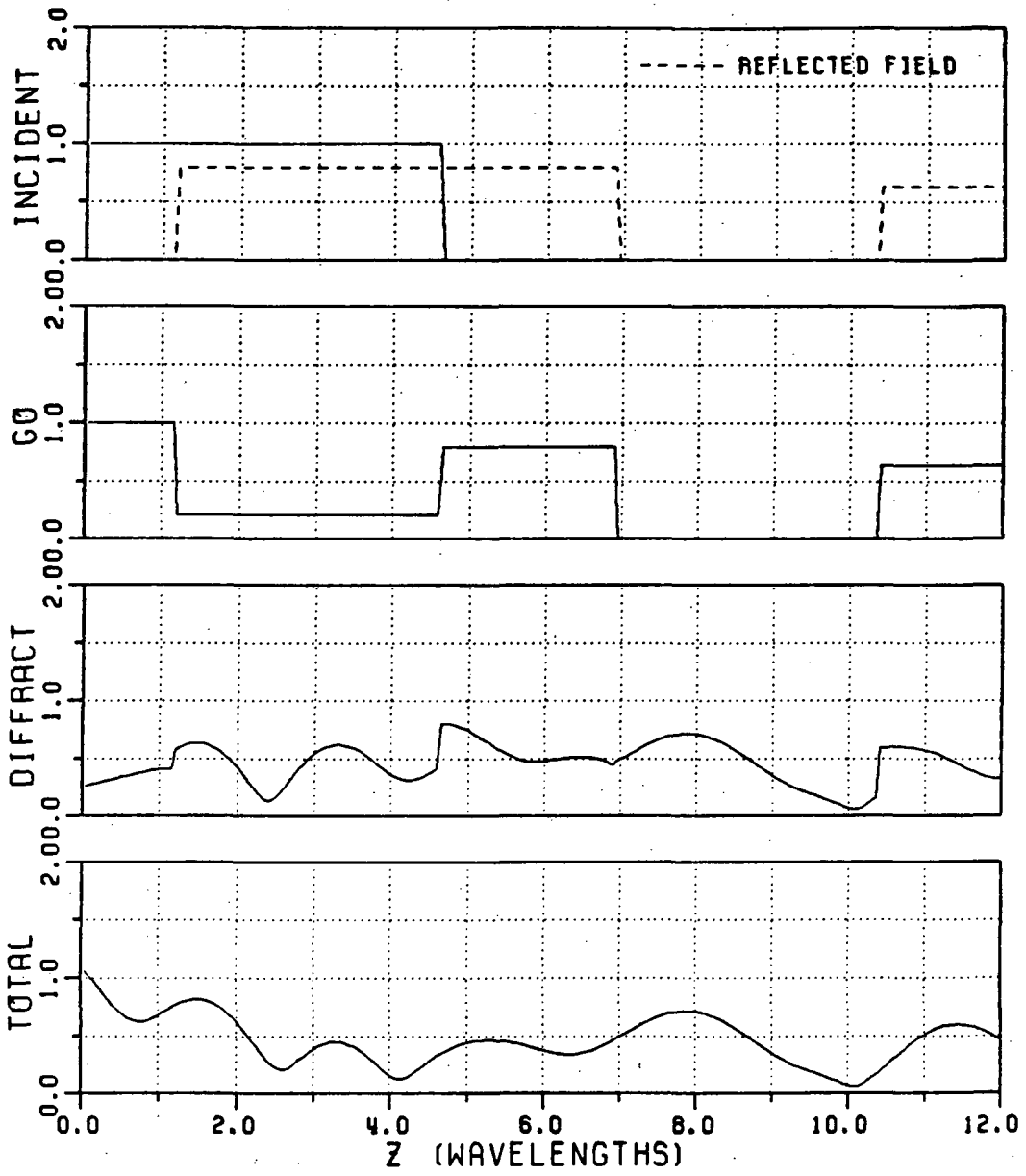

Figure 50: Each ray field within a semi-infinite parallel plate waveguide with impedance walls plotted as a function of the axial distance from the open end to the field point for an incident plane wave with a perpendicular polarization (TE_y).

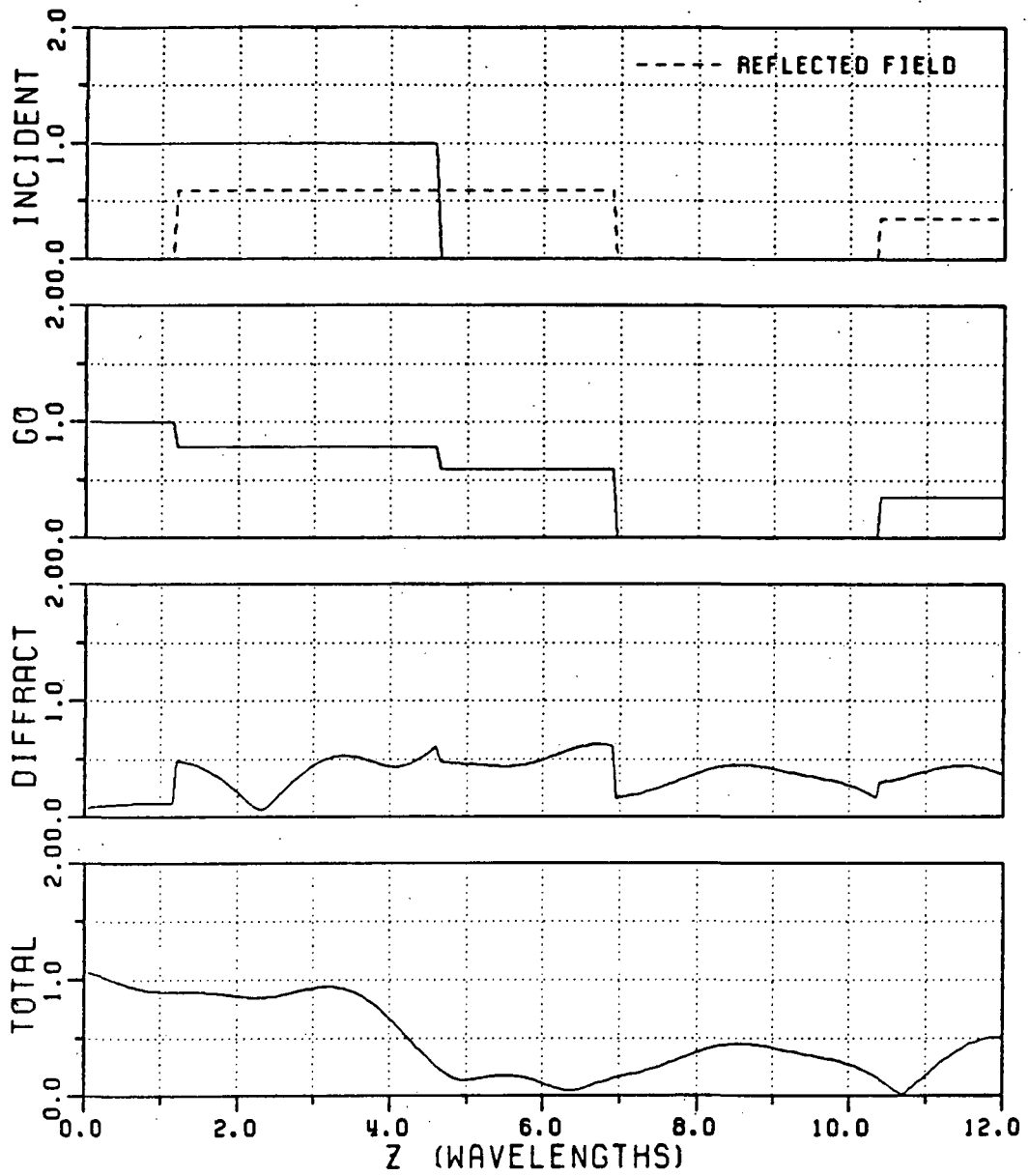

Figure 51: Each ray field within a semi-infinite parallel plate waveguide with impedance walls plotted as a function of the axial distance from the open end to the field point for an incident plane wave with a perpendicular polarization (TE_y).

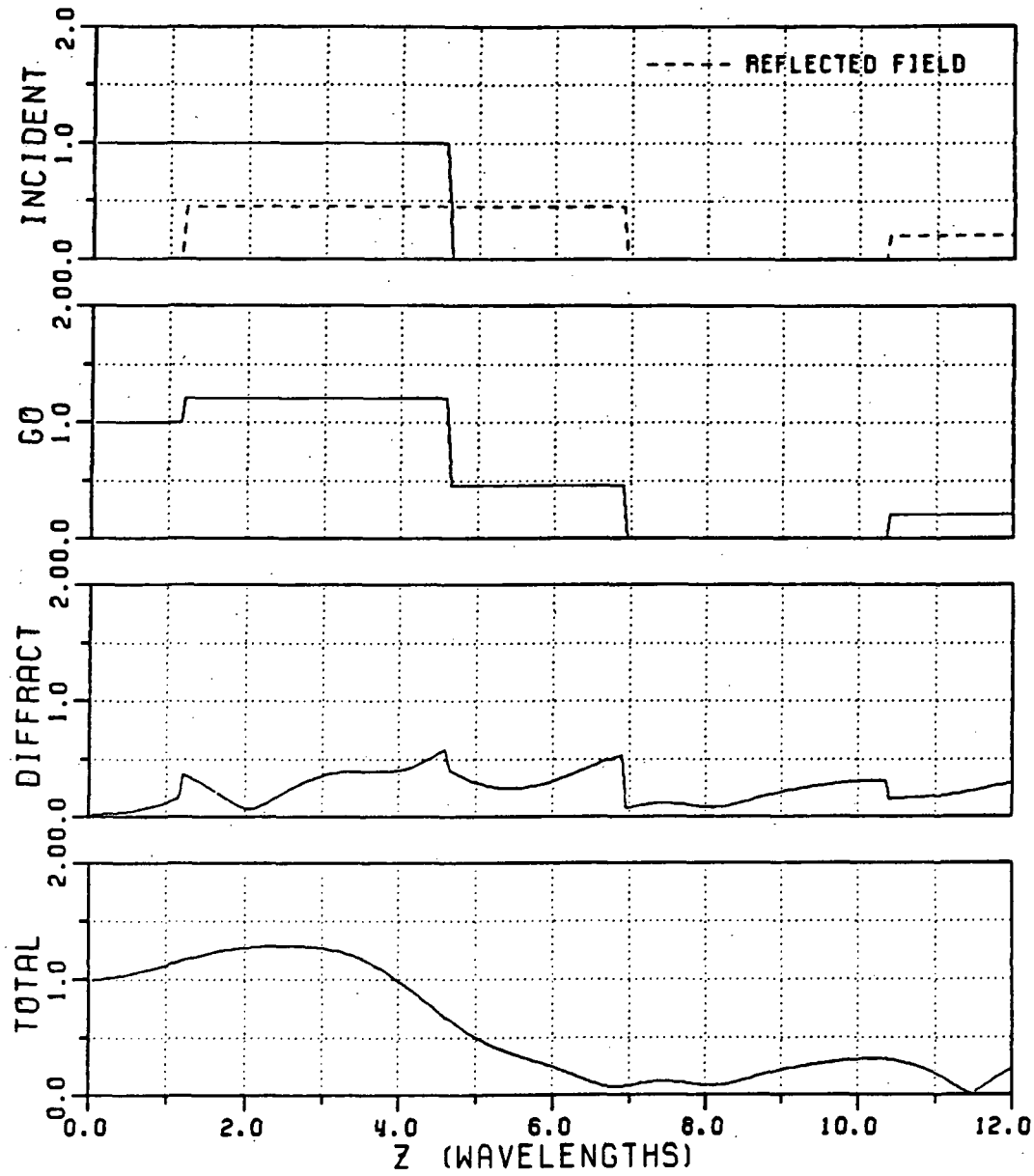

A = 10.0 (WAVELENGTHS) Φ' = 60.0 (DEGREES)
X = 8.0 (WAVELENGTHS) Z_S = (0.9, 0.9)

Figure 52: Each ray field within a semi-infinite parallel plate waveguide with impedance walls plotted as a function of the axial distance from the open end to the field point for an incident plane wave with a perpendicular polarization (TE_y).

3.2 Ray solution for the interior fields of an open-ended parallel plate waveguide coated with an absorbing material on its inner walls

Consider the waveguide whose inner walls are coated with a thin dielectric/ferrite material. The only difference between the analysis of this waveguide configuration and the one involving an impedance boundary condition which was considered in the previous section lies in the reflection coefficients in Equations (3.7) and (3.9). The reflection coefficients which must be used for the absorber coating of finite thickness, i.e. for a grounded dielectric/ferrite slab are derived in Appendix F using the usual *transverse resonance method* [4]; these new reflection coefficients should replace the ones for the impedance boundary condition obtained in Appendix D. It is noted that these *Fresnel reflection coefficients* of Appendix F are a function of the incident angle ϕ', the thickness of the slab t, and the permittivity ϵ and permeability μ of the slab; they are given below for convenience as

$$\tilde{R}_{\parallel} = \frac{\sin\phi' - \frac{j}{\epsilon_r}\sqrt{\epsilon_r\mu_r - \cos^2\phi'}\,\tan\left(kt\sqrt{\epsilon_r\mu_r - \cos^2\phi'}\right)}{\sin\phi' + \frac{j}{\epsilon_r}\sqrt{\epsilon_r\mu_r - \cos^2\phi'}\,\tan\left(kt\sqrt{\epsilon_r\mu_r - \cos^2\phi'}\right)} \tag{3.21}$$

$$\tilde{R}_{\perp} = \frac{\sin\phi' + \frac{j}{\mu_r}\sqrt{\epsilon_r\mu_r - \cos^2\phi'}\,\cot\left(kt\sqrt{\epsilon_r\mu_r - \cos^2\phi'}\right)}{\sin\phi' - \frac{j}{\mu_r}\sqrt{\epsilon_r\mu_r - \cos^2\phi'}\,\cot\left(kt\sqrt{\epsilon_r\mu_r - \cos^2\phi'}\right)} \tag{3.22}$$

where ϵ_r and μ_r are the permittivity and permeability of the absorber (dielectric/ferrite) material relative to the free-space values, respectively, and k is free-space wave number. As before, ϕ' is the angle of incidence. Then, following the same procedure as that for the impedance walled waveguide, one can calculate the reflected and diffracted (as well as diffracted-reflected) ray fields for the waveguide coated with a dielectric/ferrite composite material. The numerical results based

on that analysis are plotted in Figures 53–55 for various values of the thickness t and other parameters of the absorber coating. Similar plots are shown in Figures 56–59 for various values of the permittivity ϵ, and in Figures 60–63 for various values of the permeability μ, respectively. As shown in the figures, the interior field of the waveguide can be reduced significantly by choosing the parameters of the absorbing material in a proper way.

3.3 Ray solution for the interior fields of an open-ended parallel plate waveguide coated with an absorbing material on its inner walls and with a planar termination inside

A simple planar termination which is L wavelengths away from the open end is placed inside the waveguide as shown in the Figure 64. It is noted that the material of the termination need not be necessarily the same as that of the inner walls but for the present it is assumed to be the same for convenience. Then the field at the observation point consists of the fields associated with two groups of rays. One group is associated with the incident, reflected and diffracted rays from the open end of the waveguide as in the case of the waveguide without a termination. The other group of rays corresponds to those which are reflected back from the termination and then reach the field point. The ray field due to the reflection by the termination can be calculated by simply using an effective observation point at an image location which is symmetrical with respect to the actual observation point about the termination as shown in Figure 64.

Thus the ray field at P is calculated by adding the field of the rays from the open end reaching P without passing through the termination as well as the field of the rays reaching P' after they are extended or continued past the termination to P' and by including the reflection coefficient of the termination wall to the fields

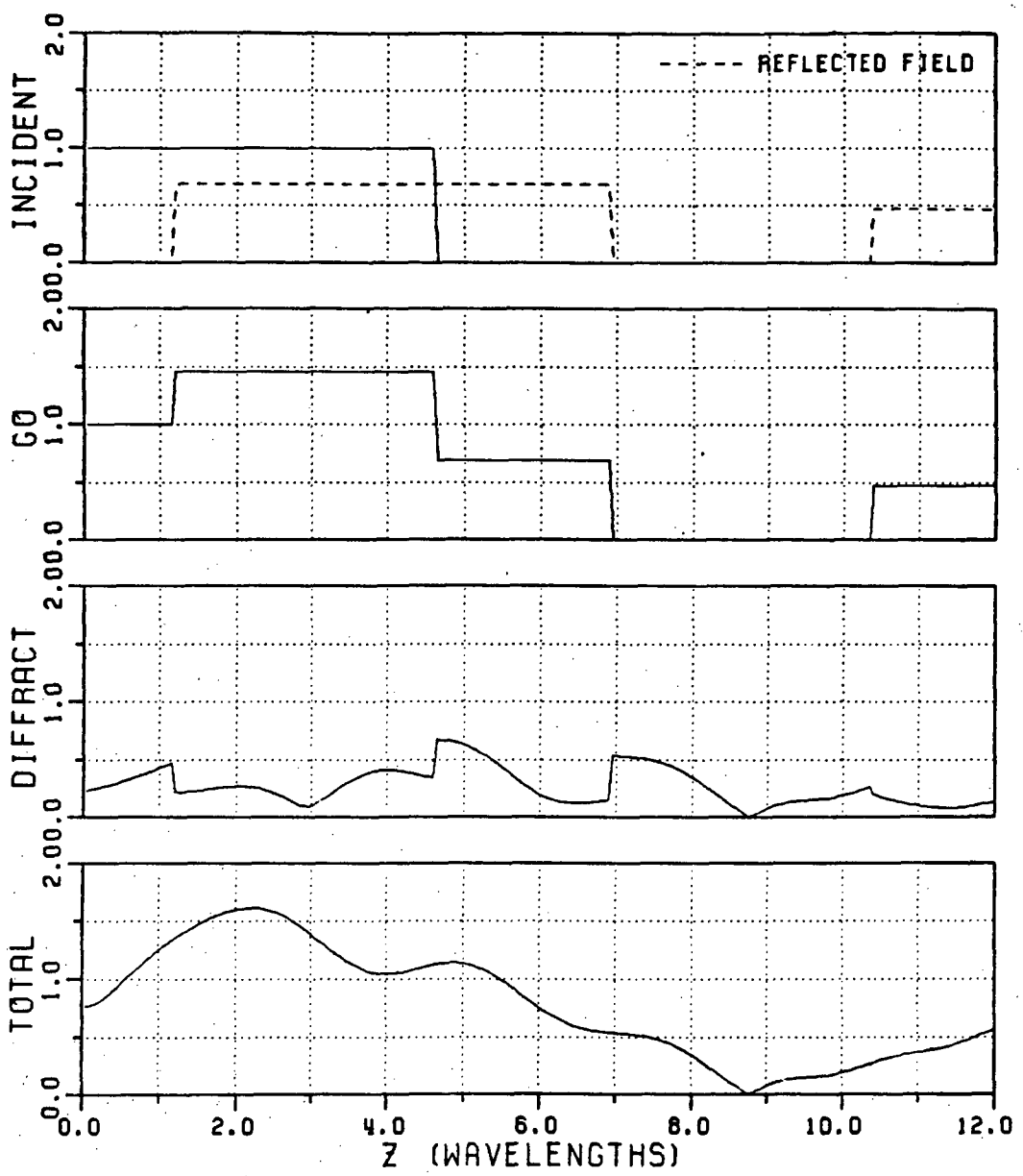

A = 10.0 (WAVELENGTHS) Φ' = 60.0 (DEGREES)
X = 8.0 (WAVELENGTHS) ϵ = (3.0, -0.30)
T = 0.025 (WAVELENGTHS) μ = (2.0, -0.20)

Figure 53: Each ray field within a semi-infinite parallel plate waveguide coated with a dielectric/ferrite material plotted as a function of the axial distance from the open end to the field point for an incident plane wave with a parallel polarization (TM_y) case.

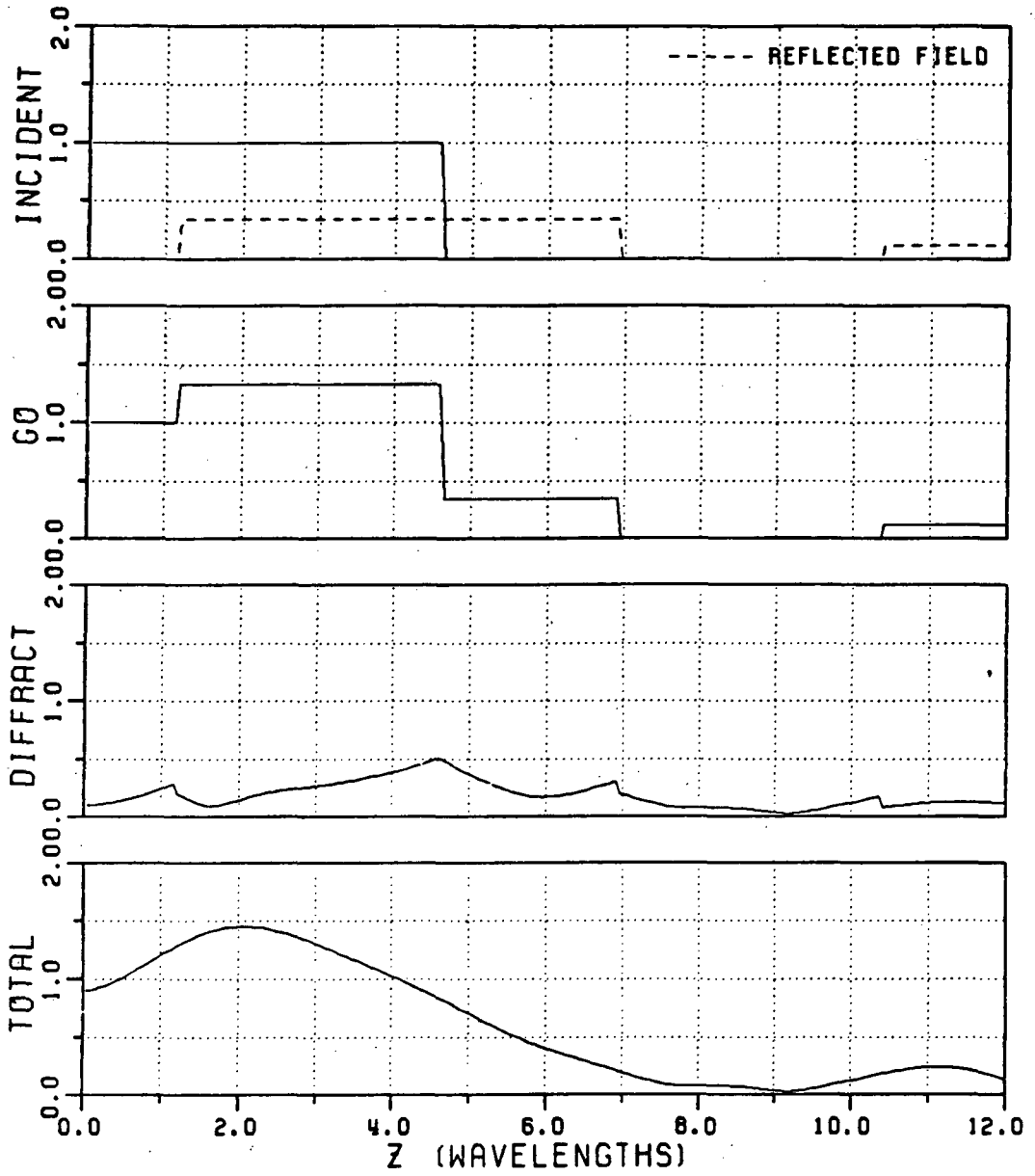

Figure 54: Each ray field within a semi-infinite parallel plate waveguide coated with a dielectric/ferrite material plotted as a function of the axial distance from the open end to the field point for an incident plane wave with a parallel polarization (TM_y) case.

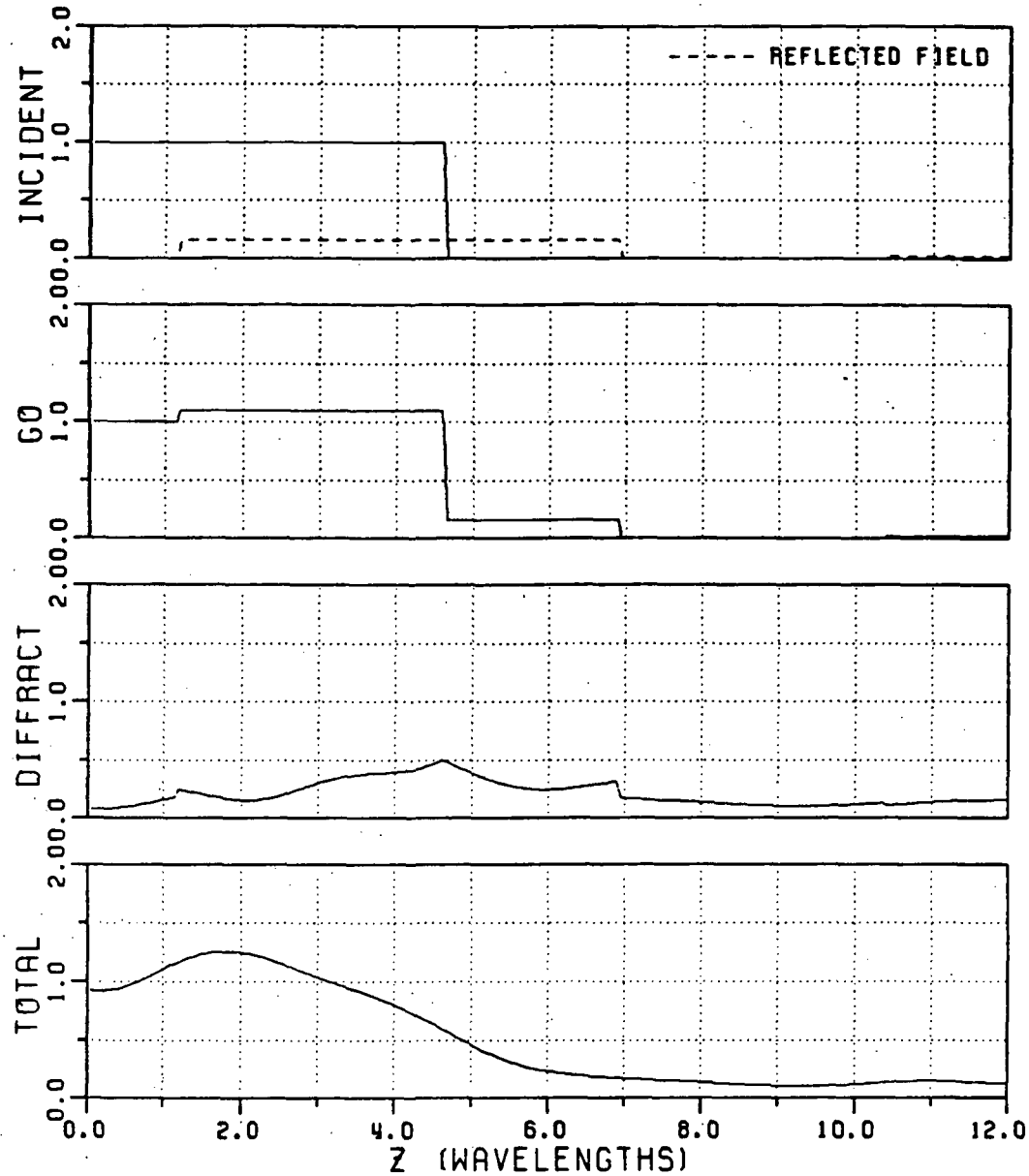

A = 10.0 (WAVELENGTHS) Φ^i = 60.0 (DEGREES)
X = 8.0 (WAVELENGTHS) ϵ = (3.0, -0.30)
T = 0.200 (WAVELENGTHS) μ = (2.0, -0.20)

Figure 55: Each ray field within a semi-infinite parallel plate waveguide coated with a dielectric/ferrite material plotted as a function of the axial distance from the open end to the field point for an incident plane wave with a parallel polarization (TM_y) case.

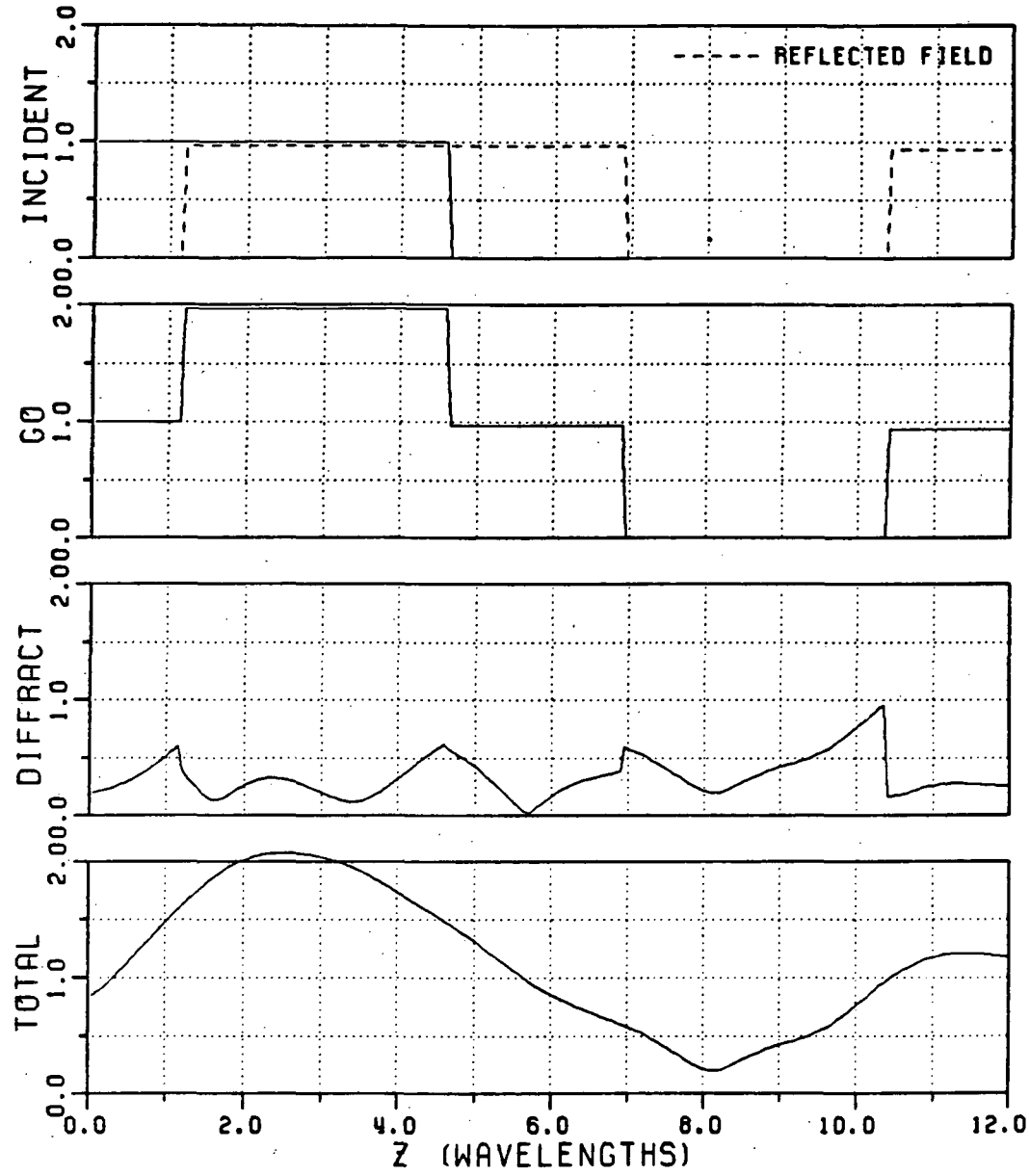

A = 10.0 (WAVELENGTHS)	Φ' = 60.0 (DEGREES)
X = 8.0 (WAVELENGTHS)	ε = (1.0, -0.10)
T = 0.050 (WAVELENGTHS)	μ = (1.0, 0.00)

Figure 56: Each ray field within a semi-infinite parallel plate waveguide coated with a dielectric/ferrite material plotted as a function of the axial distance from the open end to the field point for an incident plane wave with a parallel polarization (TM_y) case.

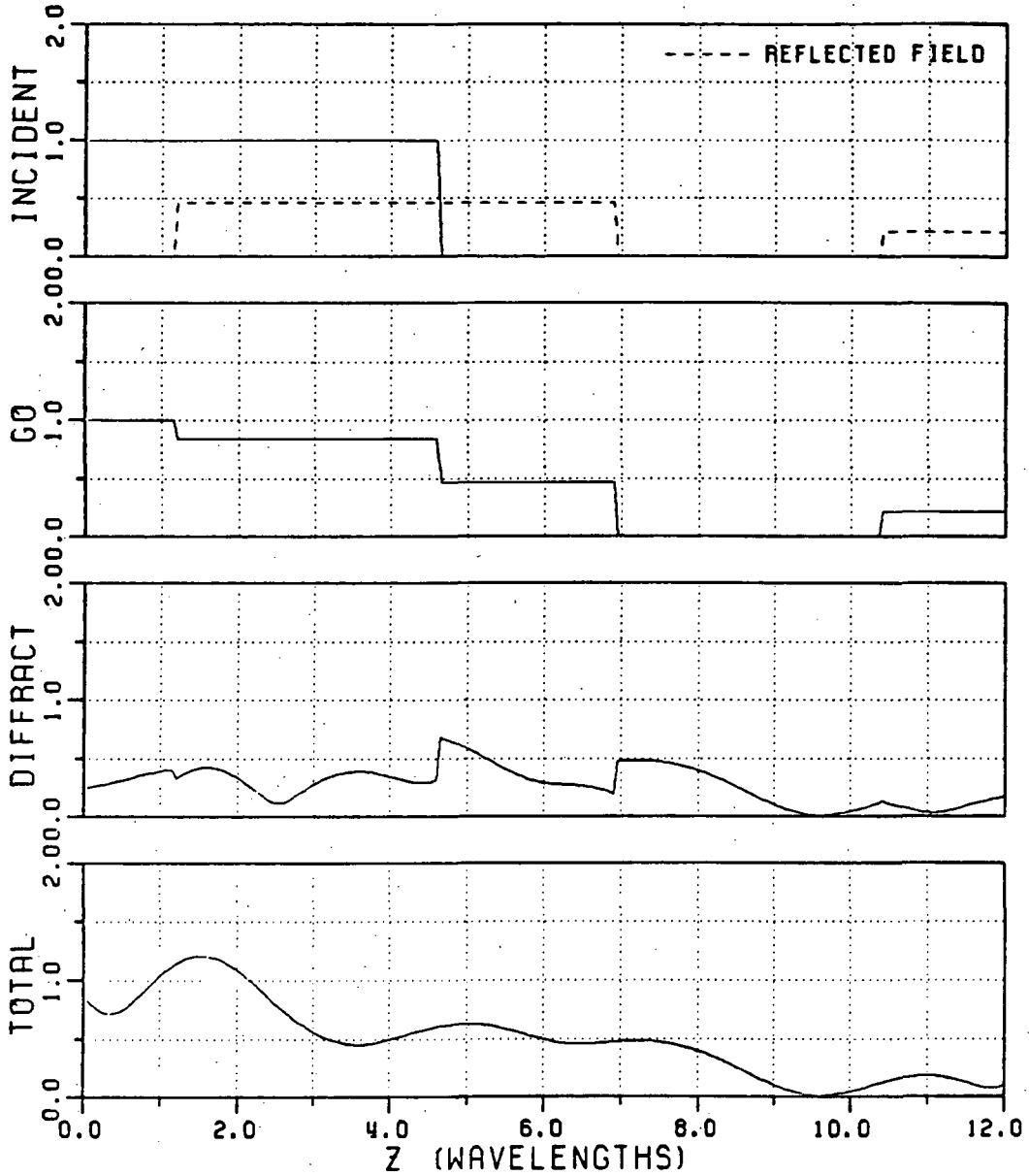

A = 10.0 (WAVELENGTHS) Φ' = 60.0 (DEGREES)
X = 8.0 (WAVELENGTHS) ε = (5.0, -0.50)
T = 0.050 (WAVELENGTHS) μ = (1.0, 0.00)

Figure 57: Each ray field within a semi-infinite parallel plate waveguide coated with a dielectric/ferrite material plotted as a function of the axial distance from the open end to the field point for an incident plane wave with a parallel polarization (TM_y) case.

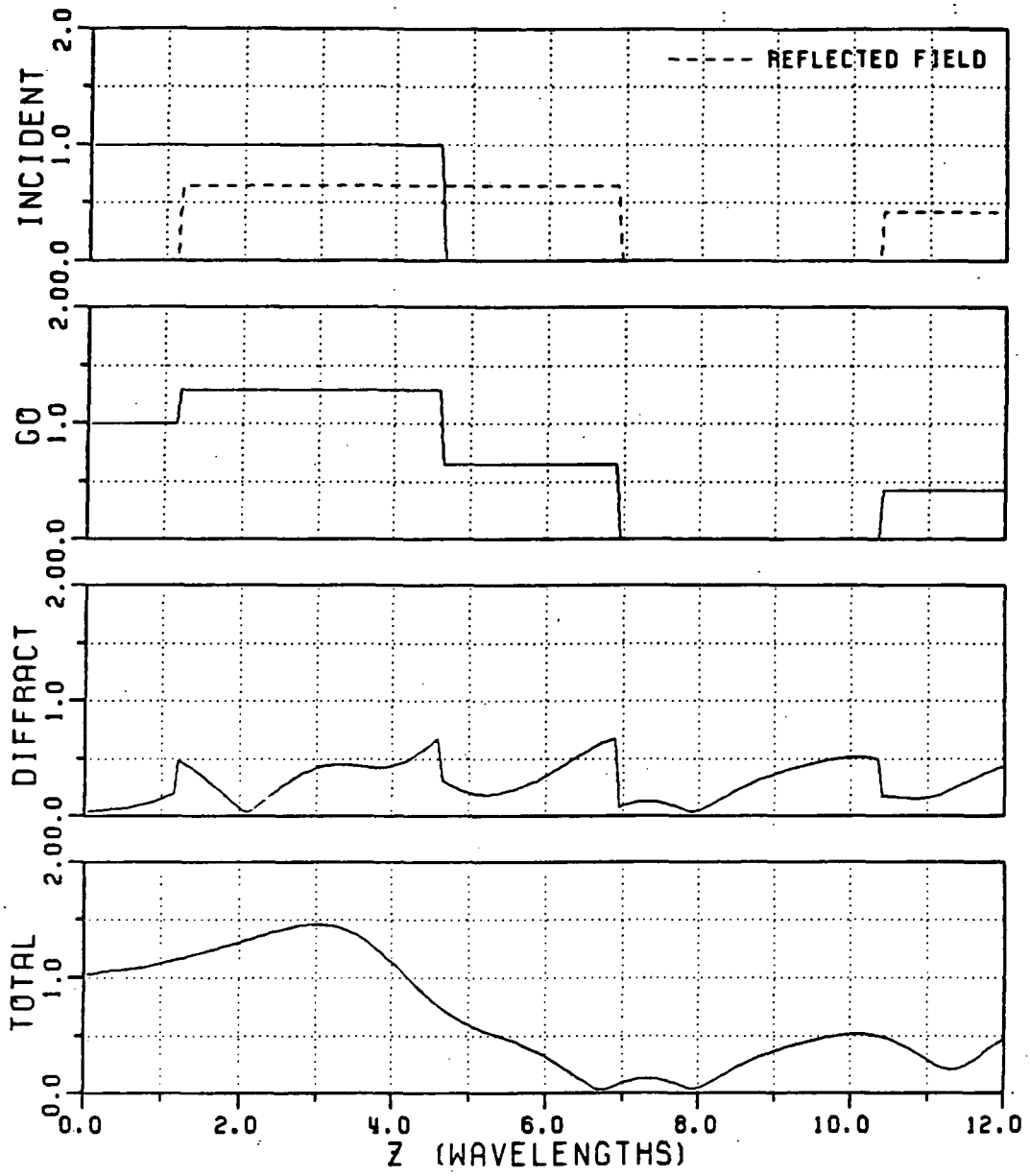

A = 10.0 (WAVELENGTHS) Φ' = 60.0 (DEGREES)
X = 8.0 (WAVELENGTHS) ε = (7.0, -0.70)
T = 0.050 (WAVELENGTHS) μ = (1.0, 0.00)

Figure 58: Each ray field within a semi-infinite parallel plate waveguide coated with a dielectric/ferrite material plotted as a function of the axial distance from the open end to the field point for an incident plane wave with a parallel polarization (TM_y) case.

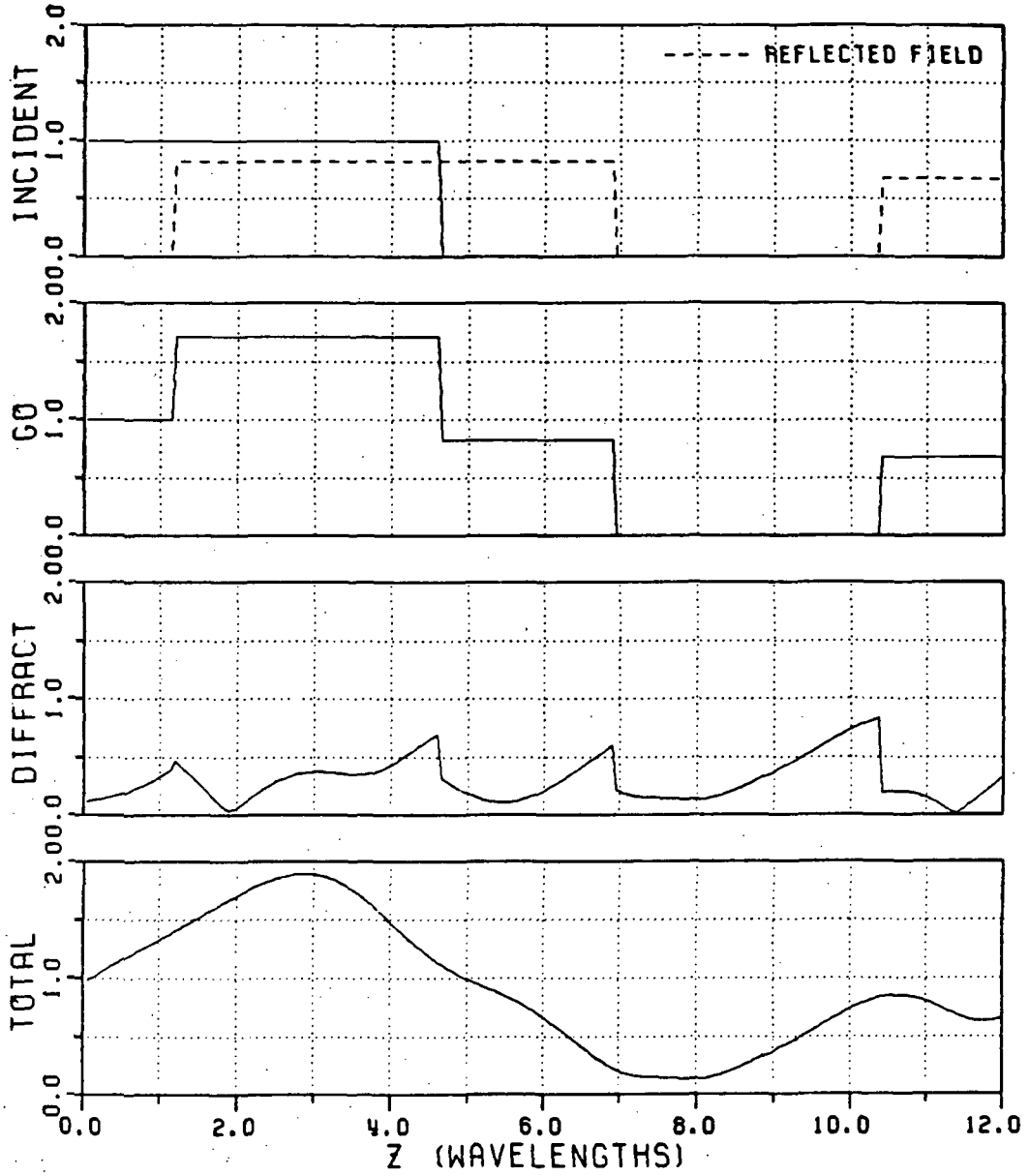

Figure 59: Each ray field within a semi-infinite parallel plate waveguide coated with a dielectric/ferrite material plotted as a function of the axial distance from the open end to the field point for an incident plane wave with a parallel polarization (TM_y) case.

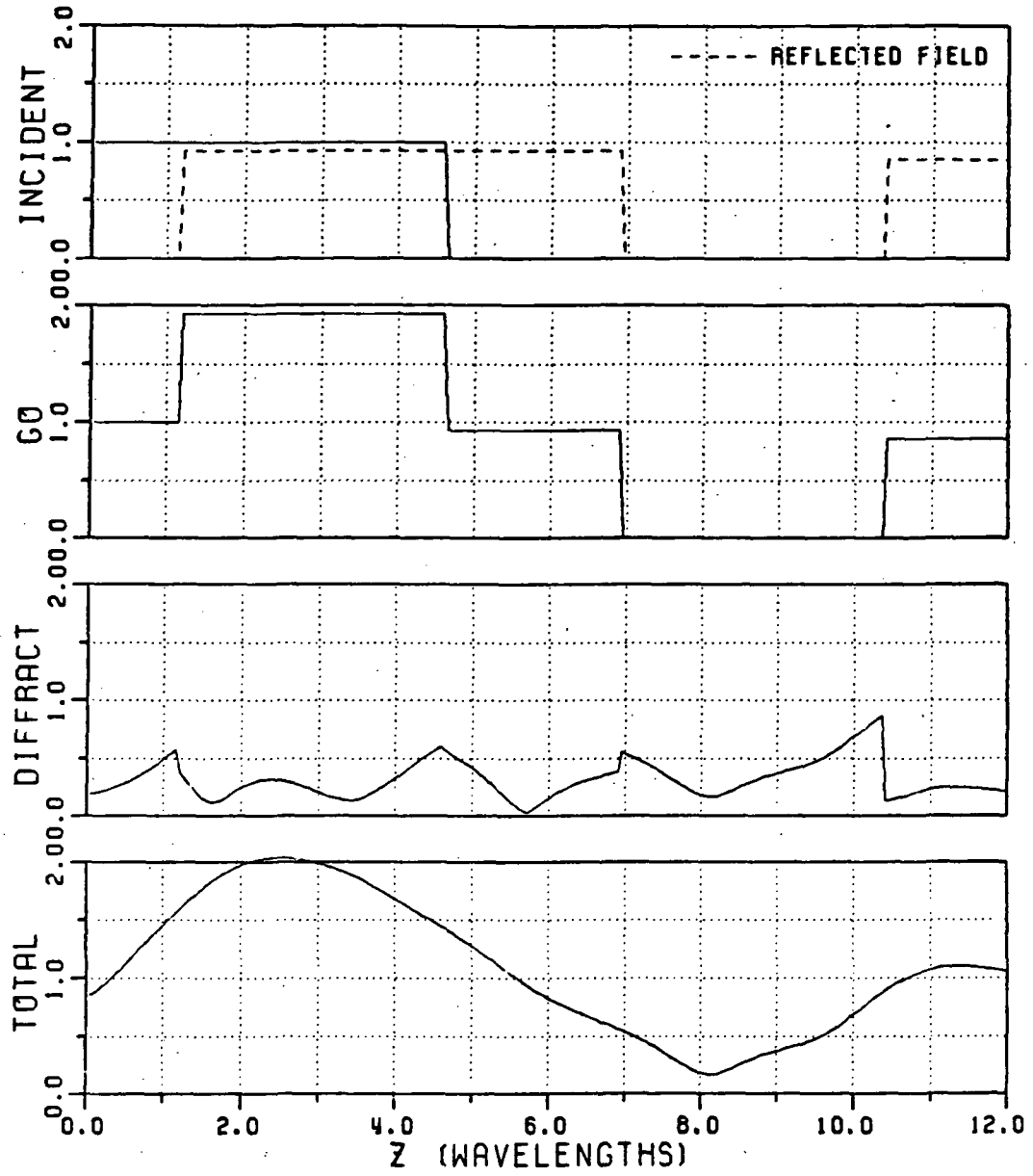

A = 10.0 (WAVELENGTHS) Φ' = 60.0 (DEGREES)
X = 8.0 (WAVELENGTHS) ε = (1.0, 0.00)
T = 0.050 (WAVELENGTHS) μ = (1.0, -0.10)

Figure 60: Each ray field within a semi-infinite parallel plate waveguide coated with a dielectric/ferrite material plotted as a function of the axial distance from the open end to the field point for an incident plane wave with a parallel polarization (TM_y) case.

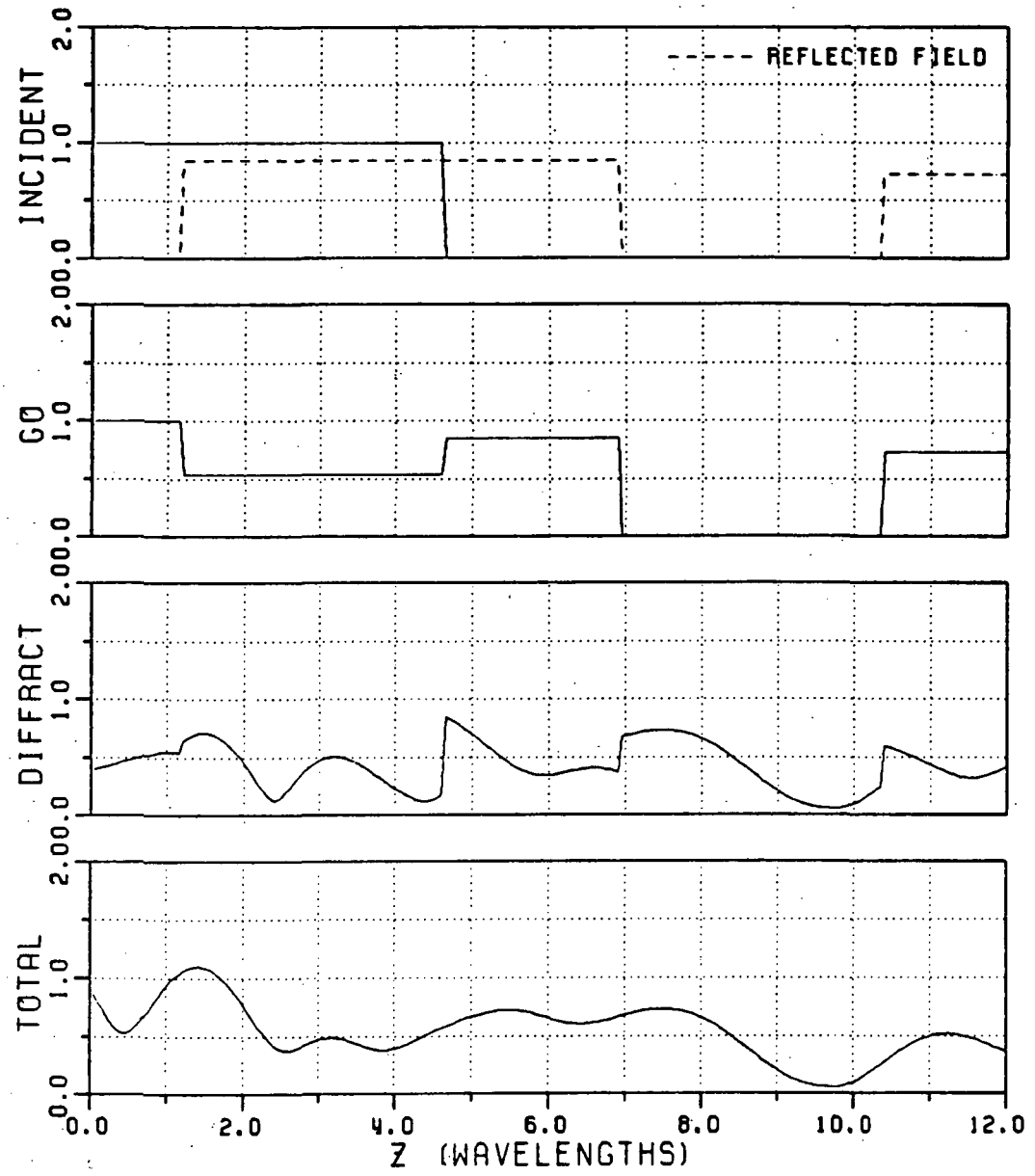

A = 10.0 (WAVELENGTHS) Φ' = 60.0 (DEGREES)
X = 8.0 (WAVELENGTHS) ε = (1.0, 0.00)
T = 0.050 (WAVELENGTHS) μ = (5.0, -0.50)

Figure 61: Each ray field within a semi-infinite parallel plate waveguide coated with a dielectric/ferrite material plotted as a function of the axial distance from the open end to the field point for an incident plane wave with a parallel polarization (TM_y) case.

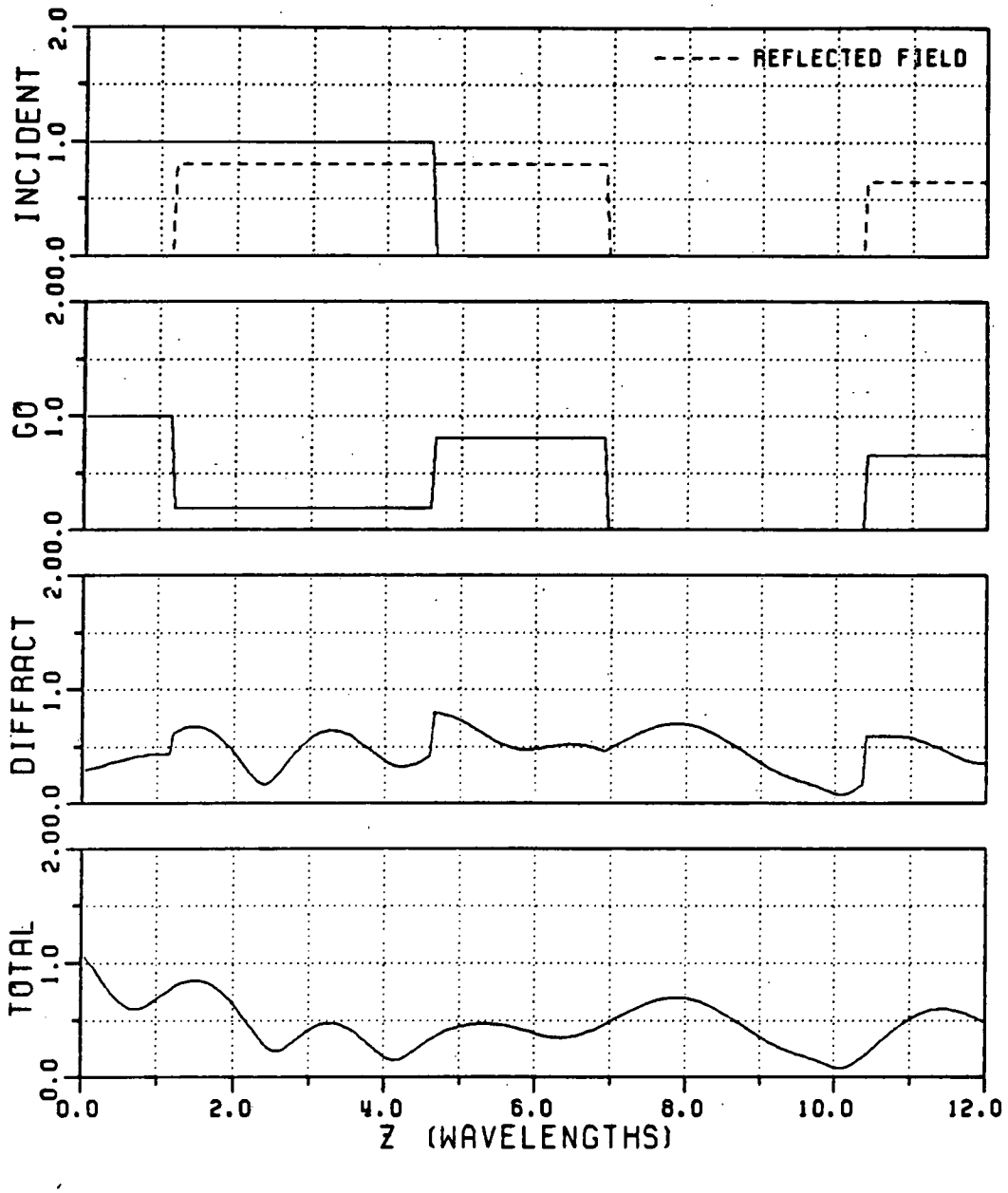

Figure 62: Each ray field within a semi-infinite parallel plate waveguide coated with a dielectric/ferrite material plotted as a function of the axial distance from the open end to the field point for an incident plane wave with a parallel polarization (TM_y) case.

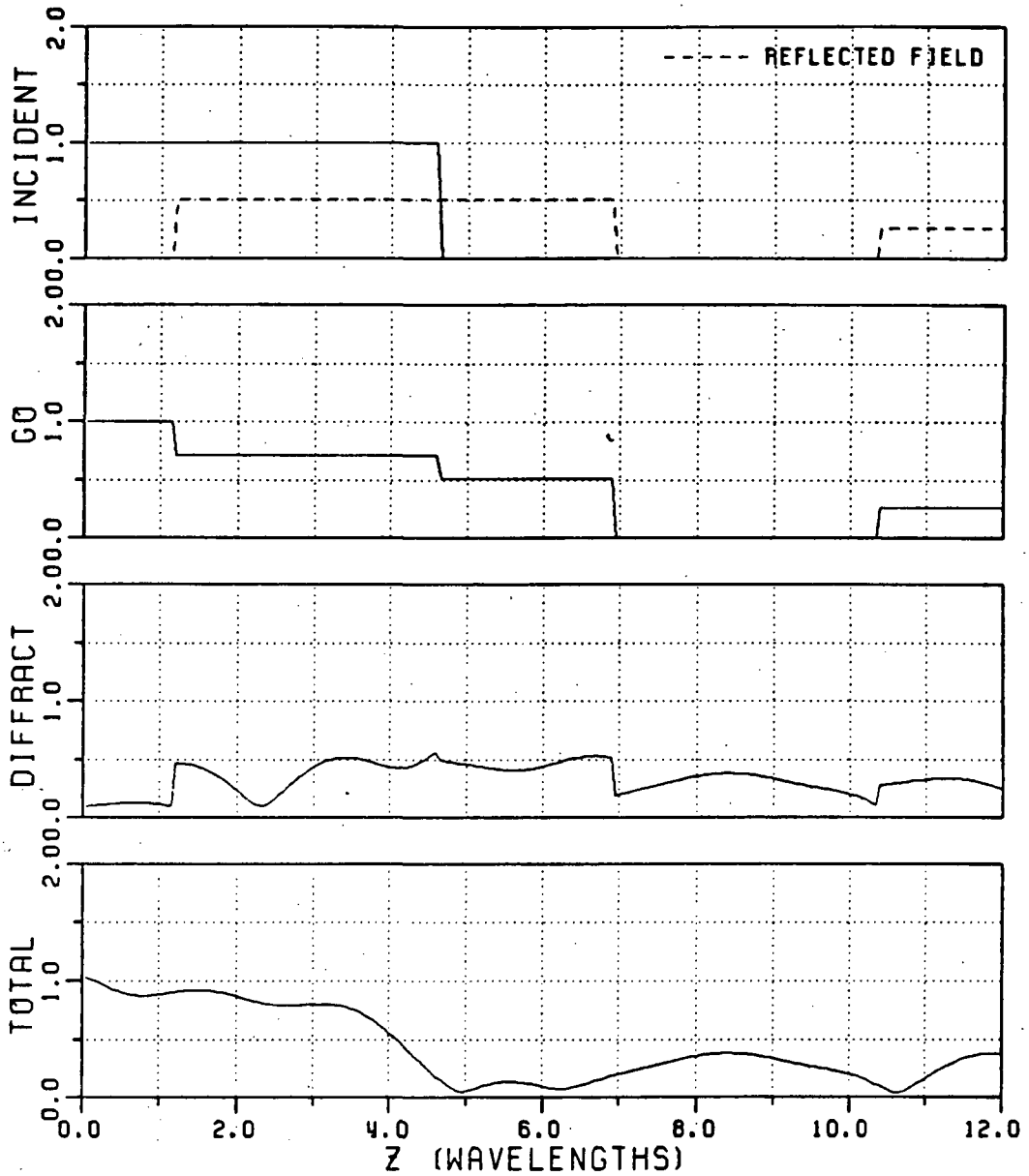

A = 10.0 (WAVELENGTHS) Φ'= 60.0 (DEGREES)
X = 8.0 (WAVELENGTHS) ε =(1.0,0.00)
T = 0.050 (WAVELENGTHS) μ =(9.0,-0.90)

Figure 63: Each ray field within a semi-infinite parallel plate waveguide coated with a dielectric/ferrite material plotted as a function of the axial distance from the open end to the field point for an incident plane wave with a parallel polarization (TM_y) case.

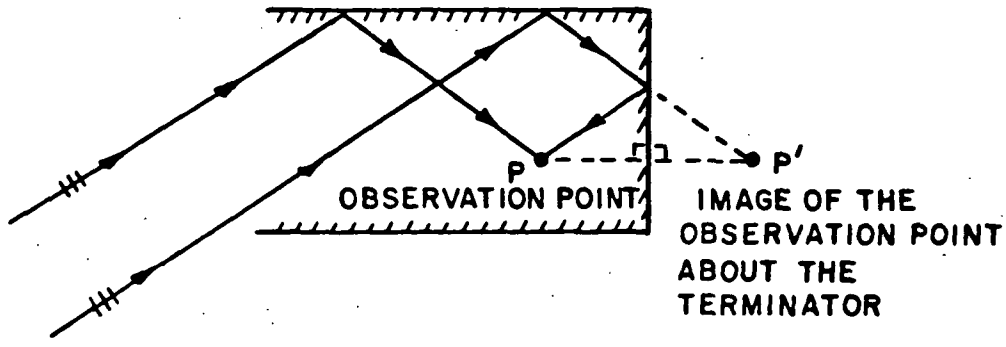

Figure 64: A semi-infinite parallel plate waveguide with a planar termination showing singly reflected ray by the upper wall and doubly reflected ray by the upper and the termination.

of the rays reaching P'. Each type of ray field is plotted in Figures 65 and 66 for the two different wave polarizations. It is noted that the small ripples in each field are due to the interaction between the rays coupled into the guide from the exterior and those reflected back from the termination after being coupled into the waveguide.

3.4 Field backscattered from a semi-infinite parallel plate waveguide with an impedance boundary condition on its inner walls

Using the same diffraction coefficients as in Equation (3.9), the far zone fields backscattered from a semi-infinite parallel plate waveguide with inner impedance walls are computed and shown in Figures 67 and 68 as a function of the incident angle for parallel and perpendicular polarization cases, respectively. The pertinent rays used in this case are shown in Figure 69. In Figure 69, R_d represents the far zone distance from the lower edge of the waveguide (zero phase reference) to the

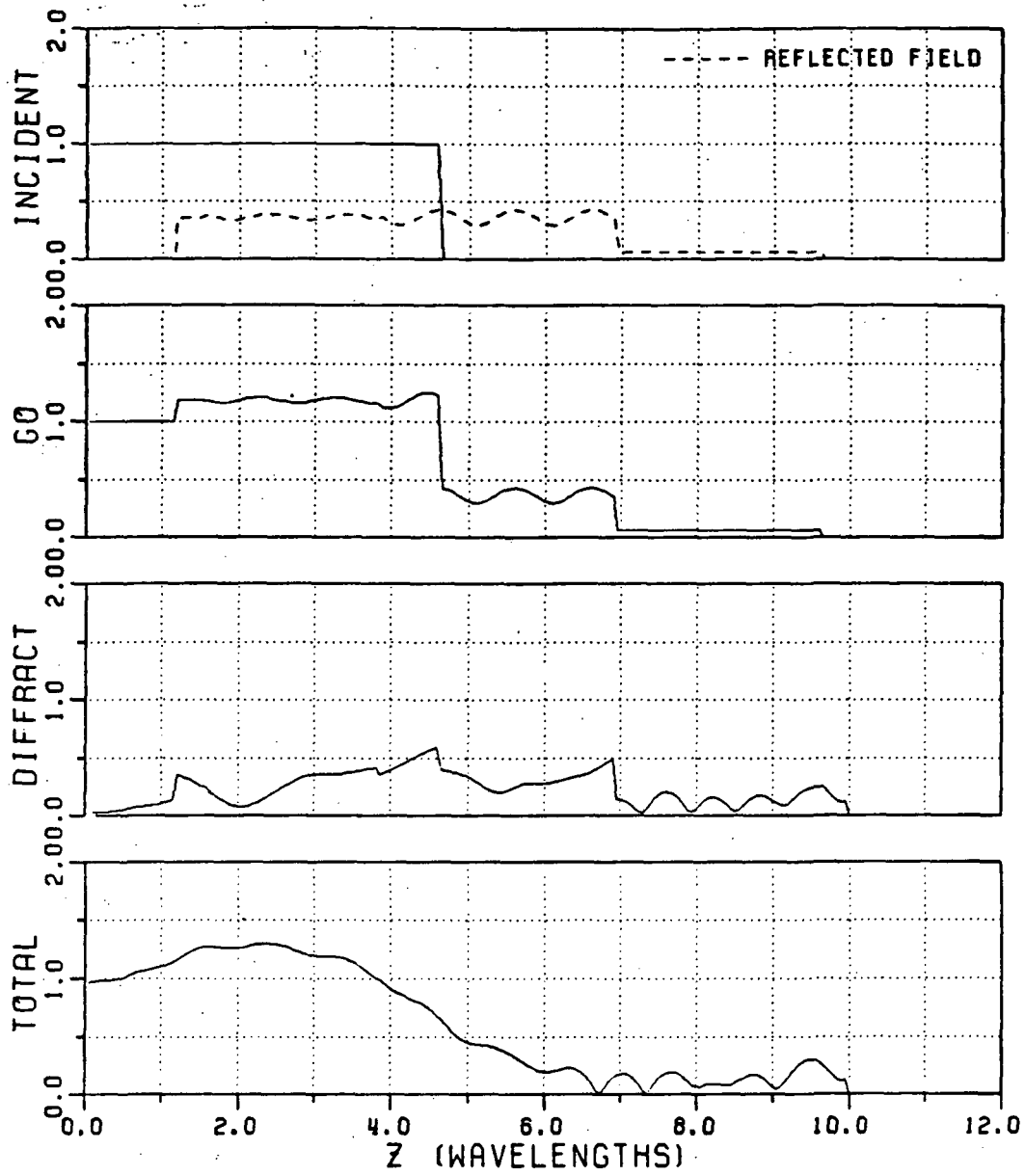

A = 10.0 (WAVELENGTHS) Φ' = 60.0 (DEGREES)
X = 8.0 (WAVELENGTHS) ε = (3.0, -0.30)
L = 10.0 (WAVELENGTHS) μ = (3.0, -0.30)
T = 0.050 (WAVELENGTHS)

Figure 65: Each ray field within a semi-infinite parallel plate waveguide coated with a dielectric/ferrite material and with a planar termination inside when a plane wave with parallel polarization is incident.

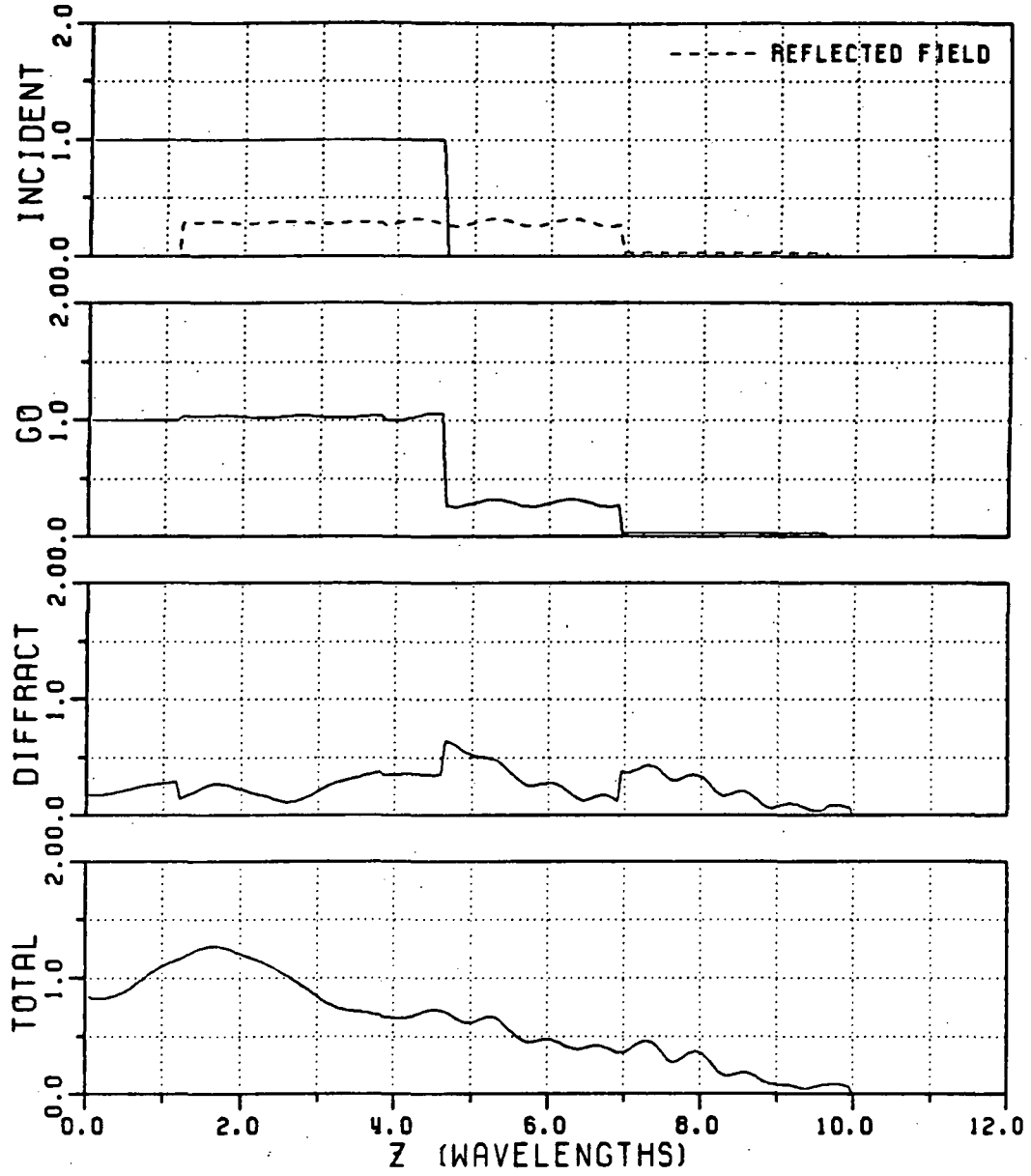

A = 10.0 (WAVELENGTHS) Φ' = 60.0 (DEGREES)
X = 8.0 (WAVELENGTHS) ε = (3.0, -0.30)
L = 10.0 (WAVELENGTHS) μ = (3.0, -0.30)
T = 0.050 (WAVELENGTHS)

Figure 66: Each ray field within a semi-infinite parallel plate waveguide coated with a dielectric/ferrite material and with a planar termination inside when a plane wave with perpendicular polarization is incident.

field point. Note that the backscattered field is entirely due to the edge diffracted rays for the semi-infinite waveguide without any interior termination, and the rays multiply diffracted across the aperture are ignored in the figures. Rays multiply diffracted across the aperture become important if the waveguide width (a) is not sufficiently large in terms of the wavelength. Additional plots are presented in Figures 70 and 71 which show the behaviour of the backscattered field as a function of the waveguide width for different incident wave polarizations. Similiar results can also be obtained for a perfectly-conducting parallel plate waveguide with absorber coating on its inner walls by simply using the results in Appendix F rather than Appendix D for the reflection coefficient which occurs in the diffraction coefficient of Equation (3.9).

3.5 Field radiated from the interior cavity region formed by the semi-infinite waveguide and its interior planar termination

The field which is initially coupled into the waveguide from the open end and then reflected from the interior termination to radiate out of the open end is calculated using an aperture integration (AI) technique together with the equivalence theorem [14,15,16] in this section. This field is referred to as the field radiated from the interior waveguide cavity region where the open-ended cavity is formed by the semi-infinite waveguide and its interior termination as shown in Figure 72. The total field scattered by the semi-infinite waveguide consists of this cavity radiation contribution and the fields scattered from the edges at the open end of the semi-infinite walls of the waveguide; the latter contribution was found in the previous Section 3.4 for the special case of backscatter. In order to use AI to calculate the cavity radiation field, one can find a set of equivalent electric and magnetic currents $\mathbf{J}_s$ and $\mathbf{M}_s$ on an appropriate surface that encloses the semi-infinite waveguide.

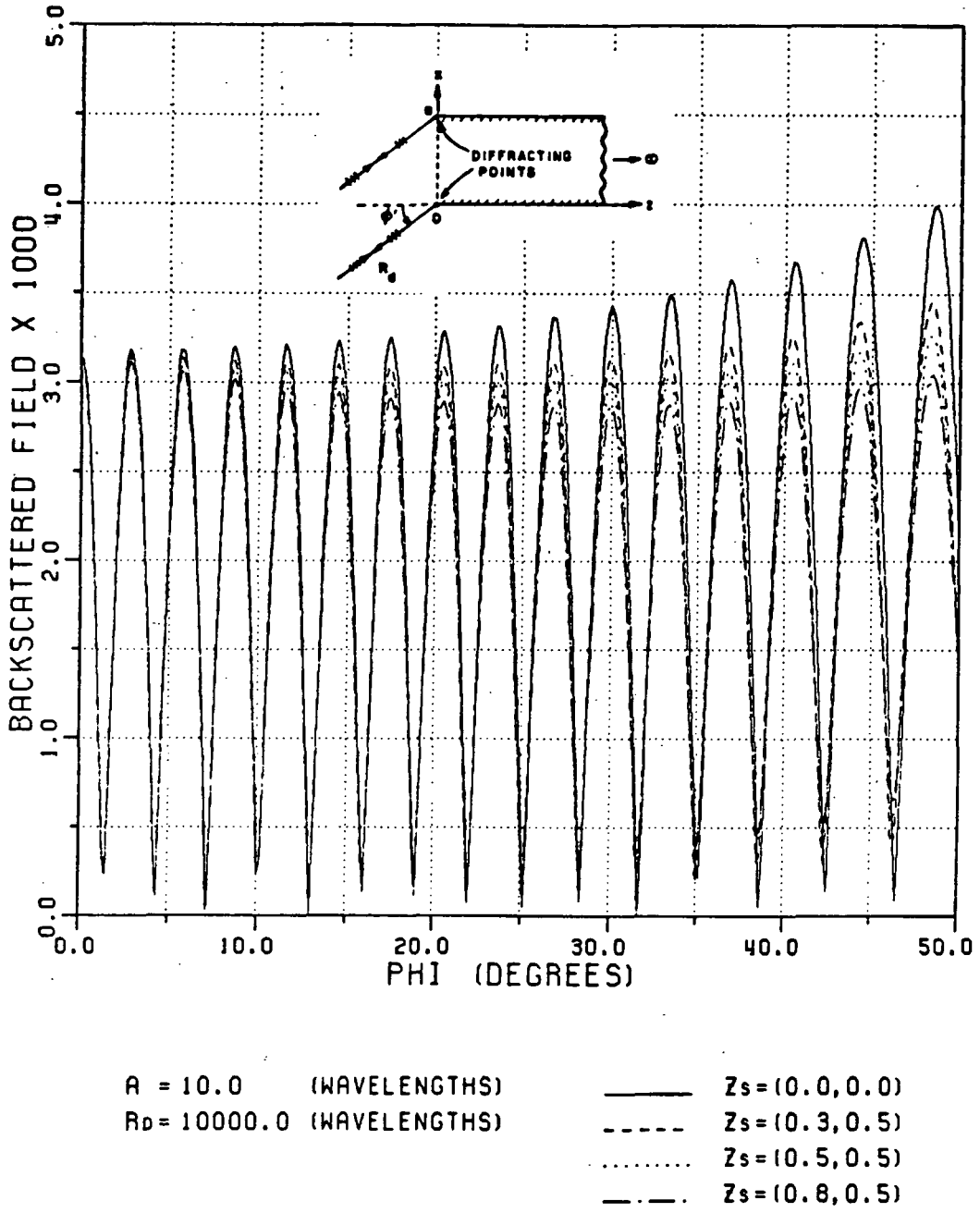

Figure 67: Plane wave backscattering by a semi-infinite parallel plate waveguide with an impedance boundary condition on its inner walls as a function of incident angle for the parallel polarization case.

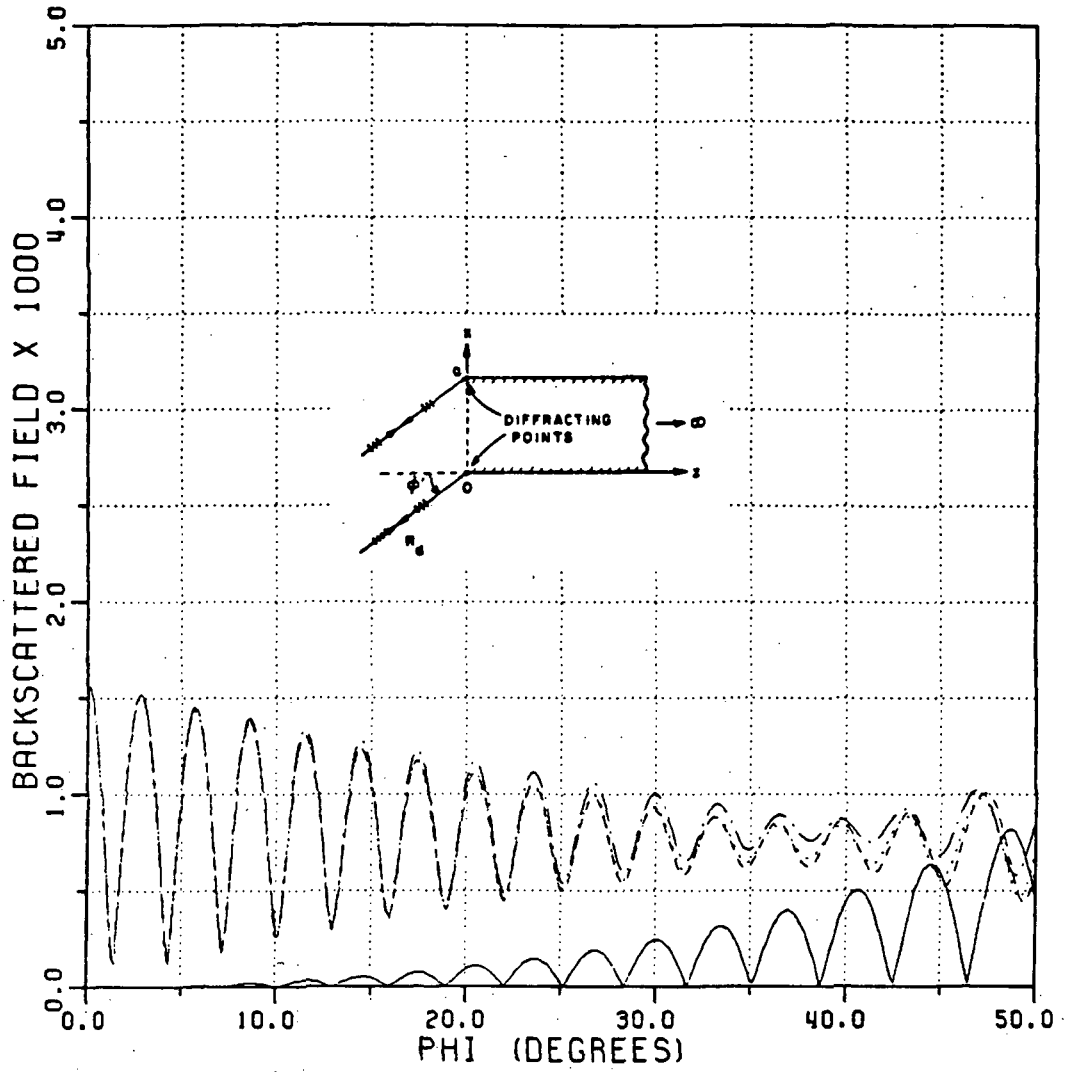

Figure 68: Plane wave backscattering by a semi-infinite parallel plate waveguide with an impedance boundary condition on its inner walls as a function of incident angle for the perpendicular polarization case.

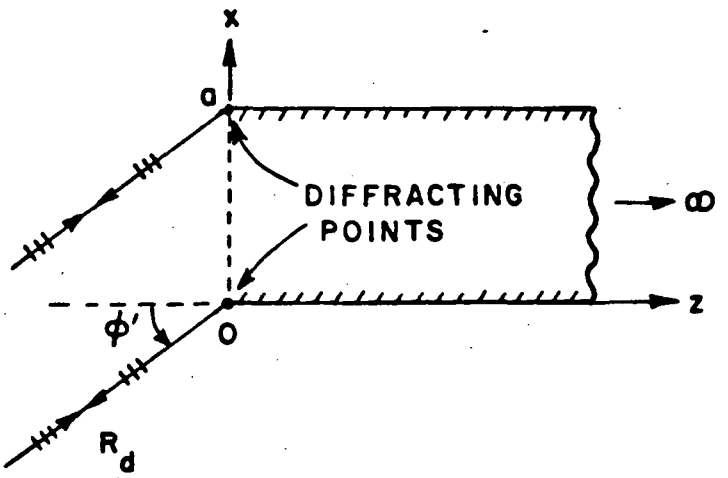

Figure 69: Plane wave backscattering by a semi-infinite parallel plate waveguide with an impedance boundary condition on its inner walls as a function of the waveguide width for the parallel polarization case.

These equivalent currents then radiate the same fields as those originally radiated from the open end by the fields reflected from the interior waveguide termination; also, $\mathbf{J}_s$ and $\mathbf{M}_s$ radiate a null field inside the chosen surface. Since the interior cavity radiation in the forward half space is of major interest in this study, it is convenient to choose a *mathematical surface* which is infinite in extent and is defined by the plane $z = 0$ (which also contains he waveguide aperture at the open end). The equivalent source $\mathbf{J}_s$ and $\mathbf{M}_s$ then reside at $z = 0^-$ and extend over $-\infty < x < \infty$, $-\infty < y < \infty$ as shown in Figure 73(a). Actually, the problem is 2-D in nature, so that there is no variation in y. The equivalent sources $\mathbf{J}_s$ and $\mathbf{M}_s$ are defined by

$$\mathbf{J}_s = \hat{\mathbf{n}} \times \mathbf{H}_{cr} \tag{3.23}$$

$$\mathbf{M}_s = \mathbf{E}_{cr} \times \hat{\mathbf{n}} \tag{3.24}$$

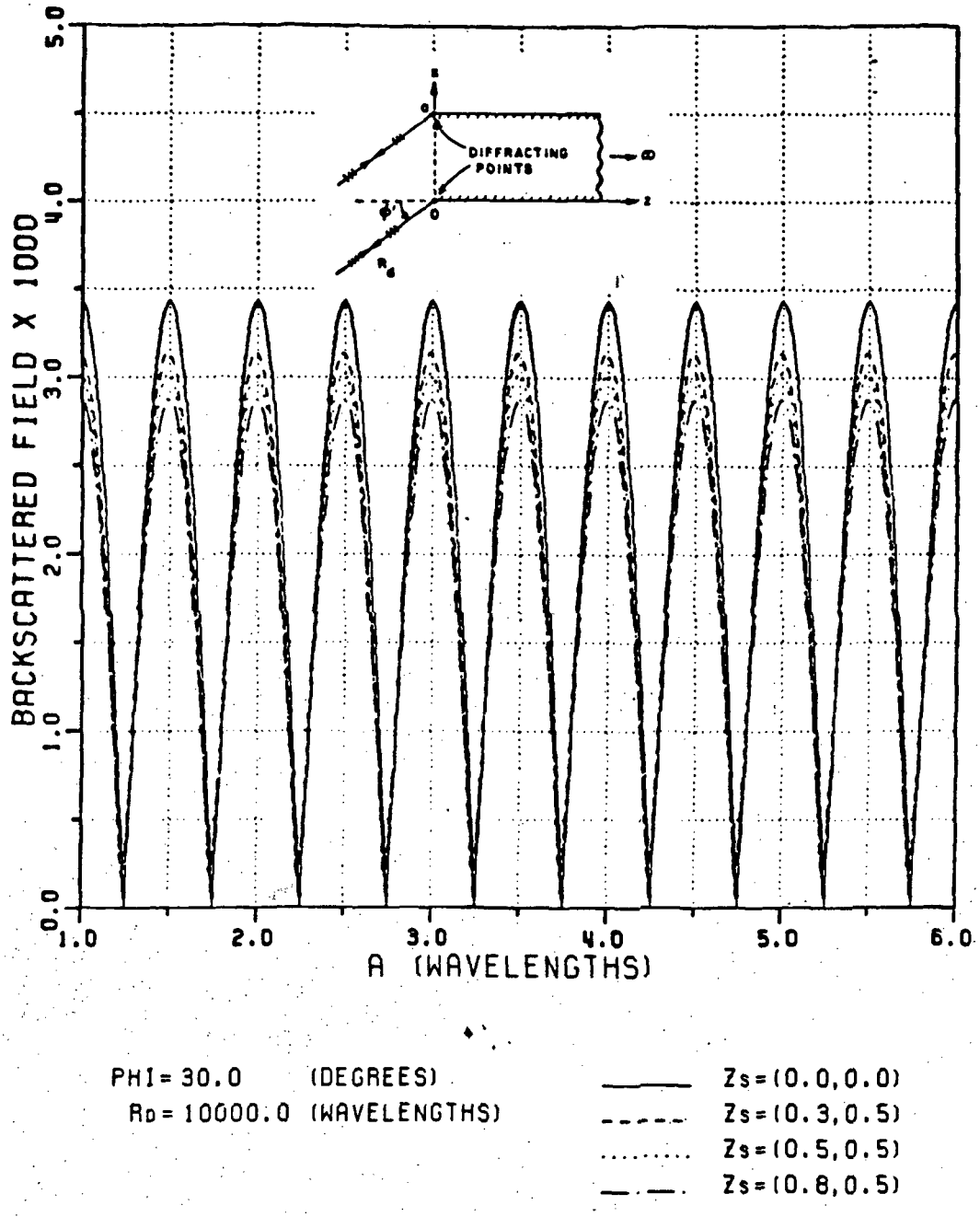

Figure 70: Plane wave backscattering by a semi-infinite parallel plate waveguide with an impedance boundary condition on its inner walls as a function of the waveguide width for the parallel polarization.

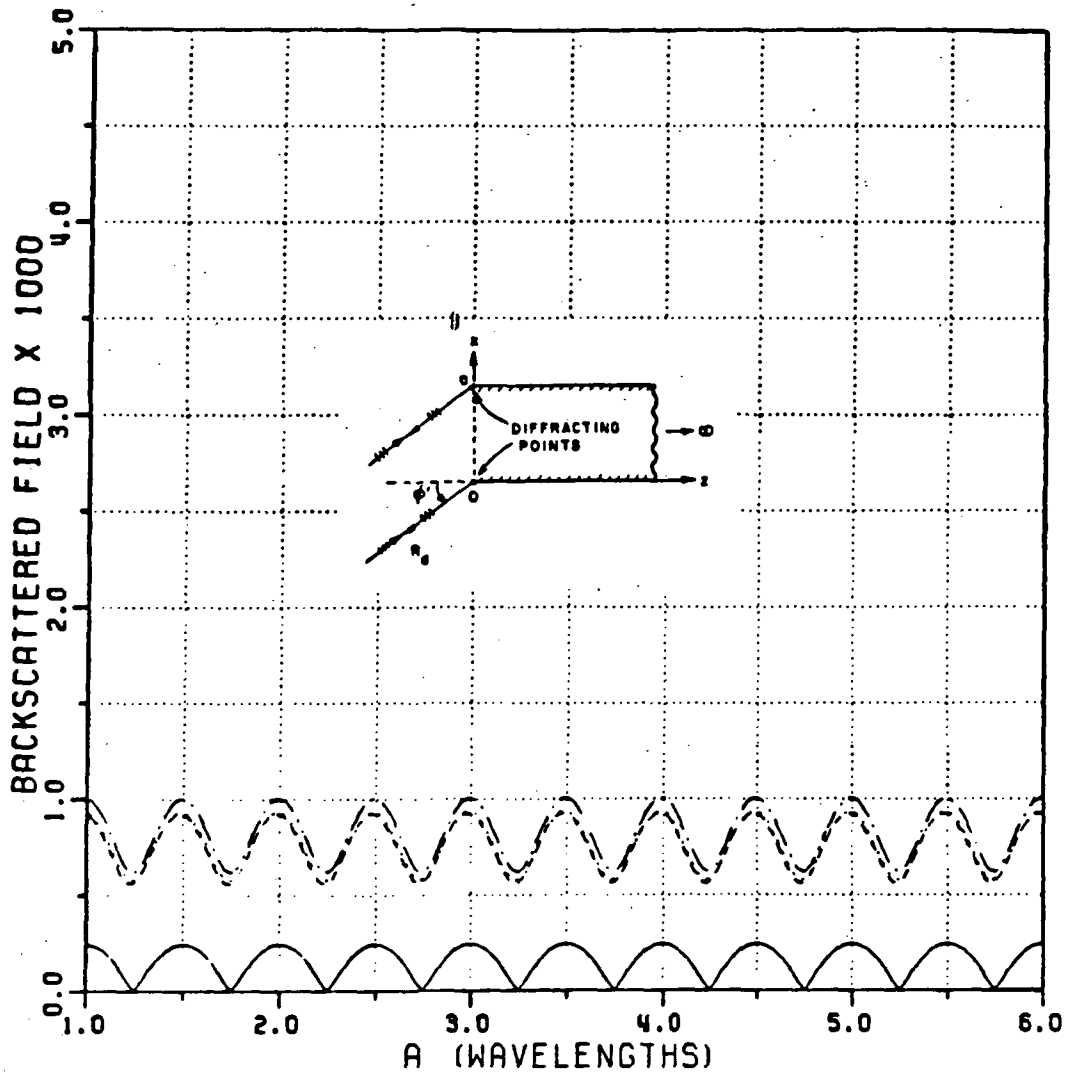

Figure 71: Plane wave backscattering by a semi-infinite parallel plate waveguide with an impedance boundary condition on its inner walls as a function of the waveguide width for the perpendicular polarization case.

in which $\hat{\mathbf{n}} = -\hat{\mathbf{z}}$ is the unit normal outward to the chosen surface (which encloses the waveguide configuration). Here, $\mathbf{E}_{cr}$ and $\mathbf{H}_{cr}$ are the electric and magnetic fields radiated by the open-ended waveguide cavity. As seen from Figure 73(a), the above $\mathbf{J}_s$ and $\mathbf{M}_s$ at $z = 0^-$ radiate null fields for $z > 0$ and they generate $\mathbf{E}_{cr}$ and $\mathbf{H}_{cr}$ for $z < 0$. A different form of the equivalence theorem shows that only $\mathbf{M}_s$ over the perfect electric conductor at $z = 0$ as in Figure 73(a) generates the same fields for $z < 0$ as the problem in Figure 73(a). It is noted that in Figures 73(a) and 73(b), the sources in the equivalent problem radiate with the original waveguide geometry removed. The fields $\mathbf{E}_{cr}$ and $\mathbf{H}_{cr}$ are themselves unknown and are quantities to be determined. Consequently, $\mathbf{J}_s$ and $\mathbf{M}_s$ as defined above in Equations (3.23) and (3.24) are also unknown at this point. However, one can introduce a Kirchhoff approximation for determining $\mathbf{J}_s$ and $\mathbf{M}_s$ in Figure 73(a), or for $\mathbf{M}_s$ in Figure 73(b). Knowing the values for the equivalent sources $\mathbf{J}_s$ and $\mathbf{M}_s$ based on the Kirchhoff approximation then allows one to find $\mathbf{E}_{cr}$ and $\mathbf{H}_{cr}$ approximately. In the Kirchhoff approximation, $\mathbf{J}_s$ and $\mathbf{M}_s$ in the present case are given by only those fields in the waveguide aperture (at $z = 0$) which arrive there after undergoing a reflection from the interior waveguide termination; additional wave interactions between the open end and the interior termination are expected to contribute weakly to the cavity radiation because the interior waveguide wall is lossy, and hence their effect is ignored. It is convenient to deal with only $\mathbf{M}_s$ as in the equivalent problem of Figure 73(b); thus, a Kirchhoff approximation to the equivalent problem in Figure 73(b) is shown in Figure 74(a), wherein $\mathbf{M}_s$ is set equal to zero outside the physical extent of the original waveguide aperture at the open end. Then the configuration equivalent to that in Figure 74(a) which is given in Figure 74(b) with the ground plane at $z = 0$ removed, and with $2\,\mathbf{M}_s$ over $0 < x < a$ at $z = 0^-$, serves as the starting point for calculating the cavity

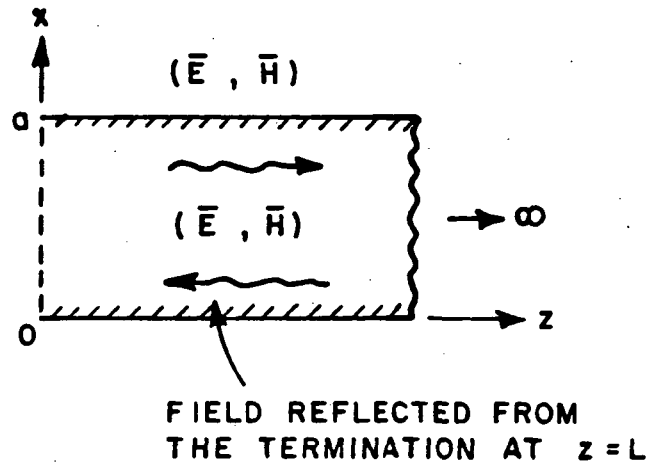

Figure 72: Radiation of the field reflected from the interior termination.

radiation field. The final equivalent configuration in Figure 74(b) may be viewed as the physical optics (PO) approximation (using magnetic currents) to the exact equivalent configuration in Figures 73(a) or 73(b). It is noted that

$$2\,\mathbf{M}_s = 2\,\mathbf{E}_a \times \hat{\mathbf{n}} \tag{3.25}$$

where $\mathbf{E}_a$ is the Kirchhoff approximation for the electric field in the aperture. For the sake of convenience, a further approximation is introduced in $\mathbf{E}_a$ such that only the geometrical optics fields which enter into the waveguide from the open end and then undergo reflection at the termination within the waveguide to return back at the open end are used to describe $\mathbf{E}_a$; i.e. the effect of edge diffracted rays which are coupled into the waveguide and then reflected by the termination are ignored. Next, an appropriate radiation integral is employed to calculate the fields radiated in the forward half space ($z < 0$) by the above magnetic current $2\,\mathbf{M}_s$.

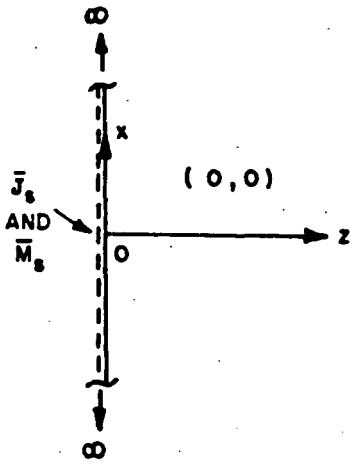

(a) Equivalent problem in which $\mathbf{J}_s$ and $\mathbf{M}_s$ reside at $z = 0^-$ over the entire domain $-\infty < x < \infty$.

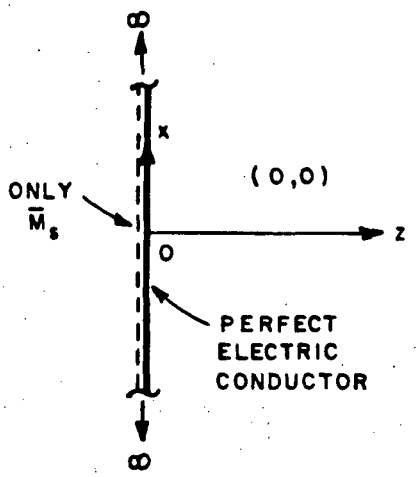

(b) A problem equivalent to that in (a). A perfect electric conductor is placed at $z = 0$; this shorts out $\mathbf{J}_s$ leaving only $\mathbf{M}_s$.

Figure 73: Equivalent configurations for calculating the cavity radiation field.

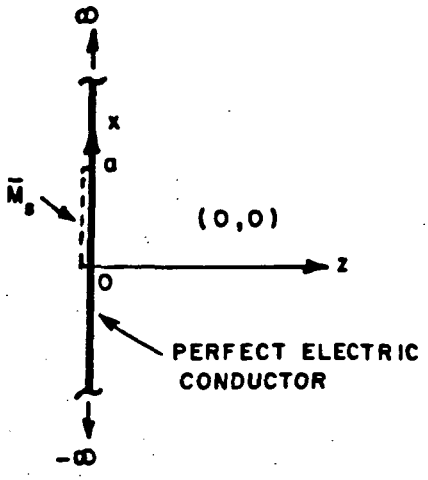

(a) Kirchhoff approximation to the problem in Figure 73(b). $\mathbf{M}_s$ is assumed to exist only over the physical extent of the aperture at the open end ($0 < x < a$).

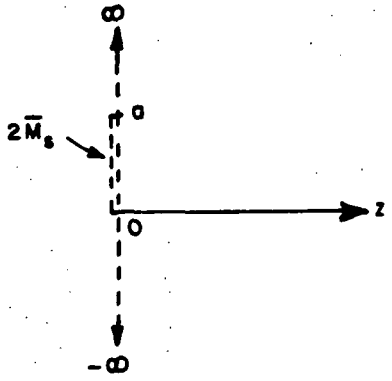

(b) A problem equivalent to that in (a). The perfect electric conductor at $z = 0$ is removed and its effect is accounted for by doubling the strength of $\mathbf{M}_s$. This is like the PO approximation using magnetic current.

Figure 74: Kirchhoff or physical optics approximated versions of the equivalent problem in Figure 73(b).

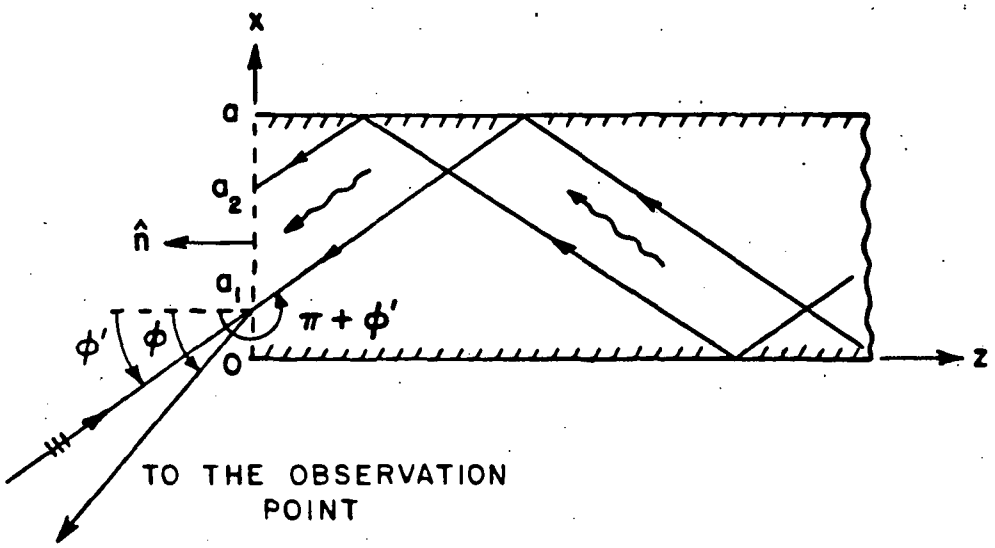

Figure 75: A ray tube reflected back from the termination.

The analysis of this radiation problem is described below; this analysis begins by giving an expression for $\mathbf{E}_a$.

Consider a ray tube which after being reflected from the termination occupies the portion $a_1 < x < a_2$ within the aperture in Figure 75. Also, the angle at which this ray tube arrives in the aperture plane is $\pi + \phi'$ as shown in the figure. The electric field at the aperture is then given by

$$\mathbf{E}_a = \begin{cases} \hat{\mathbf{y}}\, E_{ao}\, e^{-jk[(n+1)\, a \sin\phi' + 2L\cos\phi']} \cdot e^{jkx\sin\phi'} & ; \text{for odd } n \\ \hat{\mathbf{y}}\, E_{ao}\, e^{-jk[na\sin\phi' + 2L\cos\phi']} \cdot e^{-jkx\sin\phi'} & ; \text{for even } n \end{cases} \tag{3.26}$$

where

E_{ao} : electric field strength of the reflected ray tube in the aperture; this is a known quantity.

L : distance from the open end to the termination

a : waveguide height

n : number of reflections of a ray tube

The $2\,\mathbf{M}_s$ for odd values of n is given by

$$2\,\mathbf{M}_s = -2\,\hat{\mathbf{x}}\,E_a\,e^{-jk\left[\,(n+1)\,a\sin\phi'+2L\cos\phi'\,\right]}\;\cdot\;e^{jkx\sin\phi'} \tag{3.27}$$

The E_y^s radiated in the far zone exterior to the aperture by the $\mathbf{M}_s$ in Equation (3.27) is represented as [14]

$$\mathbf{E}^s = \sqrt{\frac{jk}{8\pi}}\,Z_o \int Y_o\,\hat{\mathbf{R}} \times 2\,\mathbf{M}_s\,\frac{e^{-jkR}}{\sqrt{R}}\,dl' \tag{3.28}$$

where Z_o (or Y_o) is free-space wave impedance (or admittance) and $\hat{\mathbf{R}}$ is a unit vector in radiation direction. Then the above equation reduces to

$$E_y^s = \sqrt{\frac{jk}{8\pi}}\int_{a_1}^{a_2}\hat{\mathbf{y}}\cdot(\hat{\mathbf{x}}\times\hat{\mathbf{R}})\,2M_s\,\frac{e^{-jkR}}{\sqrt{R}}\,dx' \tag{3.29}$$

where

$$R = R_0 - x'\sin\phi \tag{3.30}$$

$$\hat{\mathbf{R}} = -\hat{\mathbf{x}}\sin\phi - \hat{\mathbf{z}}\cos\phi \tag{3.31}$$

Also, ϕ is an observation angle and R_0 is the distance from the origin to the observation point. Hence, Equation (3.29) reduces to

$$\begin{aligned} E_y^s &= \sqrt{\frac{jk}{2\pi}}\,E_{ao}\,e^{-jk\left[(n+1)\,a\sin\phi'+2L\cos\phi'\right]}\,\cos\phi\,\frac{e^{-jkR_0}}{\sqrt{R_0}} \\ &\quad\cdot\int_{a_1}^{a_2} e^{jkx'\left(\sin\phi+\sin\phi'\right)}\,dx' \\ &= \sqrt{\frac{jk}{2\pi}}\,E_{ao}\,e^{-jk\left[(n+1)\,a\sin\phi'+2L\cos\phi'\right]}\,\cos\phi\,\frac{e^{-jkR_0}}{\sqrt{R_0}} \\ &\quad\cdot 2d_1\,\frac{\sin x_1^o}{x_1^o}\,e^{jkx_2^o} \end{aligned} \tag{3.32}$$

where

$$x_1^o = kd_1\,(\sin\phi + \sin\phi') \tag{3.33}$$

$$x_2^o = kd_2\,(\sin\phi + \sin\phi') \tag{3.34}$$

$$d_1 = \frac{a_2 - a_1}{2} \tag{3.35}$$

$$d_2 = \frac{a_2 + a_1}{2} \tag{3.36}$$

Similarly, the radiated field E_y^s for even values of n is expressed as

$$\begin{aligned} E_y^s &= \sqrt{\frac{jk}{2\pi}}\, E_{ao}\, e^{-jk[na\sin\phi' + 2L\cos\phi']}\, \cos\phi\, \frac{e^{-jkR_0}}{\sqrt{R_0}} \\ &\quad \cdot \int_{a_1}^{a_2} e^{jkx'(\sin\phi - \sin\phi')}\, dx' \\ &= \sqrt{\frac{jk}{2\pi}}\, E_{ao}\, e^{-jk[n\,a\sin\phi' + 2L\cos\phi']}\, \cos\phi\, \frac{e^{-jkR_0}}{\sqrt{R_0}} \\ &\quad \cdot 2d_1\, \frac{\sin x_1^e}{x_1^e}\, e^{jkx_2^e} \end{aligned} \tag{3.37}$$

where

$$x_1^e = kd_1\,(\sin\phi - \sin\phi') \tag{3.38}$$

$$x_2^e = kd_2\,(\sin\phi - \sin\phi') \tag{3.39}$$

Note that the limits a_1 and a_2 in the integral of Equation (3.29) can be determined analytically and they are functions of the incident angle ϕ', the waveguide width a and the location of the termination at $z = L$. It is also noted that there are always *two* ray tube components to be considered over the aperture with different number of reflections and arrival angle; one has n reflections with its arrival angle at $\pi + \phi'$ in the aperture and the other has $n + 1$ reflections with an arrival angle of $\pi - \phi'$ (see Figure 75). The total radiated field can then be obtained by

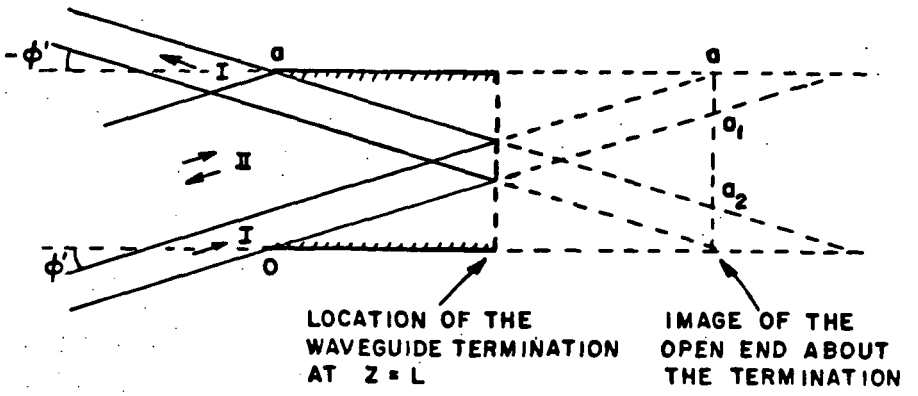

Figure 76: Rays incident on the open end of the semi-infinite parallel plate waveguide with an incident angle ϕ' and a simple planar termination at $z = L$.

superimposing the field radiated by each component. It is further noted that had the effect of the edge diffracted rays which are coupled into the waveguide and then reflected from the termination been included in the Kirchhoff approximation for $\mathbf{E}_a$, the limits of integration would have been over the whole aperture $0 < x < a$ rather than $a_1 < x < a_2$. As an example, consider the rays incident on the open end of the semi-infinite waveguide with an incident angle ϕ' and the planar termination at $z = L$ as shown in Figure 76. The rays in region I are reflected by the termination and propagate outward from the waveguide with the angle $-\phi'$. On the other hand, the rays in region II hit the top wall and the termination and are scattered backward with the angle $+\phi'$ as shown in the figure.

The EM plane wave scattering by a semi-infinite parallel plate waveguide with an impedance boundary condition on its inner walls and with an interior termination is plotted as a function of the aspect angle ϕ in Figures 77–82 for various impedance values and different polarizations. Each scattering pattern has two peaks at $\phi = +15°$ and $\phi = -15°$ directions as expected because the incident angle is defined by $\phi' = 15°$. The level of the two peaks are slightly different from each other because the width of each ray tube on the aperture is different and one ray tube has one more reflection than the other inside the waveguide as mentioned earlier. It is recalled that the planar interior termination is chosen to satisfy the same boundary conditions as those on the inner walls for convenience. Note that the pattern for the lossless case or vanishing surface impedance in Figure 77 is dominated by the interior radiation. However, as the real part of the impedance becomes larger, the interior radiation becomes weaker and the fields diffracted from the waveguide edges at the open end mainly contribute to the total scattered fields. In Figures 83–88, the plane wave scattering patterns are again plotted for a semi-infinite perfectly-conducting waveguide in which the inner waveguide walls and the planar perfectly-conducting interior termination are coated with the same dielectric/ferrite material. As shown in the figures, the interior radiation can be reduced by properly choosing the permittivity and permeability of the dielectric/ferrite coating; notice that the rim diffraction is not significantly affected by the changes in the parameters of the coating in these cases.

In order to check the accuracy of the scattering patterns shown in Figures 77–88, they are compared with those obtained by the use of a hybrid combination of a modal and high frequency techniques together with the *multiple scattering method* (MSM) [17,18,19]. Basically, the analysis in [17,18,19] combines asymptotic high frequency techniques such as the GTD ray method, the *equivalent current method*

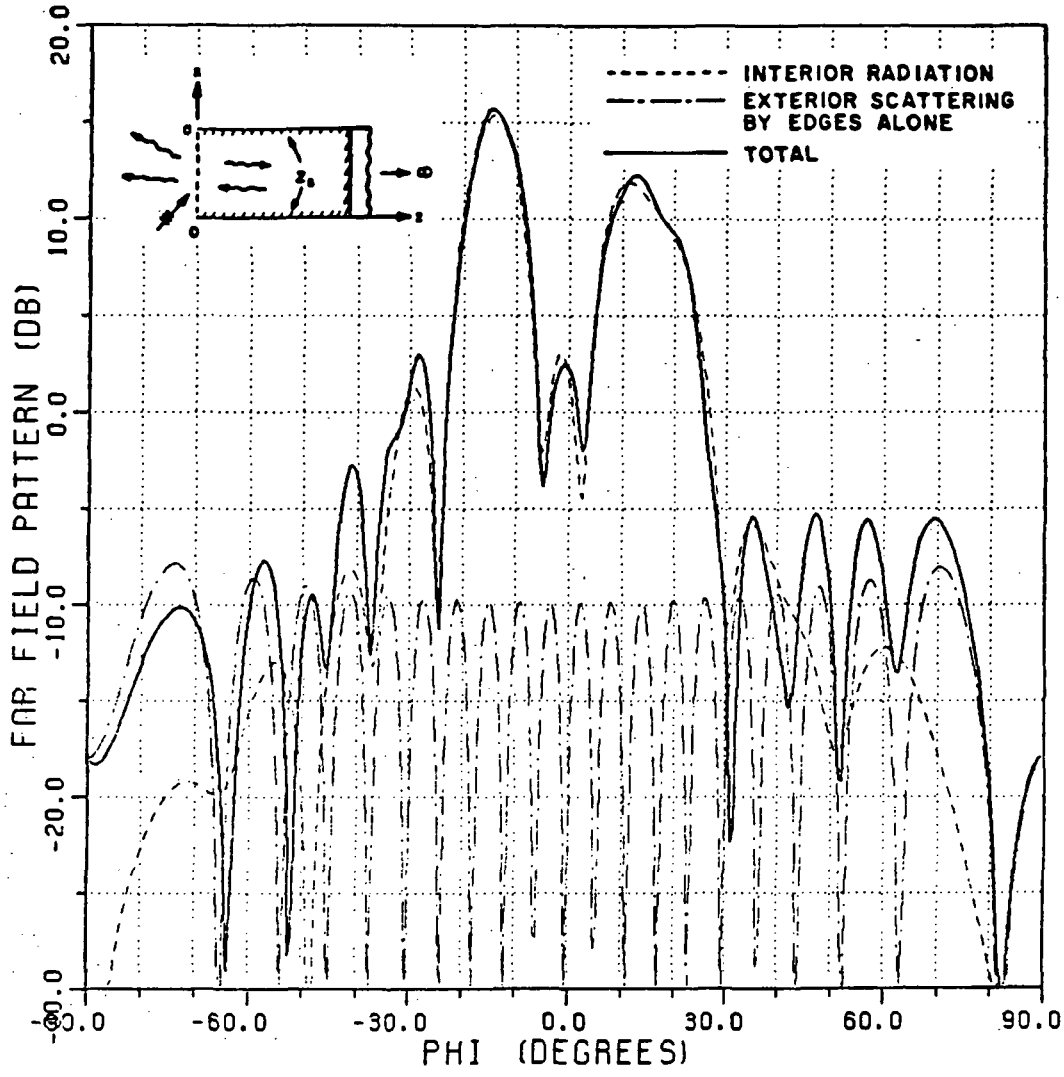

Figure 77: EM plane wave scattering by a semi-infinite parallel plate waveguide with inner impedance walls and with an interior termination as a function of aspect angle ϕ for the parallel polarization case.

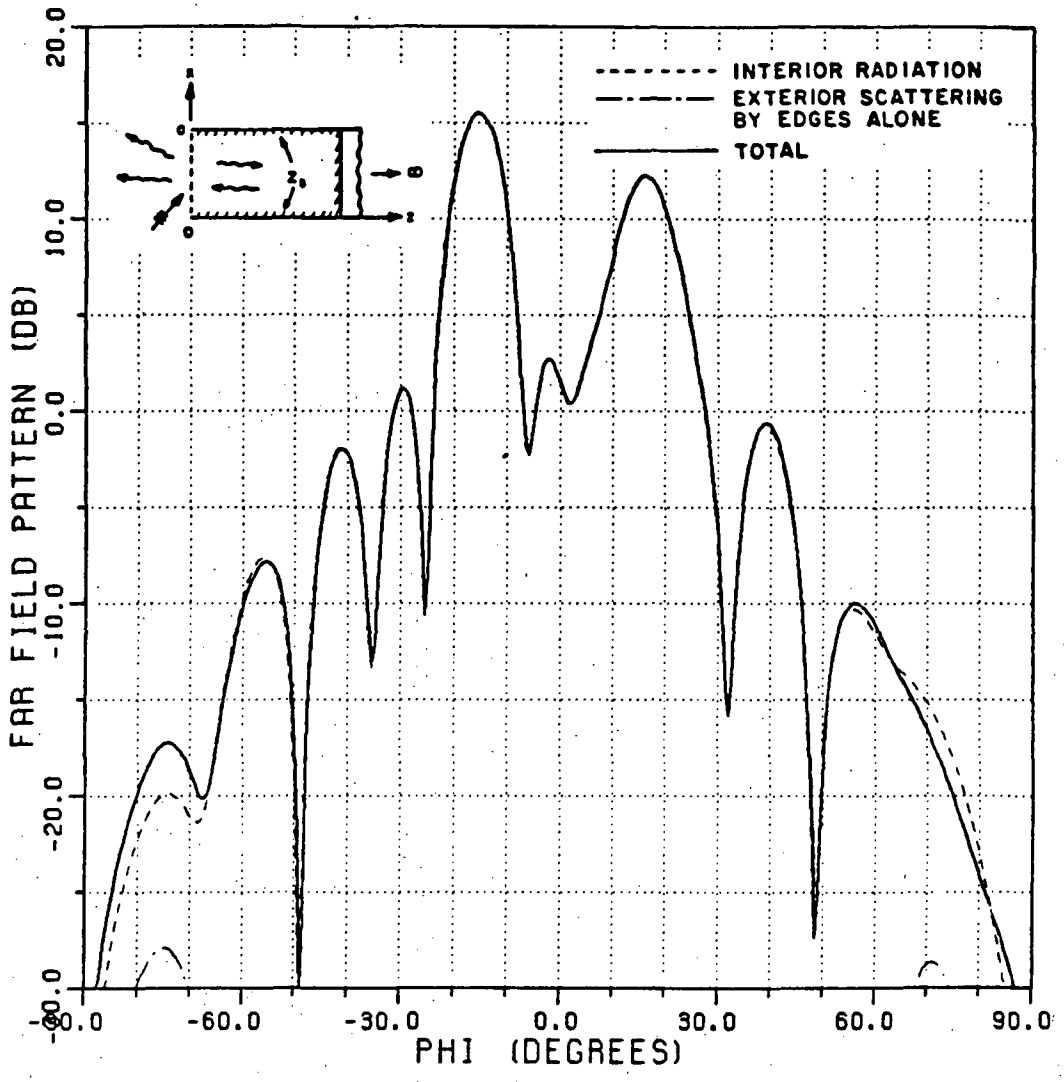

Figure 78: EM plane wave scattering by a semi-infinite parallel plate waveguide with inner impedance walls and with an interior termination as a function of aspect angle ϕ for the perpendicular polarization case.

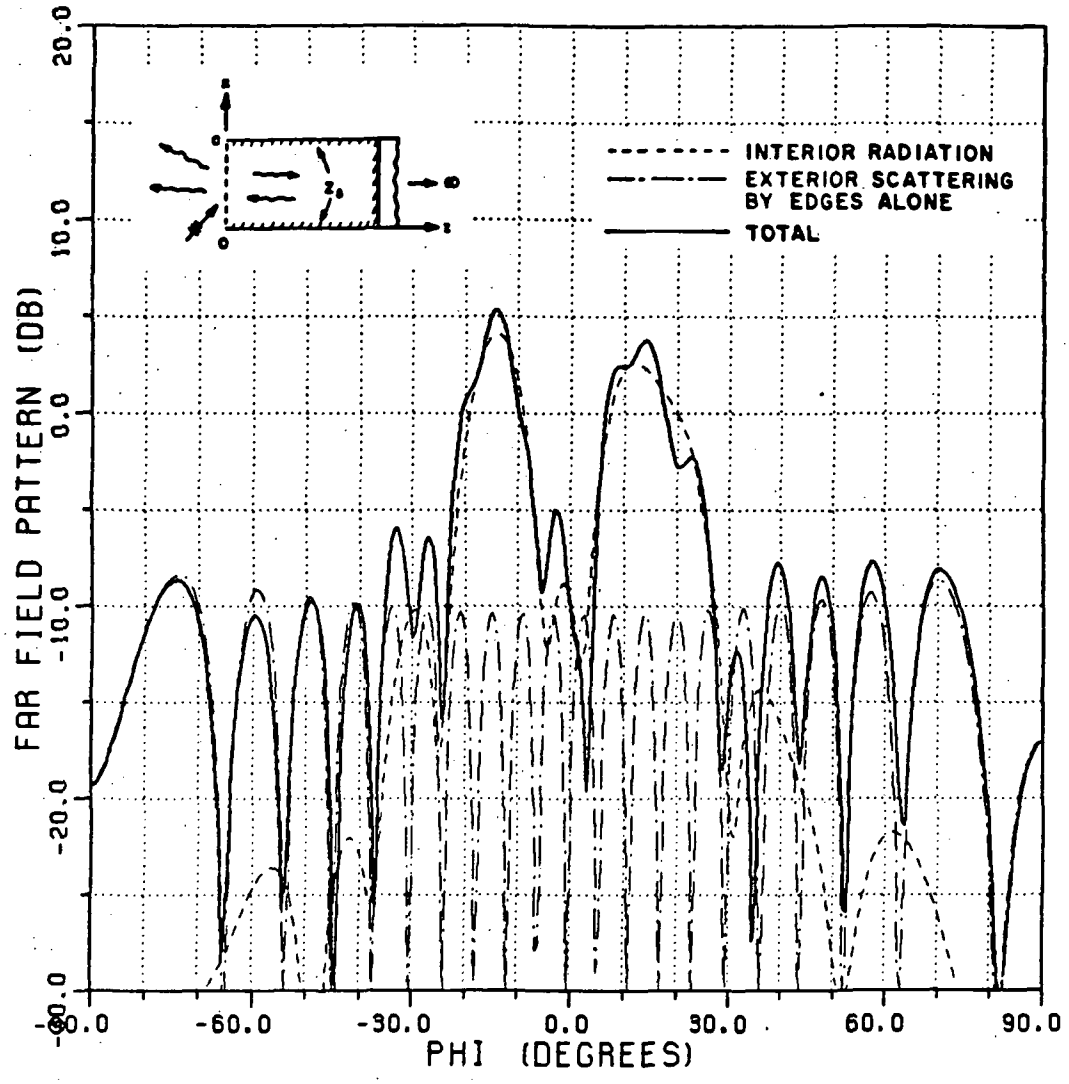

A = 10.0 (WAVELENGTHS) Φ' = 15.0 (DEGREES)
L = 30.0 (WAVELENGTHS) Z_S = (0.5, 0.5)

Figure 79: EM plane wave scattering by a semi-infinite parallel plate waveguide with inner impedance walls and with an interior termination as a function of aspect angle ϕ for the parallel polarization case.

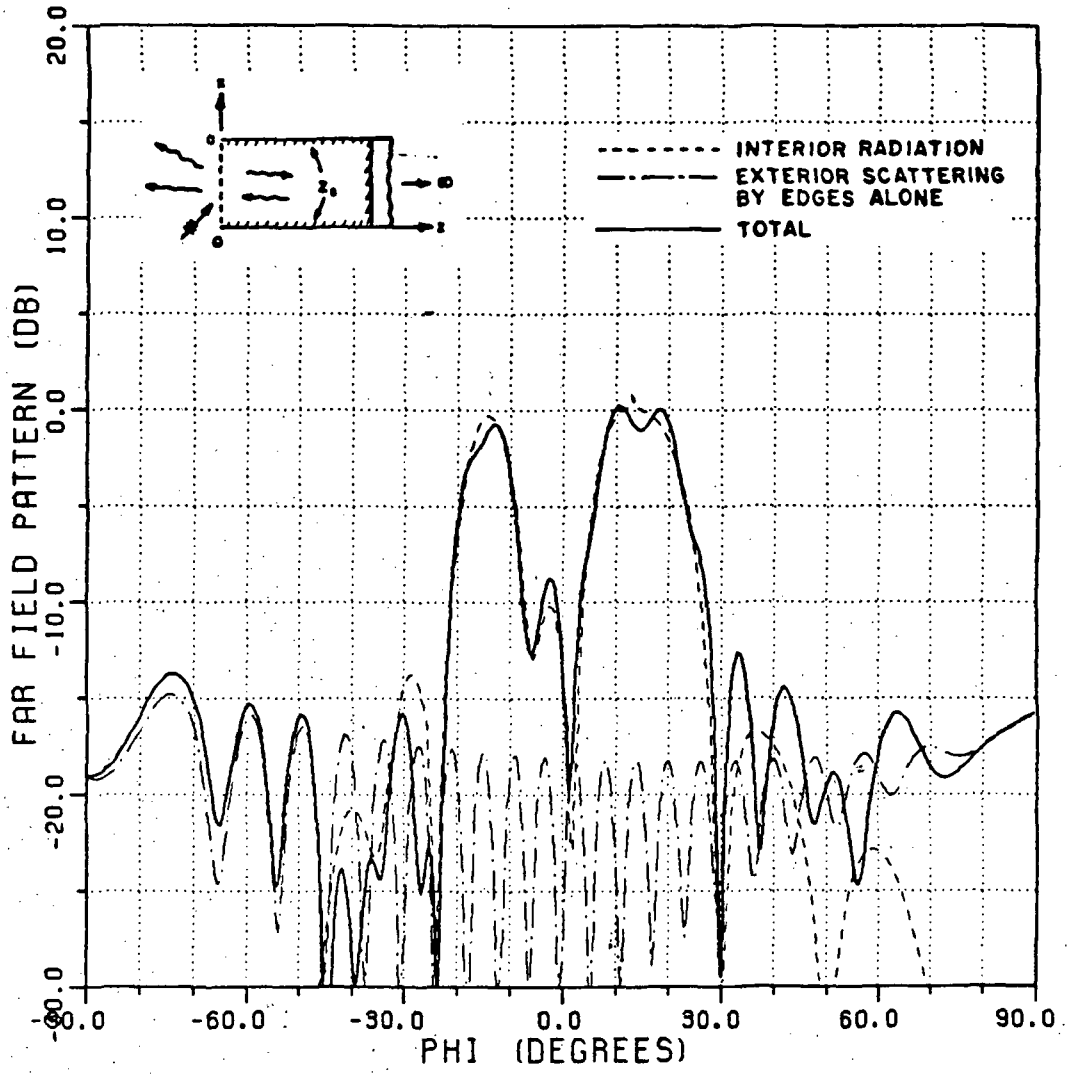

A = 10.0 (WAVELENGTHS) Φ' = 15.0 (DEGREES)
L = 30.0 (WAVELENGTHS) Z_S = (0.5, 0.5)

Figure 80: EM plane wave scattering by a semi-infinite parallel plate waveguide with inner impedance walls and with an interior termination as a function of aspect angle ϕ for the perpendicular polarization case.

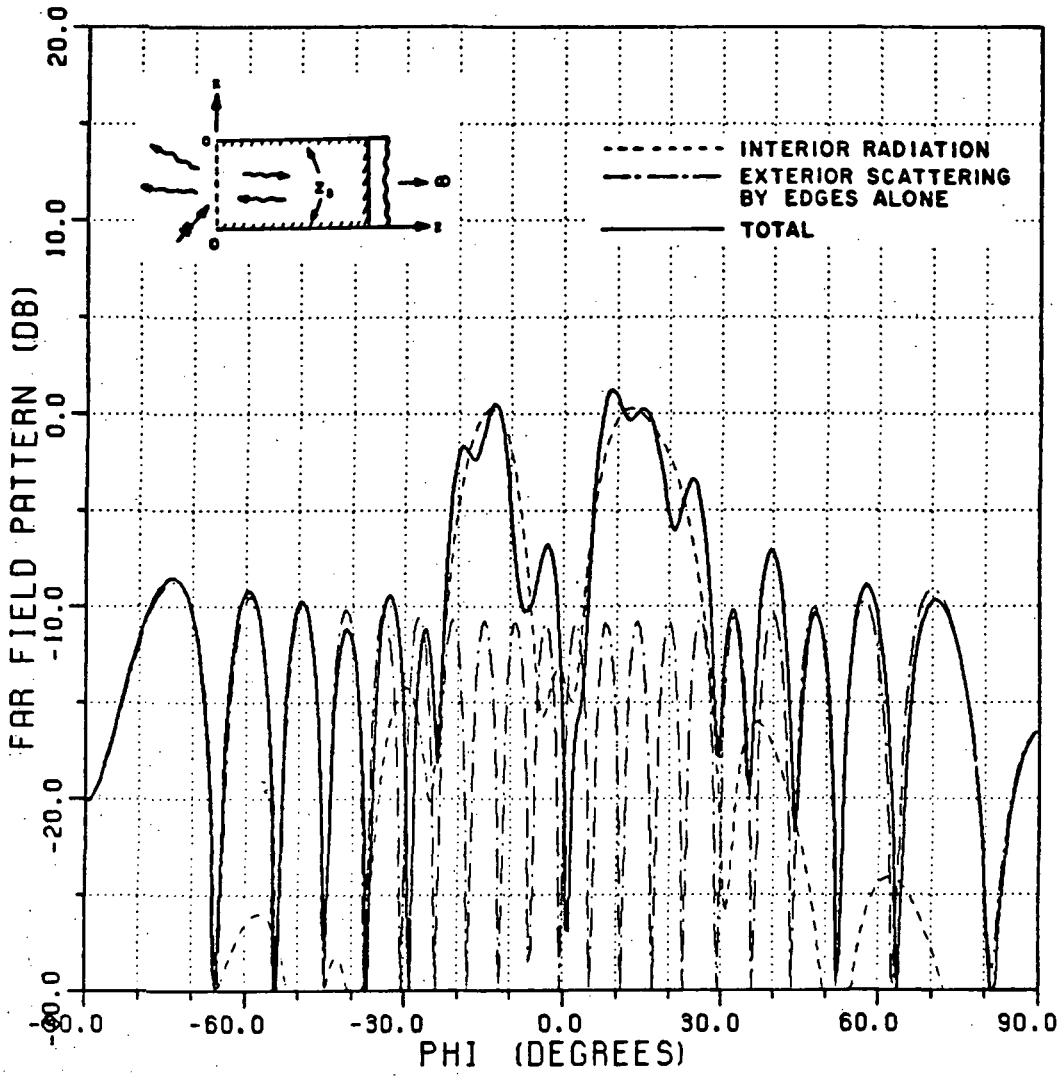

Figure 81: EM plane wave scattering by a semi-infinite parallel plate waveguide with inner impedance walls and with an interior termination as a function of aspect angle ϕ for the parallel polarization case.

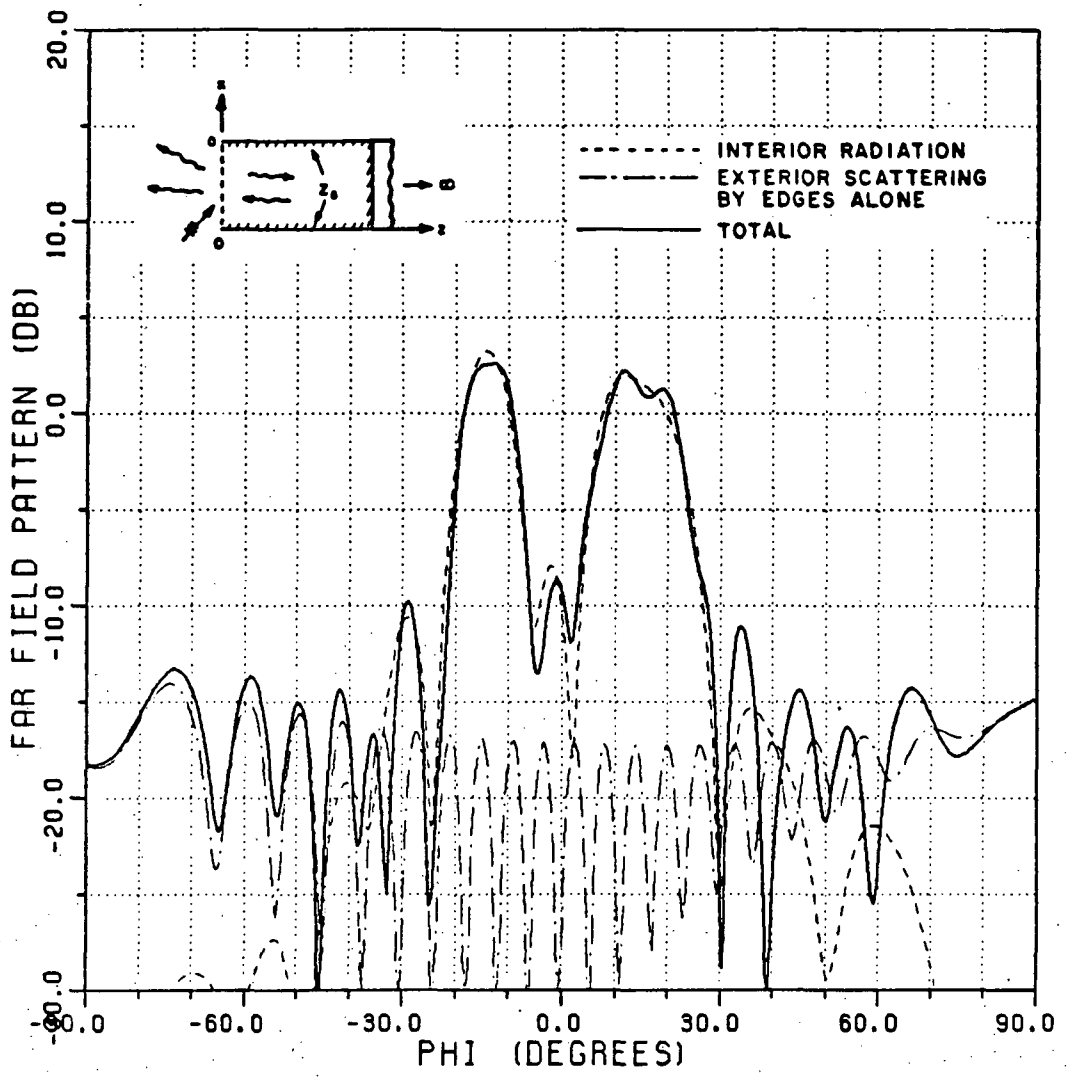

Figure 82: EM plane wave scattering by a semi-infinite parallel plate waveguide with inner impedance walls and with an interior termination as a function of aspect angle ϕ for the perpendicular polarization case.

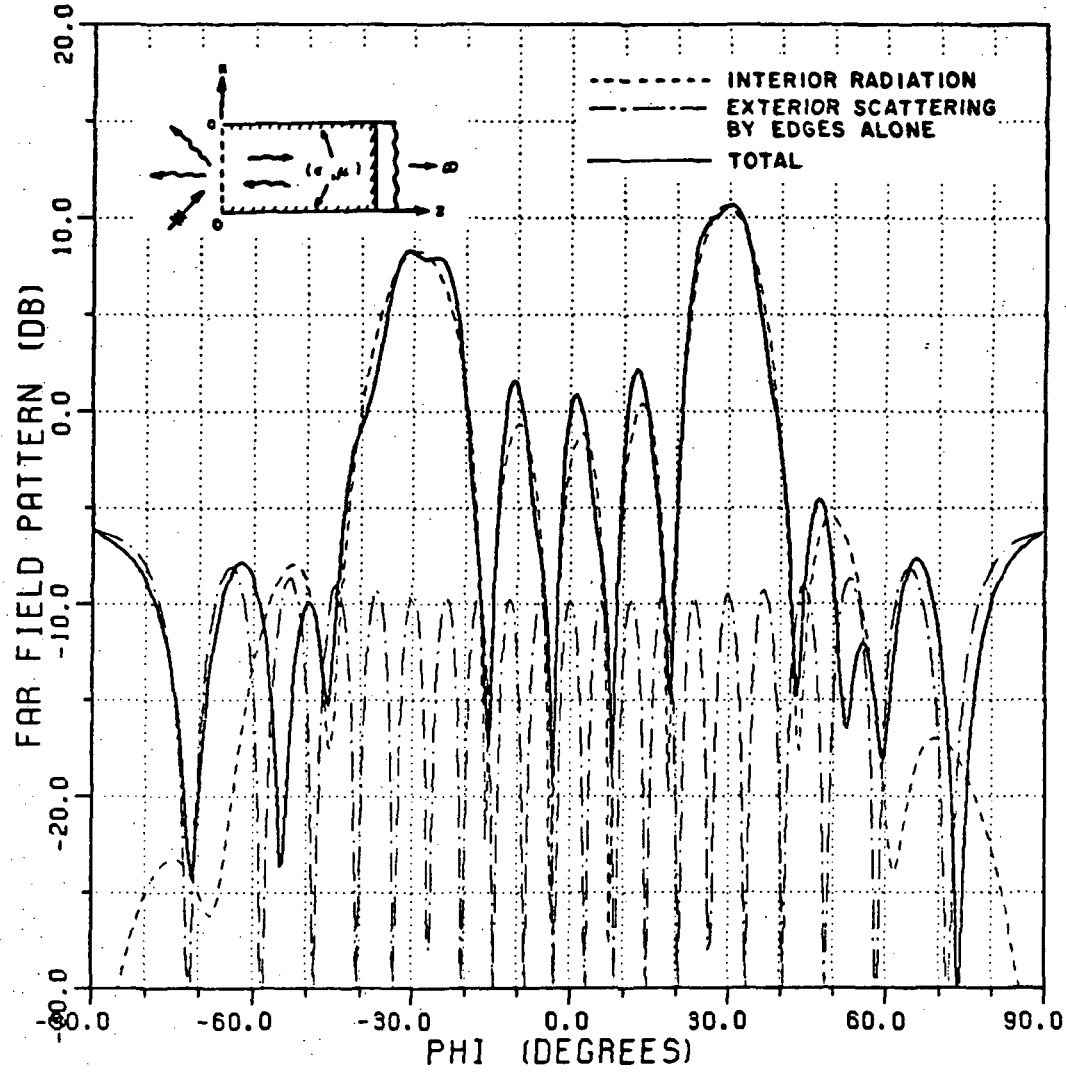

A = 10.0 (WAVELENGTHS) Φ' = 30.0 (DEGREES)
L = 30.0 (WAVELENGTHS) ε = (1.0, -0.10)
T = 0.05 (WAVELENGTHS) μ = (1.0, -0.10)

Figure 83: EM plane wave scattering by a semi-infinite parallel plate waveguide coated with a dielectric/ferrite material and with an interior termination as a function of aspect angle ϕ for the parallel polarization case.

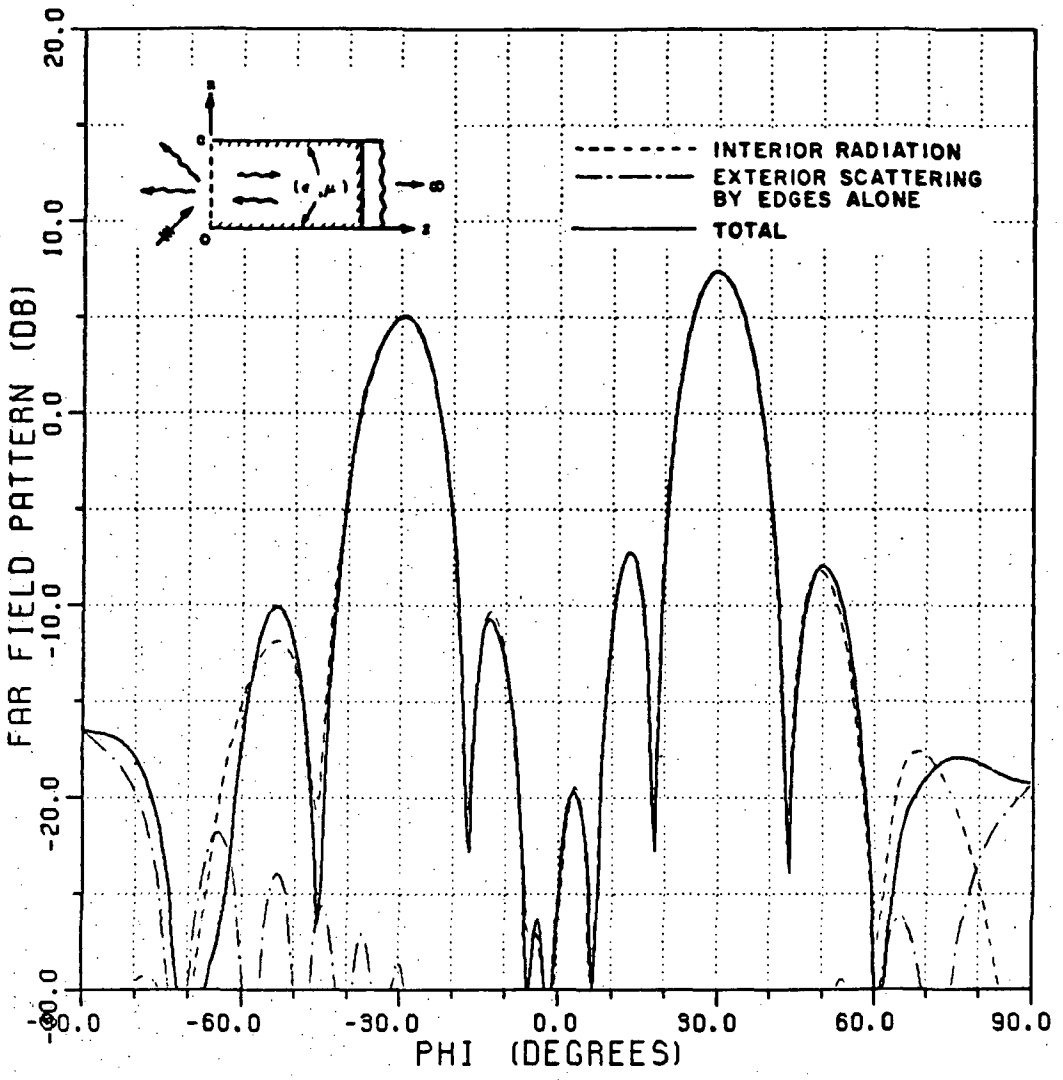

A = 10.0 (WAVELENGTHS)
L = 30.0 (WAVELENGTHS)
T = 0.05 (WAVELENGTHS)

Φ^i = 30.0 (DEGREES)
ϵ = (1.0, -0.10)
μ = (1.0, -0.10)

Figure 84: EM plane wave scattering by a semi-infinite parallel plate waveguide coated with a dielectric/ferrite material and with an interior termination as a function of aspect angle ϕ for the perpendicular polarization case.

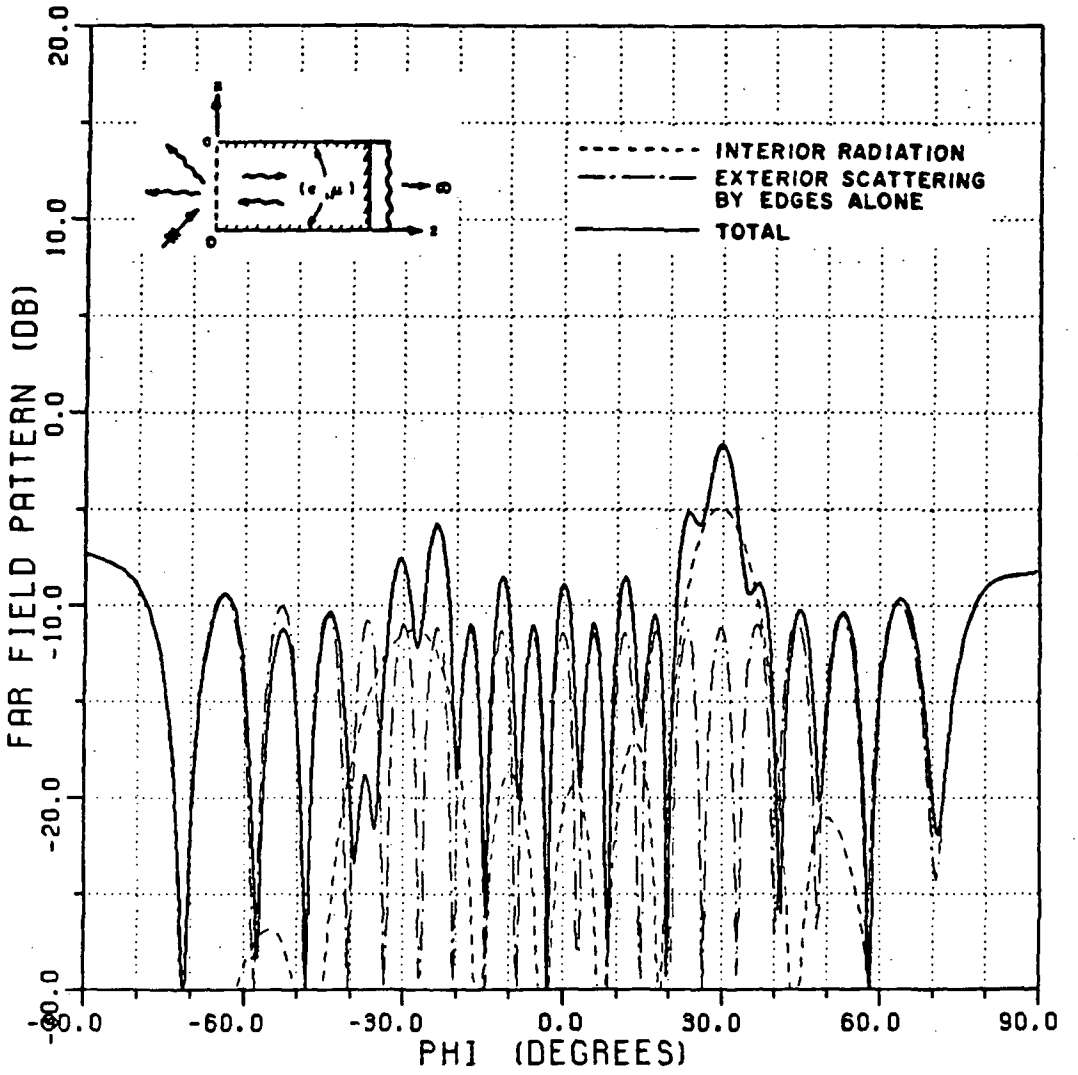

Figure 85: EM plane wave scattering by a semi-infinite parallel plate waveguide coated with a dielectric/ferrite material and with an interior termination as a function of aspect angle ϕ for the parallel polarization case.

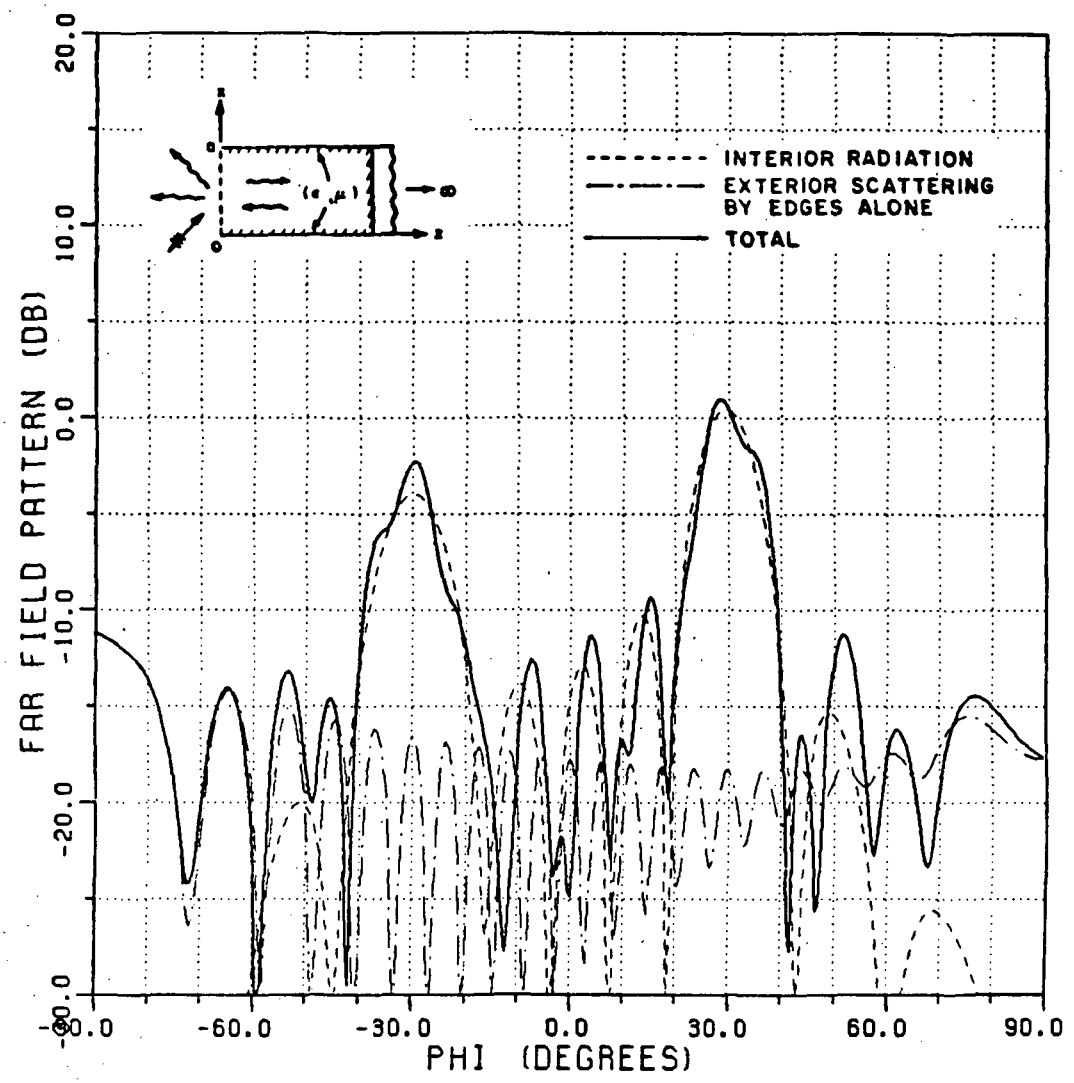

A = 10.0 (WAVELENGTHS)
L = 30.0 (WAVELENGTHS)
T = 0.05 (WAVELENGTHS)

Φ^i = 30.0 (DEGREES)
ϵ = (2.0, -0.20)
μ = (2.0, -0.20)

Figure 86: EM plane wave scattering by a semi-infinite parallel plate waveguide coated with a dielectric/ferrite material and with an interior termination as a function of aspect angle ϕ for the perpendicular polarization case.

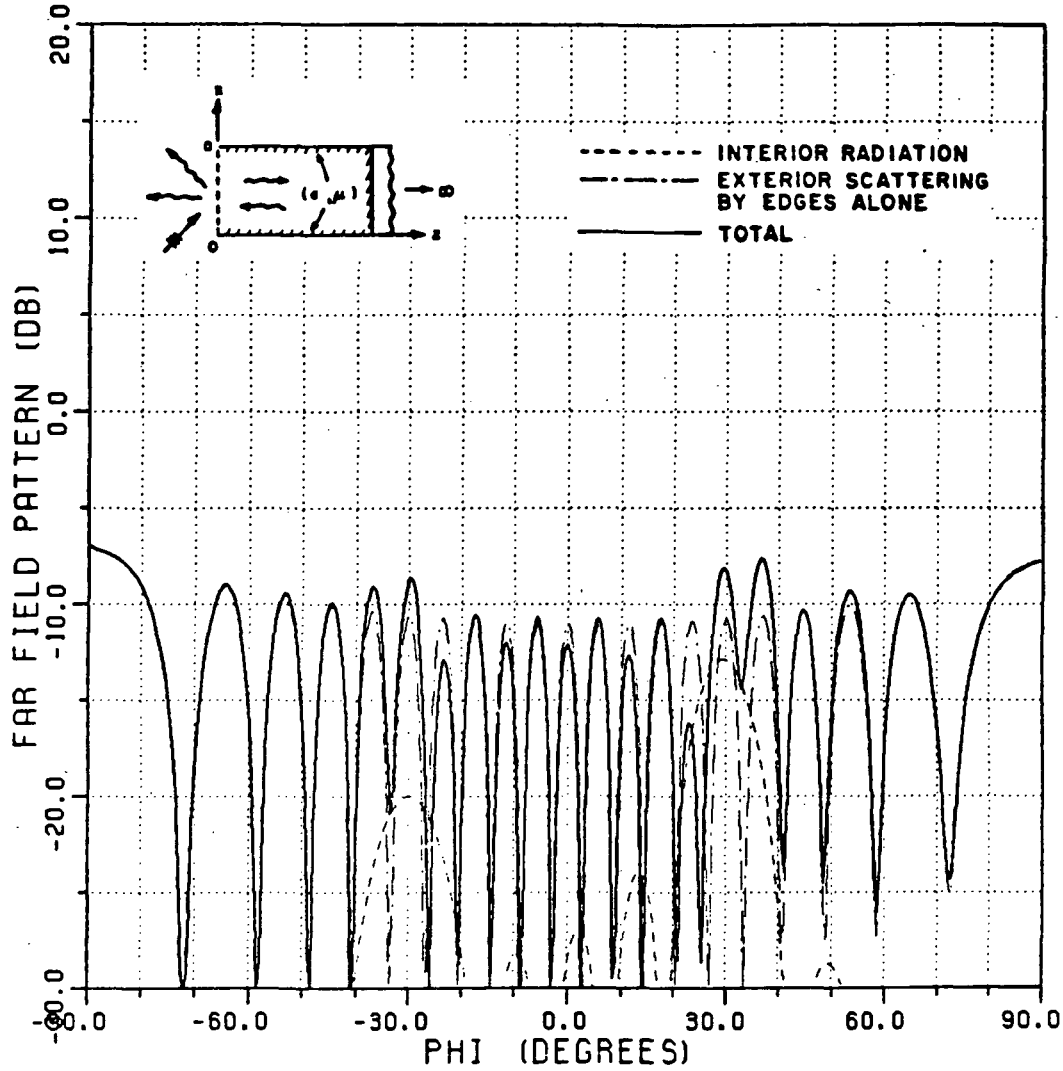

Figure 87: EM plane wave scattering by a semi-infinite parallel plate waveguide coated with a dielectric/ferrite material and with an interior termination as a function of aspect angle ϕ for the parallel polarization case.

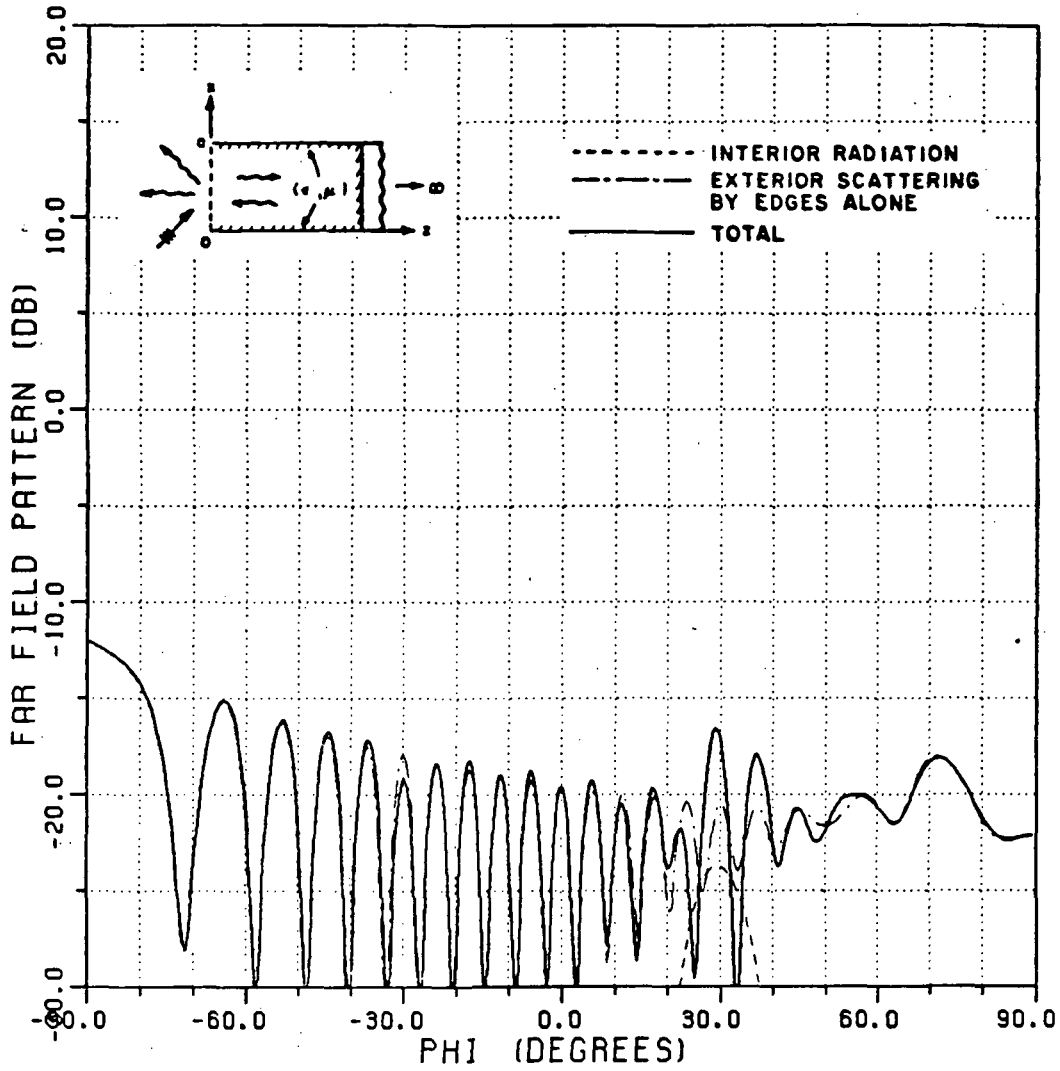

A = 10.0 (WAVELENGTHS) Φ'= 30.0 (DEGREES)
L = 30.0 (WAVELENGTHS) ε = (3.0, -0.30)
T = 0.05 (WAVELENGTHS) μ = (3.0, -0.30)

Figure 88: EM plane wave scattering by a semi-infinite parallel plate waveguide coated with a dielectric/ferrite material and with an interior termination as a function of aspect angle ϕ for the perpendicular polarization case.

(ECM), and the *physical theory of diffraction* (PTD), with the usual modal techniques to deal with only perfectly-conducting semi-infinite waveguide geometries with perfectly conducting interior terminations. In Figures 89–90, the two scattering patterns are compared for different values of the interior termination length L. As shown in Figure 89, the two solutions show good agreement in the main and the first sidelobe regions. The discrepancy in the other regions is due to the fact that the contribution from the diffracted rays to the interior radiation is *not* included in the Kirchhoff approximation for analytical simplicity in the present study as mentioned earlier. For the longer waveguide, the two solutions show some differences as indicated in Figure 90; this is because the effect of the edge diffracted rays which have been ignored contribute more significantly to the interior field in the waveguide with a larger L than those in the waveguide with a smaller L. For the waveguide with a larger L, there are more discontinuities in GO rays (see Figure 32) and the diffracted rays which compensate for these discontinuities give significant contribution to the field over the aperture. Therefore, a better agreement is anticipated if the diffracted rays are included for describing $\mathbf{E}_a$ in the present solution.

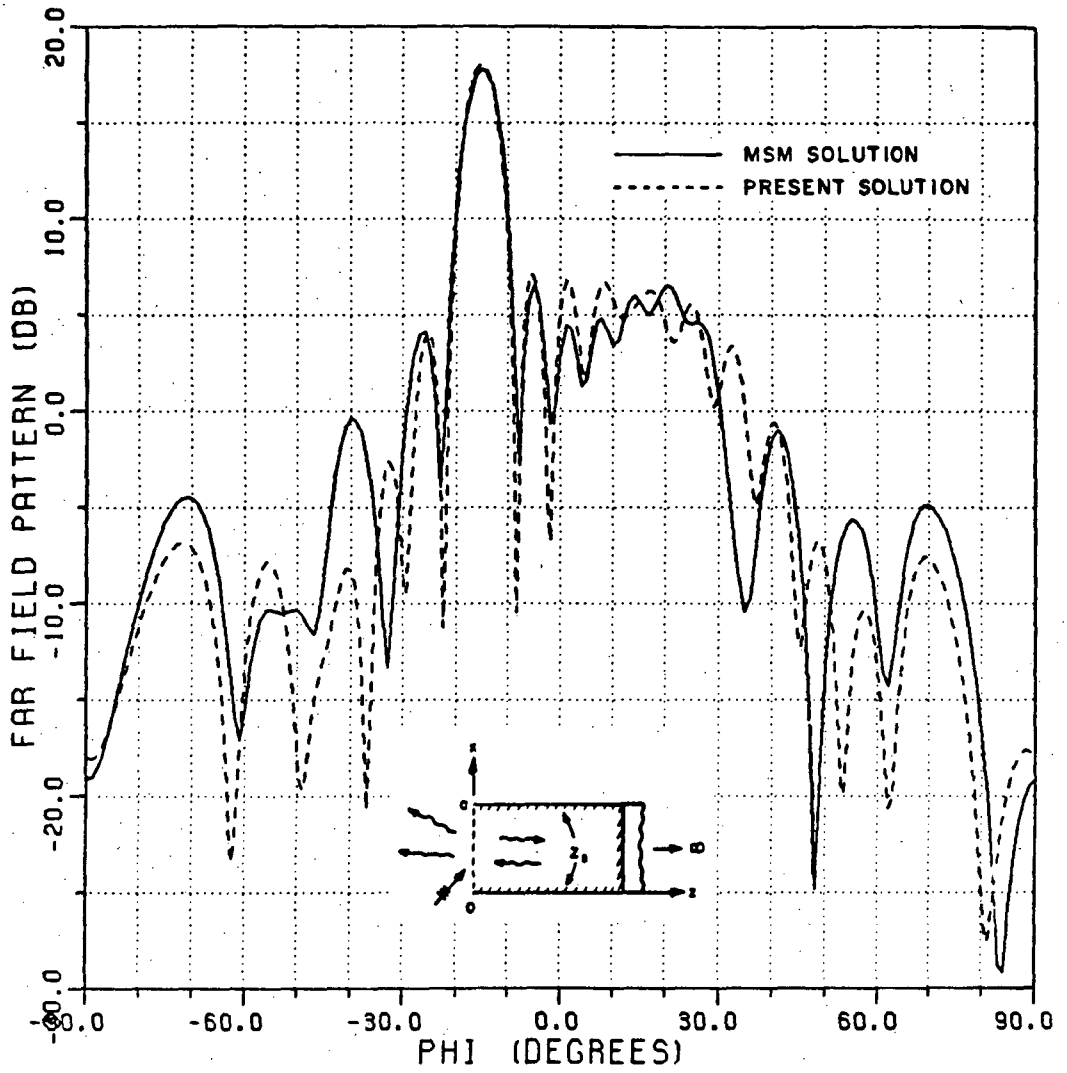

A = 10.0 (WAVELENGTHS) Φ' = 15.0 (DEGREES)

L = 3.0 (WAVELENGTHS) Z_S = (0.0, 0.0)

Figure 89: Comparison of the plane wave scattering patterns obtained by the present method and by the MSM for the parallel polarization case.

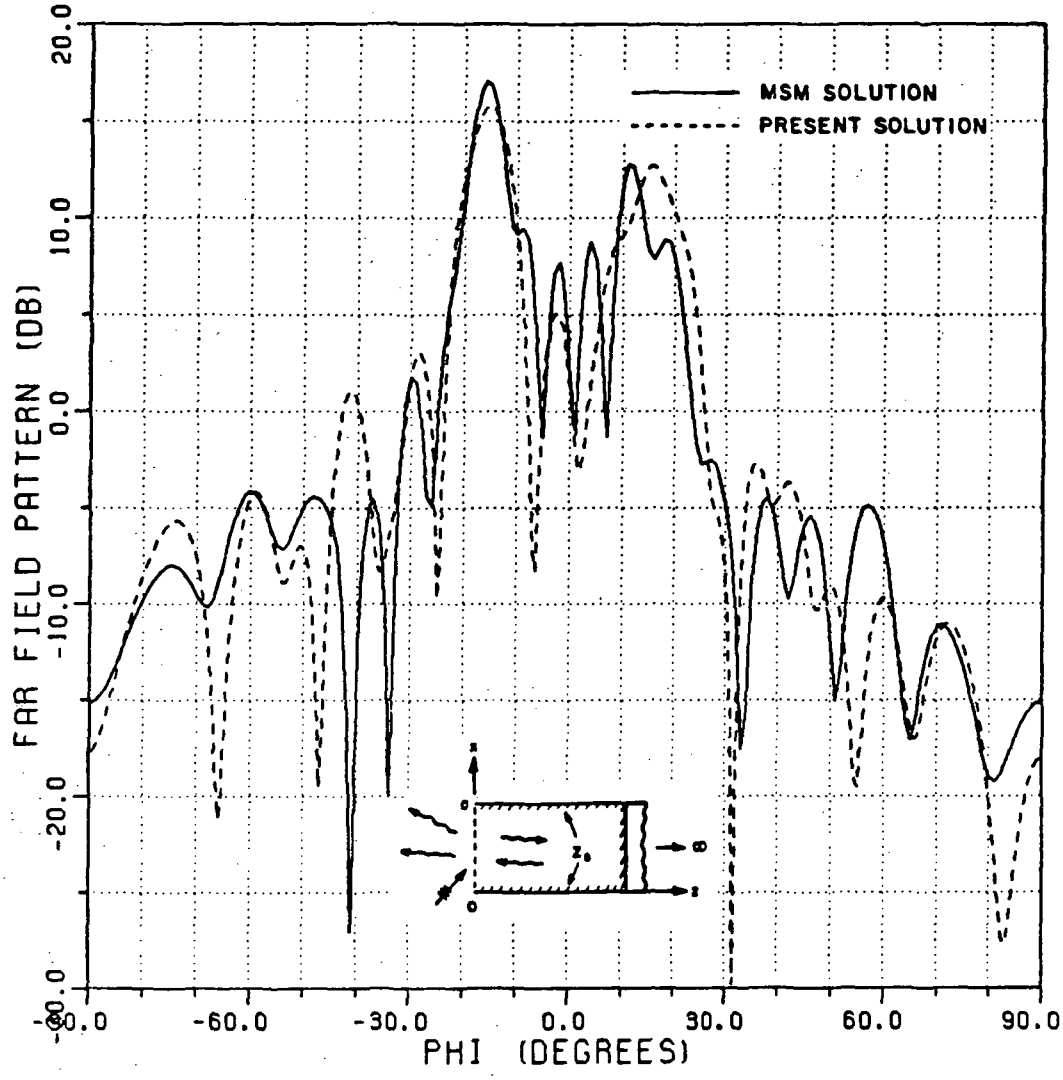

A = 10.0 (WAVELENGTHS) Φ' = 15.0 (DEGREES)
L = 30.0 (WAVELENGTHS) Z_S = (0.0, 0.0)

Figure 90: Comparison of the plane wave scattering patterns obtained by the present method and by the MSM for the parallel polarization case.

CHAPTER IV

ANALYSIS OF ELECTROMAGNETIC SCATTERING FROM A RECTANGULAR WAVEGUIDE WITH LOSSY INNER WALLS

4.1 Ray solution for the interior fields of a semi-infinite rectangular waveguide with lossy interior walls

In this chapter, the problem of electromagnetic scattering by an open-ended, perfectly-conducting rectangular waveguide with absorber coated inner walls and with an interior termination is analyzed. The geometry of this open-ended, semi-infinite rectangular waveguide structure without the termination is shown in Figure 91. The outer wall is perfectly-conducting and the inner wall is coated with a thin, uniform layer of absorbing (dielectric/ferrite) material. The height and width of the waveguide are a and b wavelengths, respectively. This open-ended, semi-infinite rectangular waveguide is illuminated by an arbitrarily polarized external plane wave field. A part of this field incident on the openend is scattered back into the exterior region and the rest is coupled into the interior waveguide region. These interior and exterior fields are analyzed using the uniform geometrical theory of diffraction (UTD) ray approach. The UTD field consists of the incident and reflected geometrical optics (GO) fields and the fields diffracted by the edges at the open end. The GO contribution to the fields coupled into the interior of the waveguide is discussed in the first part of this section. This discussion is followed by a description of the edge diffracted fields coupled into the waveguide in the second part of this section. The effect of including an interior termination is also discussed

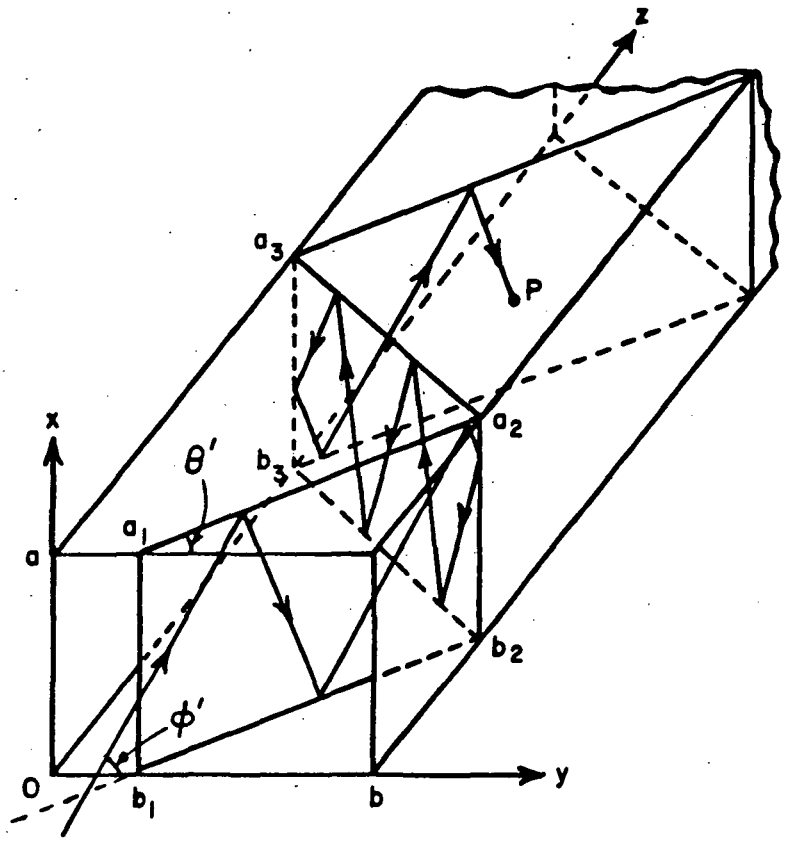

Figure 91: Geometry of an open-ended semi-infinite rectangular waveguide coated with a thin, uniform layer of lossy or absorbing material on its inner wall.

in the later sections of this chapter; in particular the field which is coupled inside the waveguide region and then undergoes reflection from the interior termination to radiate back into the exterior region is found using aperture integration (AI) in conjunction with a physical optics (PO) approximation for the aperture field as done previously for the 2-D case in Chapter III. The total scattered field is the sum of the field scattered from just the edges at the open end, and the field which is initially coupled into the waveguide and then reflected from the termination to radiate out into the exterior region of the waveguide.

4.1.1 Geometrical Optics (GO) fields

A plane wave incident on the open end sets up planes of incidence as shown in Figure 91 and the incident ray travels in these planes of incidence to reach the observation point P after reflecting off the top and side walls of the waveguide. The top and side views of this waveguide together with the ray path which reaches P and also the incident angles θ' and ϕ' are shown in Figure 92. The angle θ' is the angle between the y axis and the projection of the incident ray onto the top wall and ϕ' is the elevation angle from the $y-z$ plane to the incident ray. Note that the side view in Figure 92 is not the actual side view of the rectangular waveguide but an unfolded side view of the planes of incidence shown in Figure 91. Therefore, the ray path of the unfolded side view contains the actual length of the ray path to the field point. Note also that the angles ϕ' and θ' are defined differently from the conventional spherical coordinate angles. Then, the incident unit vector $\hat{\mathbf{I}}$ is given by

$$\hat{\mathbf{I}} = \hat{\mathbf{x}}\ \sin\phi' + \hat{\mathbf{y}}\ \cos\theta'\cos\phi' + \hat{\mathbf{z}}\ \sin\theta'\cos\phi' \tag{4.1}$$

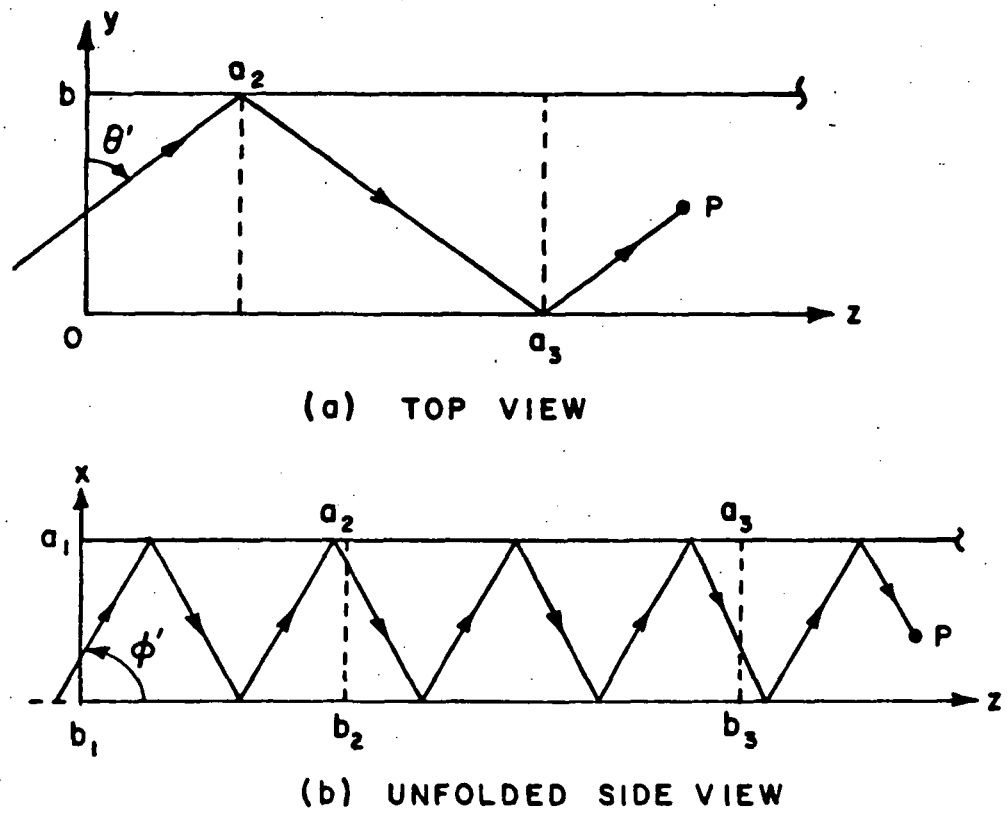

Figure 92: Top and unfolded side views of the ray path in Figure 91.

The path reaching the field point P in the top view of Figure 92 is a projection of the ray path onto the top wall of the waveguide. From these top and side views, one can easily determine the number of reflections which occur before the ray reaches the field point for a given incident angle; the top view accounts for the number of reflections by the side walls, while the side view indicates the number of reflections by the top and bottom walls. In the specific example shown in Figure 92, there are five and four reflections by the top and bottom walls, respectively, and one reflection by each side wall.

This rectangular waveguide problem can be analyzed easily in a fashion similar to that employed in the previous chapter for the 2–D semi-infinite parallel plate waveguide case. For a given observation point inside the waveguide, a possible set of different combination of rays such as direct, singly and multiply reflected rays by the side walls is determined by looking at the top view (as in Figure 92) and then using the analogy of Figure 32 given in the previous chapter. For each ray determined by the top view, this procedure is then repeated for ascertaining the set of rays which have different number of reflections from the top and side walls by looking at the side view of the rectangular waveguide as shown in Figure 92(b). Therefore, there is a maximum of four different rays reaching a given observation point inside the waveguide for a given incident angle; a maximum of two different rays which have different reflections by top and bottom walls and each ray has also a maximum of two different reflections by side walls (see Figure 32). As shown in Figure 93, each wall with its front edge is denoted by numbers '1' through '4' for convenience. It is also convenient to consider the incident GO, and the singly and mutiply reflected GO fields separately as done below.

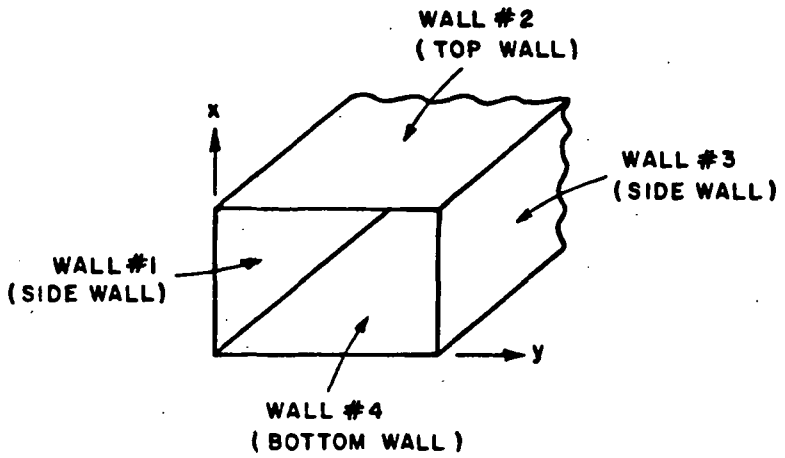

Figure 93: Rectangular waveguide showing the assignment of the wall numbers to the waveguide.

i) Incident GO field

For the three dimensional (3-D) case, it is necessary to express the fields in a reference coordinate system. The rectangular coordinate system is chosen as the reference coordinate in this study. The incident field at the observation point inside the waveguide is then computed in terms of the field incident at the origin and then by including the corresponding phase term in which the phase is referred to the origin O in Figure 91; i.e., the incident electric field $\mathbf{E}^i(P)$ at P is given by

$$\mathbf{E}^i(P) = \hat{\mathbf{x}}\, E_x^i(P) + \hat{\mathbf{y}}\, E_y^i(P) + \hat{\mathbf{z}}\, E_z^i(P) \tag{4.2}$$

where

$$\begin{bmatrix} E_x^i(P) \\ E_y^i(P) \\ E_z^i(P) \end{bmatrix} = \begin{bmatrix} E_x^i(O) \\ E_y^i(O) \\ E_z^i(O) \end{bmatrix} \cdot e^{-jks^i} \tag{4.3}$$

and s^i is the distance from the observation point to the plane which is perpendicular to the incident unit vector $\hat{\mathbf{I}}$ and which contains the origin (O); this s^i is given by

$$s^i = \sin\phi' \cdot x_p + \cos\theta' \cos\phi' \cdot y_p + \sin\theta' \cos\phi' \cdot z_p \tag{4.4}$$

where x_p, y_p and z_p are the coordinates of the observation point P. It is noted that the range of values for the axial distance z which pertains to the incident field must satisfy the following criteria; namely, that it must fall within the incident field region (Region (1) in Figure 32) in the both top and side views of Figure 92; if not, it is not an incident field, and it is then categorized as a singly reflected field. The singly and multiply reflected fields are treated next.

ii) Reflected GO fields

Each component of the reflected electric field $\mathbf{E}^r(P)$ at the field point P inside the waveguide can be represented by a matrix in terms of each component of the incident GO field at the origin as given below; namely,

$$\mathbf{E}^r(P) = \hat{\mathbf{x}}\, E_x^r(P) + \hat{\mathbf{y}}\, E_y^r(P) + \hat{\mathbf{z}}\, E_z^r(P) \tag{4.5}$$

where

$$\begin{bmatrix} E_x^r(P) \\ E_y^r(P) \\ E_z^r(P) \end{bmatrix} = \left[\tilde{R}\right] \begin{bmatrix} E_x^i(Q_R) \\ E_y^i(Q_R) \\ E_z^i(Q_R) \end{bmatrix} \cdot e^{-jks^r} \tag{4.6}$$

in which Q_R is the point of reflection and s^r is the distance from Q_R to P along the reflected ray, and $\tilde{R}$ is the reflection coefficient (involving $\tilde{R}_{\parallel}$ and $\tilde{R}_{\perp}$ as in

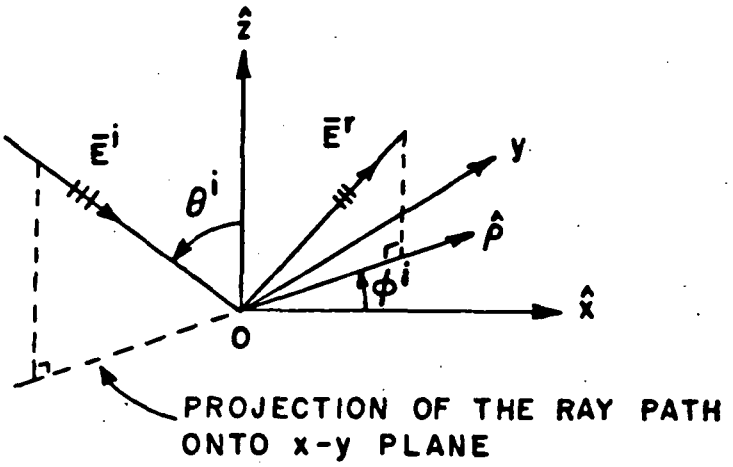

Figure 94: An electric field $\mathbf{E}^i$ incident on $x-y$ plane with incident angles θ' and ϕ'.

Appendices D and F for the impedance boundary condition and the absorber coated perfectly-conducting surfaces, respectively).

Let the field $\mathbf{E}^i$ be incident on the $x-y$ plane with incident angle θ^i as shown in Figure 94. Then $\mathbf{E}^i$ is expressed by

$$\mathbf{E}^i = \mathbf{E}^i_o \, e^{jk(\sin\theta^i \cos\phi^i \, x + \sin\theta^i \sin\phi^i \, y + \cos\theta^i \, z)} \tag{4.7}$$

where

$$\mathbf{E}^i_o = \hat{\mathbf{x}} \, E^i_{ox} + \hat{\mathbf{y}} \, E^i_{oy} + \hat{\mathbf{z}} \, E^i_{oz} \tag{4.8}$$

As shown in Figure 95, $\mathbf{E}^i_o$ can be expressed in the plane of incidence as

$$\mathbf{E}^i_o = \hat{\rho} \, E^i_\rho + \hat{\phi} \, E^i_\phi + \hat{\mathbf{z}} \, E^i_z \tag{4.9}$$

where

$$\hat{\rho} \;=\; \hat{\mathbf{x}} \cos\phi^i + \hat{\mathbf{y}} \sin\phi^i \tag{4.10}$$

$$\hat{\phi} = -\hat{\mathbf{x}} \sin\phi^i + \hat{\mathbf{y}} \cos\phi^i \tag{4.11}$$

$$E^i_\rho = E^i_{ox} \cos\phi^i + E^i_{oy} \sin\phi^i \tag{4.12}$$

$$E^i_\phi = -E^i_{ox} \sin\phi^i + E^i_{oy} \cos\phi^i \tag{4.13}$$

$$E^i_z = E^i_{oz} \tag{4.14}$$

The reflected field $\mathbf{E}^r$ is represented by

$$\mathbf{E}^r = \mathbf{E}^r_o \, e^{-jks^r} \tag{4.15}$$

where

$$\begin{aligned}
\mathbf{E}^r_o &= -\hat{\rho}\,\tilde{R}_\parallel E^i_\rho + \hat{\phi}\,\tilde{R}_\perp E^i_\phi + \hat{\mathbf{z}}\,\tilde{R}_\parallel E^i_z \\
&= -\tilde{R}_\parallel E^i_\rho(\,\hat{\mathbf{x}}\cos\phi^i + \hat{\mathbf{y}}\sin\phi^i) + \tilde{R}_\perp E^i_\phi(-\hat{\mathbf{x}}\sin\phi^i + \hat{\mathbf{y}}\cos\phi^i) + \tilde{R}_\parallel E^i_z\,\hat{\mathbf{z}} \\
&= \left[-\tilde{R}_\parallel(E^i_{ox}\cos\phi^i + E^i_{oy}\sin\phi^i)\cos\phi^i - \tilde{R}_\perp(-E^i_{ox}\sin\phi^i + E^i_{oy}\cos\phi^i)\sin\phi^i\right]\hat{\mathbf{x}} \\
&\quad + \left[-\tilde{R}\|(E^i_{ox}\cos\phi^i + E^i_{oy}\sin\phi^i)\sin\phi^i + \tilde{R}_\perp(-E^i_{ox}\sin\phi^i + E^i_{oy}\cos\phi^i)\cos\phi^i\right]\hat{\mathbf{y}} \\
&\quad + \tilde{R}_\parallel E_{oz}\,\hat{\mathbf{z}} \\
&= \left[E^i_{ox}(-\tilde{R}_\parallel cos^2\phi^i + \tilde{R}_\perp \sin^2\phi^i) + E^i_{oy}(-\tilde{R}_\parallel - \tilde{R}_\perp)\sin\phi^i\cos\phi^i\right]\hat{\mathbf{x}} \\
&\quad + \left[E^i_{ox}(-\tilde{R}_\parallel - \tilde{R}_\perp)\sin\phi^i\cos\phi^i + E^i_{oy}(-\tilde{R}_\parallel sin^2\phi^i + \tilde{R}_\perp\cos^2\phi^i)\right]\hat{\mathbf{y}} \\
&\quad + \tilde{R}_\parallel E^i_{oz}\,\hat{\mathbf{z}}
\end{aligned} \tag{4.16}$$

in which $\tilde{R}_{\parallel(\perp)}$ is a reflection coefficient for the electric field which is polarized parallel (perpendicular) to the plane of incidence. The $\tilde{R}_{\parallel(\perp)}$ have been defined previously in Appendix D for an impedance boundary condition on the inner walls, and in Appendix F for an absorber coating on the inner perfectly-conducting waveguide walls. Therefore, from the above equation the reflection coefficient can be

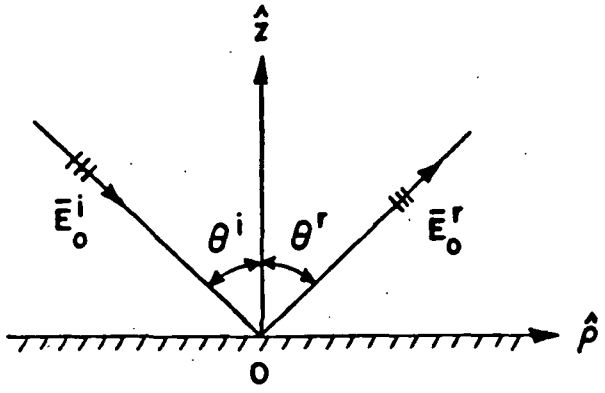

Figure 95: The incident field $\mathbf{E}_o^i$ in Figure 94 in the plane of incidence.

expressed in a matrix form

$$\left[\tilde{R}\right] = \begin{bmatrix} -\tilde{R}_{\parallel}\cos^2\phi^i + \tilde{R}_{\perp}\sin^2\phi^i & -(\tilde{R}_{\parallel} + \tilde{R}_{\perp})\sin\phi^i\cos\phi^i & 0 \\ -(\tilde{R}_{\parallel} + \tilde{R}_{\perp})\cos\phi^i\sin\phi^i & -\tilde{R}_{\parallel}\sin^2\phi^i + \tilde{R}_{\perp}\cos^2\phi^i & 0 \\ 0 & 0 & \tilde{R}_{\parallel} \end{bmatrix} \tag{4.17}$$

In order to obtain the reflected field, this reflection coefficient matrix is multiplied sequentially to the incident field each time a ray is incident on the waveguide wall, after transforming into the ray coordinate system pertaining to each waveguide wall from which the reflection occurs. It is noted that the incident unit vector $\hat{\mathbf{I}}$ is changed each time the ray is reflected by the wall.

4.1.2 Edge diffracted fields

i) 3–D edge diffraction coefficients

In this part, the 3–D edge diffraction contribution to the field inside the open-ended rectangular waveguide is discussed. Again, it is convenient to express the

2–D diffraction coefficients as in the previous chapter in terms of the ray fixed coordinate system. In this system, the incident field is expressed by components parallel and perpendicular to the *edge fixed* plane of incidence, the plane containing the incident ray and the diffracting edge, and the diffracted field expressed by components parallel and perpendicular to the edge fixed plane of diffraction, which contains the diffracted ray and the edge [12]. The "*ray fixed coordinate system*" is illustrated in Figure 96. Let $\hat{\mathbf{e}}$ be the unit vector along the edge direction and $\hat{\mathbf{D}}$ be the unit vector along the diffracted ray from the point of diffraction (Q_E) to the observation point P. Also, one may define the following:

$$\hat{\phi}' = -\frac{\hat{\mathbf{e}} \times \hat{\mathbf{I}}}{|\hat{\mathbf{e}} \times \hat{\mathbf{I}}|} \tag{4.18}$$

$$\hat{\beta}'_o = \hat{\phi}' \times \hat{\mathbf{I}} \tag{4.19}$$

$$\hat{\phi} = \frac{\hat{\mathbf{e}} \times \hat{\mathbf{D}}}{|\hat{\mathbf{e}} \times \hat{\mathbf{D}}|} \tag{4.20}$$

$$\hat{\beta}_o = \hat{\phi} \times \hat{\mathbf{D}} \tag{4.21}$$

These vectors form the two orthonormal basis of the edge fixed plane of incidence and diffraction. Note that the ordinary plane of incidence intersects the edge fixed plane of incidence along the incident ray; whereas, the plane of reflection intersects the edge fixed plane of diffraction along the reflected ray. The relationship between the *ray fixed coordinate system* and the *edge fixed coordinate system* is depicted in Figure 97. It can be shown that the angles α and α_i defined as shown in Figure 97 are related by $\alpha = -\alpha_i$. The unit vectors $\hat{\beta}'_o$, $\hat{\phi}'$ and $\hat{\mathbf{I}}$ form the spherical coordinate unit vectors fixed in the incident ray; likewise $\hat{\beta}_o$, $\hat{\phi}$ and $\hat{\mathbf{D}}$ form the spherical coordinate unit vectors fixed in the diffracted ray. It is apparent that the components of incident electric field $\mathbf{E}^i$ along the $\hat{\beta}'_o$ and $\hat{\phi}'$ direction defined by $E^i_{\beta'_o}$ and $E^i_{\phi'}$ respectively in the incident ray fixed coordinate system can be

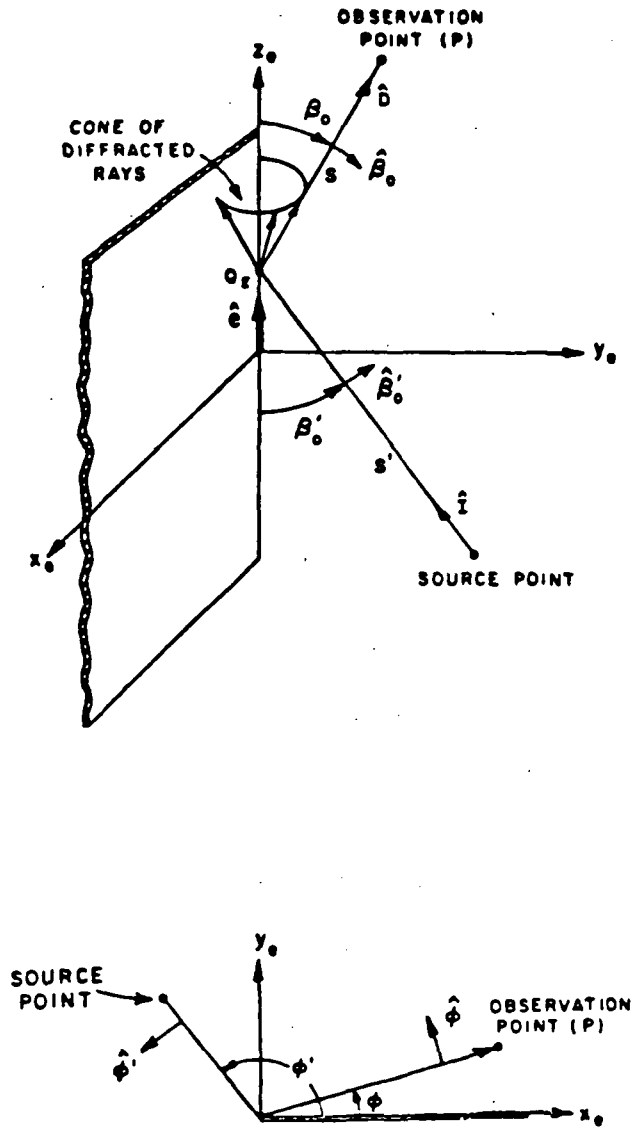

Figure 96: Ray fixed coordinate system used for 3-D diffraction.

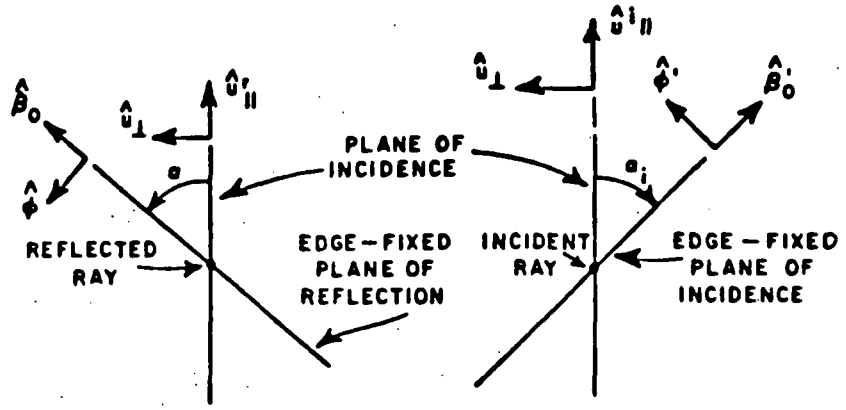

Figure 97: Comparison of the *ray fixed coordinate system* and the *edge fixed coordinate system*. The incident and reflected rays are perpendicular to the page and directed outward.

expressed in terms of the incident field components $E^i_{\parallel}$ and $E^i_{\perp}$ referred to the ordinary plane of incidence such that

$$E^i_{\beta'_o} = E^i_{\parallel} \cos\alpha - E^i_{\perp} \sin\alpha \tag{4.22}$$

$$E^i_{\phi'} = E^i_{\parallel} \sin\alpha + E^i_{\perp} \cos\alpha \tag{4.23}$$

where $\mathbf{E}^i_{\parallel(\perp)}$ is an incident electric field parallel (perpendicular) to the ordinary plane of incidence. These expressions may be written more compactly in a matrix notation as

$$E_{e.f.} = T(-\alpha)\, E^i \tag{4.24}$$

where $E_{e.f.}$ denotes incident field components ($E^i_{\beta'_o}$ and $E^i_{\phi'}$) in the edge fixed incident ray coordinates and E^i is the incident field in the ordinary plane of incidence. Also,

$$T(-\alpha) = \begin{bmatrix} \cos\alpha & -\sin\alpha \\ \sin\alpha & \cos\alpha \end{bmatrix} \tag{4.25}$$

The 3–D edge diffracted electric field $\mathbf{E}^d(P)$ at an observation point P for a half plane whose one side is perfectly-conducting and the other side is coated with a thin absorbing material (dielectric/ferrite), is written as [12]

$$\begin{bmatrix} E^d_{\beta_o}(P) \\ E^d_{\phi}(P) \end{bmatrix} = \begin{bmatrix} -D_a & -D_b \\ -D_c & -D_d \end{bmatrix} \begin{bmatrix} E^i_{\beta'_o}(Q_E) \\ E^i_{\phi'}(Q_E) \end{bmatrix} \cdot \frac{e^{-jks^d}}{\sqrt{s^d}} \tag{4.26}$$

in which

$$\mathbf{E}^i(Q_E) = \hat{\beta}'_o\, E^i_{\beta^i_o}(Q_E) + \hat{\phi}'\, E^i_{\phi'}(Q_E) \tag{4.27}$$

$$\mathbf{E}^d(P) = \hat{\beta}_o\, E^d_{\beta_o}(P) + \hat{\phi}\, E^d_{\phi}(P) \tag{4.28}$$

and s^d is the distance from the diffraction point at Q_E to the field point at P. Also the elements of the diffraction coefficient matrix are given by

$$D_a = D(1) + D(2) - D(3) - (\tilde{R}_{\parallel} \cos^2\alpha - \tilde{R}_{\perp} \sin^2\alpha)\, D(4) \tag{4.29}$$

$$D_b = -(\tilde{R}_{\parallel} + \tilde{R}_{\perp})\, D(4) \tag{4.30}$$

$$D_c = +(\tilde{R}_{\parallel} + \tilde{R}_{\perp})\, D(4) \tag{4.31}$$

$$D_d = D(1) + D(2) + D(3) + (\tilde{R}_{\parallel} \sin^2\alpha - \tilde{R}_{\perp} \cos^2\alpha)\, D(4) \tag{4.32}$$

and $D(1)$, $D(2)$, $D(3)$ and $D(4)$ are as given previously in Equations (3.10) through (3.13). $\tilde{R}_{\parallel}$ and $\tilde{R}_{\perp}$ are the reflection coefficients which are derived in Appendix D for an impedance boundary condition on the inner waveguide walls or in Appendix F for an absorber coating on the perfectly-conducting inner walls.. Note that in case of the half plane which is perfectly-conducting on one side and which

exhibits an impedance boundary condition on the other side, or which has the other perfectly-conducting side coated with an absorbing material, there is a coupling *between the TE_{edge} and TM_{edge} components of the diffracted fields; this fact is* readily evident from the non-diagonal form of the diffraction matrix as shown in Equation (4.26). Such a cross coupling takes place if the incident ray strikes the edge obliquely and it does not occur for a normal incidence on the edge; it is also absent for a normal or oblique incidence on a completely perfectly-conducting edge.

ii) Diffracted fields

The shadowing or the discontinuous behaviour of the GO incident and reflected rays by the waveguide walls is compensated for in the total field by the addition of the 3–D edge diffracted field of Equation (4.26) to the GO part of the solution. There is also diffraction by the corners of the edges in addition to the edge diffraction. However, *the contribution of this corner diffraction is neglected in this study* because it is generally weaker in comparison to the GO and edge diffracted fields, and its inclusion adds additional complexity to the ray analysis. For a given near field point, it is well known that there is only one point along an infinitely long straight edge from which the diffracted field can emanate. Therefore, one needs to determine whether a diffraction point lies on the finite length of each of the four edges at the open end of the waveguide, so that it can be included in the total scattered field.

The point of diffraction at $\mathbf{R}_d$ on an edge due to a given source location and a far zone observation point, as illustrated in Figure 98, can be obtained in a straight-forward manner. It is noted that this situation is the reciprocal of the one involving an observation point which is located at a finite distance within

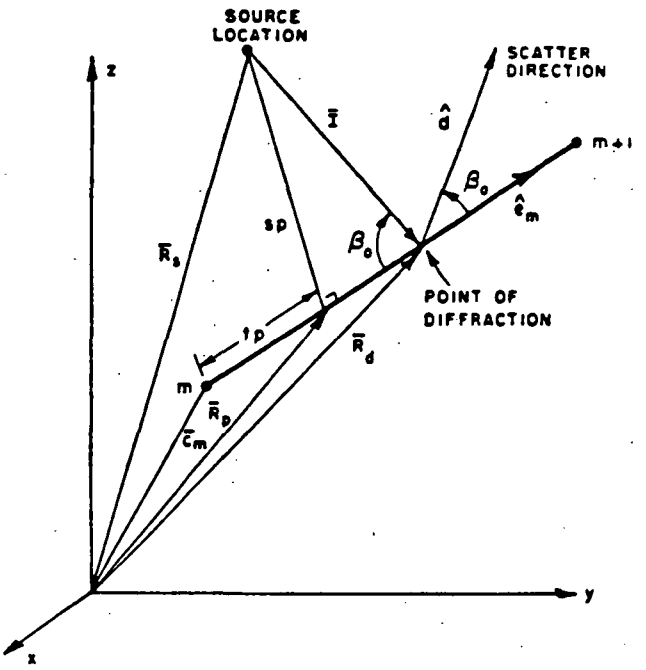

Figure 98: Geometry for finding the diffraction point along the rim edge at the open end of a waveguide.

the waveguide when the latter is excited by an external plane wave; however, the procedure to obtain the point of diffraction is the same in both cases. In particular, a vector perpendicular from the source to the edge can be found from

$$t_p = \left(\mathbf{R}_s - \mathbf{C}_m\right) \cdot \hat{\mathbf{e}}_m \tag{4.33}$$

$$\mathbf{R}_p = \mathbf{C}_m + t_p\, \hat{\mathbf{e}}_m \tag{4.34}$$

Since all the rays diffracted by the edge lie on a cone as shown in Figure 96, the scattering direction is known so that

$$\cot \beta_o = \frac{\hat{\mathbf{d}} \cdot \hat{\mathbf{e}}_m}{\sqrt{1 - (\hat{\mathbf{d}} \cdot \hat{\mathbf{e}}_m)^2}} \tag{4.35}$$

The diffraction point can now be found from

$$\mathbf{R}_d = \mathbf{R}_p + s_p \cot\beta_o \, \hat{\mathbf{e}}_m \tag{4.36}$$

where

$$s_p = \left|\mathbf{R}_s - \mathbf{R}_p\right| \tag{4.37}$$

To determine if the diffraction point (x_d, y_d and $z_d = 0$) is on the finite limits of the edge in the present waveguide problem of Figure 91, the x-coordinate of the diffracting point must fall between 0 and a for vertical edges (edge 1 and 3) and likewise, the y-coordinate must fall between 0 and b for horizontal edges (edge 2 and 4), respectively; i.e.,

$$0 < x_d < a \qquad \text{for edges 1 and 3} \tag{4.38}$$

$$0 < y_d < b \qquad \text{for edges 2 and 4} \tag{4.39}$$

Otherwise, each edge which does not satisfy the above equations has not diffracted field giving contribotion to the observation point P.

Once the diffraction point is known for any edge, the field diffracted from that edge to the field point P can be found from Equation (4.26) and this process is then repeated for the other edges of the waveguide rim. The diffracted fields which are represented by parallel ($E^d_{\beta_o}$) and perpendicular (E^d_{ϕ}) components are then transformed into the components in the rectangular coordinate system to be added to the GO field also in the latter coordinate system. For multiply diffracted–reflected rays, the same procedure as employed for the multiply reflected fields in the previous section is repeated by including the appropriate reflection coefficients at each bounce (reflection) off the walls.

As an illustration, each type of ray field in Figures 99–106 is plotted against the axial distance z from the open end to the observation point for various waveguide widths and heights, values of the inner wall impedance or absober coating, incident angles and wave polarizations. In Figures 99–106, the magnitude of the total field (which is given as a sum of its $\hat{x}$, $\hat{y}$ and $\hat{z}$ components) is plotted in each case. In Figure 100, the discontinuity at $z = 9.0\ \lambda$ is due to the corner diffraction and total field is not affected much as shown in the figure. Note that the numerical sequence appearing in the figures represents the waveguide walls which the incident ray hits during its travel to the observation point; these walls are numbered as shown in Figure 93. Figures 99–102 pertain to the rectangular waveguide with an impedance boundary condition on its inner walls. The same plots are repeated in Figures 103–106 for the perfectly-conducting waveguide coated with a dielectric and ferrite material on its inner walls. As shown in the figures, the discontinuities of the GO field at the shadow boundaries are compensated by the corresponding discontinuities of the diffracted field. From the plots of the total field in the above figures, it can be concluded that the corner diffracted field is very weak and does *not* affect the total field much inside the waveguide.

4.2 Ray solution for the interior field of a semi-infinite rectangular waveguide with an absorber coating on its inner walls and with a planar termination inside

Let a simple planar termination be placed at $z = L$ inside the semi-infinite rectangular waveguide of Figure 91 and the termination wall is designated by the number '5'. If the impedance boundary condition is assumed to hold on the inner waveguide walls (wall #1,2,3,4) then the termination (wall #5) is also assumed to satisfy the same impedance boundary condition. On the other hand, if the

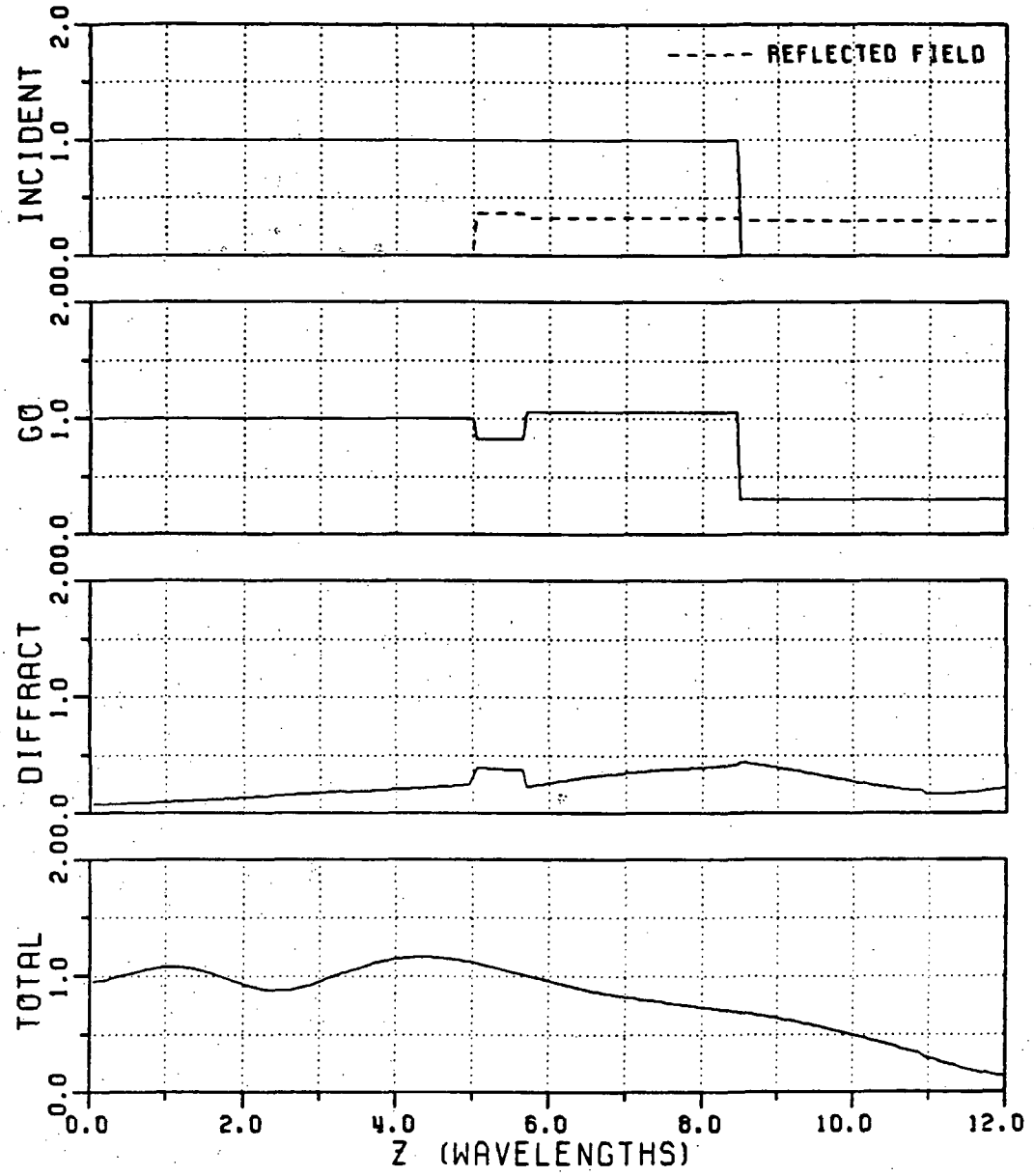

A = 20.0 (WAVELENGTHS)
B = 20.0 (WAVELENGTHS)
X = 12.0 (WAVELENGTHS)
Y = 15.0 (WAVELENGTHS)

$\Phi' = 45.0$ (DEGREES)
$\Theta' = 45.0$ (DEGREES)
$Z_S = (0.7, 0.3)$
2 3 0 0 0 0 0 0 0 0

Figure 99: Each ray field coupled into a semi-infinite rectangular waveguide with an impedance boundary condition on its inner walls for the perpendicularly polarized plane wave incidence.

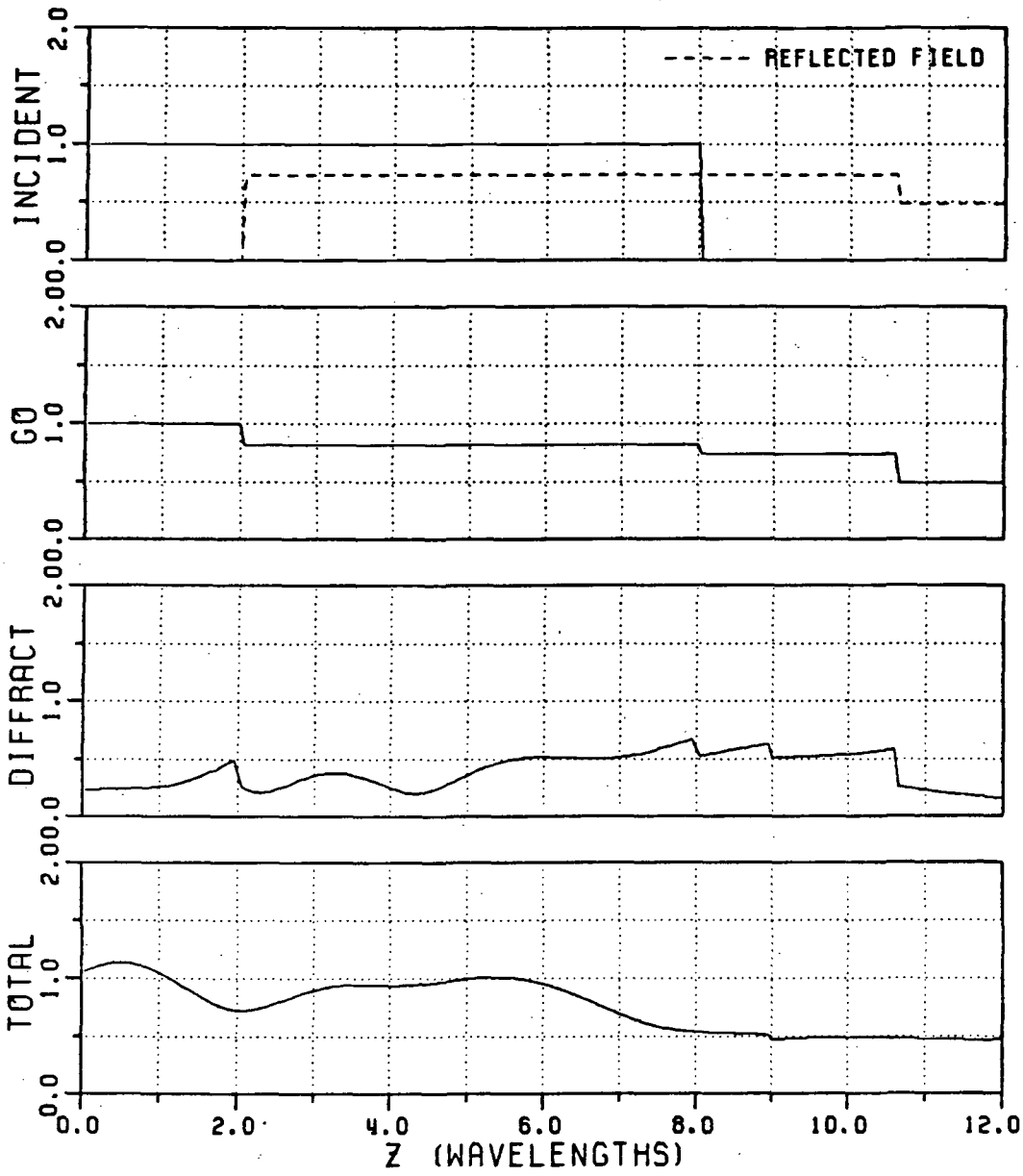

A = 30.0 (WAVELENGTHS)
B = 10.0 (WAVELENGTHS)
X = 15.0 (WAVELENGTHS)
Y = 2.0 (WAVELENGTHS)

$\Phi' = -45.0$ (DEGREES)
$\Theta' = 135.0$ (DEGREES)
$Z_S = (0.3, 0.7)$
4 1 0 0 0 0 0 0 0 0

Figure 100: Each ray field coupled into a semi-infinite rectangular waveguide with an impedance boundary condition on its inner walls for the parallel polarized plane wave incidence.

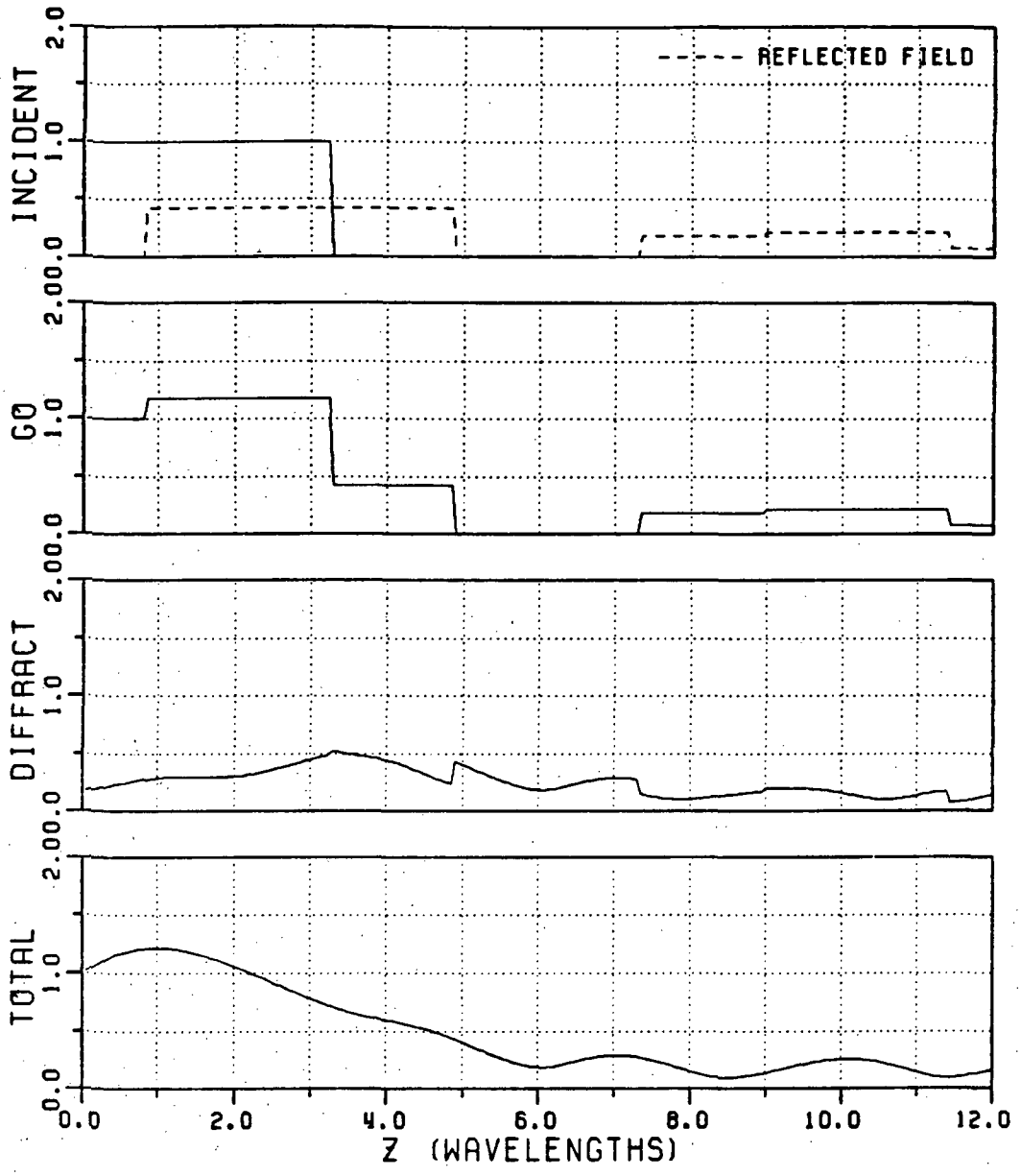

A = 10.0 (WAVELENGTHS)
B = 30.0 (WAVELENGTHS)
X = 8.0 (WAVELENGTHS)
Y = 15.0 (WAVELENGTHS)

$\Phi' = 60.0$ (DEGREES)
$\theta' = 45.0$ (DEGREES)
$Z_S = (0.5, 0.5)$
2 4 2 0 0 0 0 0 0 0

Figure 101: Each ray field coupled into a semi-infinite rectangular waveguide with an impedance boundary condition on its inner walls for the parallel polarized plane wave incidence.

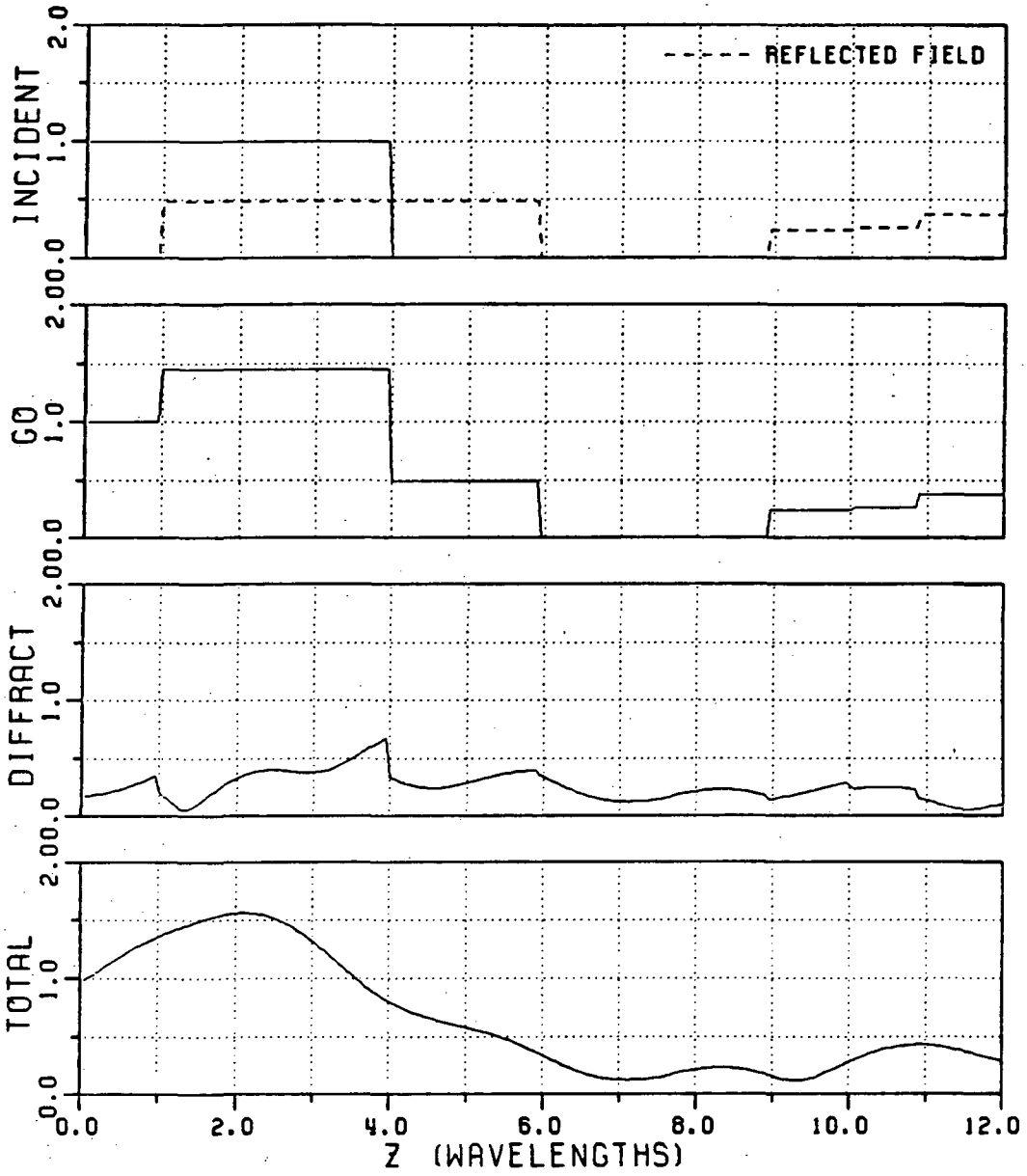

A = 10.0 (WAVELENGTHS)
B = 30.0 (WAVELENGTHS)
X = 8.0 (WAVELENGTHS)
Y = 20.0 (WAVELENGTHS)

$\Phi' = 55.0$ (DEGREES)
$\theta' = 45.0$ (DEGREES)
$Z_S = (0.5, 0.5)$
2 3 4 2 0 0 0 0 0 0

Figure 102: Each ray field coupled into a semi-infinite rectangular waveguide with an impedance boundary condition on its inner walls for the perpendicularly polarized plane wave incidence.

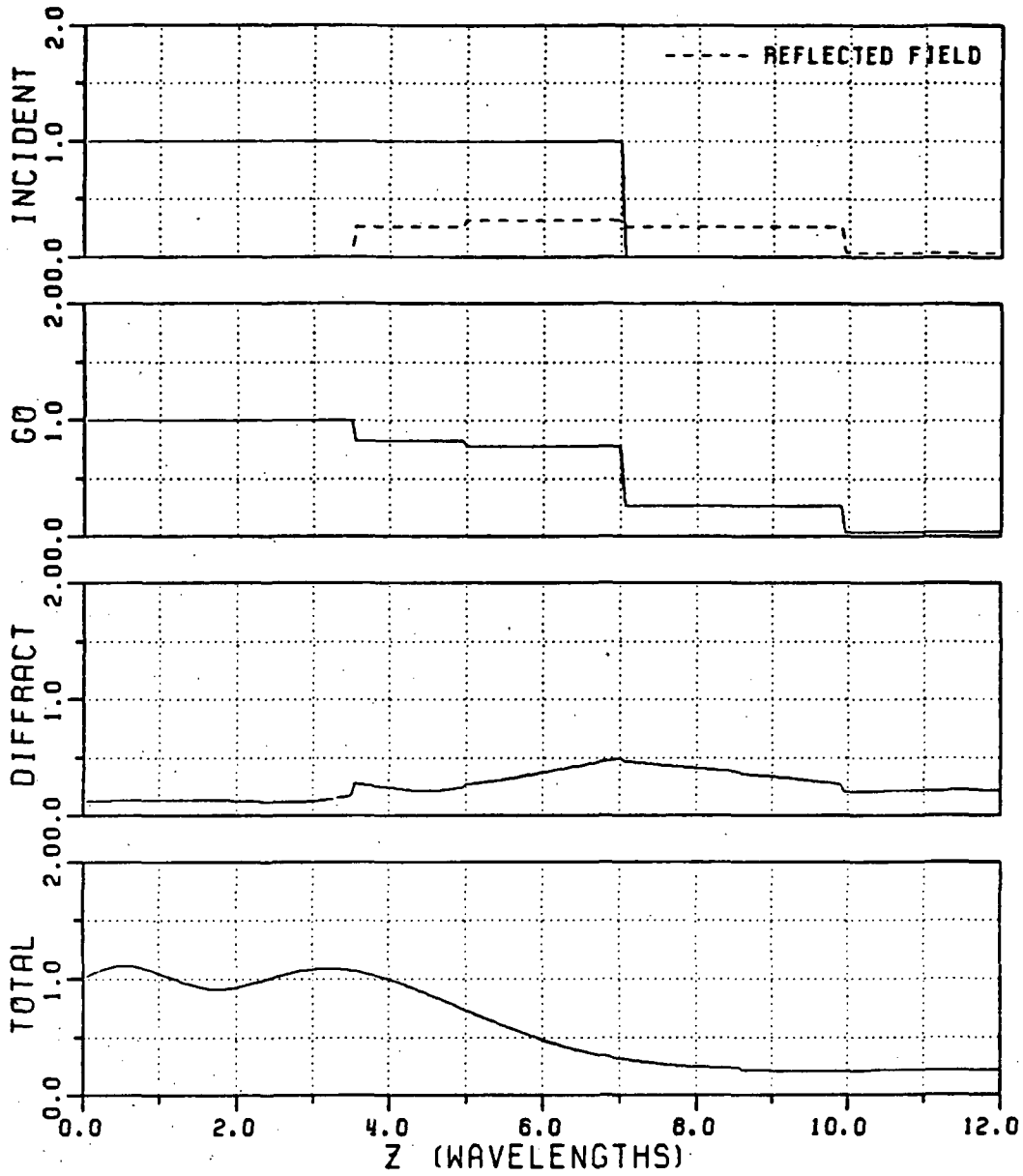

A = 15.0 (WAVELENGTHS) Φ' = 30.0 (DEGREES)
B = 15.0 (WAVELENGTHS) Θ' = 35.0 (DEGREES)
X = 10.0 (WAVELENGTHS) ϵ = (5.0, -0.50)
Y = 10.0 (WAVELENGTHS) μ = (3.0, -0.30)
T = 0.075 (WAVELENGTHS) 2 3 0 0 0 0 0 0 0 0

Figure 103: Each ray field coupled into a semi-infinite waveguide coated with a dielectric/ferrite material on its inner walls and parallel polarized plane wave incidence.

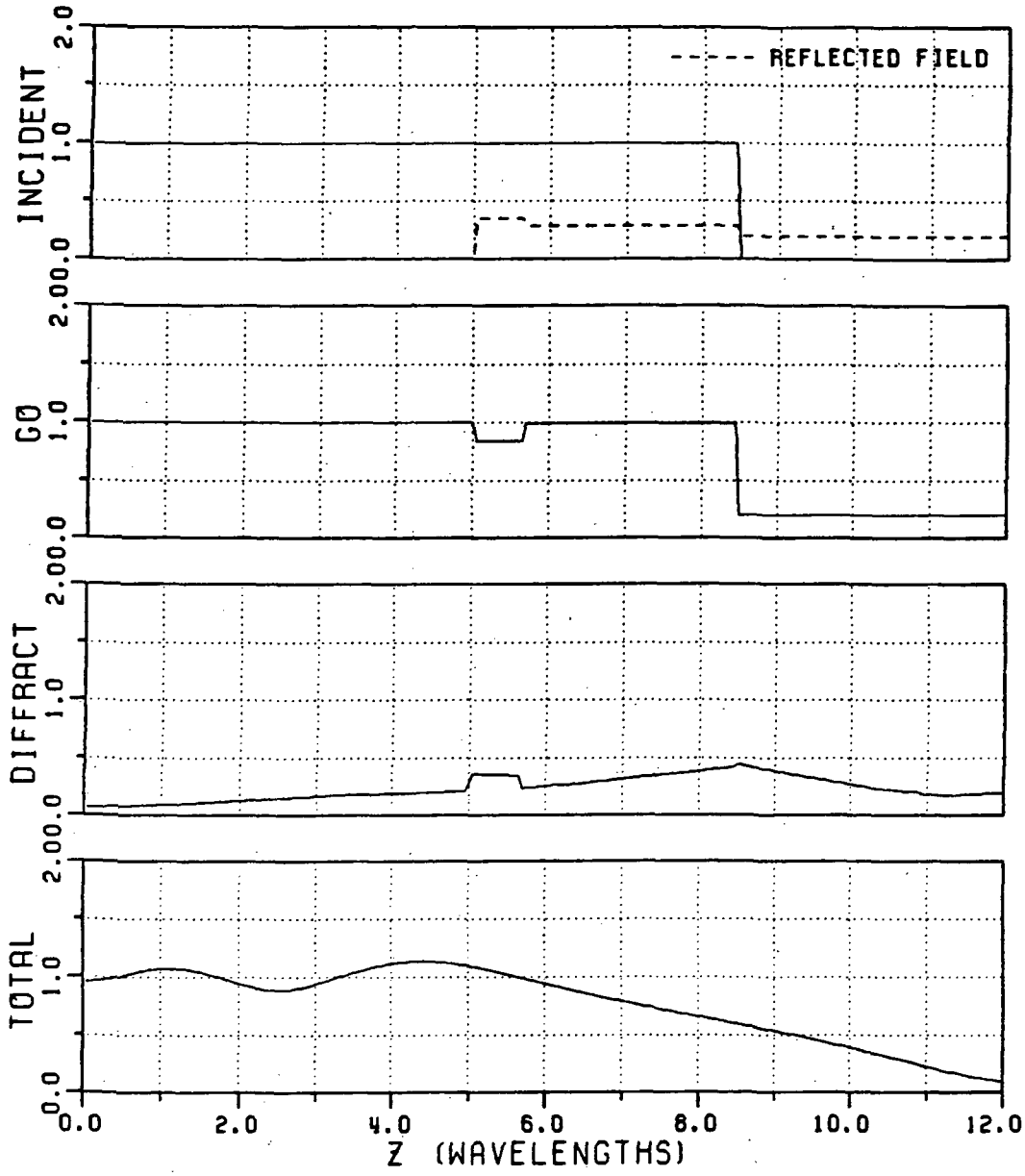

A = 20.0 (WAVELENGTHS) ϕ^i = 45.0 (DEGREES)
B = 20.0 (WAVELENGTHS) θ^i = 135.0(DEGREES)
X = 12.0 (WAVELENGTHS) ϵ = (3.0, -0.30)
Y = 5.0 (WAVELENGTHS) μ = (3.0, -0.30)
T = 0.075 (WAVELENGTHS) 2 1 0 0 0 0 0 0 0 0

Figure 104: Each ray field coupled into a semi-infinite waveguide coated with a dielectric/ferrite material on its inner walls and perpendicularly polarized plane wave incidence.

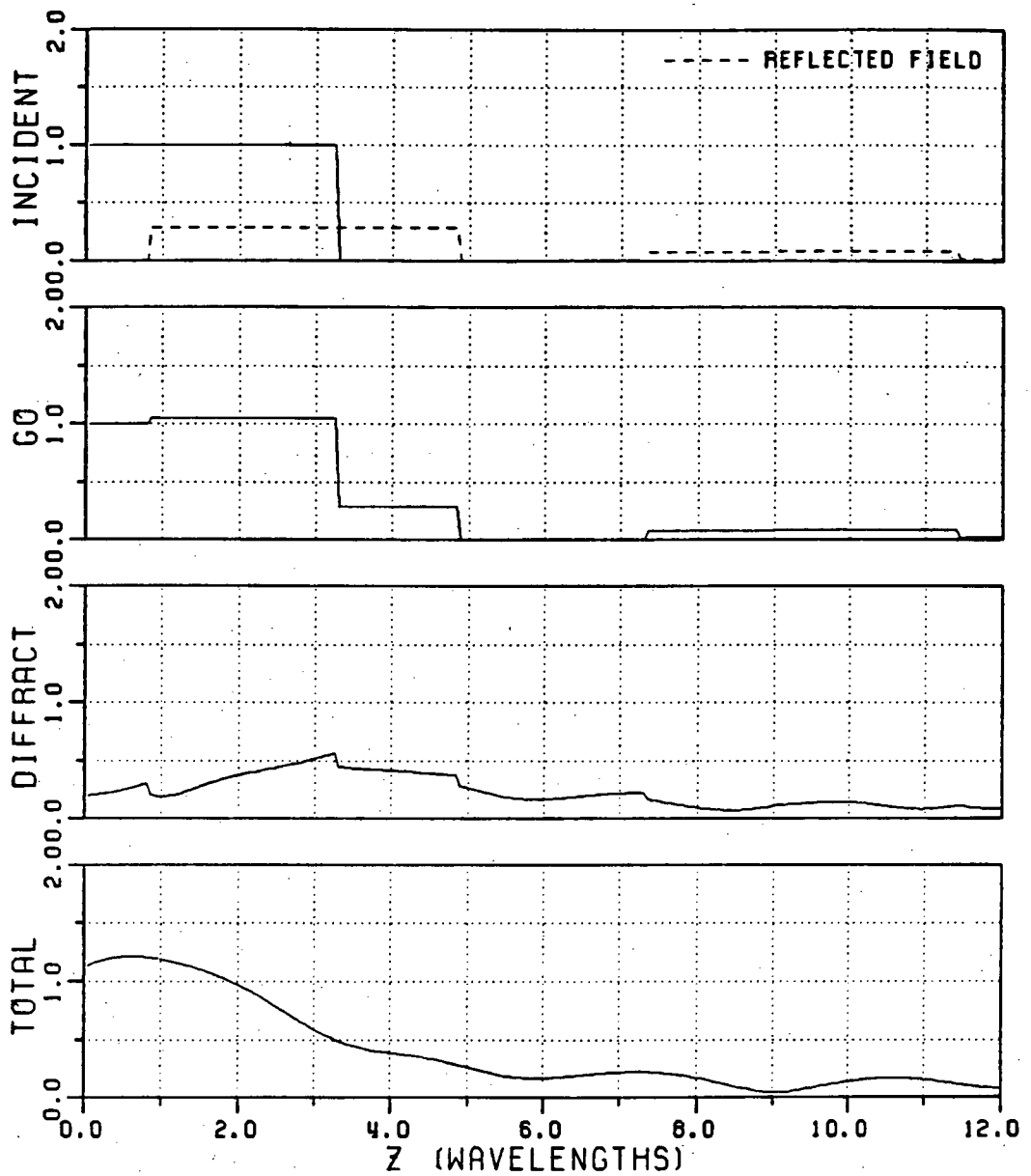

A = 10.0 (WAVELENGTHS) Φ^i = 60.0 (DEGREES)
B = 30.0 (WAVELENGTHS) Θ^i = 45.0 (DEGREES)
X = 8.0 (WAVELENGTHS) ϵ = (3.0, -0.30)
Y = 15.0 (WAVELENGTHS) μ = (3.0, -0.30)
T = 0.050 (WAVELENGTHS) 2 4 2 0 0 0 0 0 0 0

Figure 105: Each ray field coupled into a semi-infinite waveguide coated with a dielectric/ferrite material on its inner walls and parallel polarized plane wave incidence.

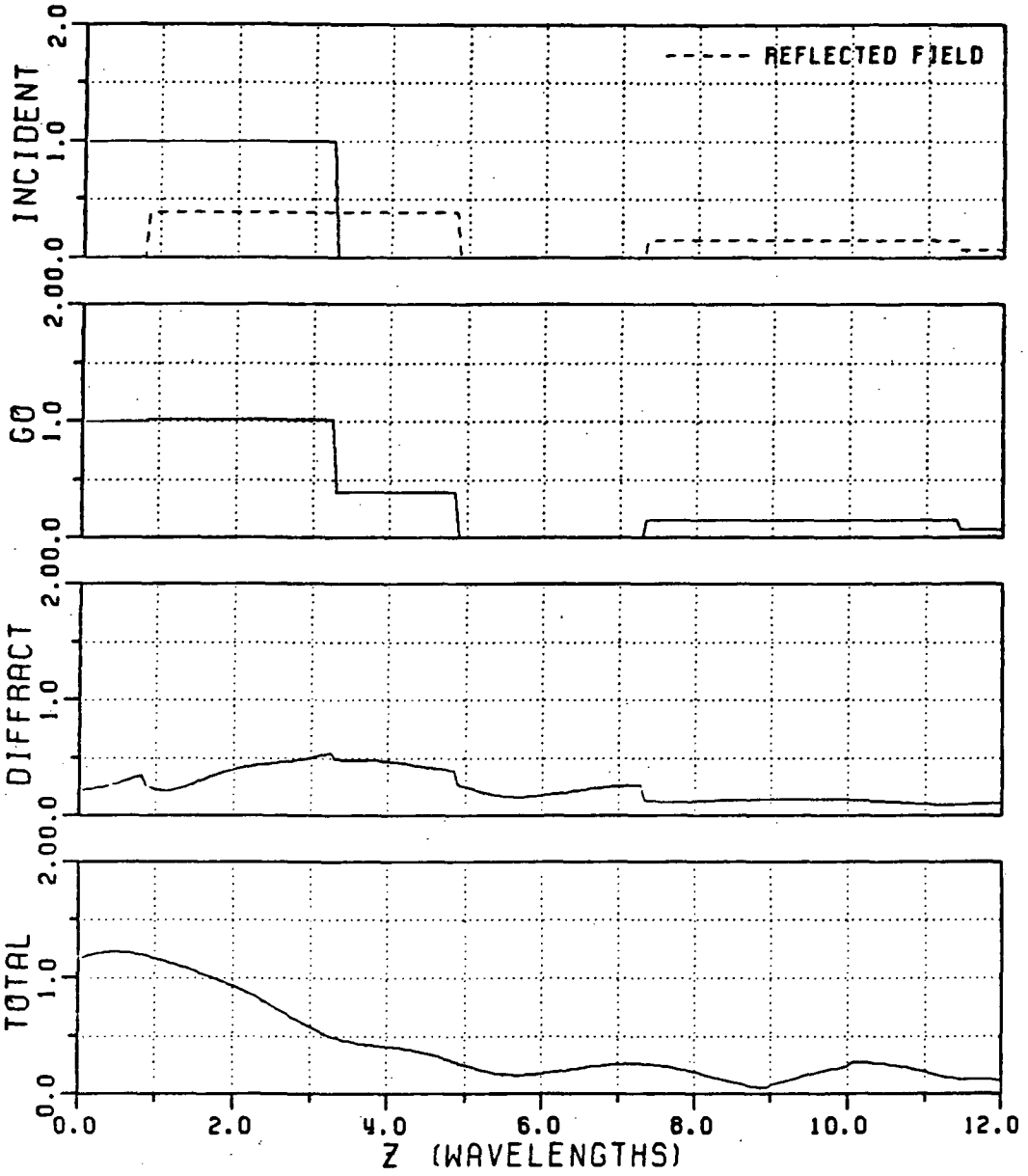

A = 10.0 (WAVELENGTHS) Φ'= 60.0 (DEGREES)
B = 30.0 (WAVELENGTHS) Θ'= 45.0 (DEGREES)
X = 8.0 (WAVELENGTHS) ϵ =(5.0,-0.50)
Y = 20.0 (WAVELENGTHS) μ =(3.0,-0.30)
T = 0.025 (WAVELENGTHS) 3 2 4 2 0 0 0 0 0 0

Figure 106: Each ray field coupled into a semi-infinite waveguide coated with a dielectric/ferrite material on its inner walls and parallel polarized plane wave incidence.

perfectly-conducting, semi-infinite waveguide is assumed to possess an absorber coating on its inner walls, then the termination wall is also assumed to be perfectly-conducting and coated with the same absorber material. The present method of analysis is also valid if the impedance or a dielectric/ferrite coating at the termination wall is not the same as that of the inner walls, but they are assumed here to be the same for the sake of convenience. The field at the observation point inside this terminated geometry can be computed in a manner which is very similar to that employed in the case of a terminated semi-infinite 2–D parallel plate waveguide as done in the previous chapter. There are two groups of rays reaching the observation point, one is from the open end side as if there is no termination inside and the other is from the the rays reflected from the termination.

Some numerical results for the fields inside a semi-infinite rectangular waveguide are shown in Figures 107–108 and 109–110 for the case of an interior planar termination with an impedance boundary condition and for a planar perfectly-conducting termination coated with a dielectric/ferrite absorbing material cases, respectively. Note that the ripples in the GO field are due to the interactions between the above-mentioned two groups of rays.

4.3 Field scattered into the exterior region by a semi-infinite rectangular waveguide with an absorber coating on its inner walls and with a planar termination inside

The field scattered outside the semi-infinite rectangular waveguide with an interior termination and with lossy inner walls is calculated in a manner similar to that done for the 2–D case in the previous chapter. The exterior scattered field consists of two basic contributions; one is the field due to the radiation from the interior effects which is found using the AI method (together with a physical optics

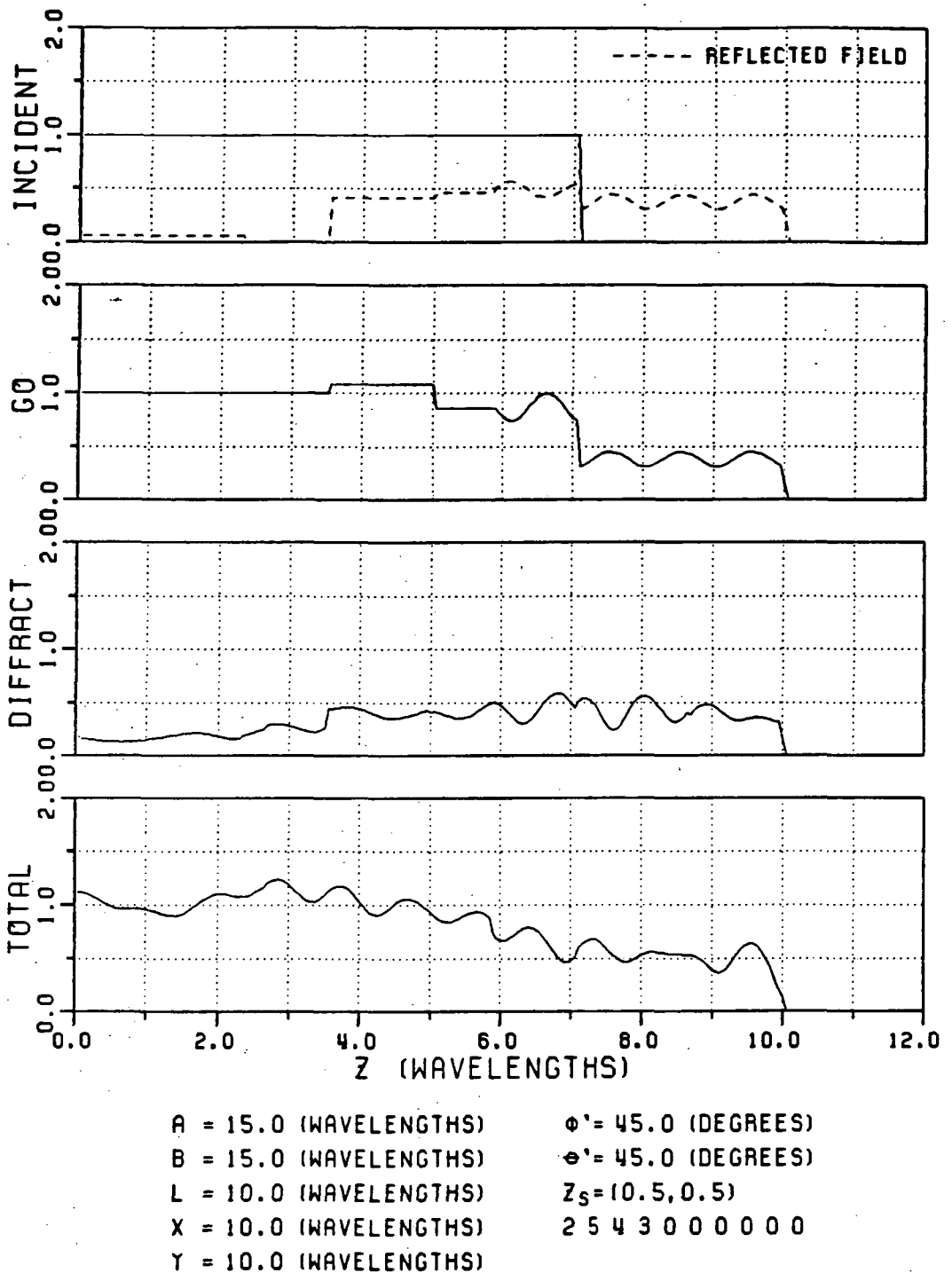

Figure 107: Each ray field for a rectangular waveguide with impedance inner walls and a planar termination inside for a parallel polarization.

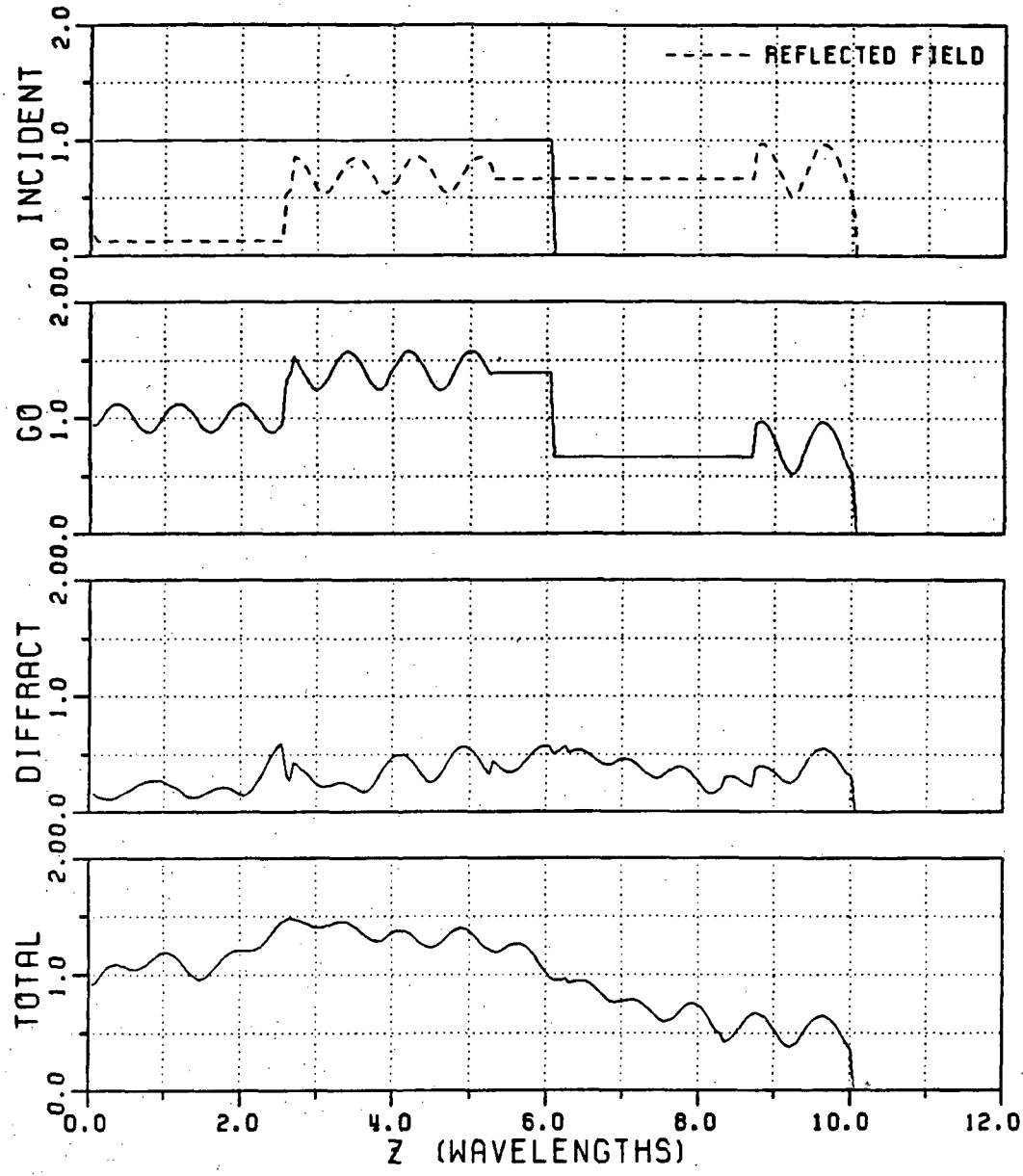

A = 10.0 (WAVELENGTHS)
B = 20.0 (WAVELENGTHS)
L = 10.0 (WAVELENGTHS)
X = 7.0 (WAVELENGTHS)
Y = 10.0 (WAVELENGTHS)

$\Phi' = 45.0$ (DEGREES)
$\Theta' = 120.0$ (DEGREES)
$Z_S = (0.3, 0.3)$
2 1 5 2 4 0 0 0 0 0

Figure 108: Each ray field for a rectangular waveguide with impedance inner walls and a planar termination inside for a perpendicular polarization.

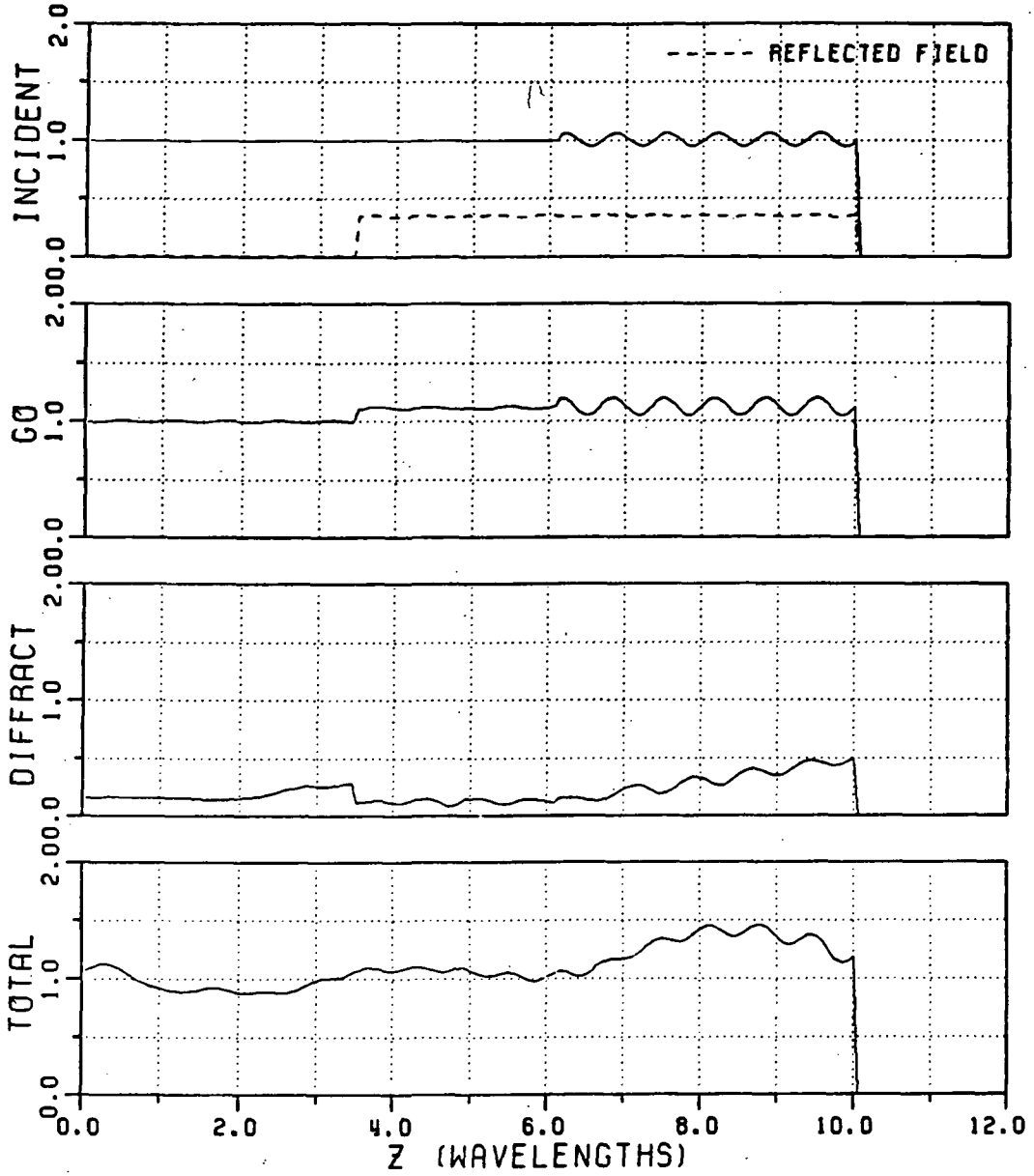

A = 20.0 (WAVELENGTHS) Φ' = 30.0 (DEGREES)
B = 10.0 (WAVELENGTHS) Θ' = 60.0 (DEGREES)
L = 10.0 (WAVELENGTHS) ε = (3.0, -0.10)
X = 10.0 (WAVELENGTHS) μ = (1.0, -0.30)
Y = 8.0 (WAVELENGTHS) 2 5 3 0 0 0 0 0 0 0
T = 0.10 (WAVELENGTHS)

Figure 109: Each ray field for a rectangular waveguide coated with a dielectric/ferrite material with a planar termination inside for a parallel polarization.

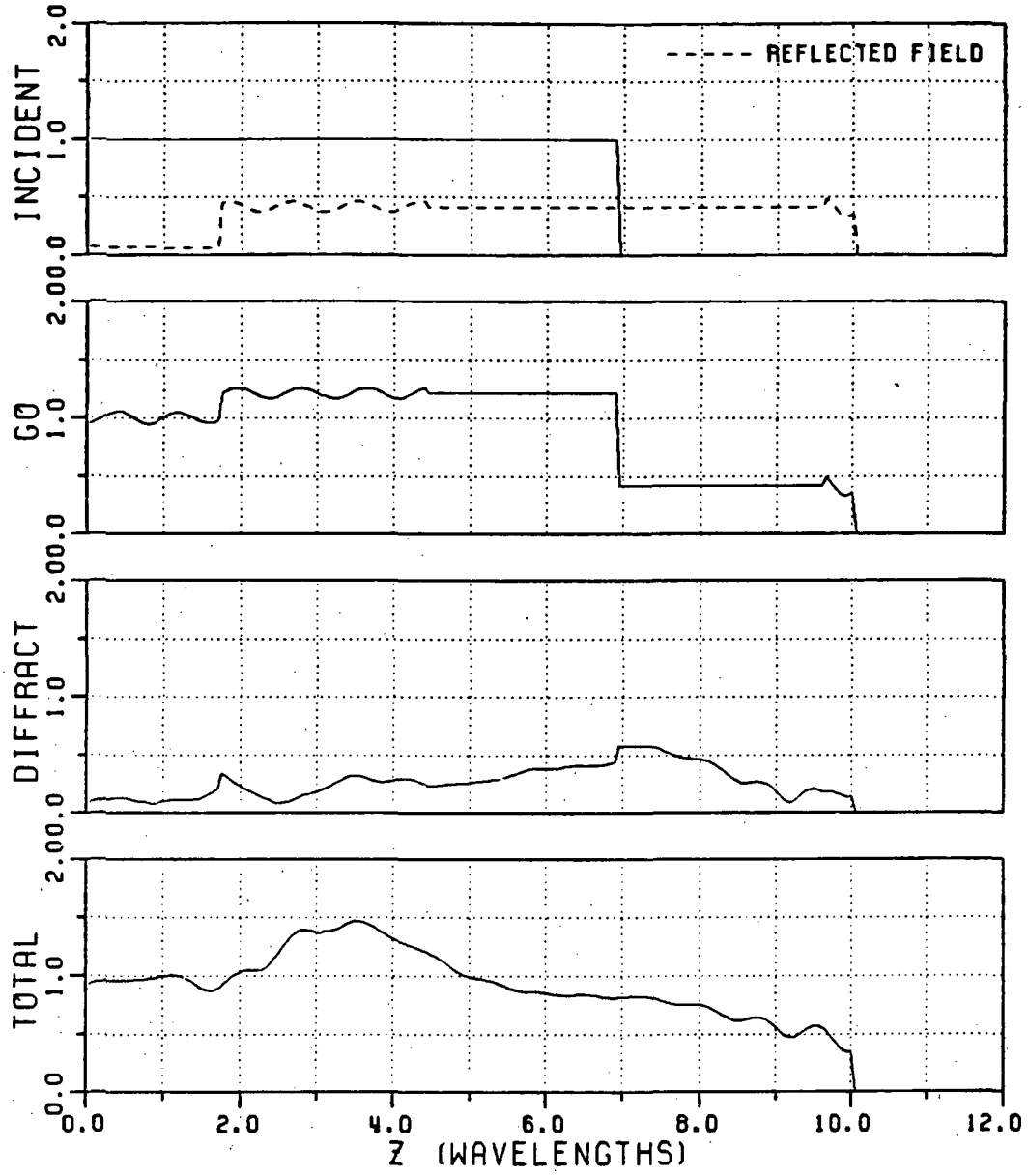

A = 10.0 (WAVELENGTHS) Φ' = -45.0 (DEGREES)
B = 30.0 (WAVELENGTHS) θ' = 60.0 (DEGREES)
L = 10.0 (WAVELENGTHS) ϵ = (3.0, -0.30)
X = 2.0 (WAVELENGTHS) μ = (3.0, -0.30)
Y = 15.0 (WAVELENGTHS) 4 2 5 4 0 0 0 0 0 0
T = 0.05 (WAVELENGTHS)

Figure 110: Each ray field for a rectangular waveguide coated with a dielectric/ferrite material with a planar termination inside for a perpendicular polarization.

approximation) and the other is due to the direct edge diffraction from the rim at the open end which is found via the UTD in conjunction with the equivalent current method (ECM).

For calculating the radiation from the interior cavity, the 3–D radiation integral (over the aperture at the open end) which is used to represent this radiated electric field $\mathbf{E}^s_{int}$ in the forward half space (see the discussion in Section 3.5 for the 2–D case) is given as [14,15]

$$\mathbf{E}^s_{int} \approx \frac{jkZ_o}{4\pi} \iint_s Y_o \hat{\mathbf{R}} \times 2\,\mathbf{M}_s \frac{e^{-jkR}}{R}\, ds \tag{4.40}$$

where Z_o (or Y_o) is free-space wave impedance (or admittance), $\hat{\mathbf{R}}$ is a unit vector in radiation direction (see Figure 111). $2\,\mathbf{M}_s$ is the equivalent magnetic current in the aperture region which radiates in the forward half space as in the previous 2–D case (which employs a 2–D rather than a 3–D radiation integral). In general, the amplitude and phase terms in the above integrand are separable in terms of the aperture coordinates as follows.

$$M_s = M_x(x)\, M_y(y) \tag{4.41}$$

$$e^{-jkR} = e^{jk_x x}\, e^{jk_y y}\, e^{-jkR_o} \tag{4.42}$$

where R_o is the distance from the origin to the field point. Thus,

$$E^s_{int} = \frac{jk}{2\pi} \frac{e^{-jkR_o}}{R_o} \int_{a_1}^{a_2} M_x(x')\, e^{jk_x x'}\, dx' \int_{b_1}^{b_2} M_y(y')\, e^{jk_y y'}\, dy' \tag{4.43}$$

Clearly, for separable aperture distribution the calculation of the radiation pattern reduces to the product of two 2–D patterns. Note that there are four patches to be integrated on the aperture each giving different radiation patterns. These four

different patches originate from the combination of two ray tubes from each top and side views as shown in Figure 76. The total radation pattern can then be obtained by superposing the field radiated by each of the patches of 2 $\mathbf{M}_s$ in the aperture.

In order to include the contribution from the field directly diffracted by the edges at the open end, the *equivalent current method* (ECM) [20–24] is employed in conjunction with the GTD. Generally, this rim edge scattered field E^s_{rim} is the sum of the fields of all the singly diffracted rays which are initiated at various points on the rim edge by the incident field in accordance with the law of edge diffraction. However, in some situations, there may be a continuum of diffraction points contributing to the scattered field [20]; in such a situation, a direct application of the GTD fails and one must resort to an integration around the edge as in the ECM. The rays diffracted from the corners of the rim of the waveguide also contribute to the diffracted fields in addition to the edge diffracted rays. It is noted that the ECM automatically but approximately takes into account the presence of the corners at the open end.

In the ECM, the equivalent currents $\mathbf{I}_{eq}$ and $\mathbf{M}_{eq}$ of the electric and magnetic type, respectively, are located at the rim edge as shown in Figure 111. These equivalent currents radiate in free-space to produce the scattered field. The strength of the equivalent currents are calculated indirectly from the GTD, but they give a bounded result even in the caustic regions where the GTD gives a singular result because a continuum of rays contribute to the field at such points of observation.

The strength of the equivalent electric and magnetic currents are given by [20,22]

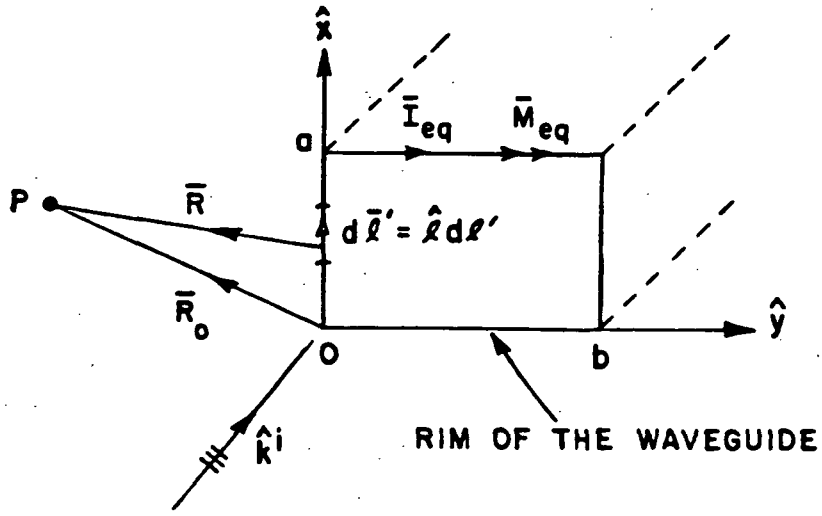

Figure 111: Equivalent currents $\mathbf{I}_{eq}$ and $\mathbf{M}_{eq}$ on the rim at the open end of the waveguide.

$$I_{eq}(l') = -Y_o\sqrt{\frac{8\pi}{jk}}\,\frac{D_E(\psi,\psi';\beta_o,\beta)}{|\sqrt{\sin\beta_o\,\sin\beta}\,|}\left(\mathbf{E}^i\cdot\hat{\mathbf{l}}'\right) \tag{4.44}$$

$$M_{eq}(l') = -Z_o\sqrt{\frac{8\pi}{jk}}\,\frac{D_M(\psi,\psi';\beta_o,\beta)}{|\sqrt{\sin\beta_o\,\sin\beta}\,|}\left(\mathbf{H}^i\cdot\hat{\mathbf{l}}'\right) \tag{4.45}$$

where $\hat{\mathbf{l}}'$ is the unit vector along the edge direction. The angles (β_o, β, ψ' and ψ) appeared in the diffraction coefficients (D_E and D_M) in Equations (4.44) and (4.45) are indicated in Figure 112. Note that the diffraction coefficients D_M and D_E correspond to D_a in Equation (4.29) and D_d in Equation (4.32), respectively.

Then, the equivalent currents $\mathbf{I}_{eq}$ and $\mathbf{M}_{eq}$ are incorporated into the radiation integral to calculated the scattered field $\mathbf{E}^s_{rim}$ [22]; i.e.,

$$\mathbf{E}^s_{int} \approx \frac{jkZ_o}{4\pi}\int_{rim}\left[\hat{\mathbf{R}}\times\hat{\mathbf{R}}\times\mathbf{I}_{eq}(l') + Y_o\,\hat{\mathbf{R}}\times\mathbf{M}_{eq}(l')\right]\frac{e^{-jkR}}{R}\,dl' \tag{4.46}$$

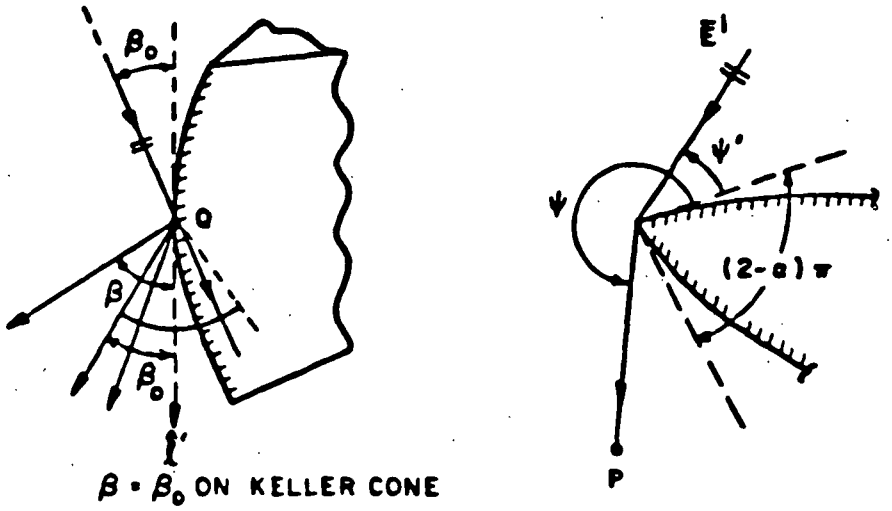

Figure 112: Angles β_o, β, ψ' and ψ which occur in the wedge diffraction coefficients D_M and D_E.

where $\mathbf{R} = R\,\hat{\mathbf{R}}$ is the vector pointing toward the observation ponit from a source point on the rim edge as in Figure 111. Although the rim scattered field $\mathbf{E}^s_{rim}$ is not expressed explicitly here, the integrand of Equation (4.46) can be calculated in terms of each component of the incident field easily for each edge of the rim once the incident and radiation vectors are specified.

Numerical results for the far zone scattering patterns in the $x - z$ plane are plotted in Figures 113–115 for the problem of plane wave scattering by a semi-infinite rectangular waveguide with an interior termination as a function of the angle γ. In these figures, the inner waveguide walls as well as the interior planar termination are assumed to satisfy an impedance boundary condition. As in the 2-D case, the field scattered from the interior cavity region dominates the total field for small values of the loss in the wall impedance, however, as the wall loss becomes larger, the field scattered by the rim contributes mostly to the total field. It is also seen that this direct rim contribution to the total scattered field can become

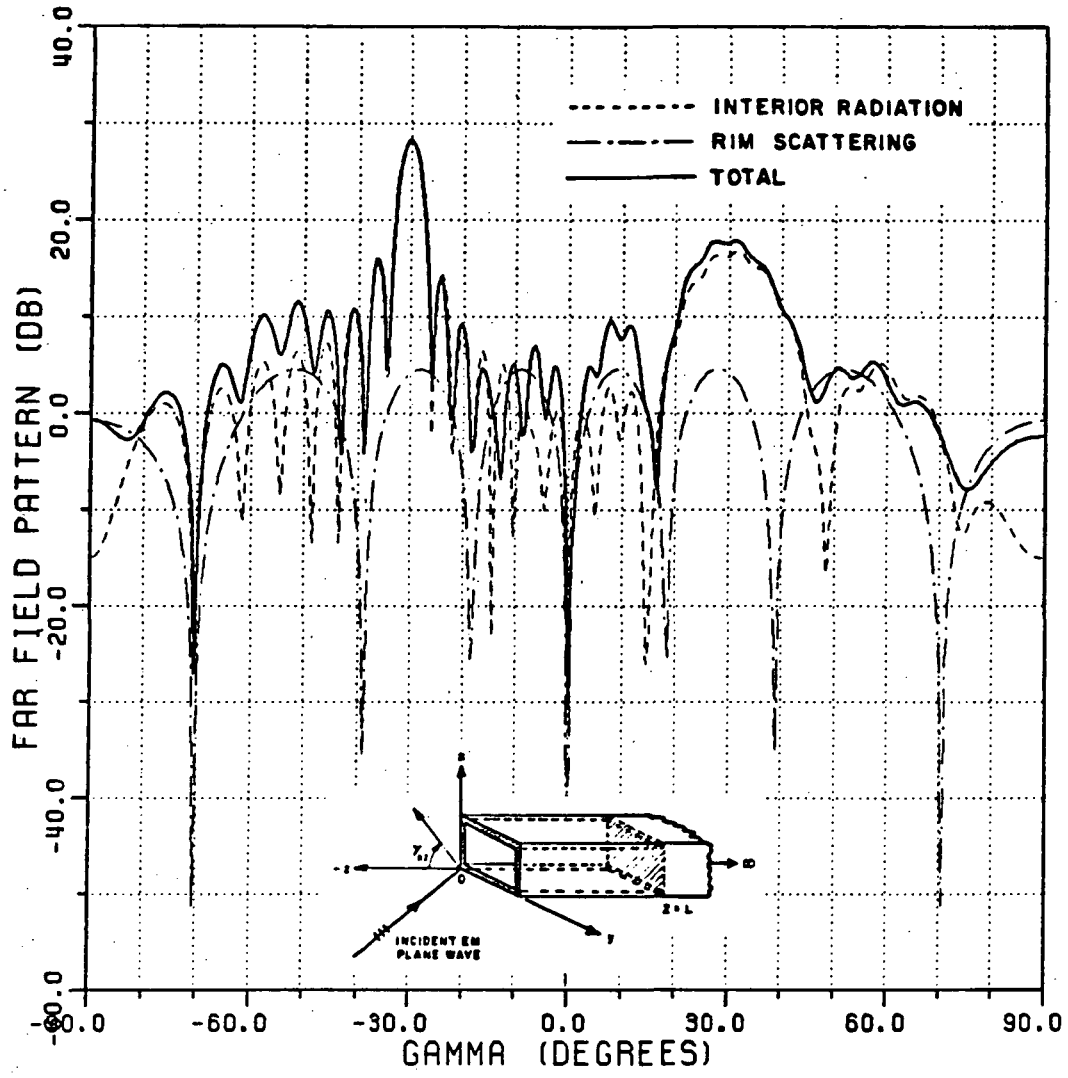

Figure 113: Far zone pattern in the $x - z$ plane of the field scattered by a semi-infinite rectangular waveguide with an interior termination illuminated by an external plane wave whose electric field is polarized parallel to the plane of incidence.

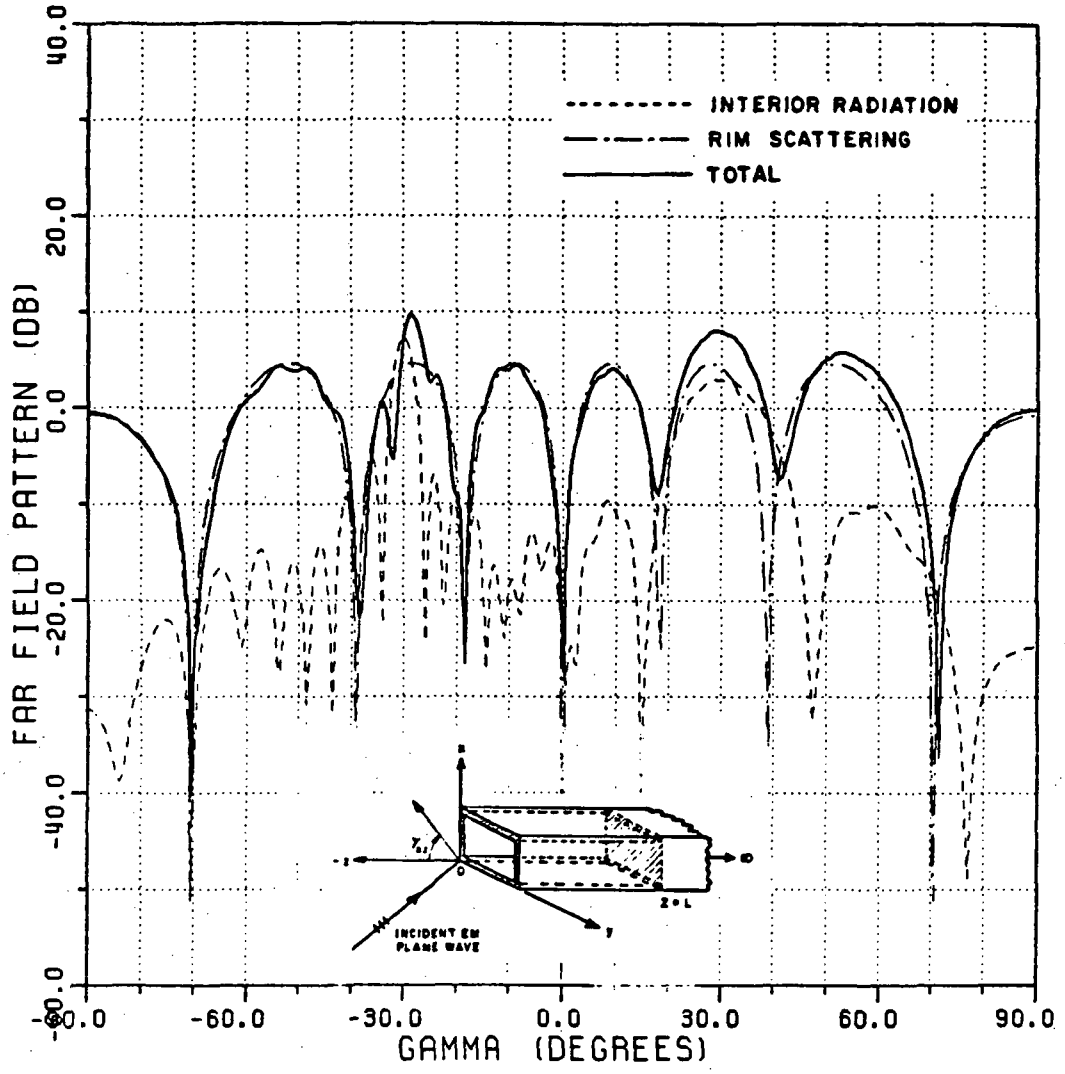

A = 20.0 (WAVELENGTHS) Φ' = 30.0 (DEGREES)
B = 30.0 (WAVELENGTHS) θ' = 75.0 (DEGREES)
L = 30.0 (WAVELENGTHS) Z_S = (0.3, 0.3)

Figure 114: Far zone pattern in the $x - z$ plane of the field scattered by a semi-infinite rectangular waveguide with an interior termination illuminated by an external plane wave whose electric field is polarized parallel to the plane of incidence.

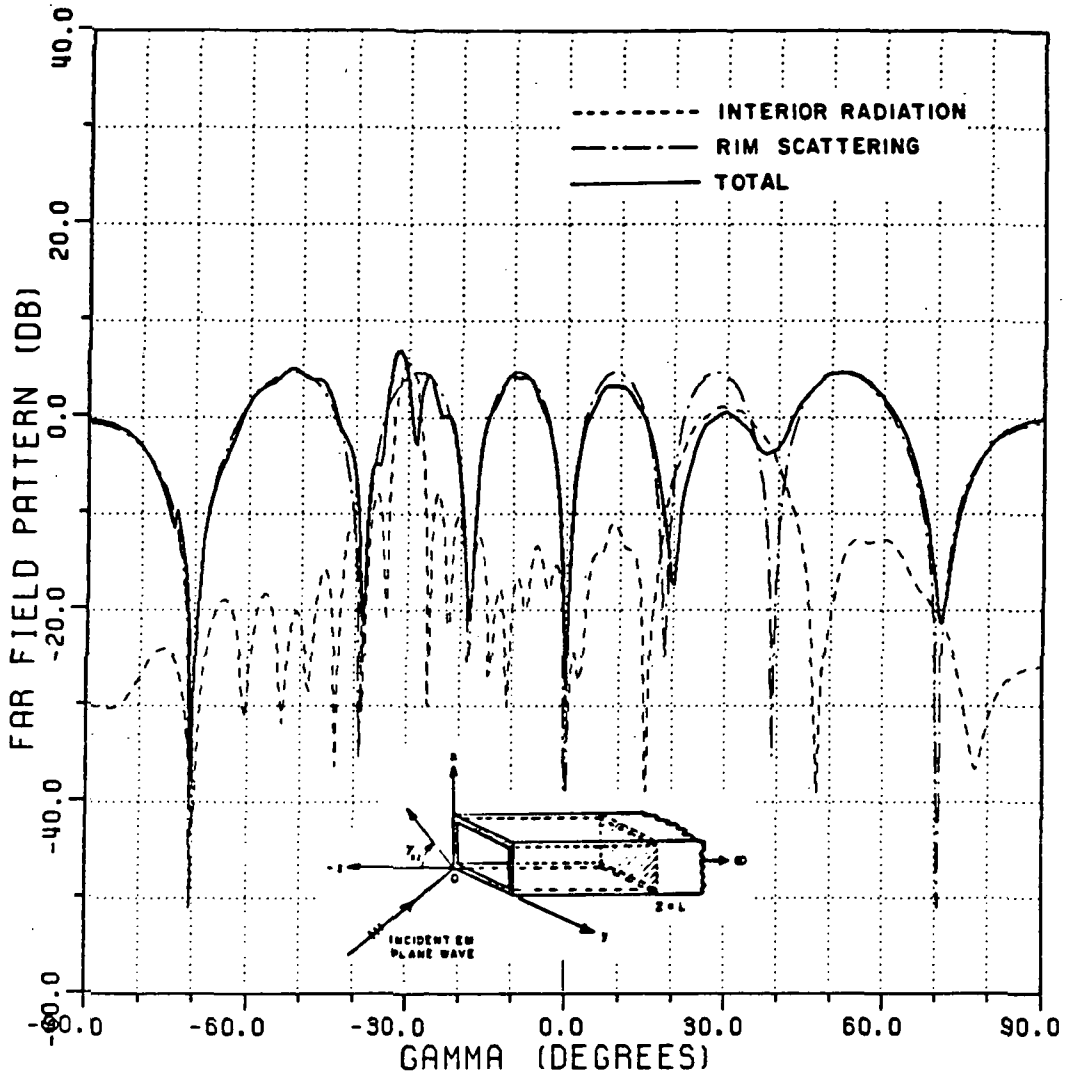

A = 20.0 (WAVELENGTHS) Φ' = 30.0 (DEGREES)
B = 30.0 (WAVELENGTHS) Θ' = 75.0 (DEGREES)
L = 30.0 (WAVELENGTHS) Z_S = (0.5, 0.5)

Figure 115: Far zone pattern in the $x - z$ plane of the field scattered by a semi-infinite rectangular waveguide with an interior termination illuminated by an external plane wave whose electric field is polarized parallel to the plane of incidence.

stronger than the contribution due to the re-radiation from the interior cavity as the incident field couples into the waveguide with incident angles far from the waveguide axis. The latter is to be expected because there will be more ray bounces inside the waveguide for these incident angles and thus making the interior field weaker due to the loss effect at each bounce. In Figures 116–118, the same plots are repeated for the case in which the perfectly-conducting waveguide and its interior planar termination are coated on the inside by an absorbing (dielectric/ferrite) material. Note that the field scattered by the rim is not changed much for different values of ϵ and μ characterizing the absorbing material, whereas, the scattered field due to the interior radiation is affected much more by the absorbing material.

The surface wave type field similar to that considered in Chapter II, which is launched by the diffraction of the incident wave at the edges of the open end of the rectangular waveguide, could reflect strongly from any discontinuity placed closely to the walls of the waveguide. The reflected surface wave could then radiate outside the rectangular waveguide again via diffraction from the edges at the waveguide opening. However, the effect of the surface wave field could be controlled to exhibit a greater attenuation along the direction of propagation with the inclusion of greater loss in the absorbing material. Assuming that the planar termination is not located too close to the open end of the waveguide and assuming that the loss in the absorbing material is sufficient to rapidly attenuate the surface wave over that distance, one can then neglect the effect of the surface wave on the radiation patterns. The above assumptions are expected to be valid for the calculations shown in Figures 113–118 in which surface wave effects are ignored.

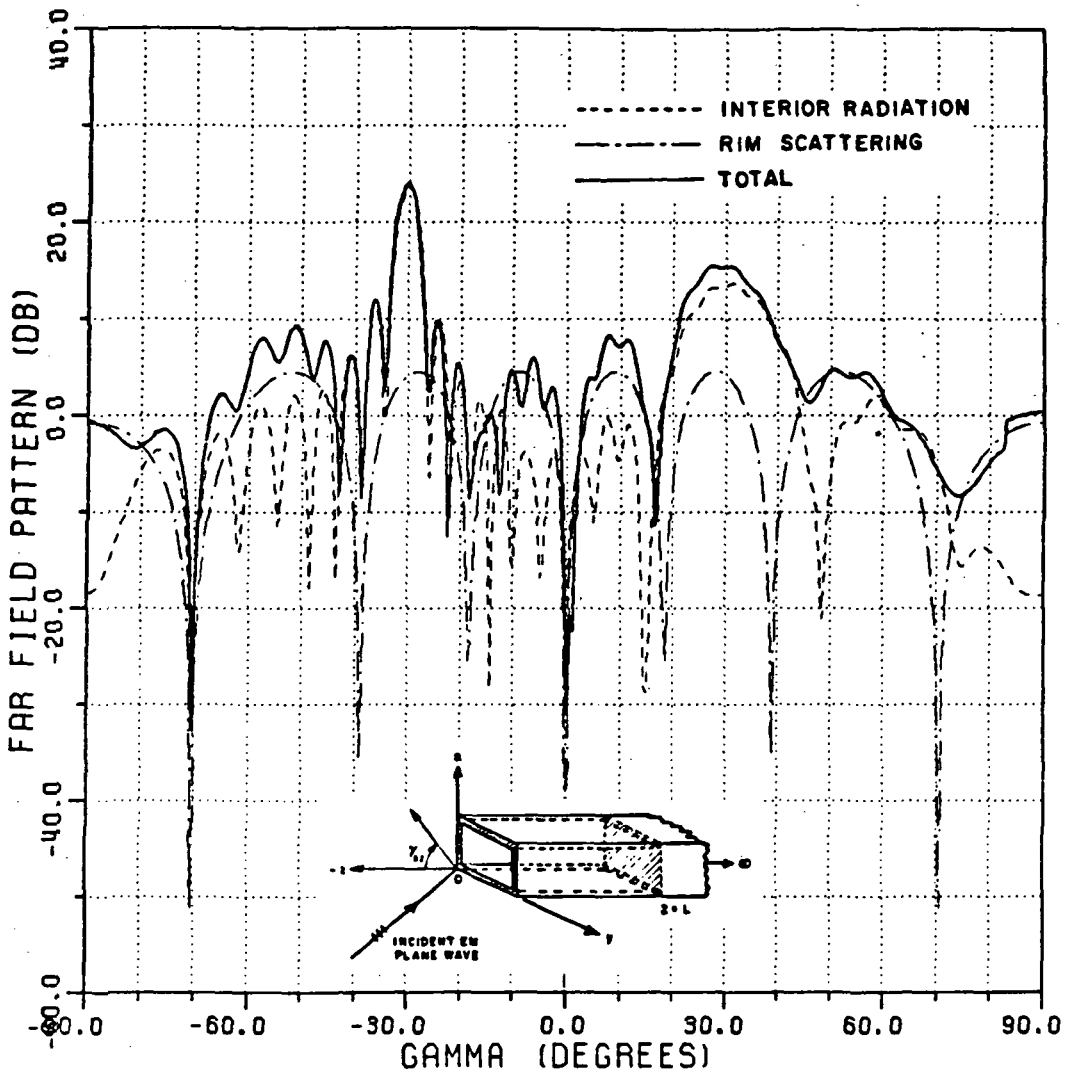

Figure 116: Far zone pattern in the $x - z$ plane of the field scattered by a semi-infinite rectangular waveguide with an interior termination illuminated by an external plane wave whose electric field is polarized parallel to the plane of incidence.

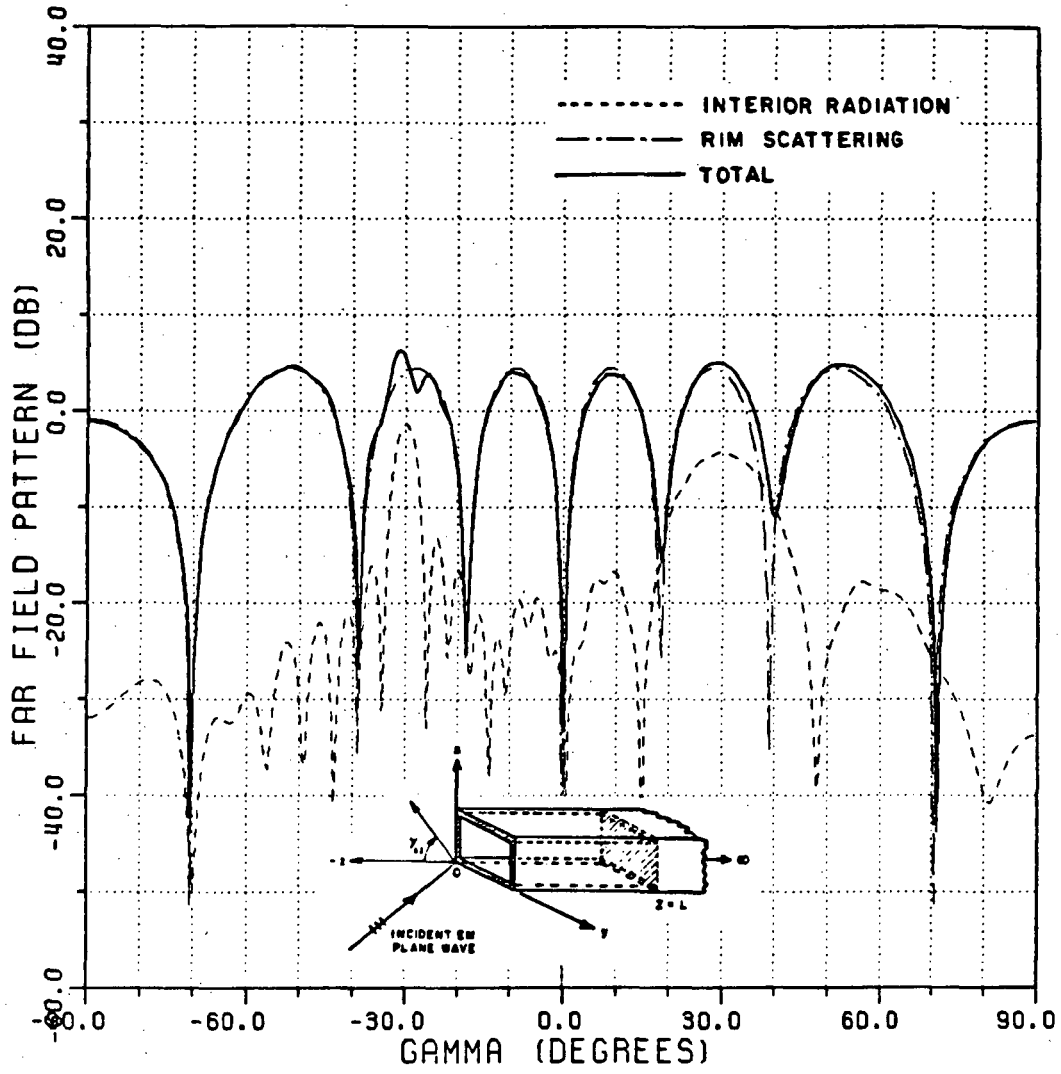

A = 20.0 (WAVELENGTHS) Φ' = 30.0 (DEGREES)
B = 30.0 (WAVELENGTHS) θ' = 75.0 (DEGREES)
L = 30.0 (WAVELENGTHS) ϵ = (3.0, -0.30)
T = 0.05 (WAVELENGTHS) μ = (3.0, -0.30)

Figure 117: Far zone pattern in the $x - z$ plane of the field scattered by a semi-infinite rectangular waveguide with an interior termination illuminated by an external plane wave whose electric field is polarized parallel to the plane of incidence.

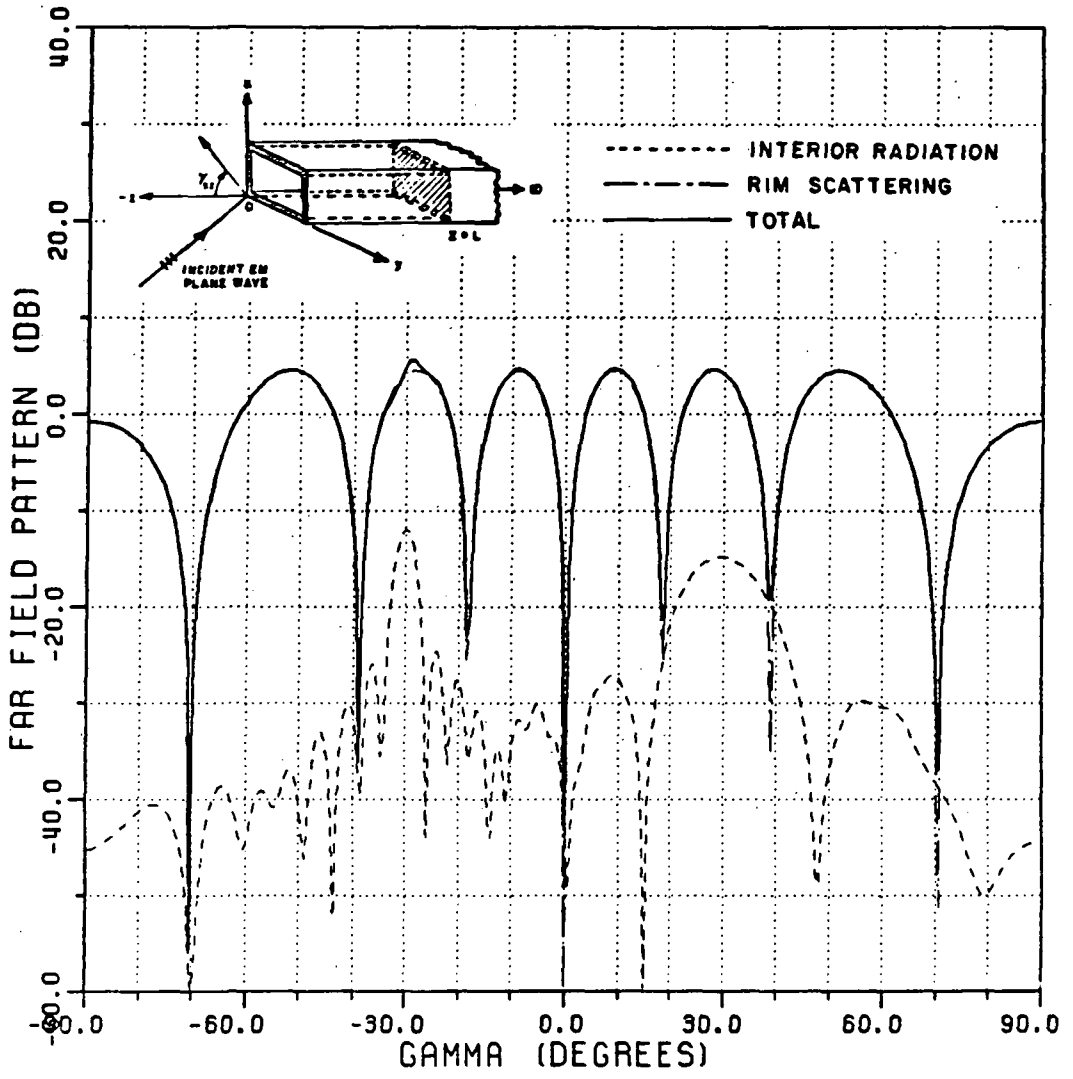

Figure 118: Far zone pattern in the $x - z$ plane of the field scattered by a semi-infinite rectangular waveguide with an interior termination illuminated by an external plane wave whose electric field is polarized parallel to the plane of incidence.

CHAPTER V

SUMMARY AND CONCLUSION

The problem of electromagnetic (EM) plane wave scattering by open-ended, perfectly-conducting, semi-infinite 2–D parallel plate as well as 3–D rectangular waveguides, with a planar interior termination and with a thin, uniform layer of lossy material on their inner walls as well as on the interior termination are analyzed here using high frequency methods. The high frequency methods provide an approximate and simple but sufficiently accurate analysis for this problem as long as the waveguide is large enough (in terms of the wavelength) so that it can support propagating modes. An impedance boundary condition on the inner walls and the termination has also been treated for both the 2–D and the 3–D semi-infinite waveguide configurations. The total field scattered from these configurations is given by a superposition of the fields scattered from the edges at the open end, and the fields which are initially coupled from the external plane wave into the waveguide region and then reflected from the interior termination to radiate back into the exterior region. The fields scattered from the open end as well as that coupled into the waveguide are found via the GTD/UTD ray method. For the fields scattered from the rim edge of the 3–D rectangular waveguide, it is necessary for some aspects to use GTD in conjunction with the equivalent current method (ECM). The contribution to the total scattered field which comes from the interior waveguide cavity radiation (due to the reflection from the interior termination) is

found using AI in conjunction with the physical optics (PO) approximation for the magnetic currents in the aperture. The effect of the edge diffracted rays is ignored in this PO approximation.

The numerical results from the GTD/UTD ray method for representing the interior waveguide fields are compared with those obtained from the formally exact, conventional modal solution for a line source excited interior 2-D waveguide problem (involving an infinitely long waveguide) with an impedance boundary condition on its inner walls in order to check the accuracy and convergence of the ray approximation. It is found that there is an excellent agreement between the two solutions. Some of the advantages of the purely ray approach over the modal approach are that it does afford some physical insight into the propagation and scattering mechanisms particularly in connection with the coupling of the fields from the exterior to the interior regions in the case of the semi-infinite waveguide configuration, as well as into the effect of the wall loss on the fields in the interior waveguide region. The ray solution does not require one to evaluate the eigenvalues which are essential for the construction of the modal solution; these modal eigenvalues must be found numerically for different values of the absorber lining on the interior walls, and for each mode, making the modal approach more cumbersome and inefficient as compared to the ray approach. Also, it is found that, in general, the ray solution converges faster than the modal solution for the case of interest, namely, when the interior waveguide wall becomes lossy. Furthermore, it is also found in this work that, in general, the rate of convergence of the modal solution does not improve significantly even with the presence of loss in the interior waveguide wall.

It is found that the electromagnetic plane wave scattering by the semi-infinite waveguides with an interior termination is strongly dependent on the interior wall

loss. As the wall loss increases, the interior radiation is reduced considerably and the field scattered by the edges at the open end then becomes the dominant contributor to the total scattered field. For the lossless perfectly-conducting case, the scattered field obtained by the present approach is compared with that calculated by a hybrid combination of modal and ray techniques in conjunction with the multiple scattering method (MSM). The two solutions show good agreement in the region of the main and the first side lobes. The discrepancy in other regions is due to the exclusion of the diffracted field for reasons of simplicity in the present calculation dealing with the interior radiation.

While a significant amount of further work is necessary to improve the AI contribution to the total scattered field in the present approach, and also to deal with the scattering by semi-infinite waveguides of arbitrary cross-section and tapers, it is hoped that the present study will efficiently provide a resonable estimate of the effect of absorber coating on the scattering properties of semi-infinite, perfectly-conducting parallel plate and rectangular waveguide configurations with an interior perfectly-conducting planar termination coated with the same absorbing material.

APPENDIX A

BOUNDARY CONDITIONS AT AN IMPEDANCE WALL

Consider an infinite parallel plate waveguide excited by a $\hat{\mathbf{y}}$ directed magnetic line source (TE_y case) as shown in Figure 119. Then, the surface impedance Z_s' at $x = 0$ is defined by the boundary condition [24]

$$\mathbf{E} - \left(\hat{\mathbf{n}} \cdot \mathbf{E}\right) \hat{\mathbf{n}} = Z_s' \, \hat{\mathbf{n}} \times \mathbf{H} \qquad at \; x = 0 \tag{A.1}$$

Since $\mathbf{H}$ has only $\hat{\mathbf{y}}$ component, the right side of Equation (A.1) is reduced to

$$\begin{aligned} Z_s' \, \hat{\mathbf{n}} \times \mathbf{H} &= Z_s' \, \hat{\mathbf{x}} \times \hat{\mathbf{y}} \, H_y \\ &= Z_s' \, \hat{\mathbf{z}} \, H_y \end{aligned} \tag{A.2}$$

Therefore, the surface impedance Z_s' is given by

$$Z_s' = \frac{E_z}{H_y} \qquad \text{at } x = 0 \tag{A.3}$$

From Maxwell's equation,

$$\begin{aligned} \nabla \times \mathbf{H} &= j\omega\epsilon_o \mathbf{E} \\ &= \hat{\mathbf{x}} \left(\frac{\partial H_z}{\partial y} - \frac{\partial H_y}{\partial z}\right) + \hat{\mathbf{y}} \left(\frac{\partial H_x}{\partial z} - \frac{\partial H_z}{\partial x}\right) + \hat{\mathbf{z}} \left(\frac{\partial H_y}{\partial x} - \frac{\partial H_x}{\partial y}\right) \end{aligned} \tag{A.4}$$

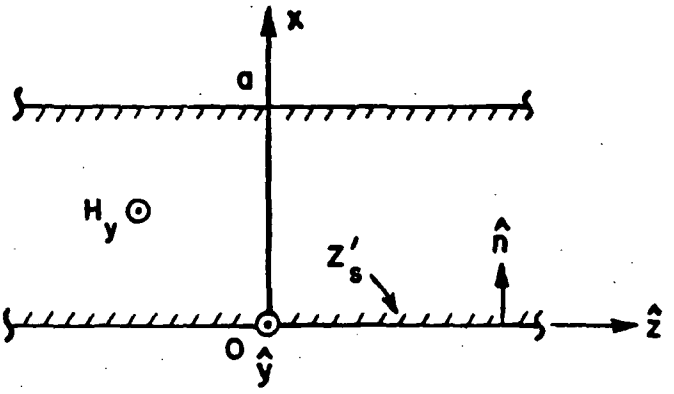

Figure 119: An infinitely long parallel plate waveguide excited by a $\hat{y}$ directed magnetic line source (TE_y).

for the given time convention ($e^{+j\omega t}$). Since $\mathbf{E}$ and $\mathbf{H}$ have $\hat{z}$ and $\hat{y}$ components, respectively, Equation (A.4) is reduced to

$$\begin{aligned} \frac{\partial H_y}{\partial x} &= j\omega\epsilon_o E_z \\ &= jk \frac{Z'_s}{Z_o} H_y \\ &\equiv jk Z_s H_y \end{aligned} \tag{A.5}$$

where Z_o is free-space wave impedance and Z_s is surface impedance normalized to Z_o. Consequently, for $H_y = G$, the boundary condition at $x = 0$ is given by

$$\frac{\partial G}{\partial x} - jk Z_s G = 0 \qquad \text{at } x = 0 \tag{A.6}$$

Similarly, the boundary condition at $x = a$ is expressed as

$$\frac{\partial G}{\partial x} + jk Z_s G = 0 \qquad \text{at } x = a \tag{A.7}$$

By employing the duality, the boundary conditions at $x = 0$ and a can be represented compactly as follows;

$$\frac{\partial G}{\partial x} - jk\varsigma_l G = 0 \qquad \text{at } x = 0 \tag{A.8}$$

$$\frac{\partial G}{\partial x} + jk\varsigma_u G = 0 \qquad \text{at } x = a \tag{A.9}$$

where

$$\varsigma_{l,u} = \begin{cases} Z_{l,u} & \text{for } TE_y \text{ case} \\ Y_{l,u} & \text{for } TM_y \text{ case} \end{cases} \tag{A.10}$$

and $Z_{l,u}$ (or $Y_{l,u}$) is the surface impedance (or admittance) at $x = 0$ and $x = a$ which is normalized to the free-space wave impedance (or admittance), respectively.

APPENDIX B

CONSTRUCTION OF ONE DIMENSIONAL GREEN'S FUNCTIONS

Let $G_x(x,x')$ satisfy the differential wave equation

$$\left[\frac{d^2}{dx^2}+k^2\right] G_x(x,x') = -\delta\,(x-x') \qquad \text{for } 0 \le x \le a \qquad (B.1)$$

and the boundary conditions

$$\frac{dG_x}{dx} - jk\,\varsigma_l\,G_x = 0 \qquad at\ x=0 \qquad (B.2)$$

$$\frac{dG_x}{dx} + jk\,\varsigma_u\,G_x = 0 \qquad at\ x=a \qquad (B.3)$$

where k is the free-space wavenumber and $\delta(x)$ is the Dirac delta function, and

$$\varsigma_{l,u} = \begin{cases} Z_{l,u} & for\ TE_y\ case \\ Y_{l,u} & for\ TM_y\ case \end{cases} \qquad (B.4)$$

where $Z_{l,u}$ (or $Y_{l,u}$) is the surface impedance (or admittance) at $x=0$ and $x=a$. Then $G_x(x,x')$ may be expressed as [11]

$$G_x(x,x') = \begin{cases} \frac{U(x)\,T(x')}{W(T,U)} & x \le x' \\ \frac{U(x')\,T(x)}{W(T,U)} & x \ge x' \end{cases} \qquad (B.5)$$

where $U(x)$ and $T(x)$ are two independent solutions of

$$\left[\frac{d^2}{dx^2}+k^2\right]\left\{\begin{array}{c} U(x) \\ T(x) \end{array}\right\}=0 \qquad 0\le x\le a \tag{B.6}$$

and $W(T,U)$ is the conjunct of $T(x)$ and $U(x)$ defined by

$$W(T,U)=\left[T(x')\,\frac{d}{dx}U(x')-U(x')\,\frac{d}{dx}T(x')\right] \tag{B.7}$$

Equation (B.5) may be compressed into a single expression by using the notation as shown below:

$$G_x(x,x')=\frac{U(x_<)\,T(x_>)}{W(T,U)} \tag{B.8}$$

where $x_<$ means use x if $x<x'$ or use x' if $x'<x$.

Let $U(x)$ be represented by

$$U(x)=e^{+jk_xx}+R_l\,e^{-jk_xx} \tag{B.9}$$

where R_l is a constant to be determined. From the boundary condition at $x=0$ given in Equation (B.2), it follows

$$k_x\left(e^{+jk_xx}-R_l\,e^{-jk_xx}\right)-k\,\varsigma_l\left(e^{+jk_xx}+R_l\,e^{-jk_xx}\right)=0 \tag{B.10}$$

Then,

$$R_l=\frac{k_x-k\,\varsigma_l}{k_x+k\,\varsigma_l} \tag{B.11}$$

and $U(x)$ is given by

$$U(x) = e^{+jk_x x} + \frac{k_x - k\,\varsigma_l}{k_x + k\,\varsigma_l}\, e^{-jk_x x} \qquad (B.12)$$

Likewise, let $T(x)$ be expressed by

$$T(x) = e^{-jk_x x} + R_u\, e^{+jk_x x} \qquad (B.13)$$

Similarly, applying the boundary condition at $x = a$ in Equation (B.3) to $T(x)$ and solving the equation for the constant R_u gives

$$T(x) = e^{-jk_x x} + \frac{k_x - k\,\varsigma_u}{k_x + k\,\varsigma_u}\, e^{-j2k_x\, a}\, e^{+jk_x x} \qquad (B.14)$$

Next, from Equations (B.7), (B.9) and (B.13) the $W(T,U)$ is given by

$$\begin{aligned} W(T,U) &= T(x)\,\frac{d}{dx}\,U(x) - U(x)\,\frac{d}{dx}\,T(x)\,\Big|_{x=x'} \\ &= \left(\, e^{-jk_x x'} + R_u\, e^{+jk_x x'} \right) \left(\, jk_x\, e^{+jk_x x'} - jk_x\, R_l\, e^{-jk_x x} \right) \\ &\quad - \left(\, e^{+jk_x x'} + R_l\, e^{-jk_x x'} \right) \left(\, -jk_x\, e^{-jk_x x'} + jk_x\, R_u\, e^{+jk_x x} \right) \\ &= 2jk_x(\,1 - R_l\, R_u\,) \end{aligned} \qquad (B.15)$$

Consequently, $G_x(x,x')$ is found to be

$$G_x(x,x') = \frac{(\,e^{jk_{x<}} + R_l\, e^{-jk_{x<}})\,(\,e^{-jk_{x>}} + R_u\, e^{jk_{x>}})}{2jk_x\,(1 - R_l Ru)} \qquad (B.16)$$

For $G_z(z,z')$, a similar procedure is repeated for the differential equation

$$\left[\frac{d^2}{dz^2} + k^2 \right] \left\{ \begin{array}{c} U(z) \\ T(z) \end{array} \right\} = 0 \qquad (B.17)$$

where $G_z(z, z')$ satisfies the boundary condition

$$\frac{dG_z}{dz} \pm jk\, G_z = 0 \qquad as\ |z| \to \infty \qquad (B.18)$$

Let $U(z)$ and $T(z)$ be represented by

$$U(z) = e^{+jk_z z} \qquad (B.19)$$

$$T(z) = e^{-jk_z z} \qquad (B.20)$$

Then, the conjunct $W(T, U)$ is given by

$$\begin{aligned} W(T,U) &= jk_z \left(e^{-jk_z z'}\, e^{+jk_z z'} + e^{-jk_z z'}\, e^{+jk_z z'} \right) \\ &= j2k_z \end{aligned} \qquad (B.21)$$

Therefore, $G_z(z, z')$ is expressed as

$$G_z(z, z') = \frac{e^{-jk_z\,|z-z'|}}{2jk_z} \qquad (B.22)$$

APPENDIX C

A METHOD FOR THE NUMERICAL SOLUTION OF MODAL EIGENVALUES

The transcendental equation for solving the modal eigenvalues is obtained by setting the denominator of the integrand in Equation (2.12) equal to zero. Let this equation be written symbolically as $F(k_x) = 0$. This transcendental equation can be re-expressed in terms of any of its roots denoted by k_x as:

$$F(k_x) = (k_x - k\varsigma_l)\,(k_x - k\varsigma_u)\,e^{-j2k_x a} - (k_x + k\varsigma_l)\,(k_x + k\varsigma_u) \qquad (C.1)$$

A popular method of finding the roots of a transcendental equation is the '*Newton–Raphson*' method. The basic theory behind this method is that the function $F(x)$ is expanded in a Taylor series about some point x_o which gives

$$F(x) = F(x_o) + (x - x_o)\,F'(x_o) + \frac{1}{2}(x - x_o)^2\,F''(x_o) + \cdots \qquad (C.2)$$

With the assumption that x is the root and x_o is a good initial guess of the root, the series can be written approximately as

$$F(x) \approx F(x_o) + (x - x_o)\,F'(x_o) \qquad (C.3)$$

since $(x - x_o)$ is small due to x being approximately equal to x_o by a good initial guess. Then the above equation can be rewritten as

$$x_o \approx -\frac{F(x_o)}{F'(x_o)} \tag{C.4}$$

which gives the iterative equation

$$x_{n+1} \approx x_n - \frac{F(x_n)}{F'(x_n)} \tag{C.5}$$

where x_n and x_{n+1} are the values of x after the n^{th} and $(n+1)^{th}$ iterations, respectively.

As seen from the above approximation, it is necessary to have a good initial guess when using the '*Newton-Raphson*' method. This will allow rapid convergence to the proper root. The eigenvalues of the waveguide with perfectly-conducting inner walls are used as the initial guess in the modal analysis of the waveguide with impedance walls. The computer program stops iterating when the percent change in the magnitude of the root between successive iterations is less than 10^{-4}.

APPENDIX D

REFLECTION COEFFICIENTS FOR AN IMPEDANCE BOUNDARY

Consider a plane wave obliquely incident on a surface impedance boundary, as shown in Figure 120. The incident and reflected waves make angles of θ^i and θ^r with the x axis, respectively, and Z_s is a normalized surface impedance. The field vectors shown in the figure are those corresponding to the TE_y case and thus $\mathbf{H}$ has only a $\hat{\mathbf{y}}$ component.

The incident and reflected magnetic fields $\mathbf{H}^i$ and $\mathbf{H}^r$ in this TE_y case are represented by

$$\mathbf{H}^i = \hat{\mathbf{y}}\, H^i = \hat{\mathbf{y}}\, e^{jk(x\cos\theta^i - z\sin\theta^i)} \tag{D.1}$$

$$\mathbf{H}^r = \hat{\mathbf{y}}\, H^r = \hat{\mathbf{y}}\, \tilde{R}_{\parallel}\, e^{jk(x\cos\theta^r - z\sin\theta^r)} \tag{D.2}$$

where $\tilde{R}_{\parallel}$ is the reflection coefficient for the $\hat{\mathbf{y}}$-directed magnetic field (or for the electric field which is polarized parallel to the plane of incidence ($x - z$ plane in Figure 120)). The total magnetic field H_y satisfies the following equation on the impedance boundary

$$\frac{\partial H_y}{\partial x} - jk\, Z_s\, H_y = 0 \qquad \text{at } x = 0 \tag{D.3}$$

Therefore, incorporating Equations (D.1) and (D.2) into Equation (D.3) gives

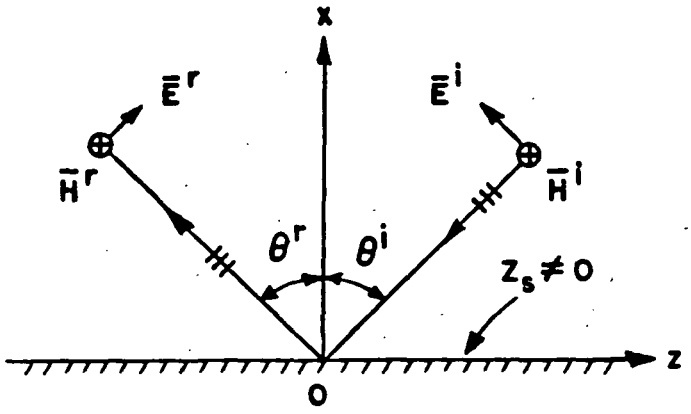

Figure 120: A plane wave obliquely incident on a surface impedance boundary.

$$\left(jk\cos\theta^i - jkZ_s\right) e^{-jkz\sin\theta^i} - \tilde{R}_{\|}\left(jk\cos\theta^r + jkZ_s\right) e^{-jkz\sin\theta^r} = 0 \qquad (D.4)$$

From Equation (D.4) one obtains the law of reflection ($\theta^i = \theta^r$) so that the fields can be phase matched at the boundary in order to satisfy Equation (D.3). As a result, Equation (D.4) reduces to

$$\tilde{R}_{\|}\left(Z_s + \cos\theta^i\right) + \left(Z_s - \cos\theta^i\right) = 0 \qquad (D.5)$$

Hence the reflection coefficient for the $\hat{y}$-directed magnetic field in the TE_y case is given by

$$\tilde{R}_{\|} = \frac{\cos\theta^i - Z_s}{\cos\theta^i + Z_s} \qquad (D.6)$$

Likewise, the reflection coefficient for the $\hat{y}$-directed electric field in the TM_y case is given by

$$\tilde{R}_{\perp} = \frac{\cos\theta^i - Z_s^{-1}}{\cos\theta^i + Z_s^{-1}} \qquad (D.7)$$

APPENDIX E

TRANSITION FUNCTION

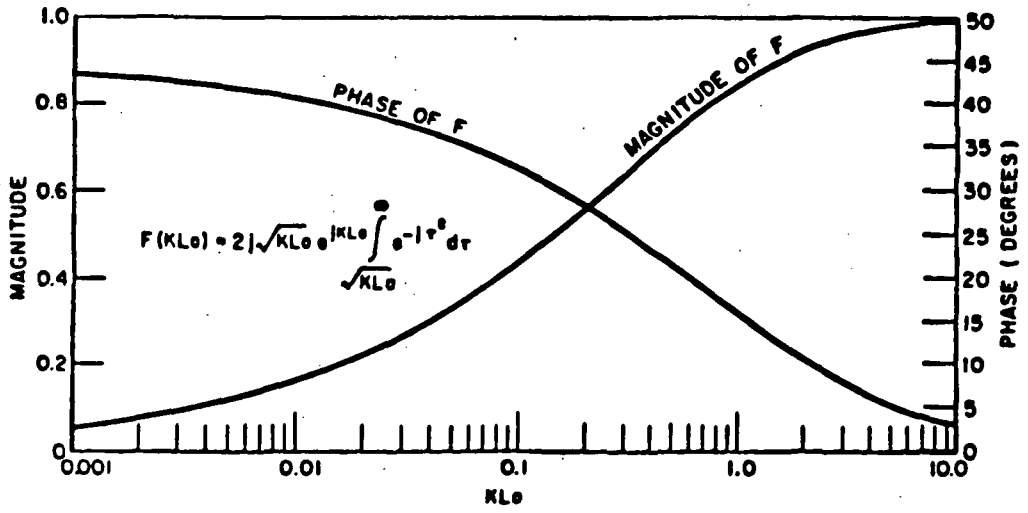

Figure 121: The magnitude and phase of the transition function.

APPENDIX F

REFLECTION COEFFICIENTS FOR A DIELECTRIC/FERRITE SLAB ON A PERFECTLY CONDUCTING GROUND PLANE

The dielectric/ferrite slab making up the semi-infinite parallel plate and rectangular waveguide walls is illustrated in Figure 122. The slab has a thickness t, and it is backed by a perfectly conductor of electricity. While the Region I (free-space) for $x > t$ is chracterized by (ϵ_1, μ_1), the Region II (dielectric/ferrite slab) is characterized by (ϵ_2, μ_2) for $0 < x < t$. A plane wave is incident on the slab at an angle of ϕ' from the x-axis. The *transverse resonance method* [4,25] is employed for the *Fresnel reflection coefficient* of the slab. The equivalent transmission–line circuit model for the Figure 122 is shown in Figure 123. Z_1 and Z_2 are wave impedances of the wave in Region I and II, respectively.

The characteristic impedances for TM_y and TE_y polarizations are given by

$$Z^e_{1,2} = \frac{k_{1,2}\,\eta_{1,2}}{\beta_{1,2}} \qquad \text{for } TM_y \text{ case} \tag{F.1}$$

$$Z^m_{1,2} = \frac{k_{1,2}\,\beta_{1,2}}{\eta_{1,2}} \qquad \text{for } TE_y \text{ case} \tag{F.2}$$

where

$$N = \sqrt{\frac{\epsilon_2\,\mu_2}{\epsilon_1\,\mu_1}} \tag{F.3}$$

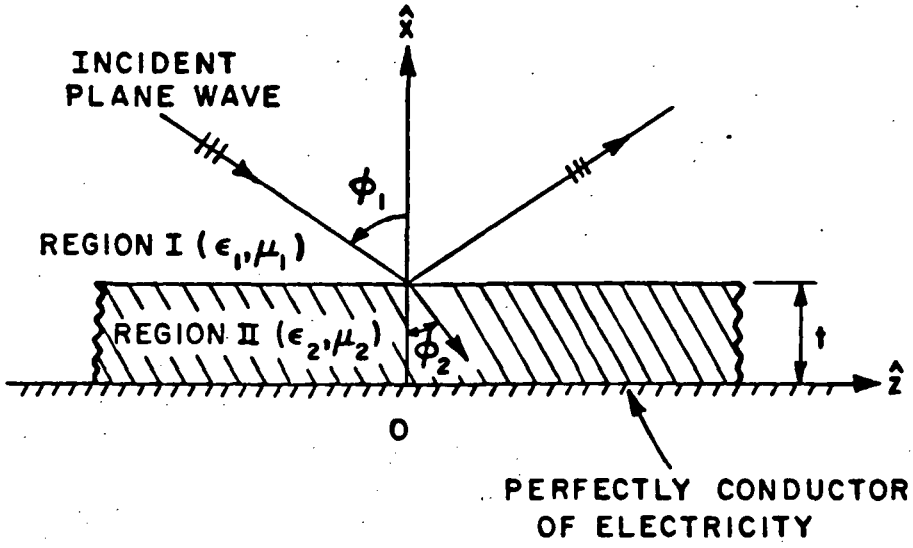

Figure 122: A Dielectric/ferrite slab grounded by a perfectly conductor of electricity.

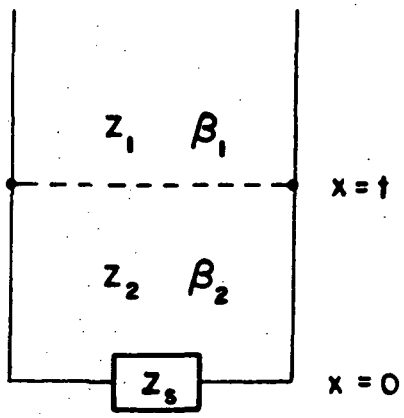

Figure 123: Equivalent transmission-line circuit for Figure 122.

$$k_{1,2} = \omega \sqrt{\epsilon_{1,2}\,\mu_{1,2}} \tag{F.4}$$

$$\beta_1 = k_1 \cos\phi_1 \tag{F.5}$$

$$\begin{aligned} \beta_2 &= k_2 \cos\phi_2 = k_2 \sqrt{1 - \sin^2\phi_2} \\ &= k_1 \sqrt{N^2 - \sin^2\phi_1} \end{aligned} \tag{F.6}$$

$$\eta_{1,2} = \sqrt{\frac{\mu_{1,2}}{\epsilon_{1,2}}} \tag{F.7}$$

From transmission-line theory, the input impedance at $x = t$ is given by

$$Z_{in}(x = t) = Z_2 \frac{Z_s + j\, Z_2 \tan(\beta_2 t)}{Z_2 + j\, Z_s \tan(\beta_2 t)} \tag{F.8}$$

Since Z_s=0 for electrically perfectly conductor at $x = 0$, Equation (F.8) reduces to

$$Z_{in}(x = t) = j\, Z_2 \tan(\beta_2 t) \tag{F.9}$$

Then, the reflection coefficient for TM_y at $x = t$ can be written as

$$\tilde{R}_\perp(x = t) = \frac{Z_{in}(x = t) - Z_1^e}{Z_{in}(x = t) + Z_1^e} \tag{F.10}$$

Therefore, incorporating Equations (F.3) through (F.7) into Equation (F.10) gives

$$\tilde{R}_\perp(x = t) = \frac{\cos\phi_1 + j\,\frac{\mu_1}{\mu_2}\sqrt{N^2 - \sin^2\phi_1}\,\cot\left(k_1 t\sqrt{N^2 - \sin^2\phi_1}\right)}{\cos\phi_1 - j\,\frac{\mu_1}{\mu_2}\sqrt{N^2 - \sin^2\phi_1}\,\cot\left(k_1 t\sqrt{N^2 - \sin^2\phi_1}\right)} \tag{F.11}$$

For TE_y the reflection coefficient is represented by

$$\tilde{R}_{\parallel}(x=t) = \frac{Z_1^m - Z_{in}(x=t)}{Z_1^m + Z_{in}(x=t)} \qquad (F.12)$$

Substituting Equations (F.3) through (F.7) into Equation (F.13) gives

$$\tilde{R}_{\parallel}(x=t) = \frac{\cos\phi_1 - j\,\frac{\epsilon_1}{\epsilon_2}\sqrt{N^2 - \sin^2\phi_1}\,\tan\left(k_1 t\sqrt{N^2 - \sin^2\phi_1}\right)}{\cos\phi_1 + j\,\frac{\epsilon_1}{\epsilon_2}\sqrt{N^2 - \sin^2\phi_1}\,\tan\left(k_1 t\sqrt{N^2 - \sin^2\phi_1}\right)} \qquad (F.13)$$

REFERENCES

[1] R.G. Kouyoumjian and P.H. Pathak, "A uniform geometrical theory of diffraction for an edge in a perfectly conducting surfac", Proc. IEEE, Vol. 62, pp. 1448–1461, 1974.

[2] J.B. Keller, "Geometrical theory of diffraction", J. Opt. Soc. of Am., Vol. 52, pp. 116–130, 1962.

[3] L.A. Weinstein, *The Theory of Diffraction and the Factorization Method*, The Golem Press, Boulder, Colorado, 1969.

[4] Robert E. Collin, *Field Theory of Guided Waves*, McGraw-Hill Book Co., New York, 1960.

[5] R. Mittra and S.W. Lee, *Analytical Techniques in the Theory of Guided Waves*, The Macmillan Company, New York, 1971.

[6] L. Lewin, *Theory of Waveguides*, John Wiley and Sons, New York, 1975.

[7] L.B. Felsen and A.H. Kamel, "Hybrid Ray–Mode Formulation of Parallel Plane Waveguide Green's Functions", IEEE Trans, AP, Vol. AP-29, No. 4, pp. 637–649, Jul. 1981.

[8] C.S. Lee, S.L. Chuang, S.W. Lee, Y.T. Lo, "Wave Attenuation and Mode Dispersion in a Waveguide Coated with Lossy Dielectric Material", Technical

Report No. 84–13, University of Illinois, Electromagnetics Laboratory, July 1984.

[9] L.B. Felsen and N. Marcuvitz, *Radiation and Scattering of Waves*, Prentice Hall, Englewood Cliffs, New Jersey, 1973.

[10] B. Friedman, *Principles and Techniques of Applied Mathematics*, John Wiley and Sons, Inc., 1966.

[11] R.G. Kouyoumjian, Class notes in electromagnetics area offered at The Ohio State University.

[12] W.D. Burnside and K.W. Burgener, "High Frequency Scattering by a Thin Lossless Dielectric Slab", IEEE Trans. AP, Vol. AP-31, No. 1, pp. 104–110, Jan. 1983.

[13] G.D. Maliuzhinets, "Excitation, Reflection and Emission of Surface Waves from a Wedge with Given Fact Impedances", Soviet Phy. Dokl., Engl. Transl., 3, pp. 752–755, 1958.

[14] R.F. Harrington, *Time Harmonic Electromagnetic Fields*, McGraw-Hill Book Co., New York, pp. 100–103, 143–263, 1961.

[15] C.A. Balanis, *Antenna Theory, analysis and design*, Harper and Row Publishers, New York, pp. 447–454, 1982.

[16] E.V. Jull, *Aperture Antennas and Diffraction Theory*, Peter Peregrinus Ltd., New York, 1981.

[17] P.H. Pathak, A. Altintas, C.W. Chuang and S. Barkeshli, "Near Field Scattering by Rectangular and Circular Inlet Configurations with an Impedance

Surface Termination", Final Report 715267-1, The Ohio State University, ElectroScience Laboratory, prepared under contract No. N60530-83-M-40RD for Naval Weapons Center, China Lake, CA, July 1984.

[18] P.H. Pathak, C.W. Chuang, "Continuation of work on Near and Far Field Scattering by Rectangular and Circular Inlet Configulations with an Impedance Surface Termination", Final Report 715979-1, The Ohio State University, ElectroScience Laboratory, prepared under contract No. N60530-84-C-0143 for Naval Weapons Center, China Lake, CA, June 1985.

[19] P.H. Pathak, C.W. Chuang, M.C. Liang, N. Wang. H.T. Kim, "Ram and Inlet Modeling Studies", Final Report 716495-2, The Ohio State University, ElectroScience Laboratory, prepared under contract No. N60530-84-C-0143 for Naval Weapons Center, China Lake, CA, October 1985.

[20] C.E. Ryan and L.Peters, Jr., "Evaluation of Edge Diffracted Fields Including Equivalent Currents for the Caustic Regions", IEEE AP, Vol. AP-17, No. 3, pp. 292-299, May 1969.

[21] W.D. Burnside and L. Peters, Jr., "Axial Radar Cross Section of Finite Cones by the Equivalent current Concept with Higher-order Diffraction", Radio Science, Vol. 7, No. 10, pp. 943-948, Oct., 1972.

[22] P.H. Pathak, "Techniques for High Frequency Problems", Chapter IV in *Handbook of Antenna Theory and Design*, Eds., Y.T. Lo and S.W. Lee, to be published by ITT-Howard W. Sams and Co., Inc.

[23] R.G. Kouyoumjian, P.H. Pathak and W.D. Burnside, "A Uniform GTD for the Diffraction by Edges, Vertices and Convex Surface", in *Theoretical Method*

for Determining the Interaction of Electromagnetic Waves with Structure, J.K. Swirzynski, ed., Netherlands, Sijthoff and Noordhoff, 1981.

[24] E.F. Knott and T.B.A. Senior, "Comparison of Three High-Frequency Diffraction Technique", Proc. IEEE, Vol. 62, pp. 1468–1474, 1974.

[25] R.G. Rojas-Teran, "A Uniform GTD Analysis of the EM Diffraction by a Thin Dielectric/ferrite Half-plane and Related Configurations", Ph.D. dissertation, The Ohio State University, Department of Electrical Engineering, Columbus, Ohio, 1985.

50272-101

REPORT DOCUMENTATION PAGE	1. REPORT NO.	2.	3. Recipient's Accession No.

4. Title and Subtitle A HIGH FREQUENCY ANALYSIS OF ELECTROMAGNETIC PLANE WAVE SCATTERING BY PERFECTLY CONDUCTING SEMI INFINITE PARALLEL PLATE AND RECTANGULAR WAVEGUIDES WITH ABSORBER COATED INNER WALLS

5. Report Date September 1986

6.

7. Author(s) Noh Hoon Myung and P.H. Pathak

8. Performing Organization Rept. No. 715723-1

9. Performing Organization Name and Address
The Ohio State University ElectroScience Laboratory
1320 Kinnear Road
Columbus, Ohio 43212

10. Project/Task/Work Unit No.

11. Contract(C) or Grant(G) No
(C)
(G) NAG 3-476

12. Sponsoring Organization Name and Address
National Aeronautics and Space Administration
Lewis Research Center
21000 Brookpark Road
Cleveland, Ohio 44135

13. Type of Report & Period Covered

14.

15. Supplementary Notes

16. Abstract (Limit: 200 words)

An approximate but sufficiently accurate high frequency solution which combines the uniform geometrical theory of diffraction (UTD) and the aperture integration (AI) method is developed in this study for analyzing the problem of electromagnetic (EM) plane wave scattering by an open-ended, perfectly-conducting, semi-infinite hollow rectangular waveguide (or duct) with a thin, uniform layer of lossy or absorbing material on its inner wall, and with a planar termination inside. In addition, a high frequency solution for the EM scattering by a two dimensional (2-D), semi-infinite parallel plate waveguide with an absorber coating on the inner walls is also developed as a first step before analyzing the open-ended semi-infinite three dimensional (3-D) rectangular waveguide geometry. The total field scattered by the semi-infinite waveguide consists firstly of the fields scattered from the edges of the aperture at the open-end, and secondly of the fields which are coupled into the waveguide from the open-end and then reflected back from the interior termination to radiate out of the open-end. The first contribution to the scattered field can be found directly via the UTD ray method; whereas, the second contribution is found via the AI method which employs rays to describe the fields in the aperture that arrive there after reflecting from the interior termination. It is assumed in the present study that the direction of the incident plane wave and the direction of observation lie well inside the forward half space that exists outside the half space containing the semi-infinite waveguide geometry. Also, the medium exterior to the waveguide is assumed to be free space.

17. Document Analysis a. Descriptors

b. Identifiers/Open-Ended Terms

c. COSATI Field/Group

18. Availability Statement	19. Security Class (This Report)	21. No. of Pages
Approved for public release; distribution is unlimited.	Unclassified	217
	20. Security Class (This Page) Unclassified	22. Price

(See ANSI-Z39.18) See Instructions on Reverse OPTIONAL FORM 272 (4-77) (Formerly NTIS-35) Department of Commerce

It is found that, in general, the ray solution used here for describing the fields within the waveguide region converges faster and is more efficient than the modal solution for the case of interest, namely, when the interior wall coating is lossy. Furthermore, it is also found in this work that, in general, the rate of convergence of the modal solution does not improve significantly even with the presence of loss in the wall coating. In addition, the level of the fields which are coupled into the interior of the semi-infinite waveguide and then re-radiated from the open end, after undergoing reflection at the interior termination, can be controlled by changing the value of the absorber lining on the interior waveguide walls as might be expected. If these fields radiated from the open-end are made sufficiently small, the only other contribution to the total exterior scattered field, which comes from the diffraction by the edges of the aperture at the open-end, will then be dominant.